ISSN 2074-272X

науково-практичний журнал 2025/3

Електротехніка і Електромеханіка

Electrical Engineering & Electromechanics

Електричні машини та апарати
Електротехнічні комплекси та системи
Промислова електроніка
Теоретична електротехніка
Техніка сильних електричних та магнітних полів, інженерна електрофізика
Електроізоляційна та кабельна техніка

Журнал включено до найвищої категорії «А» Переліку фахових видань України

З 2019 р. журнал індексується у Scopus

З 2015 р. журнал індексується у Web of Science Core Collection: Emerging Sources Citation Index

«ЕЛЕКТРОТЕХНІКА І ЕЛЕКТРОМЕХАНІКА»
«ELECTRICAL ENGINEERING & ELECTROMECHANICS»

Науковий журнал. Засновано в 2002 р.
Видання засновано і видається Національним технічним університетом «Харківський політехнічний інститут» (НТУ «ХПІ») та Інститутом енергетичних машин і систем ім. А.М. Підгорного НАН України (ІЕМС НАН України)
Ідентифікатор медіа **R30-01539**, згідно з рішенням Нацради України з питань телебачення і радіомовлення від 16.10.2023 № 1075

Адреса редакції / Editorial office address:
Національний технічний університет «Харківський політехнічний інститут», вул. Кирпичова, 2, м. Харків, 61002, Україна
National Technical University «Kharkiv Polytechnic Institute», Kyrpychova Str., 2, Kharkiv, 61002, Ukraine
тел. / phone: +380 67 3594696, e-mail: a.m.grechko@gmail.com (**Гречко Олександр Михайлович** / **Grechko O.M.)**

ISSN (print) 2074-272X
ISSN (online) 2309-3404

Підписано до друку 30.04.2025 р. Формат 60 × 90 ⅛. Папір – офсетний. Друк – лазерний. Друк. арк. 9,75.
Наклад 50 прим. Зам. № 66/172-03-2025. Ціна договірна. Надруковано ТОВ «Друкарня «Мадрид», Україна, 61024, м. Харків, вул. Гуданова, 18

ЕЛЕКТРОТЕХНІКА І ЕЛЕКТРОМЕХАНІКА
ELECTRICAL ENGINEERING & ELECTROMECHANICS
Науковий журнал
Scientific journal

EIE

Рекомендовано до видання Вченою радою НТУ «ХПІ», протокол № 5 від 18.04.2025
та Вченою радою ІЕМС НАН України, протокол № 3 від 13.03.2025

2025/3

ЗМІСТ

TABLE OF CONTENTS

Industrial Electronics

Theoretical Electrical Engineering

High Electric and Magnetic Fields Engineering, Engineering Electrophysics

Electrical Insulation and Cable Engineering

Anniversaries

ШАНОВНІ ЧИТАЧІ!

З 2024 р. з об'єктивних причин журнал «Електротехніка і Електромеханіка» вимушений припинити співпрацю з АТ «Укрпошта» щодо передплати та розповсюдження друкованих примірників нашого журналу. Якщо Ви, шановні читачі, і надалі бажаєте отримувати друковані примірники нашого журналу, то Ви можете їх замовити, звернувшись безпосередньо до редакції журналу.

ШАНОВНІ АВТОРИ ЖУРНАЛУ!

Постановою президії ВАК України від 15 січня 2003 р. № 1-08/5 науковий журнал «Електротехніка і Електромеханіка» внесено до Переліку наукових фахових видань України, в яких можуть публікуватися результати дисертаційних робіт на здобуття наукових ступенів доктора і кандидата наук та перереєстровано Наказом МОН України № 1328 від 21 грудня 2015 р. Журнал зареєстровано як фаховий з № 1 2002 року.

Згідно Наказу МОН України №1412 від 18.12.2018 р. науковий журнал «Електротехніка і Електромеханіка» включено до найвищої категорії «А» Переліку фахових видань України з технічних наук.

Електронна копія журналу «Електротехніка і Електромеханіка», зареєстрованому у Міжнародній системі реєстрації періодичних видань під стандартизованим кодом ISSN 2074-272X, надсилається до Національної бібліотеки України ім. В.І. Вернадського і, починаючи з 2005 р., представлена на сайті бібліотеки (http://nbuv.gov.ua) в розділі «Наукова періодика України», а також на офіційному сайті журналу (http://eie.khpi.edu.ua).

Починаючи з №1 за 2016 р. усі статті на сайті доступні на двох мовах – англійською і українською. Також кожній статті в журналі присвоюється унікальний цифровий ідентифікатор DOI (Digital Object Identifier) від організації Crossref (http://crossref.org).

Журнал «Електротехніка і Електромеханіка» з 2019 р. індексується у наукометричній базі даних Scopus, з 2005 р. – у Web of Science Core Collection: Emerging Sources Citation Index (ESCI), що рекомендовані МОН України. Також журнал представлений в Index Copernicus (ICV 2023: 112.75), і входить до баз даних EBSCO, ProQuest, GALE, DOAJ тощо.

Наукометричні показники журналу «Електротехніка і Електромеханіка»:
CiteScore 2023 – 2.4; H-індекс – 14, квартиль – Q3; SJR 2024 – 0.350, SNIP 2023 – 0.789; IPP – 1.44.

Звертаємо увагу авторів на необхідність оформлення рукописів відповідно до Вимог, які наведені на офіційному сайті журналу (http://eie.khpi.edu.ua), розміщеному на платформі «Наукова періодика України» (http://journals.uran.ua).

UDC 621.313.318 https://doi.org/10.20998/2074-272X.2025.3.01

V.F. Bolyukh

Electromechanical processes during the start of induction-type magnetic levitation

Purpose. *A study of induction-type magnetic levitation by determining the electromechanical processes that occur when a stationary inductor is connected to an alternating voltage source and the levitation of an anchor made in the form of a multi-turn short-circuited winding with an attached load.* ***Methodology.*** *Using a mathematical model describing an inductor and an anchor with concentrated parameters, solutions are presented for equations describing the interconnected electrical, magnetic, mechanical and thermal processes that occur in induction-type magnetic levitation.* ***Results.*** *The influence of the frequency of the alternating current source on the electromechanical processes of levitation, which occur at different parameters of the anchor, is established. Due to the phase delay of the induced anchor current in relation to the inductor current, an electrodynamic force directed downwards arises at certain moments of their period. The total force acting on the anchor, due to the electrodynamic component, is of an alternating nature with a predominance of the positive, upwardly directed component, which causes pulsations of the anchor speed.* ***Originality.*** *The force acting on the anchor due to the electrodynamic component is of an alternating nature with the positive component directed upwards dominating. The resulting oscillatory damping mechanical process occurs with an increase in the oscillation period and a decrease in its amplitude.* ***Practical value.*** *It has been established that the maximum value of the lifting force acting on the anchor is achieved at an alternating current frequency in the range from 75 to 125 Hz, and the highest value of the steady-state levitation height is realized for an anchor similar to an inductor at a frequency of 75 Hz.* References 37, figures 6.

Key words: **magnetic levitation of induction type, mathematical model, experimental test, starting electromechanical characteristics, oscillatory electromechanical process.**

Мета. *Дослідження магнітної левітації індукційного типу шляхом визначення електромеханічних процесів, що виникають при підключенні нерухомого індуктора до джерела змінної напруги та левітації якоря виконаного у вигляді багатовиткової короткозамкненої обмотки з приєднаним навантаженням.* ***Методологія.*** *За допомогою математичної моделі, яка описує індуктор та якір із зосередженими параметрами, представлені рішення рівнянь, що описують взаємопов'язані електричні, магнітні, механічні та теплові процеси, що виникають у магнітній левітації індукційного типу.* ***Результати.*** *Встановлено вплив частоти джерела змінного струму на електромеханічні процеси левітації, що виникають за різних параметрів якоря. Через фазову затримку індукованого струму якоря по відношенню до струму індуктора в певні моменти їх періоду виникає електродинамічна сила спрямована вниз. Сумарна сила, що діє на якір, через електродинамічний складник, носить знакозмінний характер з переважанням позитивної, спрямованої вгору складової, що обумовлює пульсації швидкості якоря.* ***Оригінальність.*** *Діюча на якір сила через електродинамічну складову носить знакозмінний характер з переважанням позитивної, спрямованої вгору складової. Виникаючий при цьому коливально загасаючий механічний процес відбувається зі збільшенням періоду коливань та зменшенням його амплітуди.* ***Практична цінність.*** *Встановлено, що максимальна підйомна сила, що діє на якір, досягається при частоті змінного струму в діапазоні від 75 до 125 Гц, а найбільша висота левітації, що встановилася, реалізується для якоря, аналогічного індуктору, при частоті 75 Гц.* Бібл. 37, рис. 6.

Ключові слова: **магнітна левітація індукційного типу, математична модель, експериментальне випробування, пускові електромеханічні характеристики, коливальний електромеханічний процес.**

Introduction. Magnetic levitation allows for qualitative improvement of existing technologies and finds application in transport, aerospace, chemical, biomedical engineering and other fields of science and technology. High-speed trains have been created on the basis of magnetic levitation and contactless suspension of aircraft models in wind tunnels is provided [1]. It helps circulate blood in the human chest, is used in the production of integrated circuits, measures dimensions with subatomic resolution, is involved in plasma research, melts and mixes chemically active high-temperature metals, simulates the sense of touch in tactile systems, cools laptops, enriches uranium and isotopes in centrifuges, stores energy in rotating flywheels, and powers rotors in machines [2]. Levitating micro-actuators eliminate the mechanical connection between fixed and moving parts, ensuring that inertial forces dominate over frictional forces [3]. Based on magnetic levitation, electromagnetic energy sources driven by motion are being developed, which are used for autonomous power supply of various high-tech devices, such as remote sensors, wearable devices, biomedical implants, etc. [4].

Features of the application of magnetic levitation. Magnetic levitation is used in actuators, accelerometers, gyroscopes, magnetic bearings, dampers, etc. It is used to stabilize and control sea vessels, spacecraft, and other critical objects.

In micro-drives, magnetic levitation not only eliminates friction, but also essentially creates a built-in micro-sensor with a long service life [3]. Levitating micro-actuators can operate in harsh conditions (with increased vibration and temperature, in a chemically aggressive environment, etc.), preventing contact of the micro-object with surfaces. They are used as sensors, motors, switches, accelerators, particle traps, conveyors, bearings, etc.) [3]. The micro-actuator allows for the implementation of a combination of induction-type magnetic levitation and an electrostatic actuator [5]. The mathematical model of the said levitation considers a conducting disk located between two circular currents. Such a model takes into account two degrees of freedom, allowing for the evaluation of static displacement and suspension stability.

Magnetic levitation is used to stabilize and stabilize a vessel, to reduce vibration and noise [6]. For these purposes, the accelerations of the stator and the stabilizing mass block were measured when the excitation winding was supplied with a sinusoidal voltage of 0–500 Hz.

The contactless magnetically stabilized spacecraft provides increased reliability and more precise control in a six-degree-of-freedom system [7]. Control of the excitation current of the contactless ring electromagnetic drive directly affects its orientation characteristics. Magnetic

bearings are used for the inertial drive of the spacecraft, and active control is used to eliminate unbalanced vibration in the magnetic levitation system [8].

The dual-hinged gyroscope of the magnetic levitation spacecraft provides position determination and position control [9]. The dual-axis angular velocity of the spacecraft is determined from control signals in the active magnetic suspension control system for the high-speed rotor. The angular velocity of the magnetic levitation gyroscope is measured by determining the current and noise of the tilt signal on the orientation accuracy of the spacecraft [10].

Magnetic levitation is used for magnetic bearings and dampers because they are stable and easy to use at both low and medium speeds. The magnetic damper reduces vibrations and noise in devices [11], and the active magnetic bearing suppresses disturbances in the control system and displacement vibrations [12].

The three-magnetic bearing platform provides drive weight compensation with ultra-precise installation, long stroke and high acceleration [13]. It uses magnetic bearings to provide lifting force and in-plane torque. Magnetic levitation can be effectively used in high-precision gravimeters to reduce autoseismic vibrations [14, 15].

A miniature rotating gyroscope is described in [16] in which a 0.5 mm thick aluminum rotor levitates and rotates relative to a flat coil. When high-frequency alternating current with temporal and spatial phase distribution is applied to the coil, the rotor rotates. Two internal conductors provide levitation, and the outer conductor provides lateral stability, preventing the rotor from sliding sideways. When tested for 200 hours, the micromotors remained operational at high current densities and elevated temperatures, showing no signs of degradation.

A promising direction of magnetic levitation is medicine. For a disposable extracorporeal system, a magnetically levitating centrifugal pump has been developed that provides blood circulation [17]. Such a pump, with high productivity, eliminates mechanical contact with the impeller, reduces heating and reduces blood trauma, preventing the formation of blood clots.

However, in a magnetic levitation system there is a problem of stabilizing suspended bodies. The stability of the system is affected by the mechanical interface between the levitation object and the loaded device, and self-exciting vibration occurs during operation. To study the effect of the gap size on the mechanical behavior of the system, a coupled electromagnetic-mechanical model with lumped parameters was considered in [18]. It was found that with a decrease in the gap size, the vibration frequency increases.

In [19], the dynamic electromagnetic characteristics of an electrodynamic levitation system with permanent magnets are investigated. The test setup is used to determine the speed characteristics, lateral stability and vertical vibration. A massive object is suspended in the air at a height of 30 mm [20]. Levitation can also be realized with a small gap, for example, at a distance of up to 5 mm between two ferromagnetic cores [21].

Of particular interest is magnetic levitation of the induction type (MLIT), which does not require either permanent or superconducting magnets. In it, the height of the suspension of the conductive anchor can be easily changed by regulating the alternating current feeding the inductor. Such levitation can be implemented in various devices in the presence of an electrically conductive element that is subject to an alternating or series of magnetic field pulses [22, 23].

In the work [24] an electromechanical model of the MLIT of a conductive anchor in the form of a ring is constructed and investigated. The equilibrium positions of the levitating ring are determined, the stability is investigated and an expression for the rigidity of the suspension is obtained.

To stabilize the MLIT, a magnetic resonance connection is used between a stationary inductor and a levitating multi-turn anchor [25]. To calculate such a suspension, analytical solutions of equivalent circuits were used, on the basis of which the currents in the inductor and anchor, forces relative to the gap size and the applied frequency of the alternating voltage were considered. Experimental and theoretical results show that positive rigidity is possible, which is necessary for self-stabilization of the magnetic suspension.

The MLIT allows energy to be transferred to a levitated object even if there is a large gap between the inductor and the anchor. Magnetically coupled circuits have two resonant frequencies, the attractive force is generated at a lower resonant frequency, and the repulsive force is generated at a higher resonant frequency [25]. The damping characteristics and the rigidity of the suspension depend on the size of the gap, the amplitude and frequency of the alternating voltage source.

One of the effective MLIT devices is the Thomson's Jumping Ring, which consists of a fixed inductor in the form of a multi-turn coil and a vertically located ferromagnetic core in the form of a steel rod that protrudes beyond the upper limit of the coil [26]. When alternating current is applied to the inductor, the conductive anchor, in the form of a thin ring placed on a ferromagnetic core, jumps to a certain height, after which it is held in a state of levitation relative to the coil. The Thomson apparatus was used to measure the phase delay of the current and force in the frequency range of 20–900 Hz [27]. Stroboscopic photographs of the jumping ring at room temperature and at liquid nitrogen temperature show that the jump height is determined by the time-averaged mechanism of the inductive phase delay. The stack of thin rings levitates at a higher altitude than a single ring because the inductive phase delay begins to dominate the parallel resistance of the combined rings.

Based on the analytical model of Thomson's apparatus, the dependences of the force acting on the ring on the phase, amplitude and frequency of the exciting current were established [28]. The theory of an ideal alternating current transformer is also used to calculate the parameters [29]. The electrodynamics of a levitating ring demonstrates a changing mutual inductance between the ring and the coil [30].

The dependences of the jump height of the ring on its material (copper and aluminum alloys), mass, temperature, and the number of rings of different heights were obtained [31]. The jump height increases and shifts to a lower optimal mass when the rings are cooled to a

temperature of 77 K. The throwing heights of brass, copper, and aluminum rings at room and nitrogen temperatures and different applied voltages were studied [32]. Synchronization of two rings of the Thomson apparatus, powered by alternating current, has found application in mobile robotics [2].

However, the existing Thomson devices implementing MLIT contain a ferromagnetic core protruding beyond the coil surface, which affects the design of the suspended object and introduces nonlinearity into the levitation process control system. Thomson devices were mainly used to study and demonstrate the effect of magnetic levitation without a load, and were not considered as a power suspension. This can also explain the design of the conductive anchor in the form of a ring, which is not advisable when feeding the inductor with high-frequency current. The height of the ring toss is mainly analyzed, while in the practical implementation of magnetic levitation, the size of the gap between the hovering anchor and the stator inductor and the time of the steady-state process are important.

The aim of the article is to study magnetic levitation of the induction type by determining the electromechanical processes that occur when a stationary inductor is connected to a source of alternating voltage and the levitation of an anchor made in the form of a multi-turn short-circuited winding with an attached load.

Mathematical model of MLIT. Let us consider electromechanical processes in a one-dimensional MLIT, in which a fixed inductor is connected to a high-frequency voltage source, and a coaxially mounted conductive anchor can move along only one spatial coordinate. The anchor is made in the form of a multi-turn short-circuited winding on which a load (an object being lifted) is installed. In this case, if the anchor is wound with a relatively thin wire, it is possible to analyze the influence of its height on the operation of MLIT, neglecting the skin effect.

We will assume a strictly vertical movement of the anchor along the z axis relative to the stationary inductor. Let us consider a mathematical model of MLIT, in which the magnetic connection between the inductor and anchor changes. To describe MLIT processes, we will use electric circuits with concentrated parameters of the inductor and anchor, the active resistances of which depend on their heating temperature [33].

Note that when magnetic levitation is started, the temperature of the active elements may not increase significantly, but in a steady state this temperature can significantly affect the nature of electromechanical processes. Therefore, we will consider a universal mathematical model that describes processes in different operating modes.

To take into account the interconnected electrical, magnetic, mechanical and thermal processes, we will present the solutions of the equations describing these processes in a recurrent form [34]. Electrical processes in the active elements of the MLIT (inductor and anchor) can be described by a system of equations:

$$R_1(T_1)i_1 + L_1\frac{\mathrm{d}i_1}{\mathrm{d}t} + M(z)\frac{\mathrm{d}i_2}{\mathrm{d}t} + i_2 v_z(t)\frac{\mathrm{d}M}{\mathrm{d}z} = u(t), \quad (1)$$

$$R_2(T_2)i_2 + L_2\frac{\mathrm{d}i_2}{\mathrm{d}t} + M(z)\frac{\mathrm{d}i_1}{\mathrm{d}t} + i_1 v_z(t)\frac{\mathrm{d}M}{\mathrm{d}z} = 0, \quad (2)$$

where n = 1, 2 are the indices of the inductor and anchor, respectively; $M(z)$ is the mutual inductance between the active elements; v_z is the velocity of the anchor along the z axis; $u(t) = U_m\sin(\omega t + \psi_u)$ is the voltage of the power source; i_n, R_n, L_n, T_n are the current, active resistance, inductance and temperature of the n-th active element, respectively.

Using the relationships from work [35], the following expressions can be written for the currents of the active elements of the MLIT:

$$i_1(t_{k+1}) = -\frac{i_2(t_k)v_z(t_k)}{R_1}\frac{\mathrm{d}M}{\mathrm{d}z} + \Big(u(t_k) - R_1 i_1(t_k) - i_2(t_k)v_z(t_k)\times$$
$$\times\frac{\mathrm{d}M}{\mathrm{d}z}\Big)\frac{\alpha_1\exp(\alpha_2\Delta t) - \alpha_2\exp(\alpha_1\Delta t)}{R_1(\alpha_2-\alpha_1)} + \frac{u(t_k)}{R_1} +$$
$$+\frac{\exp(\alpha_2\Delta t) - \exp(\alpha_1\Delta t)}{(\alpha_2-\alpha_1)(L_1L_2 - M^2)}\Big\{u(t_k)L_2 + \Big[v_z(t_k)M\frac{\mathrm{d}M}{\mathrm{d}z} - R_1L_2\Big]\times$$
$$\times i_1(t_k) + \Big[R_2M - v_z(t_k)L_2\frac{\mathrm{d}M}{\mathrm{d}z}\Big]i_2(t_k)\Big\}; \quad (3)$$

$$i_2(t_{k+1}) = -\frac{i_1(t_k)v_z(t_k)}{R_2}\frac{\mathrm{d}M}{\mathrm{d}z} + \Big[i_2(t_k) + \frac{i_1(t_k)v_z(t_k)}{R_2}\frac{\mathrm{d}M}{\mathrm{d}z}\Big]\times$$
$$\times\frac{\alpha_2\exp(\alpha_1\Delta t) - \alpha_1\exp(\alpha_2\Delta t)}{\alpha_2-\alpha_1} + \frac{\exp(\alpha_2\Delta t) - \exp(\alpha_1\Delta t)}{(\alpha_2-\alpha_1)(L_1L_2 - M^2)}\times$$
$$\times\Big\{i_1(t_k)\Big[R_1M - v_z(t_k)L_1\frac{\mathrm{d}M}{\mathrm{d}z}\Big] - u(t_k)M + i_2(t_k)\times$$
$$\times\Big[v_z(t_k)M\frac{\mathrm{d}M}{\mathrm{d}z} - R_2L_1\Big]\Big\}, \quad (4)$$

where $u(t_k) = U_m\sin(\omega t_k + \psi_u)$; $\Delta t = t_{k+1} - t_k$;
$R_1 = R_1(T_1)$; $R_2 = R_2(T_2)$; $M = M(z)$;

$$\alpha_{1,2} = \pm\Bigg\{\frac{\Big(L_1R_2 + L_2R_1 - 2Mv_z\frac{\mathrm{d}M}{\mathrm{d}z}\Big)^2}{4\Big(L_1L_2 - M^2\Big)^2} - \frac{R_1R_2 - v_z^2\Big(\frac{\mathrm{d}M}{\mathrm{d}z}\Big)^2}{L_1L_2 - M^2}\Bigg\} +$$
$$+\frac{Mv_z\frac{\mathrm{d}M}{\mathrm{d}z} - L_1R_2 - L_2R_1}{2\Big(L_1L_2 - M^2\Big)}.$$

The magnitude of the anchor displacement together with the connected load relative to the inductor can be represented in the form of a recurrence relation [33]:

$$h_z(t_{k+1}) = h_z(t_k) + v_z(t_k)\Delta t + \vartheta\cdot\Delta t^2/(m_a + m_2), \quad (5)$$

where $v_z(t_{k+1}) = v_z(t_k) + \vartheta\cdot\Delta t/(m_a + m_2)$ is the anchor speed together with load; $\vartheta = F_z(z,t) - 0{,}125\pi\gamma_a\beta_aD_{e2}^2v_z^2(t_k)$; $F_z(z,t) = i_1(t_k)i_2(t_k)\frac{\mathrm{d}M}{\mathrm{d}z}$ is the instantaneous value of the axial electrodynamic force acting on the anchor; m_2, m_a – mass of the anchor and the attached load respectively; h_z – magnitude of anchor displacement; γ_a – density of the medium of movement; β_a – drag coefficient; D_{e2} – outside diameter of the attached load.

The temperature of the n-th active element can be described by the recurrence relation [35]:

$$T_n(t_{k+1}) = T_n(t_k)\chi + (1-\chi)\left[T_0 + 4\pi^{-2} i^2(t_k) \times \right.$$
$$\left. \times R_n(T_n)\alpha_{Tn}^{-1} D_{en}^{-1} H_n^{-1}\left(D_{en}^2 - D_{in}^2\right)^{-1}\right], \qquad (6)$$

where $\chi = \exp\left\{-0{,}25\Delta t D_{en}\alpha_{Tn} c_n^{-1}(T_n)\gamma_n^{-1}\right\}$; D_{en}, D_{in} – the outer and inner diameters of the n-th active element, respectively; α_{Tn}, c_n, γ_n – heat transfer coefficient, heat capacity and density of the n-th element respectively.

To calculate MLIT we use the following algorithm of cyclic action. We divide the working process into a number of numerically small time intervals $\Delta t = t_{k+1} - t_k$, within which all values are considered constant. In each cycle, using the parameters calculated at time t_k, as initial values, we calculate the parameters at time t_{k+1}. In the calculation cycle, the values of currents i_n, temperatures T_n, resistances $R_n(T_n)$ of active elements, values of axial electrodynamic force $f_z(z,t)$, velocity v_z and displacement h_z of the anchor, mutual inductance $M(z)$ between active elements are successively calculated.

To determine the currents on a numerically small calculation time interval Δt, we use linear equations with constant parameter values. We select the value of the calculation step Δt in such a way that it does not have a significant effect on the calculation results, while ensuring the necessary accuracy.

Initial conditions of the mathematical model: $i_n(0)=0$; $T_n(0)=T_0$ – current and temperature of the n-th active element, respectively; $h_z(0)=h_{z0}$ – distance between active elements; $v_z(0)=0$ – armature speed along the z-axis; $u(0) = U_m \sin\psi_u$ – voltage of the alternating current source.

Main parameters of MLIT. Let us consider the electromechanical processes when starting magnetic levitation of the induction type, in which the inductor (n=1) and anchor (n=2) are made in the form of multi-turn disk windings. The active elements (inductor and anchor) are tightly wound with copper wire of diameter d_0=0.9 mm. Their outer diameter D_{en}=100 mm, and inner diameter D_{in} =4 mm. The inductor has an axial height H_1=10 mm and contains turns w_1=480.

The active elements are made in the form of massive disks by impregnation and subsequent hardening of epoxy resin. They are installed horizontally and coaxially so that the initial distance between them h_{z0}=1 mm. The amplitude of the AC source voltage U_m =100 V. The mass of the load connected to the anchor is m_a =0.5 kg.

Let us consider the influence of the anchor parameters and the frequency of the AC source f on the electromechanical processes that occur in the MLIT when the inductor is connected to the source. As anchor parameters we will use the number of turns w_2 and the axial height H_2. The change in the number of turns of the anchor w_2 is carried out layer by layer, which proportionally changes its height H_2.

Let us consider electromechanical processes when using an anchor with the following parameters: number of turns w_2=240, height H_2=5 mm. Figure 1 shows the starting electromechanical characteristics of the MLIT at the initial interval of 0.1 s when an alternating voltage with a frequency of f=50 Hz is applied to the inductor. In this case, the anchor with the connected load makes a vertical jump from the initial position. The instantaneous values of the source voltage u, the current density in the inductor j_1 and anchor j_2, the axial force F_z, the vertical velocity v_z and the displacement h_z of the anchor are presented as characteristics.

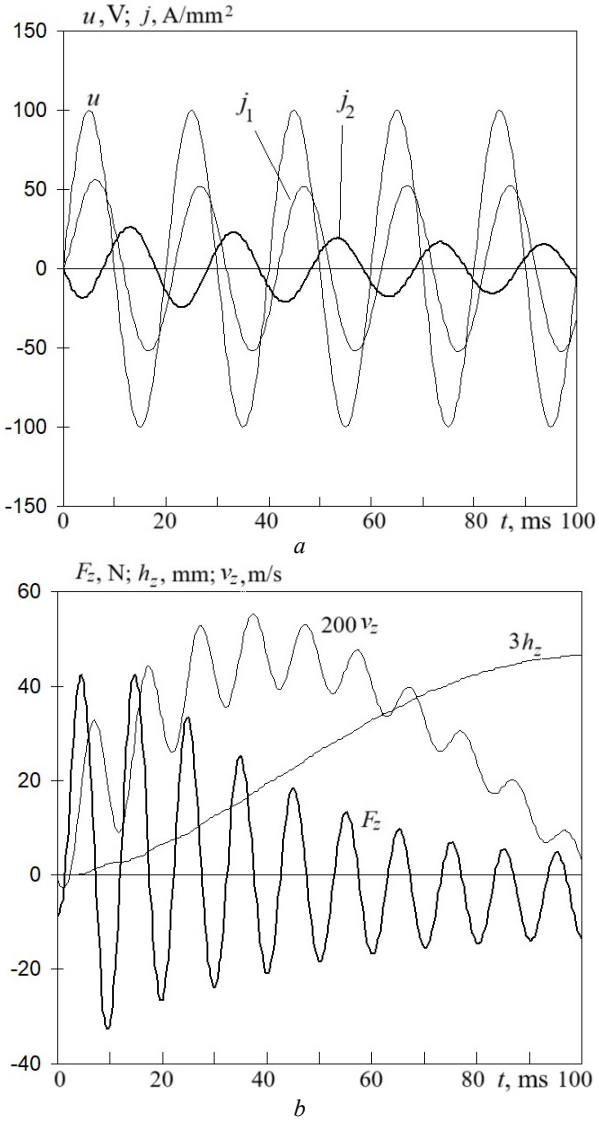

Fig. 1. Starting electromechanical characteristics of MLIT at source frequency f=50 Hz over a short interval

The inductor current lags in phase with the source voltage, which is explained by the active-inductive nature of the inductor resistance. However, the phase delay of the induced anchor current with respect to the inductor current is more important, since due to this, at certain moments, the currents flow in one direction, which leads to the emergence of a braking electrodynamic force directed downwards. Note that the total force providing vertical movement of the anchor F_z also takes into account the gravity of the anchor and the load, as well as the aerodynamic resistance during movement.

As a result, the force F_z, due to the electrodynamic component acting on the anchor, has an alternating character with the positive component directed upwards predominating. It should be noted that the effect of the occurrence of the alternating nature of the electrodynamic force acting on the moving anchor when an alternating

voltage is applied to the inductor was first described in the works of Ukrainian scientists in 1986 [36].

This character of the electrodynamic force causes the pulsations of the anchor speed v_z. When the anchor with the load moves vertically relative to the inductor by a distance h_z, the induction current of the anchor and the positive component of the force acting on it decrease. In this case, the force of gravity begins to prevail, as a result of which the anchor begins to descend. The resulting oscillatory damping mechanical process can be seen in Fig. 2.

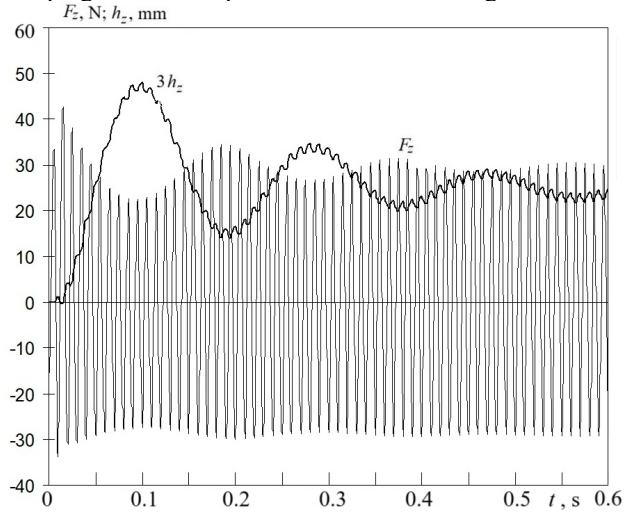

Fig. 2. Starting electromechanical characteristics of MLIT at source frequency f=50 Hz over an extended interval

When the anchor moves away from the inductor by a distance h_z, the upward component of the force F_z decreases, and when the anchor approaches the inductor, this force increases. Since when the anchor moves upward, the electrodynamic force and the force of gravity are directed oppositely, and when it falls, they are directed in agreement, the downward force F_z changes to a lesser extent than the force directed upward.

Such an oscillatory electromechanical process occurs with an increase in the oscillation period and a decrease in its amplitude. The first oscillation period is 0.17 s, the second – 0.2 s, etc. The greatest jump of the anchor with the attached load occurs initially to a height of h_z=15.9 mm, after which it drops to h_z=4.6 mm. Then the oscillation amplitude decreases and after about 1.0 s the oscillatory process practically fades out and the anchor with the attached load begins to stably levitate at a height of h_z^*=8.6 mm relative to the inductor.

When the inductor is connected to an alternating voltage source with a frequency of f =100 Hz, the electromechanical processes change as follows (Fig. 3). The current density in the inductor j_1 decreases, which is explained by an increase in the inductor resistance, and the current density in the anchor j_2 increases, which is explained by an increase in the frequency of the magnetic field from the inductor.

As a result, the maximum electrodynamic force, and therefore the resulting lifting force F_z increases, which causes the first jump of the anchor to a greater height h_z=22.7 mm. The period of mechanical oscillations is practically the same as when connecting the inductor to a voltage source with a frequency f=50 Hz, but with a greater amplitude.

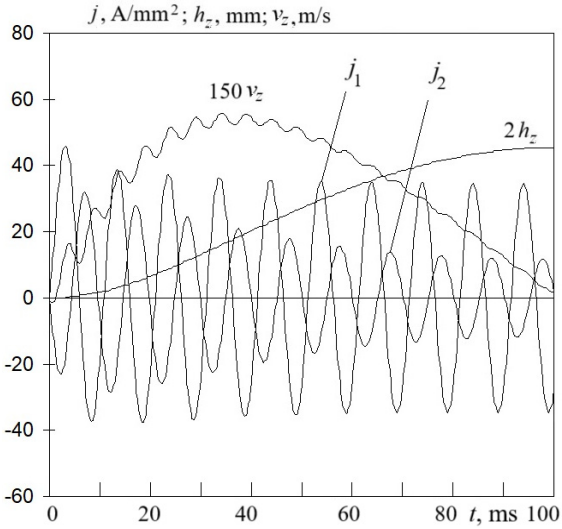

Fig. 3. Starting electromechanical characteristics of MLIT at source frequency f=100 Hz over a short interval

The higher the anchor bounce, the smaller the value of the induced current in the anchor j_2, and hence the value of the lifting force F_z (Fig. 4). Depending on the value of the anchor bounce relative to the inductor, the induced current in the anchor changes to a greater extent than in the inductor, and the electrodynamic force to an even greater extent. After approximately 1.0 s, the anchor together with the load levitate at a steady height h_z^*=11 mm relative to the inductor.

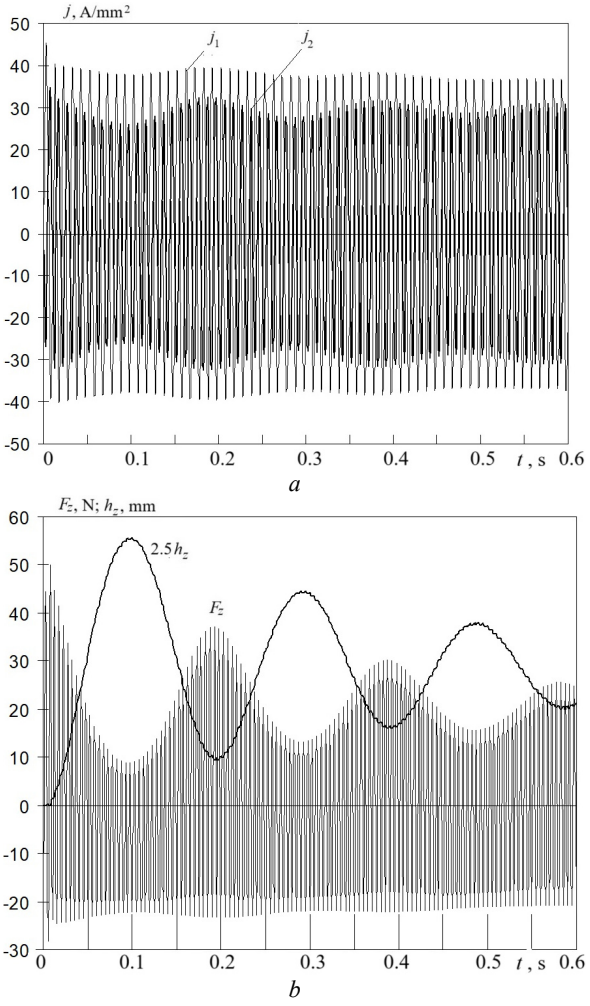

Fig. 4. Starting electromechanical characteristics of MLIT at source frequency f=100 Hz over an extended interval

The electromechanical parameters of the MLIT depend significantly on the anchor parameters and the frequency of the AC source voltage.

Figure 5 shows the maximum values of the current density in the inductor j_{1m} and anchor j_{2m}, the force F_{zm} and the steady-state height of anchor levitation with load h_z^* depending on the frequency of the source voltage f. These dependencies are constructed for different anchor parameters: the number of turns w_2 and the corresponding height H_2. Since the turns are laid in layers, then, for example, at w_2=120, H_2=2.5 mm, at w_2=600, H_2=12.5 mm. In this case, the anchor mass also naturally changes.

With increasing source frequency f, the maximum current density in the inductor j_{1m} decreases due to increasing inductive resistance. Moreover, the more turns in the anchor w_2, the greater the value of j_{1m} due to the inductive effect of the anchor on the inductor.

With increasing source frequency f, the maximum current density in the anchor j_{2m} changes ambiguously. This is due to two factors: increasing the frequency increases the EMF in the anchor, but the reduced inductor current excites a magnetic field of a smaller magnitude. In the range from 50 Hz, the value of j_{2m} increases to a certain value, and then decreases with increasing frequency to 300 Hz. The fewer turns in the anchor, the higher the specified effect occurs at the higher source frequency.

This explains the nature of the change in the maximum force F_{zm}, which has the greatest value at a frequency in the range of 75–125 Hz. The more turns of the armature winding w_2, the greater the value of F_{zm} and is achieved at a lower frequency. After the specified maximum value, the maximum force F_{zm} decreases, and there is no obvious dependence on the number of turns w_2.

The dependence of the steady-state height h_z^* of levitation of the anchor with a load on the frequency of the current in the inductor is to a certain extent similar to the dependence of the force on the frequency $F_{zm}(f)$, but with the peculiarity that with an increase in the number of turns of the anchor w_2, its mass also increases. The greatest levitation height h_z^*=15 mm is realized for the anchor w_2=480 s at a frequency of $f \sim$ 75 Hz.

That is, this anchor is made the same as the inductor. Note that at a frequency of 50 Hz, the anchor with the number of turns w_2=120 and an attached load will not levitate relative to the inductor at all.

It should be noted that the induction method of maintaining magnetic levitation in a stable mode is quite energy-consuming and significantly depends on the frequency of the supply voltage. Thus, for MLIT with the parameters considered above, when using an anchor with w_2=120 at f=50 Hz, the power of the power source is P = 1.45 kW, and at f = 300 Hz P = 0.47 kW.

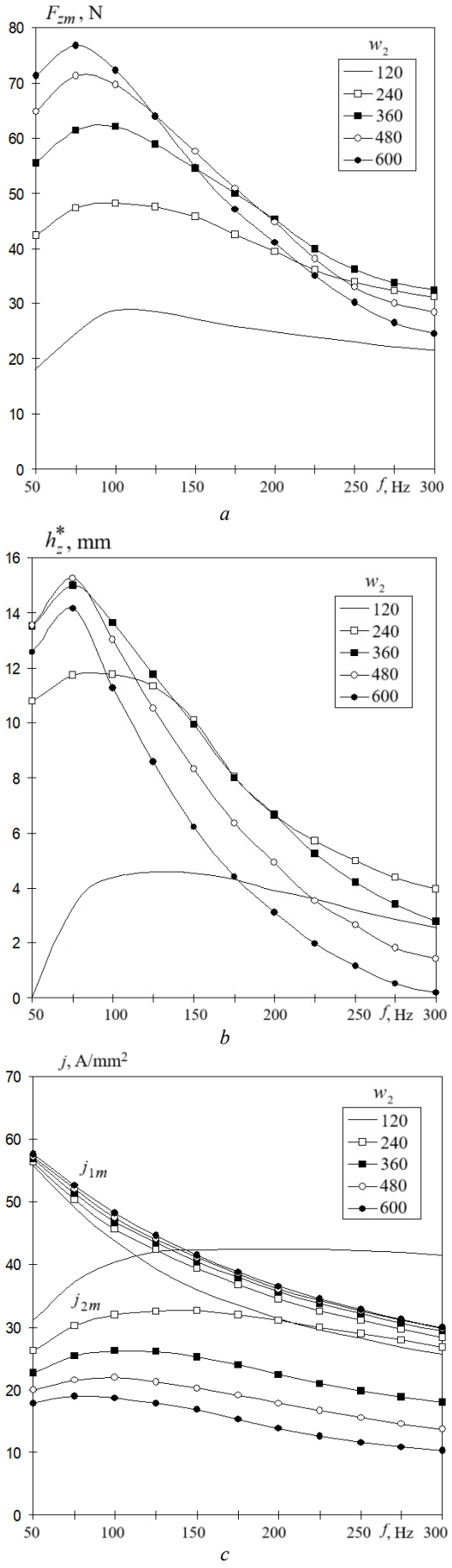

Fig. 5. Dependences of the electromechanical indicators of the MLIT on the frequency of the source voltage

To check the basic relationships, experimental studies of the MLIT were conducted in the laboratory of the General Electrical Engineering Department of NTU «KhPI». Figure 6 shows the initial position of the anchor, made in the form of an aluminum disk ring, relative to the inductor and the state of its stable levitation with an attached load (a roll of scotch tape). A plastic guide tube is used for strictly vertical movement of the anchor. Calculations performed for this installation using the proposed mathematical model coincided with the experimental data with an accuracy of 10 %.

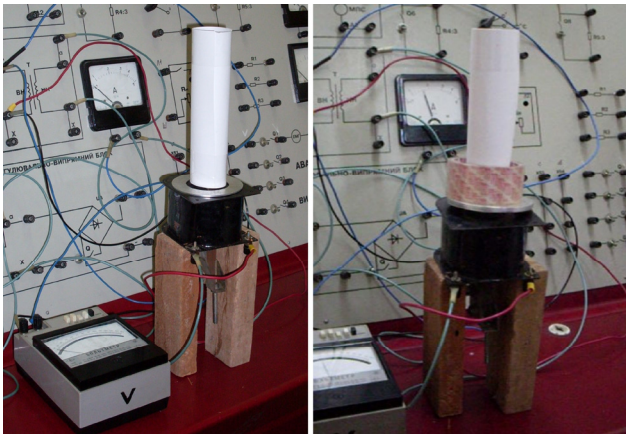

a *b*

Fig. 6. Experimental setup for studying MLIT in the initial (*a*) and working (*b*) state

The proposed magnetic levitation has a wide range of applications. For example, in high-precision gravimeters, in the vacuum chamber of which the optical angular reflector of the measuring system of the Michelson laser interferometer is freely moved in the gravitational field of the Earth, it can reduce autoseismic oscillations. Due to this, it is possible to increase the performance of the ballistic gravimeter with a symmetrical measurement scheme, which is the state primary standard of the unit of acceleration of free fall (National Scientific Center «Institute of Metrology», Kharkiv) [37].

Conclusions.

1. An analysis of magnetic levitation systems and their practical implementation is carried out, and the advantages of induction levitation are shown.

2. A mathematical model of magnetic levitation of the induction type with concentrated parameters of the inductor and anchor, represents solutions of equations describing interconnected electrical, magnetic, mechanical and thermal processes, in a recurrent form.

3. The influence of the frequency of the alternating current source on the electromechanical processes that occur when starting magnetic levitation of the induction type with different parameters of a multi-turn short-circuited anchor has been established.

4. When magnetic levitation is started, an oscillatory electromechanical process occurs, which is established after approximately 1 s. The highest established levitation height is realized for an anchor similar to an inductor, at a frequency of 75 Hz.

5. The results of experimental studies on the levitation of an aluminum disk with an attached load coincided with the calculated results obtained using the proposed mathematical model with an accuracy of 10 %.

Conflict of interest. The author declares no conflicts of interest.

REFERENCES

1. Han H.-S., Kim D.-S. *Magnetic Levitation. Maglev Technology and Applications*. Springer Publ., 2016. 247 p. doi https://doi.org/10.1007/978-94-017-7524-3.

2. Ramirez-Neria M., Gonzalez-Sierra J., Garcia-Antonio J.L., Garcia-Antonio J.A., Ramirez-Neria E. On the Sliding Mode Control of a Magnetic Levitation System Case: Thomson's Jumping Ring. *Proceedings of the International Conference of Control, Dynamic Systems, and Robotics*, 2014, paper no. 105. 8 p.

3. Poletkin K.V., Asadollahbaik A., Kampmann R., Korvink J.G. Levitating Micro-Actuators: A Review. *Actuators*, 2018, vol. 7, no. 2, art. no. 17. doi: https://doi.org/10.3390/act7020017.

4. Carneiro P., Soares dos Santos M.P., Rodrigues A., Ferreira J.A.F., Simões J.A.O., Marques A.T., Kholkin A.L. Electromagnetic energy harvesting using magnetic levitation architectures: A review. *Applied Energy*, 2020, vol. 260, art. no. 114191. doi: https://doi.org/10.1016/j.apenergy.2019.114191.

5. Poletkin K. On the Static Pull-In of Tilting Actuation in Electromagnetically Levitating Hybrid Micro-Actuator: Theory and Experiment. *Actuators*, 2021, vol. 10, no. 10, art. no. 256. doi: https://doi.org/10.3390/act10100256.

6. Zhou B., Dai C., Liu Z., Yu J., Liu H., Zhang B. Design and optimization of H-type asymmetric magnetic suspension vibration absorber for ships. *Journal of Vibration and Control*, 2025, vol. 31, no. 3–4, pp. 344-354. doi: https://doi.org/10.1177/10775463241226840.

7. Liao H., Yuan H., Xie J. High-Precision Composite Control of Driving Current for Non-Contact Annular Electromagnetic Stabilized Spacecraft Subject to Multiple Disturbances. *Aerospace*, 2024, vol. 11, no. 8, art. no. 627. doi: https://doi.org/10.3390/aerospace11080627.

8. Han W., Cai Y., Han W., Yin Z., Yu C. Review on Active Vibration Control Method of Magnetically Suspended System. *IEEE Access*, 2023, vol. 11, pp. 108117-108125. doi: https://doi.org/10.1109/ACCESS.2023.3317333.

9. Fang J., Zheng S., Han B. Attitude Sensing and Dynamic Decoupling Based on Active Magnetic Bearing of MSDGCMG. *IEEE Transactions on Instrumentation and Measurement*, 2012, vol. 61, no. 2, pp. 338-348. doi: https://doi.org/10.1109/TIM.2011.2164289.

10. Cai Y., Yu C., Ren Y., Wang W., Yin Z., Xia C. High Precision Attitude-Rate Measurement of Magnetically Suspended Control and Sensing Gyroscope Using Variational Mode Decomposition and Wavelet Transform. *IEEE Sensors Journal*, 2022, vol. 22, no. 2, pp. 1188-1198. doi: https://doi.org/10.1109/JSEN.2021.3131994.

11. Dai C., Liu Z., Wang Y., Lin X., Liu H., Zhou B. Design and Optimization of a New Type of Magnetic Suspension Vibration Absorber for Marine Engineering. *Journal of Marine Science and Engineering*, 2023, vol. 11, no. 11, art. no. 2070. doi: https://doi.org/10.3390/jmse11112070.

12. Li A.J., Zhou B.M., Jiang C.D., Liu D.Z., Wang E.H. Frequency-doubling displacement disturbance suppression of active magnetic bearing based on repetitive control. *2024 IEEE 10th International Power Electronics and Motion Control Conference (IPEMC2024-ECCE Asia)*, 2024, pp. 707-711. doi: https://doi.org/10.1109/IPEMC-ECCEAsia60879.2024.10567916.

13. Cao S., Niu P., Wang W., Zhao T., Liu Q., Bai J., Sheng S. Novel Magnetic Suspension Platform with Three Types of Magnetic Bearings for Mass Transfer. *Energies*, 2022, vol. 15, no. 15, art. no. 5691. doi: https://doi.org/10.3390/en15155691.

14. Bolyukh V.F., Vinnichenko A.I. Concept of an Induction-Dynamic Catapult for a Ballistic Laser Gravimeter.

Measurement Techniques, 2014, vol. 56, no. 10, pp. 1098-1104. doi: https://doi.org/10.1007/s11018-014-0337-z.
15. Bolyukh V.F., Omel'chenko A.V., Vinnichenko A.I. Effect of Self-Seismic Oscillations of the Foundation on the Readout of a Ballistic Gravimeter with an Induction-Dynamic Catapult. *Measurement Techniques*, 2015, vol. 58, no. 2, pp. 137-142. doi: https://doi.org/10.1007/s11018-015-0675-5.
16. Shearwood C., Ho K.Y., Williams, C.B., Gong H. Development of a levitated micromotor for application as a gyroscope. *Sensors and Actuators A: Physical*, 2000, vol. 83, no. 1–3, pp. 85-92. doi: https://doi.org/10.1016/S0924-4247(00)00292-2.
17. Hatakenaka K., Hijikata W., Fujiwara T., Ohuchi K., Inoue Y. Prevention of thrombus formation in blood pump by mechanical circular orbital excitation of impeller in magnetically levitated centrifugal pump. *Artificial Organs*, 2023, vol. 47, no. 2, pp. 425-431. doi: https://doi.org/10.1111/aor.14443.
18. Tang J., Li C., Zhou J., Wu Z. Effects of mechanical interfaces on magnetic levitation systems and analysis of self-excited vibration mechanisms in coupled systems. *Science China Technological Sciences*, 2024, vol. 67, no. 12, pp. 3925-3939. doi: https://doi.org/10.1007/s11431-024-2776-8.
19. Shi H., Deng Z., Ke Z., Li Z., Zhang W. Linear permanent magnet electrodynamic suspension system: Dynamic characteristics, magnetic-mechanical coupling and filed test. *Measurement*, 2024, vol. 225, art. no. 113960. doi: https://doi.org/10.1016/j.measurement.2023.113960.
20. Wang X.G., Liu Q., Zhang Y.J., Chen H.H. Research on Characteristic of Electromagnetic Force of Magnetic Suspension Device with Large Air-Gap. *Applied Mechanics and Materials*, 2013, vol. 401-403, pp. 239-244. doi: https://doi.org/10.4028/www.scientific.net/AMM.401-403.239.
21. Abd. Aziz P.D., Li Q., Rodriguez E., Deng Z. A Preliminary Study on Electromagnetic Levitation Design Topology. *2020 IEEE International Conference on Applied Superconductivity and Electromagnetic Devices (ASEMD)*, 2020, pp. 1-2. doi: https://doi.org/10.1109/ASEMD49065.2020.9276251.
22. Bolyukh V.F., Shchukin I.S. Improving the Efficiency of a Linear Pulse Electromechanical Accelerator Due to Excitation by a Series of Pulses. *2020 IEEE KhPI Week on Advanced Technology (KhPIWeek)*, 2020, pp. 205-210. doi: https://doi.org/10.1109/KhPIWeek51551.2020.9250077.
23. Bolyukh V.F. Effect of electric conducting element on indicators of linear pulse electromechanical converter induction type. *Technical Electrodynamics*, 2020, no. 3, pp. 22-29. doi: https://doi.org/10.15407/techned2020.03.022.
24. Skubov D.Y., Indeitsev D.A., Udalov P.P., Popov I.A., Lukin A.V., Poletkin K.V. Nonlinear Dynamics of a Micromechanical Non-Contact Induction Suspension. *Mechanics of Solids*, 2023, vol. 58, no. 6, pp. 2011-2023. doi: https://doi.org/10.3103/S0025654423600307.
25. Rahman A., Mizuno T., Takasaki M., Ishino Y. An Equivalent Circuit Analysis and Suspension Characteristics of AC Magnetic Suspension Using Magnetic Resonant Coupling. *Actuators*, 2020, vol. 9, no. 3, art. no. 52. doi: https://doi.org/10.3390/act9030052.
26. Jeffery R.N., Amiri F. Thomson's Jumping Ring Over a Long Coil. *The Physics Teacher*, 2018, vol. 56, no. 3, pp. 176-180. doi: https://doi.org/10.1119/1.5025301.
27. Tjossem P.J.H., Cornejo V. Measurements and mechanisms of Thomson's jumping ring. *American Journal of Physics*, 2000, vol. 68, no. 3, pp. 238-244. doi: https://doi.org/10.1119/1.19407.
28. Donoso G., Ladera C.L. The naked toy model of a jumping ring. *European Journal of Physics*, 2014, vol. 35, no. 1, art. no. 015002. doi: https://doi.org/10.1088/0143-0807/35/1/015002.
29. Ng C. The Thomson Jumping Ring Experiment and Ideal Transformer. *The Physics Teacher*, 2022, vol. 60, no. 5, pp. 376-379. doi: https://doi.org/10.1119/5.0036490.
30. Ladera C.L., Donoso G. Unveiling the physics of the Thomson jumping ring. *American Journal of Physics*, 2015, vol. 83, no. 4, pp. 341-348. doi: https://doi.org/10.1119/1.4902891.
31. Tjossem P.J.H., Brost E.C. Optimizing Thomson's jumping ring. *American Journal of Physics*, 2011, vol. 79, no. 4, pp. 353-358. doi: https://doi.org/10.1119/1.3531946.
32. Taweepong J., Thamaphat K., Limsuwan S. Jumping ring experiment: effect of temperature, non-magnetic material and applied current on the jump height. *Procedia Engineering*, 2012, vol. 32, pp. 982-988. doi: https://doi.org/10.1016/j.proeng.2012.02.042.
33. Bolyukh V.F., Shchukin I.S. Influence of an excitation source on the power indicators of a linear pulse electromechanical converter of induction type. *Technical Electrodynamics*, 2021, no. 3, pp. 28-36. doi: https://doi.org/10.15407/techned2021.03.028.
34. Bolyukh V.F., Katkov I.I. Influence of the Form of Pulse of Excitation on the Speed and Power Parameters of the Linear Pulse Electromechanical Converter of the Induction Type. *Proceedings of the ASME 2019 International Mechanical Engineering Congress and Exposition. Volume 2B: Advanced Manufacturing*, 2019, V02BT02A047. doi: https://doi.org/10.1115/IMECE2019-10388.
35. Bolyukh V.F., Kashansky Y.V., Schukin I.S. Features of excitation of a linear electromechanical converter of induction type from an AC source. *Electrical Engineering & Electromechanics*, 2021, no. 1, pp. 3-9. doi: https://doi.org/10.20998/2074-272X.2021.1.01.
36. Vaskovsky Yu.M., Chemeris V.T., Petrovsky V.P., Shats A.N. Physical modeling of the features of anchor acceleration in a pulse electromechanical converter of induction type. *Technical Electrodynamics*, 1986, no. 3, pp. 66-69.
37. Bolyukh V., Vinnichenko O., Neyezhmakov P., Omelchenko A. Reduction of auto seismic oscillations of the ballistic laser gravimeter on account of the excitation of the induction-dynamic catapult by a pulse packet. *Ukrainian Metrological Journal*, 2020, no. 3, pp. 3-11. doi: https://doi.org/10.24027/2306-7039.3.2020.216765.

Received 13.12.2024
Accepted 02.02.2025
Published 02.05.2025

V.F. Bolyukh [1], *Doctor of Technical Science, Professor,*
[1] National Technical University «Kharkiv Polytechnic Institute», 2, Kyrpychova Str., Kharkiv, 61002, Ukraine,
e-mail: vfbolyukh@gmail.com (Corresponding Author)

How to cite this article:
Bolyukh V.F. Electromechanical processes during the start of induction-type magnetic levitation. *Electrical Engineering & Electromechanics*, 2025, no. 3, pp. 3-10. doi: https://doi.org/10.20998/2074-272X.2025.3.01

UDC 621.3 https://doi.org/10.20998/2074-272X.2025.3.02

S. Adiche, M. Larbi, D. Toumi

Optimizing voltage control in AC microgrid systems with fuzzy logic strategies and performance assessment

Introduction. *Microgrids (MGs) have garnered significant attention for their numerous advantages, providing a solution for powering remote and distant locations while enhancing system reliability. In MGs, distributed generation inverters generally operate in parallel with the droop control strategies. This study focuses on the approach based on the P-f/Q-V droop control technique with virtual impedance for AC MG management. Essentially, the virtual impedance loop aims to decouple reactive and active power control without the need for additional physical components.* ***Novelty****. This research proposes enhancing voltage control in AC MG systems by introducing new methods of various control strategies, including PI and Fuzzy Logic Controller (FLC), and evaluating the effectiveness of each approach. The mathematical model of a system is always an approximation of real systems, variations or errors between mathematical models and real systems are referred to as uncertainty. This concept of uncertainty is present in both signals and models. In our study, uncertainties may involve factors related to the filter LC components. By employing advanced control strategies like FLC, the* ***purpose*** *of this research aims to contribute to the optimization and reliability of AC MG systems through the improvement of voltage control, which leads to guaranteed equitable power-sharing.* ***Results****. The major advantages of the FLC are robustness for any variation on the system and fast response. MATLAB software is used to simulate and validate the suggested control.* ***Practical value****. The simulation results show that the suggested control performs better in precise tracking optimization and robustness for all disturbances on the system compared to a PI controller.* References 24, table 5, figures 11.
Key words: **microgrid, droop control technique, distributed generation inverters, PI control, voltage control, virtual impedance, fuzzy logic.**

Вступ*. Мікромережі привернули значну увагу своїми численними перевагами, надаючи рішення для живлення віддалених місць, одночасно підвищуючи надійність системи. У мікромережах інвертори розподіленої генерації зазвичай працюють паралельно зі стратегіями управління спадами. Це дослідження фокусується на підході, що ґрунтується на техніці управління спадами P-f/Q-V з віртуальним імпедансом для управління мікромережею змінного струму. По суті контур віртуального імпедансу спрямований на розв'язку управління реактивною та активною потужністю без необхідності додаткових фізичних компонентів.* ***Новизна****. Це дослідження пропонує покращити управління напругою в системах мікромережі змінного струму шляхом впровадження нових методів різних стратегій управління, включаючи ПІ та нечіткий логічний контролер (FLC), та оцінку ефективності кожного підходу. Математична модель системи завжди є наближенням реальних систем, зміни чи помилки між математичними моделями та реальними системами називаються невизначеністю. Ця концепція невизначеності присутня як у сигналах, так і у моделях. У нашому дослідженні невизначеності можуть включати фактори, пов'язані з компонентами LC фільтра. Використовуючи передові стратегії управління, такі як FLC,* ***мета*** *даного дослідження полягає у сприянні оптимізації та надійності систем змінного струму мікромережі за допомогою покращення управління напругою, що призводить до гарантованого коректного розподілу потужності.* ***Результати****. Основними перевагами FLC є надійність для будь-яких змін у системі та швидкий відгук. Програмне забезпечення MATLAB використовується для моделювання та перевірки запропонованого керування.* ***Практична цінність****. Результати моделювання показують, що пропоноване управління працює краще у точній оптимізації відстеження та надійності для всіх збурень у системі порівняно з ПІ-регулятором.* Бібл. 24, табл. 5, рис. 11.
Ключові слова: **мікромережа, метод керування спадом, інвертори розподіленої генерації, ПІ-регулювання, керування напругою, віртуальний імпеданс, нечітка логіка.**

Introduction. A microgrid (MG) refers to a compact and self-contained network comprising distributed generation (DG) [1, 2] to provide local loads with dependable and effective power [3] it can be categorized as AC, DC and hybrid MG [4, 5]. MGs are becoming increasingly popular due to their flexibility, capable of operating in two primary modes: stand alone and grid-connected mode to clarify, to guarantee seamless mode transition and to enable grid-connected and stand alone functions, MGs should be controlled [6, 7]. DG with smaller generating systems based on renewable energy resources, such as solar power and wind power, combined with loads and energy storage systems brings evolutionary changes to the traditional electric utilities and becomes a new pattern of power grid. In comparison to traditional generators, the concept of MG is emerging as an effective way to integrate renewable energy resources. Droop control is the recommended method for regulating many inverters in parallel because it does away with the need for external communication between them.

Traditional droop control employs reactive power/voltage (Q/V) control and active power/frequency (P/f) control to accomplish the decoupling of the regulation of active and reactive power [8]. The concept of virtual impedance has been introduced to uphold uniform primary inductive output impedance among paralleled inverters. It guarantees reactive power based on voltage amplitude and active power determined by power angle. Furthermore, virtual impedance aids in decoupling active and reactive powers [9]. To maintain the voltage regulation across the inverters, the internal control loop also identified as the low-level voltage and current controllers consists of 2 loops: an external voltage loop and an internal current loop, this level of control is elaborated in [10]. An efficient control mechanism is needed to regulate the voltage in the AC MG because voltage control is required to achieve power balance in the bus. This paper proposes an improvement of voltage control in AC MGs and a comparative study including PI and Fuzzy Logic Controllers (FLCs). The PI controller is frequently employed in MG. However, this controller necessitates precise mathematical models. The PI controller demonstrates satisfactory performance but it becomes difficult to control the voltage when variations in parameters and system operating conditions impact the performance of the PI controller potentially leading to system instability. The FLC, on the other hand, has been demonstrated advantage over conventional controllers. Recent years have seen the widespread use of FLC because of its less complex mathematical ideas and flexibility

concerning input modifications. FLC differs from conventional controllers in that they rely on knowledge [11, 12]. However, the performance of the voltage and current controls in AC MG under various control strategies has not been investigated in previous research studies. PI controllers are frequently used by them to account for errors [13, 14]. FLC controller is given in this article as an error-compensation technique for voltage control for AC island MG. It has been demonstrated that employing FLC can effectively reduce output overshoot and decrease the time required for the system to reach its steady-state value. A comprehensive simulation study using the MATLAB/Simulink environment is used to determine the effectiveness of the suggested control under various system parameter variations. It includes several test cases that measure the performance of the system concerning maximum overshoot, rising time, and settling time.

The goal of the paper is to propose a robust and adaptive control technique using FLC systems stabilizing the voltage of islanded microgrids under both normal and variation operation modes. Additionally, it highlights the superiority and robustness of FLC systems compared to conventional PI controllers.

Configuration of the proposed microgrid. Figure 1 depicts the MG running in islanding mode. This MG comprises 2 decentralized generators that operate in a parallel configuration. The load is connected to each through output impedances and LC filters.

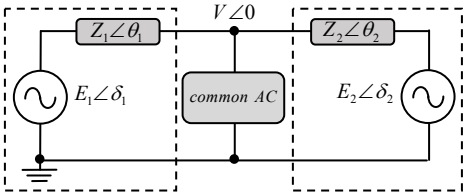

Fig. 1. Equivalent circuit for DG inverters in autonomous mode

The model consists of an ideal voltage source of amplitude E and internal angle δ in series with output impedance «Z». This output impedance encompasses both the filter impedance at the output and line impedance connecting each elementary DG to the point of common coupling (PCC), where $V\angle 0$ is the AC bus voltage amplitude.

Control of the microgrid system. The core components of an MG's DG system control structure are:

a) inner loops are the cascading voltage/current control loops that manage the 3-phase inverter's voltage;

b) primary loop, also known as the external power control loop, employs the droop technique to regulate the DG system's active and reactive power outputs.

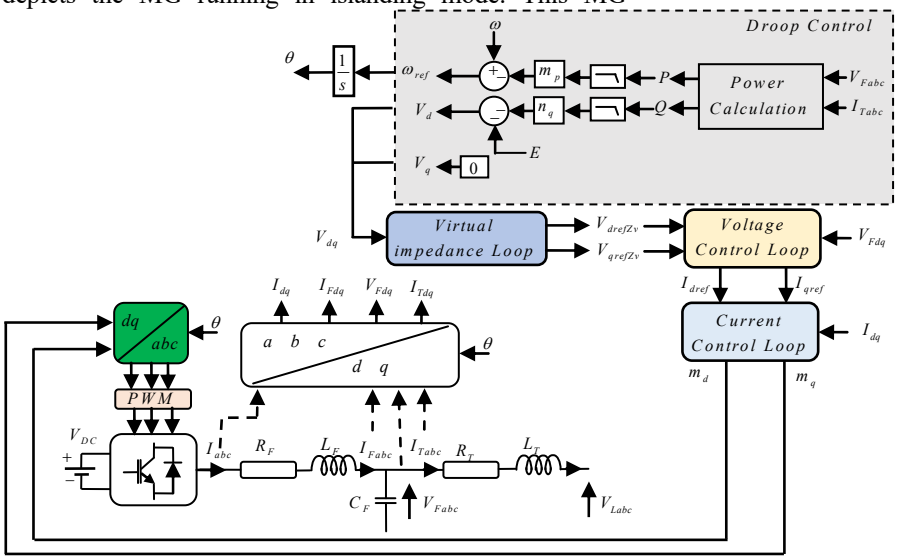

Fig. 2. DG control system block diagram

$$\begin{cases} P = \dfrac{\omega_c}{s+\omega_c} p \Rightarrow p = \dfrac{3}{2}\left(V_{Fd} I_{Td} + V_{Fq} I_{Tq}\right), \\ Q = \dfrac{\omega_c}{s+\omega_c} q \Rightarrow q = \dfrac{3}{2}\left(V_{Fd} I_{Tq} - V_{Fq} I_{Td}\right), \end{cases} \quad (1)$$

where $\omega_c/(s+\omega_c)$ is the low pass filter; V_{Fd}, V_{Fq} are the voltage command values of *d*-*q* axis components; I_{Td}, I_{Tq} are the *d*-*q* axis output currents flowing through the filter $R_T L_T$.

The notion of droop control [16] is based on measuring active and reactive powers to adjust frequency and voltage. Through the use of the conventional droop technique, the different DGs in an MG may share the power required by the loads. By using a power theory-based method, DGs systems may simulate the actions of a synchronous generator [17]. Depending on the predominance of the output impedance of each DG, different variants of conventional droop controls can be used, for more details [18]. The basic droop *P-f*/*Q-V* technique equations are written as:

$$\begin{cases} \omega = \omega_{nom} - m_p P; \\ V = V_{nom} - n_q Q, \end{cases} \quad (2)$$

where ω_{nom}, V_{nom} are the respectively the frequency and the RMS values of the reference voltage; P, Q are the respectively the active and reactive power at the output of each inverter; m_p, n_q are the proportional droop coefficients for frequency and voltage, chosen according to the rated active and reactive powers.

Droop control technique and output impedance for DG systems. As seen in Fig. 2, while in islanding mode, operating DG units are interfaced to the MG utilizing voltage source converters in a grid-forming architecture, with the droop control handling the voltage and frequency set points.

The *dq* voltage and current outputs can be used to calculate the active power P and reactive power Q, which can then be averaged using a low-pass filter with a narrow bandwidth. The following equation describes the observed powers P and Q [15]:

Virtual impedance. It's added to the droop control as indicated by (3), Modifying the virtual impedance variable creates an inductive network, guaranteeing that the active and reactive power may be controlled using the droop (3) [19, 20]:

$$Z_v = \left(R_v + \mathrm{j} L_v \omega\right), \quad (3)$$

where R_v, L_v, Z_v stand for virtual resistance, reactance and impedance droop, respectively.

The reference voltage obtained by droop control is modified as:

$$V_{zv} = V_{d\ droop} - R_v.I_{Fabc} - L_v \frac{dI_{Fabc}}{dt}, \qquad (4)$$

where V_{zv} is the voltage obtained by the virtual impedance; I_{Fabc} is the current flowing through the R_F, L_F filter.

Through transforming (4) to *d-q* reference frame:

$$\begin{bmatrix} V_d \\ V_q \end{bmatrix}_{Zv} = \begin{bmatrix} V_d \\ V_q \end{bmatrix}_{droop} - R_v \begin{bmatrix} I_{Fd} \\ I_{Fq} \end{bmatrix} - L_v \begin{bmatrix} -\omega I_{Fd} \\ +\omega I_{Fq} \end{bmatrix} = \\ = \begin{bmatrix} V_{d\ droop} \\ 0 \end{bmatrix} - \begin{bmatrix} R_v & -\omega L_v \\ \omega L_v & R_v \end{bmatrix} \begin{bmatrix} I_{Fd} \\ I_{Fq} \end{bmatrix}. \qquad (5)$$

The cascading voltage/current control loops. The inner control loop, including the current and voltage loops, regulates the 3-phase inverter voltage to assess the DG unit's operational condition. Using Kirchhoff's law, the following equations are:

$$\begin{cases} I_{Fabc} = I_{Cabc} + I_{Tabc}; \\ e_{abc} = R_F I_{Fabc} + L_F \, \mathrm{d}I_{Fabc}/\mathrm{d}t + V_{Fabc}; \\ \mathrm{d}V_{Fabc}/\mathrm{d}t = (1/C_F) I_{Cabc}; \\ V_{Fabc} = R_T I_{Tabc} + L_T \, \mathrm{d}I_{Tabc}/\mathrm{d}t + V_{Labc}, \end{cases} \qquad (6)$$

where I_{Cabc} is the current flowing through the filter capacitor; I_{Tabc} is the current flowing through the R_T and L_T filters; e_{abc} is the converter's output voltage; R_F is the equivalent series resistance; L_F is the inductance of the converter-side filter; C_F is the capacitance of the filter; V_{Fabc} is the voltage across the filter capacitor; R_T, L_T are respectively the equivalent series resistance and the inductance; V_{labc} is the voltage at the PCC point; ω is the frequency of MG.

Through the use of the Park transformation, the expressions obtained can be shown as:

$$\begin{cases} I_{Fd} = I_{Cd} + I_{Td}; \\ I_{Fq} = I_{Cq} + I_{Tq}; \end{cases} \qquad (7)$$

$$\begin{cases} e_d = R_F I_{Fd} + L_F \dfrac{\mathrm{d}I_{Fd}}{\mathrm{d}t} + V_{Fd} - \omega L_F I_{Fq}; \\ e_q = R_F I_{Fq} + L_F \dfrac{\mathrm{d}I_{Fq}}{\mathrm{d}t} + V_{Fq} + \omega L_F I_{Fd}; \end{cases} \qquad (8)$$

$$\begin{cases} V_{Fd} = R_T I_{Td} + L_T \dfrac{\mathrm{d}I_{Td}}{\mathrm{d}t} + V_{Ld} - \omega L_T I_{Tq}; \\ V_{Fq} = R_T I_{Tq} + L_T \dfrac{\mathrm{d}I_{Tq}}{\mathrm{d}t} + V_{Lq} + \omega L_T I_{Td}; \end{cases} \qquad (9)$$

$$\begin{cases} I_{Fd} = C_F \dfrac{\mathrm{d}V_{Fd}}{\mathrm{d}t} - \omega C_F V_{Fq} + I_{Td}; \\ I_{Fq} = C_F \dfrac{\mathrm{d}V_{Fq}}{\mathrm{d}t} + \omega C_F V_{Fd} + I_{Tq}. \end{cases} \qquad (10)$$

Current control loop. The current controller produces the PWM signal for the inverter in the *d-q* reference frame [21]. It minimizes the error between the measured and reference current using a PI regulator (Fig. 3).

Voltage control loop. PI approach. This voltage control loop uses a regulator PI. To compensate for output current disturbances and give the *d-q* current reference components, a feed-forward gain is added to the signal created by comparing the sampled output voltage to the power controller's reference value (Fig. 4).

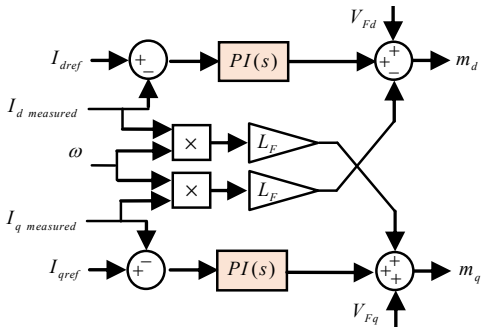

Fig. 3. Detailed diagram of the current control

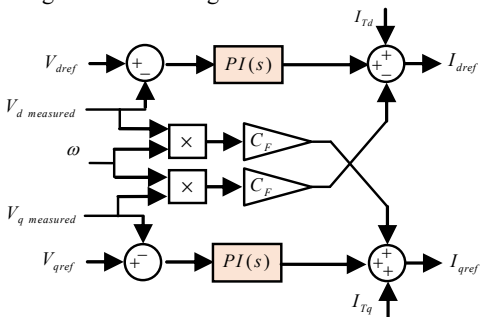

Fig. 4. Detailed diagram of the voltage control

Proposed voltage controller using fuzzy logic. Fuzzy logic is an AI technology that quickly creates nonlinear controllers from heuristic data [22]. Unlike traditional PI controllers, it relies on experiential control methods. A key advantage of FLC systems is their ability to manage complex controlled systems without requiring mathematical modeling. The fuzzy controller has 2 inputs and 1 output. The error signal between the specified reference voltage and the measured voltage is the first input; its derivative is the second; and the reference current is the output. The linguistic variables *N*, *Z*, and *P* where *N* stands for negative, *P* for positive, and *Z* for zero. Most of the controllers that have been built make use of the basic approach proposed by outlined Mamdani (Fig. 5–7).

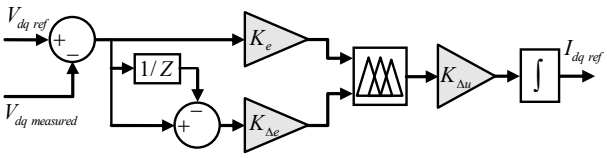

Fig. 5. Block diagram of a proposed FLC

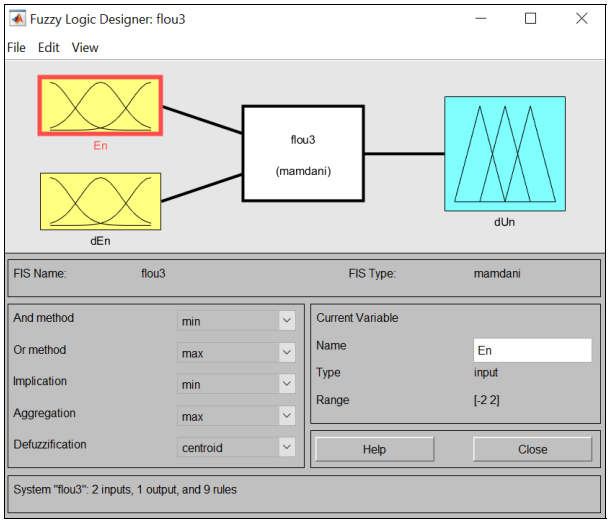

Fig. 6. MATLAB's fuzzy inference system editor window

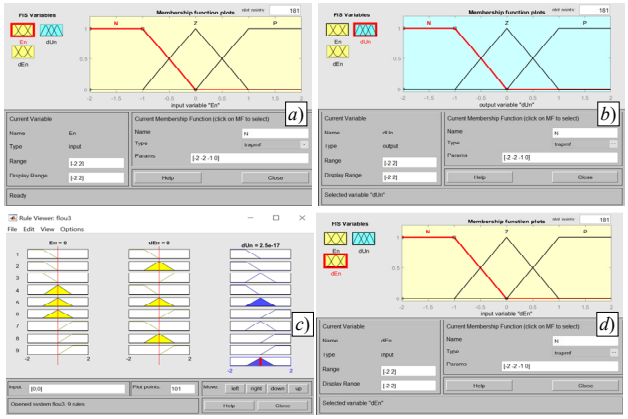

Fig. 7. Different structures of FLC: *a* – membership functions generated error; *b* – derivative of error; *c* – derivative of command of the proposed FLC; *d* – FLC rule viewer

Inference method. The inference engine comprises 2 key components: the fuzzy rule base and the fuzzy implication subblocks. The fuzzified inputs are fed into the inference engine, where the rule base is applied. This process results in the determination of the output fuzzy set (Table 1).

Table 1

Fuzzy inference

The order		Derivative of error		
		N	*Z*	*P*
Error	*N*	*N*	*N*	*Z*
	Z	*N*	*Z*	*P*
	P	*Z*	*P*	*P*

Mathematical modeling of uncertainty. Term «*uncertainty*» refers to discrepancies between mathematical models and real systems. This study focuses on component uncertainty in DG power converters using an LC filter. This approach is vital for creating a robust control system. The system's 2 cascading loops (voltage and current) add complexity due to the LC filter and parametric uncertainty, with model transfer functions treated as uncertain. In our case study, uncertainties in the DG model may include uncertainties in the LC filter components. The following is a representation of the unknown filter parameters [23]:

$$\begin{cases} R_{lF} = R_F\left(1+\rho_R\Delta_R\right); \\ L_{lF} = L_F\left(1+\rho_L\Delta_L\right); \\ C_{lF} = C_F\left(1+\rho_C\Delta_C\right), \end{cases} \qquad (11)$$

where R_F, L_F, C_F are the nominal values of R_{lF}, L_{lF}, C_{lF} respectively; Δ_R, Δ_L, Δ_C are the possible disturbances on these parameters; ρ_R, ρ_L, $\rho_C \in [-1, 1]$ are the maximum deviation between the real system and the mathematical model.

Simulation results. In this section, a simulation study based in AC MG was created by using MATLAB/Simulink software to validate the proposed controller. Several cases were done to examine and analyze the voltage controller's reaction. The main objective here is to design a robust FLC that stabilizes the MG, while comparing FLC and conventional PI controllers under load and system parameter fluctuations. Table 2 represents the parameters for the controller and power stage used in this study.

Proposed droop control with load variation. The proposed droop control principle with virtual impedance was validated against established standards, allowing for a 5 % voltage variation and a frequency variation below 1.4 % [24]. Power sharing among parallel inverters was tested

Table 2

Parameters for the controller and power stage

DC bus voltage	850 V	
Max active power	8 kW	
Max reactive power	6 kVAr	
Switching frequency	5 kHz	
RMS	400 V	
Filter	$R_F = 0.1\ \Omega$, $L_F = 1.35$ mH, $C_F = 50\ \mu$F	
Line	$R_T = 0.35\ \Omega$, $L_T = 0.03$ mH	
Virtual inductance	$L_v = 2$ mH	
Sample time	$t_s = 2\cdot10^{-6}$ s	
Voltage PI control		
d axis control parameters	Proportional term	$K_{pv_d} = 0.3142$
	Integral term	$K_{iv_d} = 10.071$
q axis control parameters	Proportional term	$K_{pv_q} = 0.5944$
	Integral term	$K_{iv_q} = 36.0467$
Current control		
d axis control parameters	Proportional term	$K_{pi_d} = 21.1057$
	Integral term	$K_{ii_d} = 1699$
q axis control parameters	Proportional term	$K_{pi_q} = 42.3115$
	Integral term	$K_{ii_q} = 6798$
Proportional frequency droop		$m_p = 8.75\cdot10^{-5}$
Proportional voltage droop		$n_q = 0.0025$

with a common load $P_{load} = 5$ kW, $Q_{load} = 3$ kVAr, and a sudden change at 0.5 s to evaluate the dynamic response. The droop control technique enabled all DG units to meet the maximum active and reactive power requirements for islanding at full load, effectively sharing the total load demand.

Figure 8 shows the performance evaluation of MG controllers using FLC without uncertainty. The comparative study reveals that FLC outperforms PI control by delivering a faster transient response and improved performance in reaching steady-state, as evidenced by the simulation results.

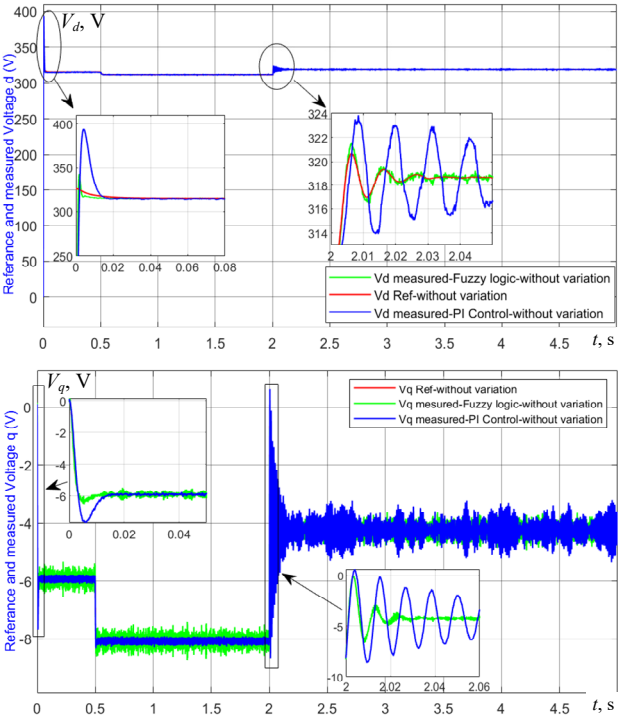

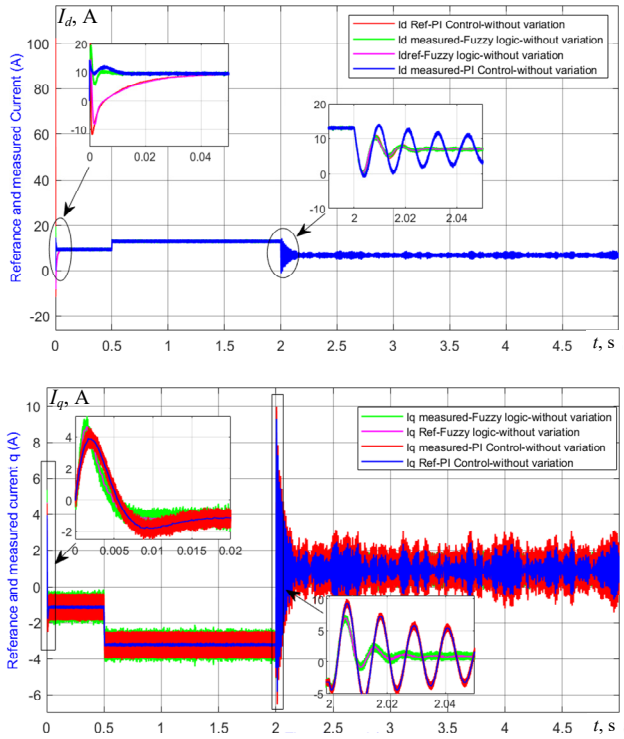

Fig. 8. Performance evaluation of MG controllers using FLC and PI controllers *without* uncertainty model

Figure 9 illustrates the study state value of the frequency and voltage amplitude in the MG as well as the active and reactive power delivered by the DG1 and DG2 for load variation at 0.5 s. Therefore, the *P-f*/*Q-V* droop control with virtual impedance ensures that the voltage fluctuations do not exceed 5 % and frequency deviations remain below 1.4 %. This established that better accuracy and effectiveness are achieved in the MG system.

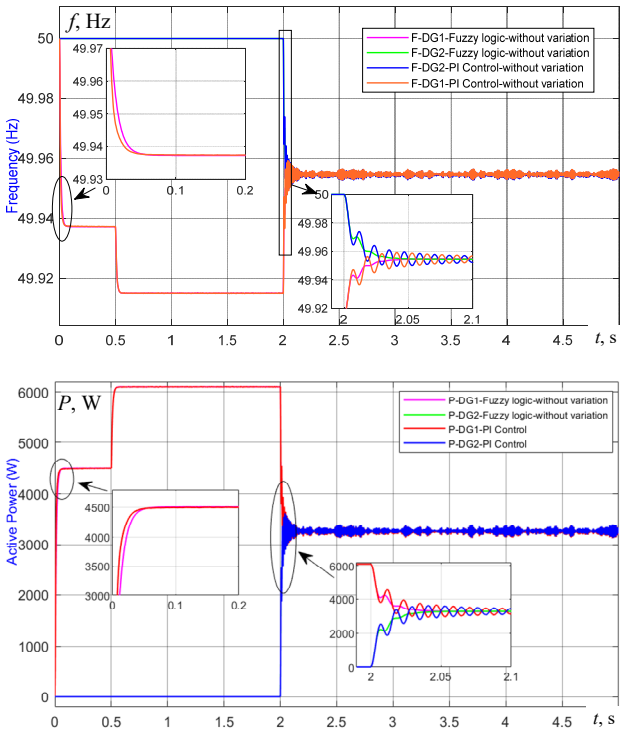

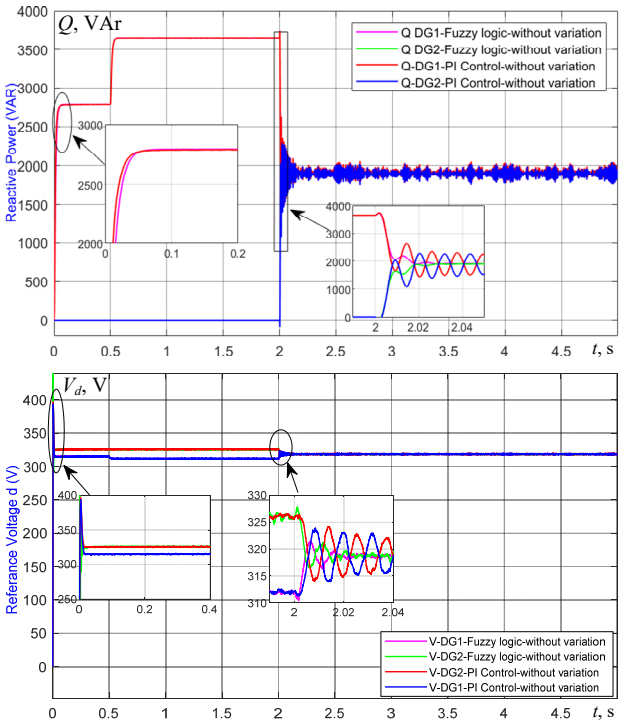

Fig. 9. Comparative study of FLC and PI controllers using *P-f*/*Q-V* droop with virtual impedance *without* uncertainty model

Sequence of DG connection/disconnection. As illustrated in Table 3, a test sequence was employed in this study, involving the activation and deactivation of the second unit at various times. This setup was used to evaluate the performance of inverters connected in parallel and their ability to share power effectively.

Table 3

Reconnection and disconnection sequence of DGs

Time, s	0	1	2+t_s	3	4	5
First DG	connected					
Second DG	disconnected			connected		

Figure 10 shows the performance evaluation of various controllers using an uncertainty model for the *d*-axis regulator voltage. The results indicate that the performance is affected by the PI controller as the parameters change. From 0 to 0.15 s the measured voltage rises to 388 V due to a 50 % reduction in the LC filter parameter. By using the FLC, the measured voltage converges seamlessly into the desired value with less impact compared to PI control where the measurement voltage increases to 335.8 V with variation of the LC filter parameters and the contrast is most pronounced when DG2 is connected at (2+t_s) s (Fig. 11). For *q*-axis the results obtained prove that the FLC is robust and better than the PI controller for all disturbances on the system.

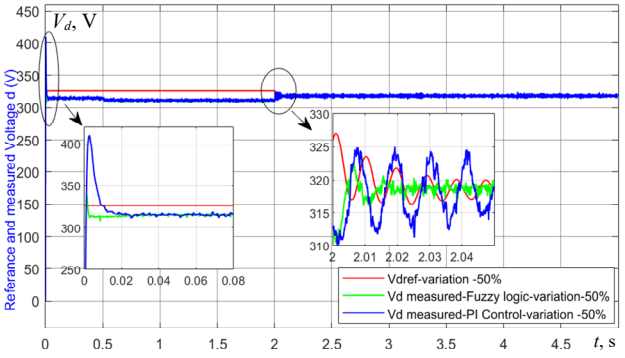

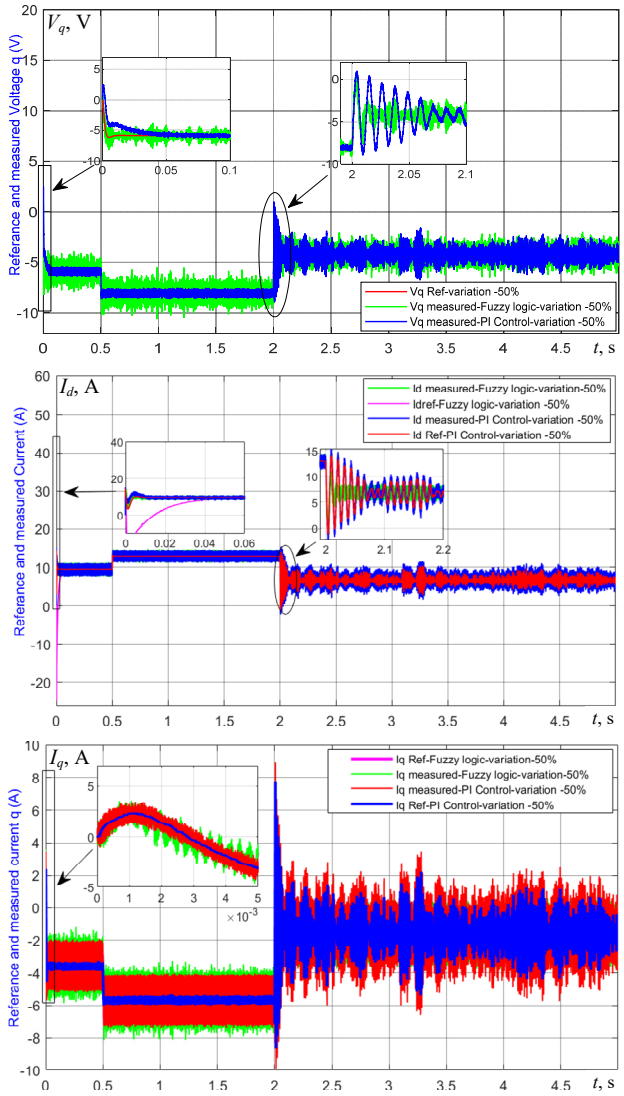

Fig. 10. Performance evaluation of MG controllers using FLC and PI controllers *with* uncertainty model

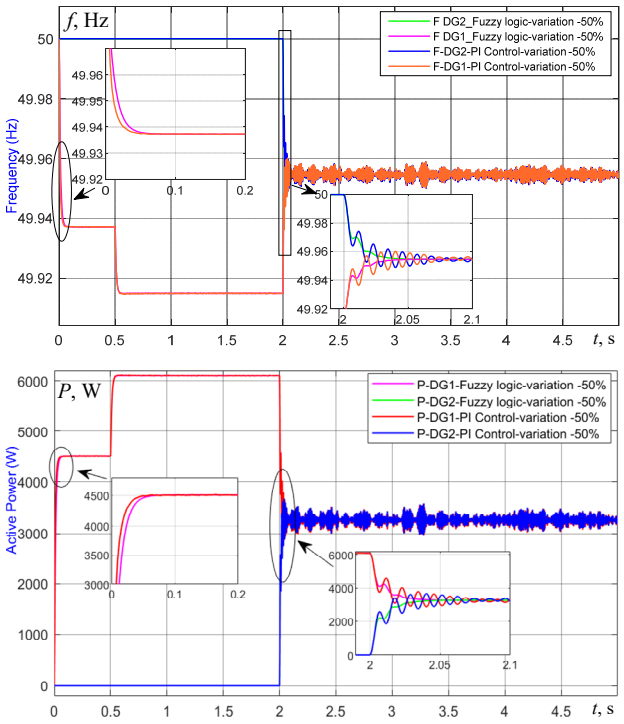

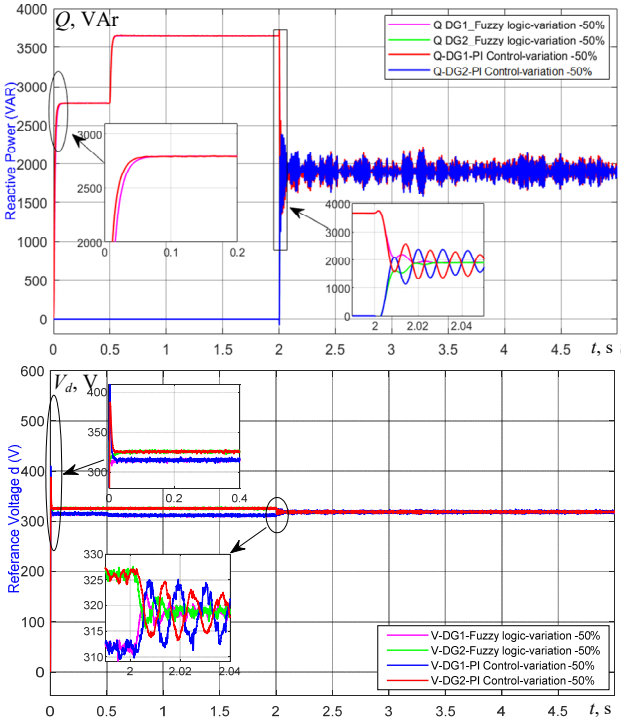

Fig. 11. Comparative study of FLC and PI controllers using *P-f*/*Q-V* droop with virtual impedance *with* uncertainty model

Tables 4, 5 show the assessing the performance of PI and FLC controllers. The voltage stabilization time was notably faster when using FLC. This indicates that FLC outperforms PI control in terms of dynamic performances. The voltage variance is greater with PI control as compared to FLC because it diminishes rapidly due to the effective response of the fuzzy controller.

Table 4

Performance comparison between different controllers *without* uncertainty model

Parameter	PI control		Fuzzy logic	
	d-axis	*q*-axis	*d*-axis	*q*-axis
Overshoot, %	63.962	2.245	10.556	1.992
Undershoot, %	14.955	10.918	1.962	3.125
Rise time, ms	1.84	1.311	0.76476	0.914

Table 5

Performance comparison between different controllers *with* uncertainty model

Parameter	PI control		Fuzzy logic	
	d-axis	*q*-axis	*d*-axis	*q*-axis
Overshoot, %	71.296	75.545	1.531	1.993
Undershoot, %	8.239	13.274	1.985	5.851
Rise time, ms	1.789	1.565	0.82689	0.9716

Conclusions. This paper offers a comparative analysis of voltage control enhancement in microgrids, utilizing both conventional PI controllers and fuzzy logic controllers. The performance evaluation shows that the proposed control, even with changes in the load or system characteristics, the voltage control can be efficiently regulated to the appropriate level. Furthermore, the fuzzy logic controller employed in this study exhibits excellent performance in various transient conditions, offering rapid voltage reference tracking, adaptability to load fluctuations, and superior robustness against system disturbances as compared to the PI controller. These advantages position fuzzy logic controllers as a more effective solution for

voltage control in microgrid applications, highlighting their potential for enhancing the reliability and efficiency of future energy systems.

Conflict of interest. The authors declare that they have no conflicts of interest.

REFERENCES

1. Abbasi M., Abbasi E., Li L., Aguilera R.P., Lu D., Wang F. Review on the Microgrid Concept, Structures, Components, Communication Systems, and Control Methods. *Energies*, 2023, vol. 16, no. 1, art. no. 484. doi: https://doi.org/10.3390/en16010484.

2. Manikandan K., Sasikumar S., Arulraj R. A novelty approach to solve an economic dispatch problem for a renewable integrated micro-grid using optimization techniques. *Electrical Engineering & Electromechanics*, 2023, no. 4, pp. 83-89. doi: https://doi.org/10.20998/2074-272X.2023.4.12.

3. Bakhshi-Jafarabadi R., Lekić A., Marvasti F.D., de Jesus Chavez J., Popov M. Analytical Overvoltage and Power-Sharing Control Method for Photovoltaic-Based Low-Voltage Islanded Microgrid. *IEEE Access*, 2023, no. 11, pp. 134286-134297. doi: https://doi.org/10.1109/ACCESS.2023.3336945.

4. Shahgholian G. A brief review on microgrids: Operation, applications, modeling, and control. *International Transactions on Electrical Energy Systems*, 2021, vol. 31, no. 6, art. no. e12885. doi: https://doi.org/10.1002/2050-7038.12885.

5. Uddin M., Mo H., Dong D., Elsawah S., Zhu J., Guerrero J.M. Microgrids: A review, outstanding issues and future trends. *Energy Strategy Reviews*, 2023, vol. 49, art. no. 101127. doi: https://doi.org/10.1016/j.esr.2023.101127.

6. Hirsch A., Parag Y., Guerrero J. Microgrids: A review of technologies, key drivers, and outstanding issues. *Renewable and Sustainable Energy Reviews*, 2018, vol. 90, pp. 402-411. doi: https://doi.org/10.1016/j.rser.2018.03.040.

7. Wang Y., Li Y., Cao Y., Tan Y., He L., Han J. Hybrid AC/DC microgrid architecture with comprehensive control strategy for energy management of smart building. *International Journal of Electrical Power & Energy Systems*, 2018, vol. 101, pp. 151-161. doi: https://doi.org/10.1016/j.ijepes.2018.02.048.

8. Saeed M.H., Fangzong W., Kalwar B.A., Iqbal S. A Review on Microgrids' Challenges & Perspectives. *IEEE Access*, 2021, vol. 9, pp. 166502-166517. doi: https://doi.org/10.1109/ACCESS.2021.3135083.

9. Hosseinimoghadam S.M.S., Roghanian H., Dashtdar M., Razavi S.M. Power-Sharing Control in an Islanded Microgrid using Virtual Impedance. *2020 8th International Conference on Smart Grid (IcSmartGrid)*, 2020, pp. 73-77. doi: https://doi.org/10.1109/icSmartGrid49881.2020.9144802.

10. Siddaraj S., Yaragatti U.R., Nagendrappa H., Jhunjhunwala V.K. Autonomous microgrid based parallel inverters using droop controller for improved power sharing. *Bulletin of Electrical Engineering and Informatics*, 2020, vol. 9, no. 6, pp. 2302-2310. doi: https://doi.org/10.11591/eei.v9i6.2663.

11. Benchouia M.T., Ghadbane I., Golea A., Srairi K., Benbouzid M.E.H. Implementation of adaptive fuzzy logic and PI controllers to regulate the DC bus voltage of shunt active power filter. *Applied Soft Computing*, 2015, vol. 28, pp. 125-131. doi: https://doi.org/10.1016/j.asoc.2014.10.043.

12. Ikhe A., Pahariya Y. Voltage regulation using three phase electric spring by fuzzy logic controller. *Electrical Engineering & Electromechanics*, 2023, no. 4, pp. 14-18. doi: https://doi.org/10.20998/2074-272X.2023.4.02.

13. Yilmaz U., Kircay A., Borekci S. PV system fuzzy logic MPPT method and PI control as a charge controller. *Renewable and Sustainable Energy Reviews*, 2018, vol. 81, pp. 994-1001. doi: https://doi.org/10.1016/j.rser.2017.08.048.

14. Has Z., Rosyidi A.Z., Pakaya I., Mardiyah N.A., Nurhadi N., Effendy M. Integrated Frequency Control of Microhydro Power Plant Based Flow Valve Control and Electronic Load Controller. *2018 IEEE Conference on Systems, Process and Control (ICSPC)*, 2018, pp. 244-249. doi: https://doi.org/10.1109/SPC.2018.8704153.

15. Adiche S, Larbi M., Toumi D. Improvement of voltage control in AC microgrid using neural network-based adaptive PI controller. *1st International Conference on Renewable Energies and Power Systems (ICREPS'2024)*, University Centre of Naama, Algeria, 2024.

16. Matayoshi H., Kinjo M., Rangarajan S.S., Ramanathan G.G., Hemeida A.M., Senjyu T. Islanding operation scheme for DC microgrid utilizing pseudo Droop control of photovoltaic system. *Energy for Sustainable Development*, 2020, vol. 55, pp. 95-104. doi: https://doi.org/10.1016/j.esd.2020.01.004.

17. Khefifi N. *Élaboration de stratégies de contrôle-commande basées sur la passivité pour le pilotage d'un micro-réseau de génération décentralisée de type AC en mode autonome*. PhD Dissertation, Nantes, 2021. Available at: https://theses.fr/2021NANT4031 (Accessed: 23 may 2024). (Fra).

18. Adiche S., Larbi M., Toumi D. Performance comparison between PI and fuzzy logic controllers of AC microgrids distributed generators. *The 6th International Conference on Electrotechnics*, Oran, 2023.

19. Pournazarian B., Seyedalipour S.S., Lehtonen M., Taheri S., Pouresmaeil E. Virtual Impedances Optimization to Enhance Microgrid Small-Signal Stability and Reactive Power Sharing. *IEEE Access*, 2020, vol. 8, pp. 139691-139705. doi: https://doi.org/10.1109/ACCESS.2020.3013031.

20. Zambroni de Souza A.C., Castilla M. (Eds.). *Microgrids Design and Implementation*. Springer Publ., 2019. 538 p. doi: https://doi.org/10.1007/978-3-319-98687-6.

21. Sepehrzad R., Khojasteh Rahimi M., Al-Durra A., Allahbakhshi M., Moridi A. Optimal energy management of distributed generation in micro-grid to control the voltage and frequency based on PSO-adaptive virtual impedance method. *Electric Power Systems Research*, 2022, vol. 208, art. no. 107881. doi: https://doi.org/10.1016/j.epsr.2022.107881.

22. Al Sumarmad K.A., Sulaiman N., Wahab N.I.A., Hizam H. Energy Management and Voltage Control in Microgrids Using Artificial Neural Networks, PID, and Fuzzy Logic Controllers. *Energies*, 2022, vol. 15, no. 1, art. no. 303. doi: https://doi.org/10.3390/en15010303.

23. Bouzid A.E.M. *Élaboration d'une méthode de contrôle pour améliorer la robustesse d'un micro réseau électrique*. PhD Thesis, University of Quebec at Trois-Rivières, 2017. 229 p. Available at: https://depot-e.uqtr.ca/id/eprint/8169/1/031873046.pdf (Accessed: 23 may 2024). (Fra).

24. *IEEE Std 1547.2-2008. IEEE Application Guide for IEEE Std 1547(TM). IEEE Standard for Interconnecting Distributed Resources with Electric Power Systems*. 2009, 217 p. doi: https://doi.org/10.1109/IEEESTD.2008.4816078.

Received 27.09.2024
Accepted 14.01.2025
Published 02.05.2025

S. Adiche [1], *Phd Student,*
M. Larbi [1], *Full Professor,*
D. Toumi [1], *Senior Lecturer,*
[1] Department of Electrical Engineering, L2GEGI Laboratory, University of Tiaret, Algeria,
e-mail: sarra.adiche@univ-tiaret.dz (Corresponding Author); djilali.toumi@univ-tiaret.dz; mhamed.larbi@univ-tiaret.dz

How to cite this article:
Adiche S., Larbi M., Toumi D. Optimizing voltage control in AC microgrid systems with fuzzy logic strategies and performance assessment. *Electrical Engineering & Electromechanics*, 2025, no. 3, pp. 11-17. doi: https://doi.org/10.20998/2074-272X.2025.3.02

UDC 621.3 https://doi.org/10.20998/2074-272X.2025.3.03

A. Bourouina, R. Taleb, G. Bachir, Z. Boujama, T. Bessaad, H. Saidi

Comparative analysis between classical and third-order sliding mode controllers for maximum power extraction in wind turbine system

Introduction. *Maximizing power extraction in wind energy conversion systems is crucial for efficiency but remains a challenge due to rapid wind speed variations and the high inertia of the generator. Conventional controllers, such as the PI controller, struggle to maintain optimal performance under such dynamic conditions, leading to suboptimal power capture and increased system oscillations. The* ***goal*** *of this study is to enhance the efficiency of wind turbine systems by applying linear and nonlinear controllers in a maximum power point tracking (MPPT) strategy. This approach focuses on improving generator speed regulation and power conversion performance.* ***Methods.*** *A comparative analysis is conducted using three different control strategies: third-order sliding mode control (TO-SMC), classical sliding mode control (SMC) and PI control. These controllers are implemented in the generator speed loop of a wind turbine system, and their performance is evaluated through MATLAB/Simulink simulations. The assessment focuses on key performance metrics such as tracking accuracy, total harmonic distortion (THD), response time, and system stability.* ***Results****. The simulation results confirm that all controllers achieve MPPT, but with varying levels of effectiveness. The TO-SMC outperforms both SMC and PI controllers, offering higher efficiency, reduced chattering, better disturbance rejection, and lower THD (reduced from 73 % in SMC to 68.09 %). Additionally, TO-SMC significantly improves dynamic response, reducing overshoot and enhancing system stability.* ***Originality.*** *This study introduces a TO-SMC for MPPT in wind turbine systems, demonstrating its superiority over conventional control techniques. The findings highlight its ability to maintain optimal power extraction even under rapid wind variations, making it a promising solution for advanced wind energy systems.* ***Practical value.*** *By improving power quality, reducing system oscillations, and enhancing overall wind turbine efficiency, the proposed TO-SMC contributes to the reliable integration of wind energy into power grids. These advancements can benefit renewable energy operators, power system engineers, and researchers seeking efficient and robust MPPT solutions for wind turbines.* References 13, figures 11.
Key words: **wind turbine, maximum power point tracking, third-order sliding mode control, variable speed wind turbines.**

Вступ*. Максимізація відбору потужності в системах перетворення енергії вітру має вагоме значення для ефективності, але залишається проблемою через швидкі зміни швидкості вітру та високу інерцію генератора. Звичайні контролери, такі як ПІ-контролер, важко підтримують оптимальну продуктивність в таких динамічних умовах, що призводить до неоптимального відбору потужності і збільшення коливань системи.* ***Метою*** *статті є підвищення ефективності систем вітряних турбін шляхом застосування лінійних та нелінійних контролерів у стратегії відстеження точки максимальної потужності (MPPT). Цей підхід фокусується на покращенні регулювання швидкості генератора та продуктивності перетворення енергії.* ***Методи****. Порівняльний аналіз проводиться з використанням трьох різних стратегій управління: керування ковзним режимом третього порядку (TO-SMC), класичне керування ковзним режимом (SMC) та ПІ-керування. Ці контролери реалізовані в контурі швидкості генератора системи вітряних турбін, а їх продуктивність оцінюється за допомогою моделювання MATLAB/Simulink. Оцінка фокусується на ключових показниках продуктивності, таких як точність відстеження, повне гармонічне спотворення (THD), час відгуку та стабільність системи.* ***Результати*** *моделювання підтверджують, що ці контролери досягають MPPT, але з різним рівнем ефективності. TO-SMC перевершує як SMC, так і ПІ-регулятори, пропонуючи більш високу ефективність, знижене коливань, краще зменшує перешкоди та має менше THD (знижений з 73 % у SMC до 68,09 %). Крім того, TO-SMC значно покращує динамічний відгук, зменшуючи перерегулювання та підвищуючи стабільність системи.* ***Оригінальність****. Це дослідження представляє TO-SMC MPPT в системах вітряних турбін, демонструючи його перевагу над традиційними методами управління. Результати підкреслюють його здатність підтримувати оптимальний відбір потужності навіть за швидких змін вітру, що робить його перспективним рішенням для сучасних вітроенергетичних систем.* ***Практична цінність****. За рахунок покращення якості електроенергії, зниження коливань системи та підвищення загальної ефективності вітрових турбін пропонований TO-SMC сприяє надійній інтеграції енергії вітру в електромережі. Ці досягнення можуть принести користь операторам відновлюваних джерел енергії, інженерам енергосистем та дослідникам, які шукають ефективні та надійні рішення MPPT для вітрових турбін.* Бібл. 13, рис. 11.
Ключові слова: **вітряна турбіна, відстеження точки максимальної потужності, керування ковзним режимом третього порядку, вітряні турбіни зі змінною швидкістю.**

Introduction. The use of renewable energies is increasing day by day, all over the world to reduce pollution and carbon dioxide emissions, and to reduce climate change. Due to the significant rise in oil and gas prices many countries have put within their strategies to develop the electricity sector the exploitation of wind energy as a priority because it is one of the cleanest and most preferred sources of electricity generation [1]. Among the most widely used wind energy conversion systems that depend on the doubly fed induction generator (DFIG) [2, 3], its main advantage is that the rotor side converter, which exceeds 30 % of the rated power and therefore the lowest cost of the power converter, and their capacity to power at constant voltage and frequency, whatever the speed of the rotor rotation [4, 5]. There are modern methods developed to control wind turbines in order to maximum power point tracking (MPPT) [6, 7]. The principle of the method is modeling turbine and the DFIG, and then a synthesis of the different control strategies [8, 9]. We can cite some strategies which are used. The vector control is the most popular method used in the DFIG [10].

The **goal** of this paper is the enhancement of wind turbine system performance through the application of a third-order sliding mode control (TO-SMC) controller. This controller improves performance by minimizing overshoot, ensuring a more stable and controlled response, reducing response time to enhance efficiency, and eliminating the error between reference and measured values. Additionally, addressing the chattering problem is crucial, as it mitigates high-frequency disturbances around the sliding mode surface, leading to smoother operation and greater overall stability. This controller can also reduce the mechanical stresses by isolating the vibration between the rotor blades and generator shaft. The TO-SMC controller is used to perform the non-linear system compared to PID controller which can only be used for linear system.

Modeling of wind turbine. The main purpose of wind turbines is to convert kinetic energy into aerodynamic power through the blades. In order to model a wind turbine, the following elements must be modeled: Modeling of the wind speed, modeling of the aerodynamic part and modeling of the mechanical system.

Modeling of wind speed. It is usually modeled by complex and random variations with deterministic effects and stochastic fluctuations due to turbulence:

$$V(t) = A_0 + \sum_{i=1}^{n} A_i \sin\left(\frac{2\pi t}{T_i}\right), \quad (1)$$

where A_0 is the average wind value; A_i is the amplitude of each turbulence; $2\pi/T_i$ is the pulsation of every turbulence.

Modeling of the aerodynamic part. This model represents the aerodynamic power at the slow part level of a turbine. In addition, it evaluates the aerodynamic torque T_{ar} as a function of wind turbine angular speed ω_t. In general, the aerodynamic power available form a wind turbine changes with wind speed and can be expressed as:

$$P_{ar} = \frac{1}{2}\rho C_p(\lambda,\beta) S V^3, \quad (2)$$

where P_{ar} is the aerodynamic power; ρ is the air density; C_p is the power coefficient; λ is the tip-speed ratio; β is the pitch angle; S is the blade surface; V is the wind speed.

Knowing the speed of the wind turbine, the aerodynamic torque can be expressed as [5–8]:

$$T_{ar} = \frac{1}{2\Omega_t}\rho C_p(\lambda,\beta) S V^3, \quad (3)$$

where Ω_t is the turbine speed.

Modeling of the mechanical system. In fact, the mechanical system of wind turbines consists of many elements, and therefore its entire representation is complex. In this system, there are many models: 6 masses, 3 masses, 2 masses and 1 mass. It is hence essential to choose the dynamics to represent and the typical values of their characteristic parameters. In this work, the mechanical system is represented by one mass model. In this model, the inertia of the wind turbine on the slow shaft is transferred to the fast shaft. The turbine speed Ω_t and driving torque T_g in the fast shaft are given by:

$$\begin{cases} \Omega_t = \Omega_g / N; \\ T_g = T_{ar} / N, \end{cases} \quad (4)$$

where N is the gearbox ratio.

The generator speed Ω_g is given by:

$$J_t \frac{d\Omega_g}{dt} = T_g - T_{em} - f_t \Omega_g, \quad (5)$$

where

$$J_t = J_r / N^2 + J_g \quad \text{and} \quad f_t = f_r / N^2 + f_g,$$

J_g is the inertia of the generator; J_r is the inertia of the wind turbine; J_t is the total moment of inertia; f_g is the viscous friction coefficient of the generator rotor; f_r is the viscous friction coefficient of the turbine rotor; f_t is the total viscous friction coefficient.

To optimize the power generated, it is therefore appropriate for the generator to have a power or characteristic torque follows the maximum line $C_{p,\max}$ with the angle of $\beta = 0°$. Figure 1 shows an example of power coefficient curves of a wind turbine, showing the evolution of the power coefficient C_p as a function of the tip-speed ratio λ for different values of the pitch angle β.

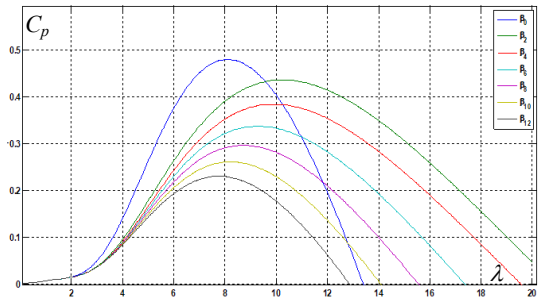

Fig. 1. Power coefficient C_p as a function of λ and β

Figure 2 shows the block diagram of the aerodynamic and mechanical modeling for the wind turbine.

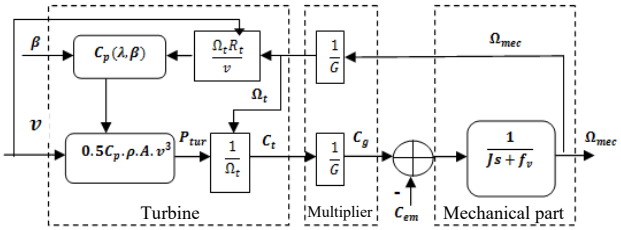

Fig. 2. Modeling of the mechanical part of the wind turbine

Control of variable speed wind turbine below rated power. The objective of variable speed wind turbine control, when the wind speed is below the rated speed, is to maximize the aerodynamic power by using the different power maximization strategies. This power is maximized through the electromagnetic torque control. At a wind speed above the rated speed, the objective of the control is to limit the aerodynamic power transmitted to the generator and to keep the turbine within its operating limits by using the different control strategies. Indeed, effective control of variable speed wind turbines can improve the dynamic characteristics, increase the turbine lifetime and reduce the transient load on the drive shaft. Many techniques have been proposed for the maximum extraction or limitation of aerodynamic power from variable speed wind turbine in the last decade. Generally, the control of wind turbine goes through 3 different operating zones which depend on the wind speed, the maximum allowable generator speed and the desired power (Fig. 3) [8].

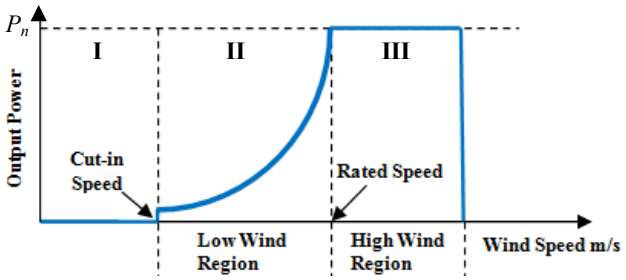

Fig. 3. Wind region classification

Zone I. In this zone, the generator is stopped, because the wind speed is not high enough to operate the wind system, and therefore it does not produce any electrical power P_{el}

$$\begin{cases} V \le V_{\min}; \\ P_{el} = 0. \end{cases} \quad (6)$$

Zone II. This area is characterized by operation at wind speeds less than or equal to the nominal speed. For this reason, we seek to maximize the aerodynamic power in order to extract the maximum aerodynamic power. With this strategy, we seek the maximum power point for each wind speed, it is the MPPT. This area is called is characterized by operation at partial load. In this case, it should be noted that the orientation angle of the blades must be constant and always equal to zero ($\beta = 0°$), and the relative speed of the turbine is at its optimum value (λ_{opt}). In this area:

$$\begin{cases} V_{\min} < V \le V_n; \\ P_{aer,\max} = 0.5 \cdot C_{p,\max} \rho S V^3. \end{cases} \quad (7)$$

Zone III. This zone is characterized by operation at wind speeds higher than the nominal speed. It is called the nominal load operating zone. In this zone, a control action is used on the turbine blades to maintain the aerodynamic power P_{aer} within its nominal power value P_n, to ensure the safety of the generator and to limit the mechanical loads transmitted to the nacelle and the tower. If the wind speed exceeds the maximum speed, the control system adjusts the blade pitch angle to the value ($\beta = 90°$) to stop the generator. In this zone:

$$\begin{cases} V_n < V \le V_{\max}; \\ P_{aer} = P_n. \end{cases} \quad (8)$$

The synthesis of this controller can be carried out in 3 successive steps [11, 12]:

- definition of the surface;
- choice of the Lyapunov's function to ensure the stability of the system;
- determination of the equivalent control law.

The purpose of the TO-SMC controller is to ensure that the measured value follows the trajectory of the reference value. The generator speed tracking error can be defined as follows. To apply the SMC strategy a surface must be defined. Equation (9) represents a sliding surface for controlling the speed generator:

$$S_{\Omega g} = \lambda \Omega_g^* - \lambda \Omega_g + \frac{\mathrm{d}(\Omega_g^* - \Omega_g)}{\mathrm{d}t}. \quad (9)$$

From (9) the derivative of the error is given by:

$$\dot{S}_{\Omega g} = \lambda \dot{\Omega}_g^* - \lambda \dot{\Omega}_g + \ddot{\Omega}_g^* - \ddot{\Omega}_g. \quad (10)$$

Substituting (5) and the derivative of (5) into (10) we obtain:

$$\dot{S}_{\Omega g} = \lambda \dot{\Omega}_g^{ref} - \frac{\lambda}{J_g}\left[T_g - T_{em} - f_g \Omega_g\right] + \\ + \ddot{\Omega}_g^* - \frac{1}{J_g}\left[\dot{T}_g - \dot{T}_{em} - f_g \dot{\Omega}_g\right] \quad (11)$$

For the stability study of the closed-loop system, we will use the Lyapunov's stability theorem. The Lyapunov's candidate stability function is defined by:

$$V_{\Omega g} = \frac{1}{2} S(\Omega_g)^2. \quad (12)$$

The derivative of the Lyapunov's function is defined in the next expression:

$$\dot{V}_{\Omega g} = \dot{S}(\Omega_g) \cdot S(\Omega_g) < 0. \quad (13)$$

The control law has to ensure the stability condition and the convergence of the trajectories of the system on the sliding surface $S(\Omega_g) = 0$ from:

- if $S(\Omega_g) < 0$ and $\dot{S}(\Omega_g) < 0$, therefore $S(\Omega_g)$ will increase to 0;
- if $S(\Omega_g) > 0$ and $\dot{S}(\Omega_g) < 0$, therefore $S(\Omega_g)$ will increase to 0.

In steady state, the equivalent control is calculated by considering that the developed electromagnetic torque and its reference are equal, so the control law becomes:

$$T_{em}^* = \alpha_{\Omega g} \sqrt{\left|S(\Omega_g)\right|} \operatorname{sign}\left(S(\Omega_g)\right) + \beta_{\Omega g} \int \operatorname{sign}\left(S(\Omega_g)\right) \mathrm{d}t, \quad (14)$$

where $\alpha_{\Omega g}$ and $\beta_{\Omega g}$ are the controller gains and must be positive.

Simulation results and discussion. In order to highlight the performance of the MPPT control algorithms applied to the one-mass wind turbine and the objective a comparison of the control techniques that we have presented, we will carry out a series of simulations in MATLAB/Simulink environment (Fig. 4). All these simulations will be carried out under the same conditions:

- the wind speed profile by (1);
- the blade orientation angle is maintained at its zero value ($\beta = 0°$). The wind turbine parameters are reported in [12, 13].

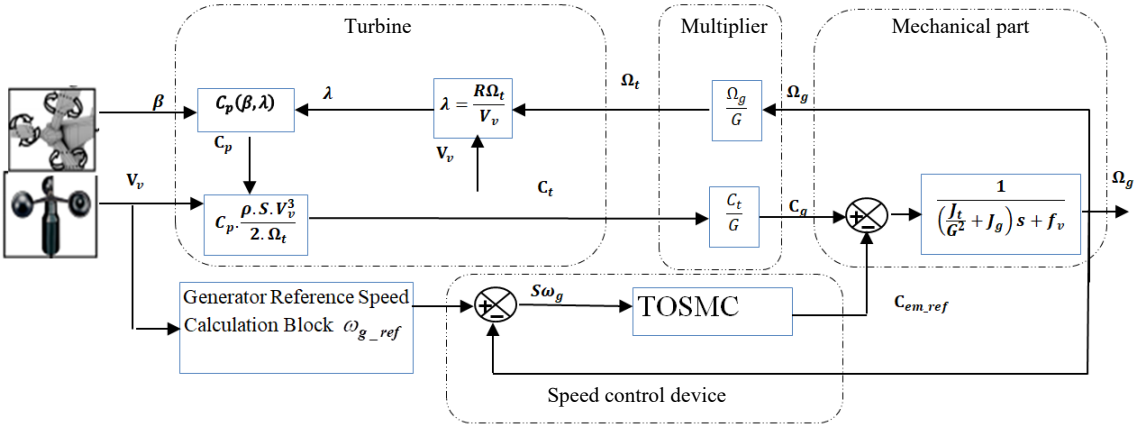

Fig. 4. Block diagram of the TO-SMC

Figures 5–10 illustrate wind turbine MPPT performance as a function of wind speed using (1). From the simulation results it is observed that for TO-SMC the power extracted by the turbine follows the desired trajectory with good efficiency. For the SMC and PI controllers the variations of the wind speed cause significant oscillations of the aerodynamic torque, which increases the mechanical stress of the turbine and electromagnetic vibrations at the generator level, which affects the quality of the electrical energy supplied to the electrical grid. From Fig. 5–10 it can be seen that this proposed TO-SMC strategy has better response characteristics in settling time and overshoot compared with both SMC and PI.

Figures 11,*a*,*b* show harmonic spectral analysis, which show the total harmonic distortion with the SMC controller (THD = 73.2 %) are significantly attenuated with the TO-SMC controller (THD = 68.09 %).

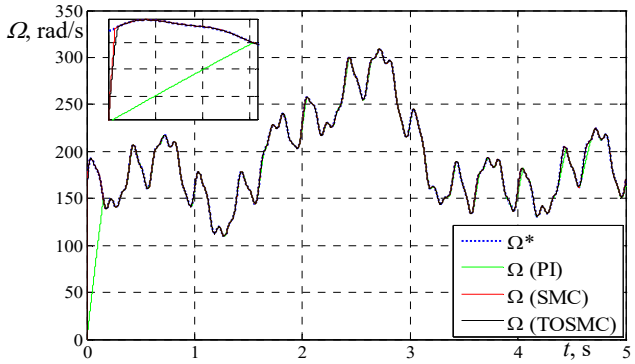

Fig. 5. Generator rotation speed

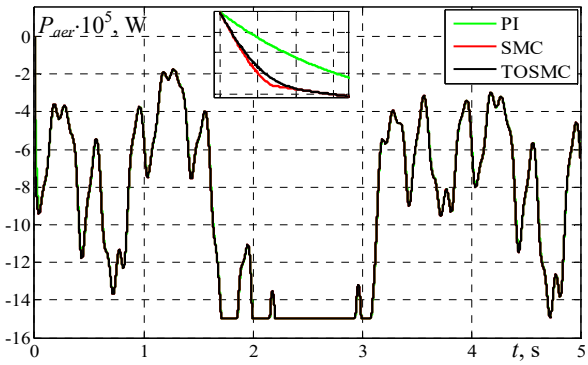

Fig. 6. Aerodynamic power

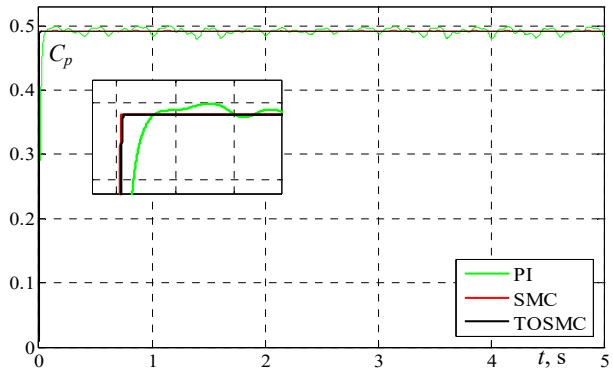

Fig. 7. Power coefficient

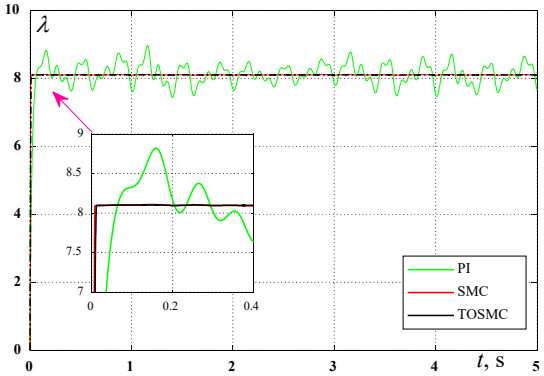

Fig. 8. Tip speed ratio

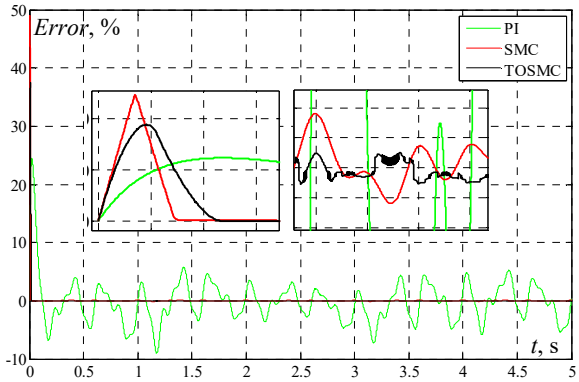

Fig.9. Generator rotation speed error

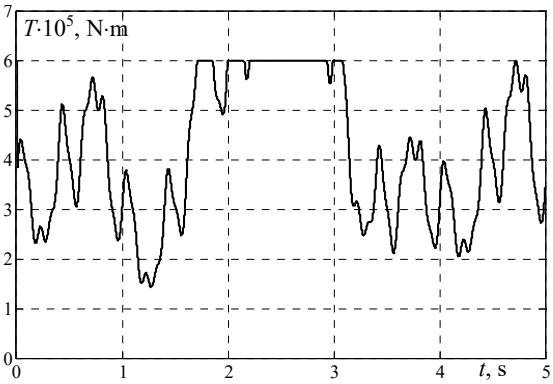

Fig. 10. Generator torque

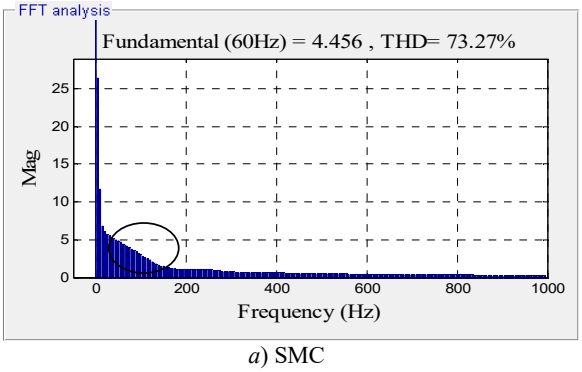

a) SMC

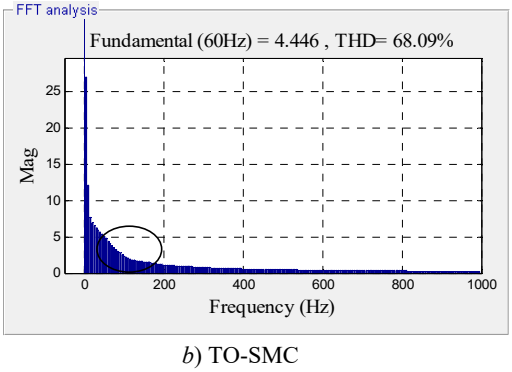

b) TO-SMC

Fig. 11. Total harmonic distortion

Conclusions. In this study, the TO-SMC is used to perform the tip speed ratio strategy in order to extract maximum power from the wind energy. The results obtained illustrate that non-linear controller TO-SMC can improve the performance of wind turbine system by accurately tracking the generator speed reference and achieving the maximum power coefficient. A comparative analysis of PI, SMC and TO-SMC controllers highlights the superior effectiveness of TO-SMC controller. Compared to the other controllers, TO-SMC generates less chattering, provides better disturbance rejection, and reduces mechanical stress on the transmission shaft. In contrast, conventional PI-based direct speed control and classic SMC exhibit lower efficiency, increased oscillations, and diminished overall performance.

The practical significance of this work is evident in the improved wind turbine efficiency, reflected by a reduction in THD from 73 % to 68.09 %, along with enhanced dynamic response, minimized overshoot, and faster settling time. These improvements contribute to more stable and higher-quality power generation, supporting the seamless integration of wind energy into electrical grids.

Conflict of interest. The authors declare that they have no conflicts of interest.

REFERENCES

1. *Rapport annuel mondial sur l'énergie - Edition 2024*. Available at: https://kpmg.com/fr/fr/insights/energie/rapport-annuel-energie-edition-2024.html (Accessed: 30 July 2024). (Fra).

2. Nair R., Gopalaratnam N. Stator Flux Based Model Reference Adaptive Observers for Sensorless Vector Control and Direct Voltage Control of Doubly-Fed Induction Generator. *IEEE Transactions on Industry Applications*, 2020, vol. 56, no. 4, pp. 3776-3789. doi: https://doi.org/10.1109/TIA.2020.2988426.

3. Hassainia S., Ladaci S., Kechida S., Khelil K. Impact of fractional filter in PI control loop applied to induction motor speed drive. *Electrical Engineering & Electromechanics*, 2022, no. 5, pp. 14-20. doi: https://doi.org/10.20998/2074-272X.2022.5.03.

4. Muthukaruppasamy S., Dharmaprakash R., Sendilkumar S., Parimalasundar E. Enhancing off-grid wind energy systems with controlled inverter integration for improved power quality. *Electrical Engineering & Electromechanics*, 2024, no. 5, pp. 41-47. doi: https://doi.org/10.20998/2074-272X.2024.5.06.

5. Kerboua A., Abid M. Hybrid fuzzy sliding mode control of doubly-fed induction generator speed in wind turbines. *Journal of Power Technologies*, 2015, vol. 95, no. 2, pp. 126-133.

6. Mousa H.H.H., Youssef A.-R., Mohamed E.E.M. Variable step size P&O MPPT algorithm for optimal power extraction of multi-phase PMSG based wind generation system. *International Journal of Electrical Power & Energy Systems*, 2019, vol. 108, pp. 218-231. doi: https://doi.org/10.1016/j.ijepes.2018.12.044.

7. Abdullah M.A., Yatim A.H.M., Chee Wei Tan. A study of maximum power point tracking algorithms for wind energy system. *2011 IEEE Conference on Clean Energy and Technology (CET)*, 2011, pp. 321-326. doi: https://doi.org/10.1109/CET.2011.6041484.

8. Bourouina A., Djahbar A., Chaker A., Boudjema Z. High Order Sliding Mode Direct Torque Control of a DFIG Supplied by a Five-Level SVPWM Inverter for the Wind Turbine. *Elektrotehniski Vestnik*, 2018, vol. 85, no. 5, pp. 263-270.

9. Saidi Y., Mezouar A., Miloud Y., Yahiaoui M., Benmahdjoub M.A. Modeling and adaptive power control-designed based on tip speed ratio method for wind turbines. *Przeglad Elektrotechniczny*, 2019, vol. 95, no. 6, pp. 40-46. doi: https://doi.org/10.15199/48.2019.06.08.

10. Oualah O., Kerdoun D., Boumassata A. Comparative study between sliding mode control and the vector control of a brushless doubly fed reluctance generator based on wind energy conversion systems. *Electrical Engineering & Electromechanics*, 2022, no. 1, pp. 51-58. doi: https://doi.org/10.20998/2074-272X.2022.1.07.

11. Oualah O., Kerdoun D., Boumassata A. Super-twisting sliding mode control for brushless doubly fed reluctance generator based on wind energy conversion system. *Electrical Engineering & Electromechanics*, 2023, no. 2, pp. 86-92. doi: https://doi.org/10.20998/2074-272X.2023.2.13.

12. Benbouhenni H., Driss A., Lemdani S. Indirect active and reactive powers control of doubly fed induction generator fed by three-level adaptive-network-based fuzzy inference system – pulse width modulation converter with a robust method based on super twisting algorithms. *Electrical Engineering & Electromechanics*, 2021, no. 4, pp. 31-38. doi: https://doi.org/10.20998/2074-272X.2021.4.04.

13. Ahmed S., Ahmed A., Mansoor I., Junejo F., Saeed A. Output Feedback Adaptive Fractional-Order Super-Twisting Sliding Mode Control of Robotic Manipulator. *Iranian Journal of Science and Technology, Transactions of Electrical Engineering*, 2021, vol. 45, no. 1, pp. 335-347. doi: https://doi.org/10.1007/s40998-020-00364-y.

Received 26.10.2024
Accepted 11.01.2025
Published 02.05.2025

A. Bourouina[1], *PhD Student,*
R. Taleb[2], *Professor,*
G. Bachir[1], *Professor,*
Z. Boudjema[3], *Professor,*
T. Bessaad[3], *Associate Professor,*
H. Saidi[2], *Associate Professor,*
[1] Electrical Engineering Department,
University of Science and Technology of Oran Mohamed Boudiaf (USTO-MB),
Laboratoire de Development Durable de l'Energie Electrique (LDDEE), Algeria,
e-mail: abdelka.bourouina@gmail.com (Corresponding Author); ghalem.bachir@univ-usto.dz
[2] Laboratoire Genie Electrique et Energies Renouvelables (LGEER), Electrical Engineering Department,
Hassiba Benbouali University of Chlef,
Research Centre for Scientific and Technical Information (CERIST), Algeria,
e-mail: r.taleb@univ-chlef.dz; hem.saidi@gmail.com
[3] Electrical Engineering Department,
Hassiba Benbouali University of Chlef,
Laboratoire Genie Electrique et Energies Renouvelables (LGEER), Algeria,
e-mail: boudjemaa1983@yahoo.fr; ta.bessaad@gmail.com

How to cite this article:
Bourouina A., Taleb R., Bachir G., Boujama Z., Bessaad T., Saidi H. Comparative analysis between classical and third-order sliding mode controllers for maximum power extraction in wind turbine system. *Electrical Engineering & Electromechanics*, 2025, no. 3, pp. 18-22. doi: https://doi.org/10.20998/2074-272X.2025.3.03

UDC 621.3 https://doi.org/10.20998/2074-272X.2025.3.04

H. Chaib, S. Hassaine, Y. Mihoub, S. Moreau

Intelligent power control strategy based on self-tuning fuzzy MPPT for grid-connected hybrid system

Introduction. *This paper investigates various methods for controlling the Maximum Power Point Tracking (MPPT) algorithm within the framework of intelligent energy control for grid-connected Hybrid Renewable Energy Systems (HRESs).* ***The purpose*** *of the study is to improve the efficiency and reliability of the power supply in the face of unpredictable weather conditions and diverse energy sources. Intelligent control techniques are used to optimize the extraction of energy from available sources and effectively regulate energy distribution throughout the system.* ***Novelty*** *study is employing intelligent control strategies for both energy optimization and control. This research distinguishes itself from conventional approaches, particularly through the application of Self-Tuning Fuzzy Logic Control (ST-FLC) and fuzzy tracking. Unlike conventional methods that rely on logical switches, this intelligent strategy utilizes fuzzy rules adapted to different operating modes for more sophisticated energy control. The proposed control strategy minimizes static errors and ripples in the direct current bus and challenges in meeting load demands.* ***Methods*** *of this research includes a comprehensive analysis of several optimization techniques under varying weather scenarios. The proposed strategy generates three control signals that correspond to selected energy sources based on solar irradiation, wind velocity and battery charging status.* ***Practical value.*** *ST-FLC technique outperforms both conventional methods and standard Fuzzy Logic Controllers (FLCs). It consistently delivers superior performance during set point and load disturbance phases. The simulation, conducted using MATLAB/Simulink.* ***The results*** *indicate that fuzzy proposed solution enables the system to adapt effectively to various operational scenarios, displaying the practical applicability of the proposed strategies. This study presents a thorough evaluation of intelligent control methods for MPPT in HRESs, emphasizing their potential to optimize energy supply under varying conditions.* References 27, tables 6, figures 18.

Key words: **maximum power point tracking algorithm, hybrid renewable energy system, conventional controller, fuzzy logic controller, self-tuning fuzzy logic control.**

Вступ. *У цій статті досліджуються різні методи керування алгоритмом стеження за точкою максимальної потужності (MPPT) в рамках інтелектуального керування енергією для підключених до мережі гібридних систем відновлюваної енергетики (HRESs).* ***Метою*** *дослідження є підвищення ефективності та надійності електропостачання в умовах непередбачуваних погодних умов та різноманітних джерел енергії. Інтелектуальні методи управління використовуються для оптимізації видобутку енергії з доступних джерел та ефективного регулювання розподілу енергії по всій системі.* ***Новизна*** *дослідження полягає у застосуванні інтелектуальних стратегій управління як для оптимізації, так і для контролю енергії. Це дослідження відрізняється від традиційних підходів, зокрема, завдяки застосуванню самонастроюваного нечіткого логічного керування (ST-FLC) та нечіткого відстеження. На відміну від традиційних методів, які покладаються на логічні перемикачі, це інтелектуальне управління використовує нечіткі правила, адаптовані до різних режимів роботи для більш складного управління енергією. Запропонована стратегія керування мінімізує статичні похибки та пульсації в шині постійного струму, а також проблеми з задоволенням потреб навантаження.* ***Методи*** *дослідження включають комплексний аналіз декількох методів оптимізації за різних погодних умов. Запропонована стратегія генерує три сигнали керування, які відповідають обраним джерелам енергії на основі сонячного випромінювання, швидкості вітру та стану заряду акумуляторів.* ***Практична цінність****. Технологія ST-FLC перевершує як традиційні методи, так і стандартні контролери нечіткої логіки (FLC). Вона стабільно забезпечує високу продуктивність під час фаз заданого значення та збурення навантаження. Моделювання проводилося за допомогою MATLAB/Simulink.* ***Результати*** *показують, що запропоноване нечітке рішення дозволяє системі ефективно адаптуватися до різних сценаріїв роботи, демонструючи практичну застосовність запропонованих стратегій. Це дослідження представляє ретельну оцінку інтелектуальних методів управління для MPPT в HRES, підкреслюючи їх потенціал для оптимізації енергопостачання за різних умов.* Бібл. 27, табл. 6, рис. 18.

Ключові слова: **алгоритм стеження за точкою максимальної потужності, гібридна система відновлюваної енергетики, традиційний регулятор, регулятор нечіткої логіки, самонастроюваний регулятор нечіткої логіки.**

Introduction. In light of the massive increase in population, the demand for energy has increased, obliging people to think about new non-traditional energy sources. Conventional energy sources are exhaustible and not ecology friendly due to the carbon dioxide CO_2 emissions, in addition to this their market is not stable. The trend is towards renewable energies in particular solar, wind and hydrogen. Renewable energy has various advantages such as being free, sustainable and respecting environment. In the other side, there is non-linearity and intermittence caused by climatic conditions. To overcome this constraint, great achievement in power sector has been deployed. Wind and solar are the most exploited renewable resources [1]. The stability of the grid depends on the equilibrium between consumption and production. The widespread use of renewable energies must be supported by the use of additional electrical energy storage devices. The Hybrid Renewable Energy Systems (HRESs) that runs mostly on solar and wind energy is commonly used. There are two configurations standalone or grid connected [2–4].

A number of works has been reported to study power control. Electrification and microgrids are treated in [5, 6], smart grids – in [7]. Various configurations of HRESs often consist of energy sources (wind energy and solar energy), in addition to storage systems with the possibility of connecting to the grid or standalone. Fuzzy Logic Control (FLC), Perturb and Observe (P&O), hill climbing and incremental conductance have been most used for photovoltaic (PV) Maximum Power Point Tracking (MPPT) [8–11]. To extract the maximum energy from Wind Turbines (WTs) the most used configuration are realized by rectifier or by chopper. Several studies have been developed using classic control method (PI, PID, sliding mode control so on) or artificial intelligence (FLC, Self-Tuning Fuzzy Logic Control (ST-FLC), neural network and genetic algorithms) [12–16].

In general, the energy control is still based on checks and balances. A number of studies have proposed different methods of power control [17–24].

Literature review. The paper [25] discusses the use of a ST-FLC PID controller for MPPT in variable-speed

WTs. While the proposed controller enhances MPPT performance, it still exhibits static errors and ripples at the DC bus. In [26], energy control strategies for HRESs with battery storage are examined. This hybrid system, comprising PV panels, WTs and diesel generators, operates without grid connection. A FLC is implemented to optimize power allocation among the PV, WT, diesel and battery systems. However, the established rules fail to effectively manage power distribution among sources and battery storage, leading to challenges in meeting load demands. The study [27] presents a PI controller for energy control in HRES. Despite its application, this conventional regulator struggles with disturbances in the DC voltage. Additionally, the mathematical models based on PI control calculate the gains for a nonlinear system. This approach suffers from static errors at the DC bus level and experiences significant voltage spikes during system startup.

The goal of the article is to improve the energy efficiency and reliability of the power supply in various and unpredictable weather conditions. Intelligent (FLC and ST-FLC) MPPT strategies are suggested and compared to conventional (PI and P&O) MPPT. An intelligent power control system based on fuzzy rules adapted to different operating modes of a HRESs with battery storage. The control also minimizes static errors and ripples in the direct current bus.

The suggested algorithms are employed to regulate the output voltage to a predefined value in order to extract the maximum possible power from WT and PV systems. A FLC is used to act on the HRES according to the proposed intelligent strategy. The FLC has many advantages over conventional strategies based mainly on logical states. It is simple and very close to human reasoning. The main advantage is that expert knowledge is captured and used at any time to improve the existing system by adding some rules or acting on the power organization controller for accurate selection of the source at the right time to feed the telecommunication loads and manage the whole hybrid power system. The different control strategies developed were implemented in the MATLAB/Simulink environment. The obtained results showed that the ST-FLC technique is superior to the others, and the results confirm the superiority of FLC to supervise the system according to the proposed strategy.

System description. The studied HRES is connected to the grid and has two renewable energy sources (PV and WT) with storage. The power tracking is based on FLC. The purpose is to match the power demand of the load and to keep the battery bank in a state of charge in order to prevent power outages and to extend the lifetime of the batteries independently of fluctuations in solar irradiation and wind velocity. The design of the presented system is shown in Fig. 1.

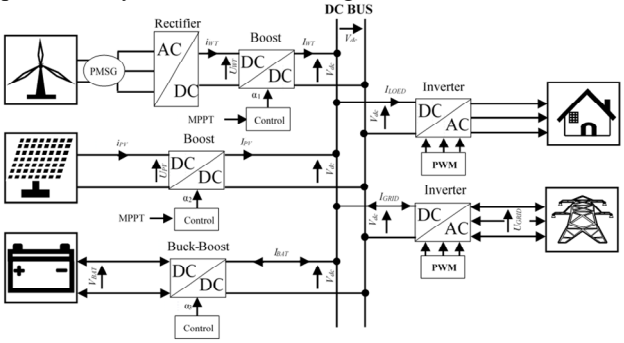

Fig. 1. Hybrid power system

WT system model. The WT-derived mechanical energy is detailed as follows:

$$P_m = \tfrac{1}{2}\rho\pi R^2 V_w^3 c_p(\lambda,\beta), \quad (1)$$

where P_m is the power extracted from the WT; ρ is the density of the air; R is the radius of the blade; V_w is the wind velocity; $C_p(\lambda, \beta)$ is the power coefficient, where λ is the tip speed ratio. The definition of the parameter λ is:

$$\lambda = \omega_m R / V_w . \quad (2)$$

The pitch angle β is maintained constant during MPPT control ($\beta = 0$), ω_m is the mechanical speed of the WT. The input torque for the turbine is:

$$T_m = P_m / \omega_m . \quad (3)$$

The generator is modelled by the following voltage equations in d_q-axis:

$$V_{sd} = R_s I_{sd} + \frac{\mathrm{d}\phi_{sd}}{\mathrm{d}t} + \omega_e \phi_{sq}; \quad (4)$$

$$V_{sq} = R_s I_{sq} + \frac{\mathrm{d}\phi_{sq}}{\mathrm{d}t} + \omega_e \phi_{sd}, \quad (5)$$

where i_{sd}, i_{sq} are the currents in the d-q reference frame; R_s is the stator resistance; ω_e is the electrical rotation speed; φ_{sd} along with φ_{sq} indicate the stator flux linkages along the d and q-axis are acquired through:

$$\phi_{sd} = L_d i_{sd} + \varphi_m; \quad (6)$$

$$\phi_{sq} = -L_q i_{sq}, \quad (7)$$

where L_d, L_q are the inductances in the d-q reference frame; ϕ_m is the rotor magnetic flux generated by the generator.

The electromagnetic torque expression T_e is:

$$T_e = \tfrac{3}{2} p(L_d - L_q) i_{sd} i_{sq} + \phi_m i_{sq}, \quad (8)$$

where p is the number of pole pairs.

The mechanical equation connecting the generator and WT is:

$$J_{eq} \frac{\mathrm{d}w_g}{\mathrm{d}t} = T_e + T_l - B_m w_g, \quad (9)$$

where J_{eq} is the equivalent inertia moment of the system; w_g is the angular speed of the generator; T_e is the electromagnetic torque produced by the generator; T_l is the torque exerted by the turbine on the generator; B_m is the viscous damping coefficient.

PV system model. Figure 2 shows the equivalent circuit of a standalone solar cell, which includes a single diode, and, using Kirchhoff's current law, the output current I_{pv} of the solar PV cell can be expressed as:

$$I_{pv} = I_{ph} - I_d - I_{sh}; \quad (10)$$

$$I_d = I_0\left(\exp\left[\frac{V_{pv}}{nV_t}\right] - 1\right); \quad V_t = \frac{kT}{q}, \quad (11)$$

$$I_{pv} = I_{ph} - I_0\left(\exp\left[\frac{q(V_{pv} + R_s I_{pv})}{nkT}\right] - 1\right) - \frac{V_{pv} + R_s I_{pv}}{R_{sh}}, \quad (12)$$

where I_d is the current through the diode; I_{sh} is the current through the resistor R_{sh}; R_s, R_{sh} are the series and shunt resistances, respectively; I_0 is the saturation current; I_{ph} is the photocurrent; n is the diode ideality factor; V_t is the thermal voltage of the diode; k is the Boltzmann constant; T is the operating temperature of the cell; q is the electron charge.

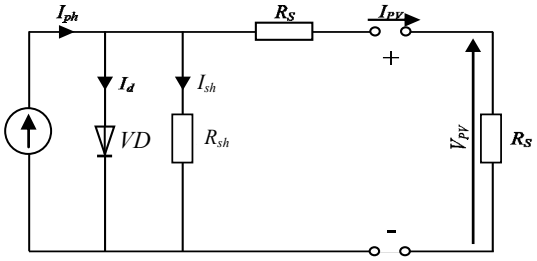

Fig. 2. Equivalent circuit of solar cell

Storage modelling. It is based on the electrical diagram (Fig. 3), containing 3 elements: a voltage source, the internal resistance and the capacitor:

$$U_{bat} = E_0 - K.\frac{\int I_b dt}{Q_0} + R_b I_b\,, \tag{13}$$

where E_0 is the open circuit voltage of the battery; K is the battery-dependent constant; R_b is the internal battery resistance; I_b is the discharging current; Q_0 is the battery capacity; $\frac{K}{Q_0}\int I_b \mathrm{d}t$ indicates the battery discharge status.

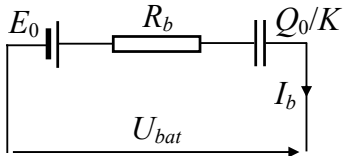

Fig. 3. Electrical model of the battery

Grid model. The dynamic grid connection model, employing a reference frame that synchronously rotates with the grid voltage space vector, is depicted as:

$$U_{gd} = -R_g i_{gd} - \frac{L_g \mathrm{d}i_{gd}}{\mathrm{d}t} - w_{gr} L_g i_{gq} + e_{gd}\,; \tag{14}$$

$$U_{gq} = -R_g i_{gq} - \frac{L_g \mathrm{d}i_{gq}}{\mathrm{d}t} - w_{gr} L_g i_{gd}\,, \tag{15}$$

where R_g is the resistance and L_g is the inductance of the filter, with the latter positioned between the converter and the grid; u_{gd}, u_{gq} are the inverter voltage components, while w_{gr} stands for the electrical angular velocity of the grid.

FLC design. The FLC code comprises 3 sections: pre-processing, the fuzzy and interface rule engine, and post-processing. In the pre-processing phase, the fuzzy control (FC) input variables are the rate error (e) and the change in error (Δe). The gain factors for input scale and error scale are denoted as Ge and $G\Delta e$, respectively. The final phase of the FLC system involves post-processing, where the output signal ΔI is scaled by the factors d$u(t)$

$$e(t) = S^*(t) - S(t)\,; \tag{16}$$

$$\Delta e(t) = \frac{e(t) - e(t-1)}{t_{samp}}\,; \tag{17}$$

$$I^* = I^*(t-1) + \mathrm{d}u(t)\,, \tag{18}$$

with Mamdani's method, the input fuzzy variables are converted into suitable linguistic values, then treated in the region of the fuzzy set that includes the membership function (MF) where a suitable fuzzy output is obtained using fuzzy rules, and then the fuzzy output is transformed into a crisp value in the defuzzification using the method of centroid, also known as the method of center of gravity given by:

$$\Delta U = \sum_{i=1}^{n} c_i + u_i \Big/ \sum_{i=1}^{n} u_i\,, \tag{19}$$

where c_i is the discrete element within an output fuzzy set; u_i is its membership function; n is the total number of fuzzy rules. Upon converting the inputs into linguistic variables, the FLC facilitates a controlled adjustment in the voltage reference, aiming to achieve maximum power, relying on the rules outlined in Table 1.

Table 1

Set of fuzzy rules

dU		ΔE				
		NB	NS	Z	PS	PB
E	NB	NB	NB	NS	NS	Z
	NS	NB	NS	NS	Z	PS
	Z	NS	NS	Z	PS	PS
	PS	NS	Z	PS	PS	PB
	PB	Z	PS	PS	PB	PB

Figure 4 represents the input and output variables' MFs encompass triangular and trapezoidal shapes denoted as Negative Big (*NB*), Negative Small (*NS*), Zero (*Z*), Positive Small (*PS*) and Positive Big (*PB*).

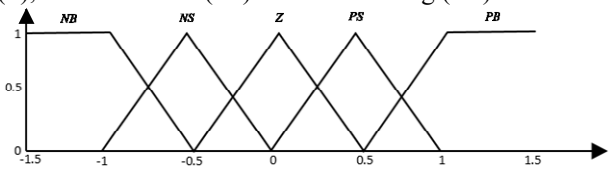

Fig. 4. MFs of e, Δe and Δu

The proposed ST-FLC. Figure 5 shows the overall structure of ST-FLC. The proposed ST-FLC uses a straightforward algorithm that reduces the system complexity and computational burden. The MFs for the 2 normalized inputs (e and Δe) and the output (Δu) of the controller were given on the normalized common area [–1.5, 1.5]. The following are the relationships between the scaling factors (G_e, $G_{\Delta e}$ and G_u) and the ST-FLC input and output variables:

$$e = G_e \times e\,; \tag{20}$$

$$\Delta e = G_{\Delta e} \times \Delta e\,; \tag{21}$$

$$\Delta u = (\beta \times G_u) \times \Delta u\,, \tag{22}$$

where:

$$\beta = K_1\left(\frac{1}{m} + |\Delta e|\right). \tag{23}$$

The variable β is formulated based on the system's expert understanding, following this principle. If the system approaches its desired operating point rapidly (small Δe), the output action (Δu) should be heightened (decreasing G_u) to prevent significant overshoot or undershoot. Conversely, if the system deviates swiftly from the target operating point (large Δe), the output action (Δu) must be increased (augmenting G_u) to restrict these deviations and expedite the system's return to its target operating point. Therefore, β is expressed using this design by adding (Δe) to the fraction ($1/m$) to prevent a lower gain multiplication (G_u) when (Δe) is exceedingly small. A lower gain multiplication could lead to oscillations and non-steady state behavior during steady-state operation. The value of m is set to be equal to the number of fuzzy uniform input partitions (e and Δe) (MF number). The value of K_1 is selected to allow the variation of β, set to 4 during the tuning process. The other fuzzy settings remain unchanged, adhering to the standard fixed parameter FLC.

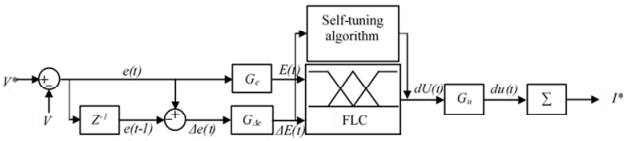

Fig. 5. ST-FLC structure

The proposed MPPT algorithm. Figure 6 represents the proposed MPPT algorithm for WT which based on ST-FLC.

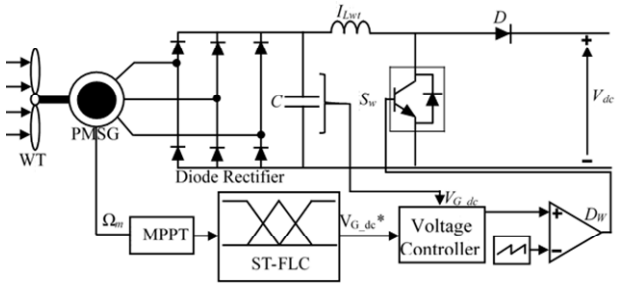

Fig. 6. ST-FLC MPPT of WT control

The MPPT algorithm proposed for solar system is based on ST-FLC is shown in Fig. 7.

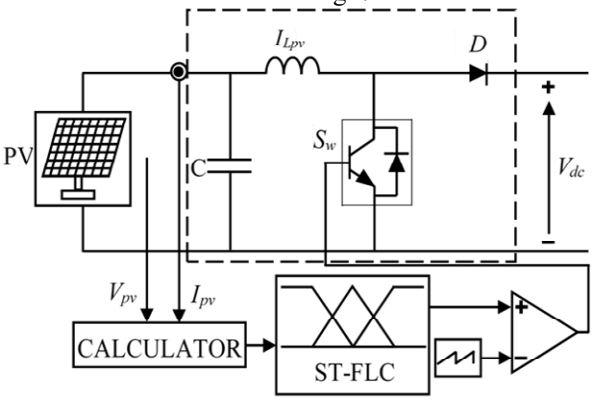

Fig. 7. ST-FLC MPPT of PV control

It relies on the Mamdani input controller. As per the MPPT algorithm, the recommended approach utilizes the error E as input and modifies the output through a distinctive ST algorithm. By taking $E = (D_P/D_V)$ for each step and considering the sign of D_P and D_V, and modify the output, which is the duty cycle dD.

$$if\ E < 0 \text{ then } D = D + \Delta D\ ; \tag{24}$$

$$if\ E > 0 \text{ then } D = D - \Delta D\ ; \tag{25}$$

$$if\ E = 0 \text{ then } D = D\ , \tag{26}$$

where the integrator with forward Euler method (the standard method) to obtain the duty cycle (D); where the gain value k and the sample time T of the integrator were respectively set to 1 and 0.01:

$$D(k) = D(k-1) + kT\mathrm{d}D(k-1)\ . \tag{27}$$

Power control with FC. The hybrid system control strategy must satisfy load demand under various weather conditions and control energy flow while keeping the different energy sources operating efficiently. Figure 8 shows the global system configuration. The FLC inputs are respectively solar irradiation G, wind velocity V_w, battery state of charge (SOC) and load demand. The outputs are switches corresponding to the selected source according to the proposed strategy, which will be explained in power control with FC section.

The scheme parameters are next. **PV generator**: rated power P_{wt} = 2,7 kW. **WT generator**: power rating P_{pv} = 6 kW; power rating of the turbine P_{tur} = 8,5 kW; radius of the turbine R_{tur} = 3.24 m. **Battery bank**: rated voltage V_{bat} = 200 V; capacity C = 100 A·h. **DC bus**: V_{dc} = 630 V. **Load**: minimum power P_l = 1 kW; maximum power P_{lM} = 8 kW. **Grid**: effective voltage value V_g = 220 V; maximum voltage value V_{gM} = 381 V.

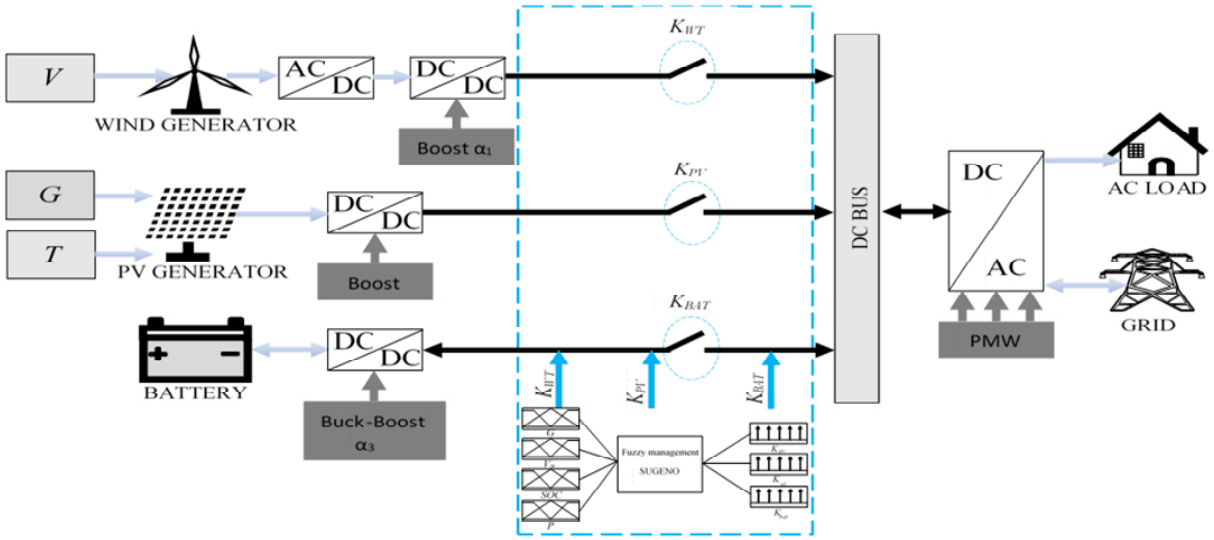

Fig. 8. Power control with FC general structure

The proposed strategy uses the energy produced by PV, WT and battery to satisfy the demands of the load. The FLC principle is to generate 3 signals of control K_{pv}, K_{wt} and K_{bat} from 3 inputs: G, V_w and SOC. K_{pv}, K_{wt} and K_{bat} are the switches that control the PV system, WT and battery, respectively. Table 2 presents the rule table for the fuzzy controller, where the inputs are fuzzy sets representing SOC, V_w and G. The output indicates the states of the 3 switches K_{pv}, K_{wt} and K_{bat}.

Table 2

Interval of fuzzy controller inputs

	Low	Medium	High
SOC, %	0–20	20–95	95–100
V_w, m/s	0–2	2–9	9–12
G, W/m^2	0–200	200–600	600–1000

Depending on the (ON/OFF) states of the K_{pv}, K_{wt} and K_{bat} switches, with the power supplied to the load expressed as:

$$P_{load} + P_{lost} + P_{bat} = P_{wt}K_{wt} + P_{pv}K_{pv}, \qquad (28)$$

where P_{wt}, P_{pv} are the power generated by the WT and the PV system; P_{bat} is the battery power; P_{load} is the power consumed by the load; P_{lost} is the power lost in the system; $P_{bat} > 0$ – when the batteries are charged; $P_{bat} < 0$ – when the batteries are discharged.

To guarantee the effective operation of the system under all conditions, we developed a range of scenarios based on system inputs (V_w, G and SOC) while considering the load. The resulting set is displayed below.

Mode 1 (M1). WT and PV power supply the load, the total energy is enough to power the load and the excess used to charge the batteries. The battery is charging.

Mode 2 (M2). WT and PV energy insufficient to supply the load, in this case, power is supplied by the battery to satisfy the demand. The battery is discharging.

Mode 3 (M3). PV power is the only source, sufficient to satisfy the load and the excess used to charge the batteries, this mode occurs during a sunny day (summer). The battery is charging.

Mode 4 (M4). PV source is insufficient to supply the load. Power is supplied by the battery to satisfy the load demand, the battery is discharging.

Mode 5 (M5). WT energy is the only source, sufficient to satisfy the load and the excess used to charge the batteries, which is the situation on a winter day with no solar radiation or at night with a good wind velocity. The battery is charging.

Mode 6 (M6). WT power source is insufficient to supply the load. Power is supplied by the battery to satisfy the load. The battery is discharging.

Mode 7 (M7). Only the battery powered the load. The battery is discharging.

Mode 8 (M8). No source available and the battery is empty, so the grid therefore supplied the power needed to satisfy the load demand.

Figure 9 shows the flowchart governing the energy control system utilizing the fuzzy system. This fuzzy system processes the inputs shown in Table 2, along with the total energy sum represented in (28). The control system evaluates 4 inputs to determine which mode, as previously described, should be implemented.

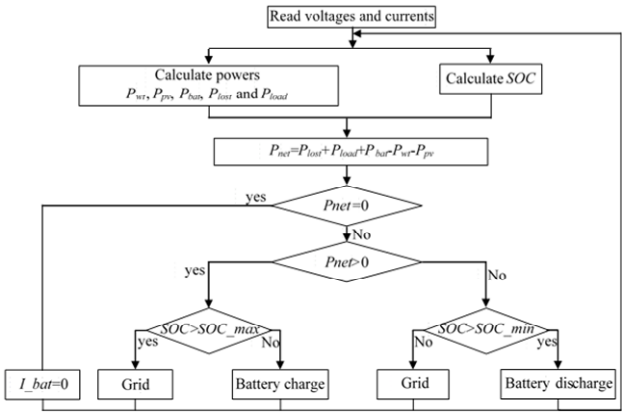

Fig. 9. Flowchart of the power control algorithm

Results simulation analysis. The simulation, conducted in MATLAB/Simulink, assesses the energetic efficiency and feasibility of the proposed strategy across various potential climatic conditions, as depicted in Fig. 8. The selected profiles include wind velocity (Fig. 10) and solar irradiance (Fig. 11).

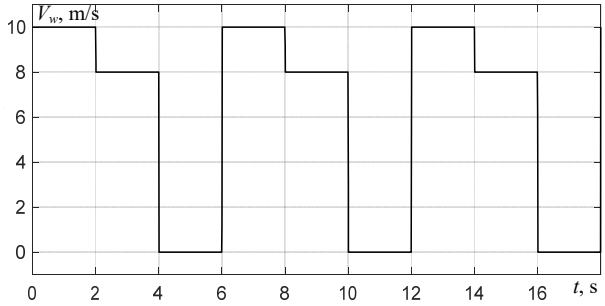

Fig. 10. Profile of the wind velocity

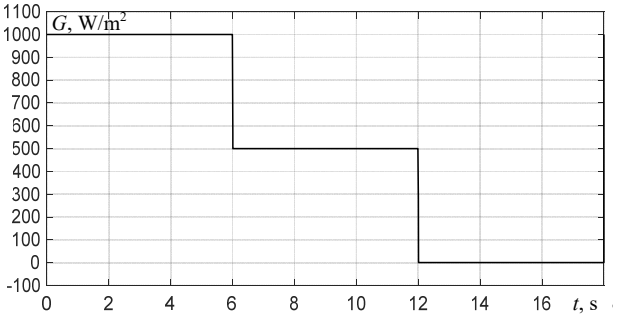

Fig. 11. Profile of the solar irradiation

The speed control response of the ST-FLC exhibits superior tracking characteristics compared to other controllers. In time-critical situations where the speed supervision controller operates, the permanent magnet synchronous generator demonstrates very short speed response times, no overshoot, and no steady-state error (Fig. 12).

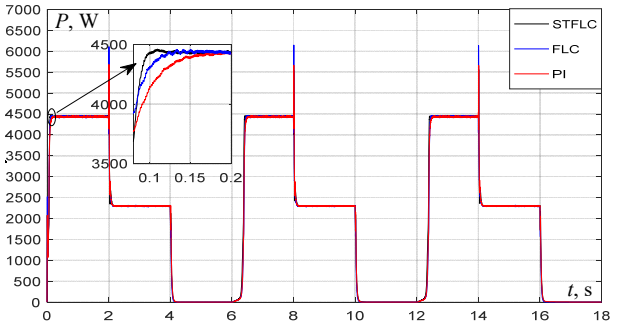

Fig. 12. Output power of the WT

Table 3 presents a comparison among 3 controllers. It's evident that the ST-FLC controller exhibits a shorter response time and reduced overshoot when compared to the other controllers. Additionally, the ST-FLC demonstrates smaller rise time and settling time in comparison to the other 2 controllers.

Table 3

MPPT WT performance metrics for PI, FLC and ST-FLC

Operation	Measure	PI	FLC	ST-FLC
MPPT WT	Setting time, s	0.193	0.124	0.104
	Rise time, s	0.123	0.102	0.077
	Overshoot, %	0.909	0.405	0.315

The ST-FLC has better tracking characteristics than other power control modules, the PV response time is very short compared to other controllers (Fig. 13).

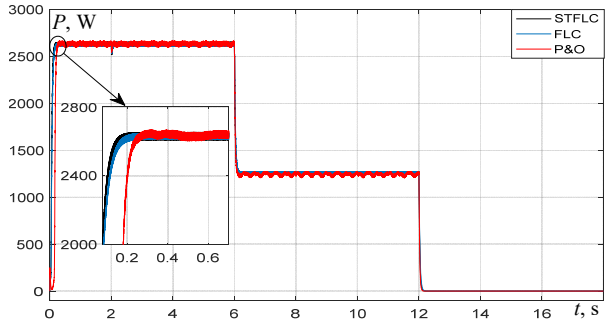

Fig. 13. Output power of the PV

Table 4 displays the outcomes of comparing the three controllers. The ST-FLC controller showcases shorter rise time and settling time. Moreover, both the ST-FLC and FLC controllers exhibit lesser overshoot when compared to the P&O controller.

Table 4

MPPT PV performance metrics for P&O, FLC and ST-FLC

Operation	Measure	P&O	FLC	ST-FLC
MPPT PV	Setting time, s	0.273	0.221	0.177
	Rise time, s	0.204	0.115	0.105
	Overshoot, %	0.506	0.189	0.189

A more detailed analysis of the steady-state power was carried out. A fast Fourier transform analysis has been used to calculate the Total Harmonic Distortion (THD) produced by the power. 20 cycles of the power were selected, starting at 0.2 s, the frequency fundamental and limited 50 Hz and 1000 Hz respectively to obtain a clear view of the THD spectrum. Tables 5, 6 show the power and THD spectrum for the 3 controllers.

Table 5

Phase a power THD of WT comparison

Controller	P, W	THD, %
PI	4395	3.94
FLC	4417	3.26
ST-FLC	4425	2.29

Table 6

Phase a power THD of PV comparison

Controller	P, W	THD, %
P&O	2559	7.21
FLC	2582	6.21
ST-FLC	2591	5.46

The performance evaluation of the proposed strategy, encompassing control and optimization, utilized the selected profiles: wind velocity (Fig. 10), solar irradiance (Fig. 11), and load power (Fig. 14). Figures 15, 16 depict the voltage shape and SOC, respectively, showcasing fluctuations of increase and decrease. When the load power surpasses the power supplied by sources (PV, WT), both the voltage and battery SOC decrease (indicating battery discharge). Conversely, they increase when the load power is lower, allowing the sources to charge the battery. Figure 17 shows the maintenance of V_{dc} at the reference value. Moreover, the powers generated by PV, WT, and batteries are presented in Fig 18. The obtained results affirm the effectiveness of the proposed FLC-based strategy, clearly demonstrating the successful achievement of its objectives.

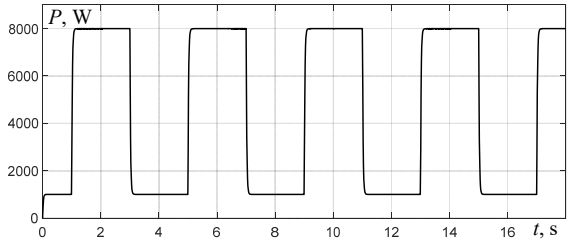

Fig. 14. Profile of the load power

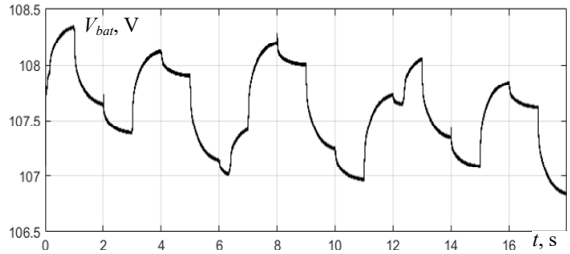

Fig. 15. Voltage of the battery

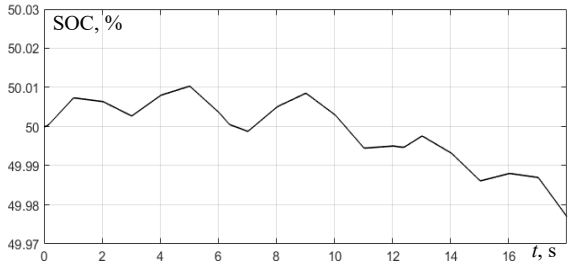

Fig. 16. The battery SOC

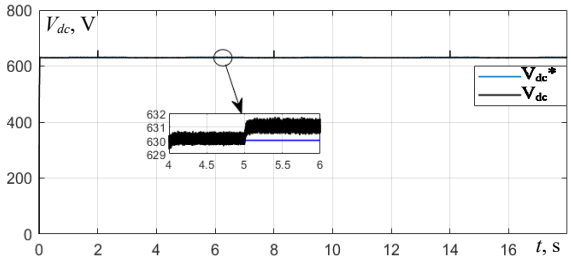

Fig. 17. Voltage V_{dc}

Conclusions.

1. This study explores the modelling, optimization, and control of a grid-connected HRES comprising two renewable sources (PV and WT) along with a storage system. The research conducts a comprehensive evaluation, highlighting a comparison between conventional and fuzzy-based approaches in controlling the MPPT. The FLC demonstrates notably enhanced performance compared to conventional methods, particularly beneficial when the model lacks clear definition, leveraging human experiential knowledge. The primary objective of this investigation revolves around assessing two advanced MPPT control strategies for WTs and PV systems: FLC, which utilizes error and its change to adjust control through fixed gain scaling factors, and ST-FLC, where the output gain dynamically adapts according to the prevailing system conditions.

2. The simulation outcomes demonstrate the superior performance of FLC over a conventional controller in terms of response speed and its capability to effectively track the maximum WT power. The ST-FLC strategy, employing a straightforward block design, exhibits robust performance and showcases commendable results compared to other utilized approaches.

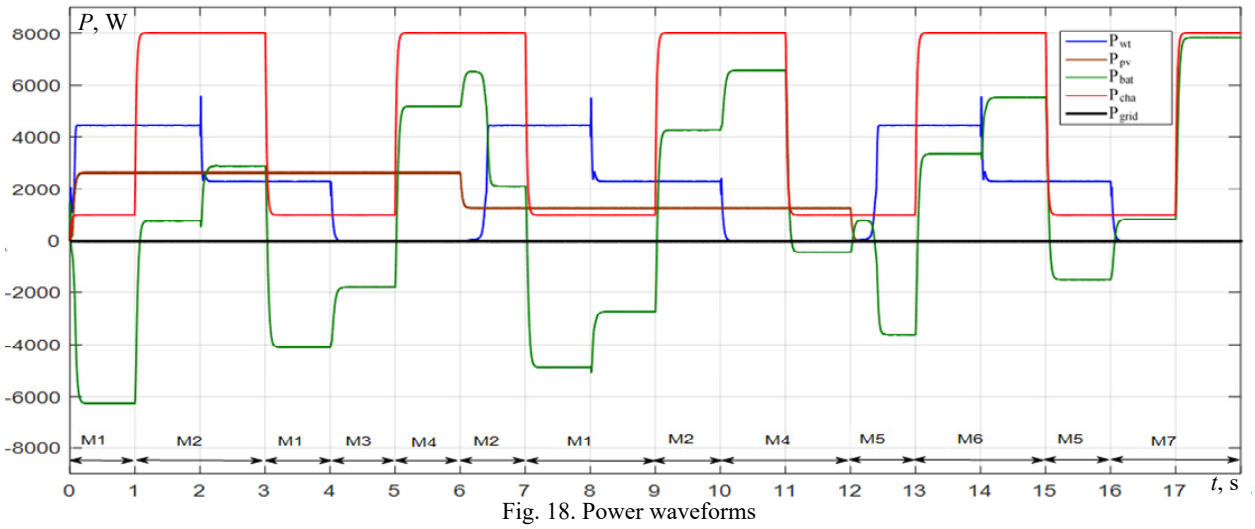

Fig. 18. Power waveforms

3. The introduced intelligent control strategy allows for diverse operating modes tailored to varying weather conditions, enabling seamless and rapid power supply from each source while considering the battery bank's state of charge. FLC serves a pivotal role in providing optimization and control within this framework.

4. These simulation findings unequivocally affirm the effectiveness and practicality of the proposed control strategy. The primary objectives, including substantial power gains, reduced battery load, and intelligent control, are successfully attained.

Conflict of interest. The authors declare that they have no conflicts of interest.

REFERENCES

1. *Renewables 2024. Global Status Report. Global Overview 2024*. Available at: https://www.ren21.net/gsr2024_GO_report (Accessed: 02 July 2024).

2. Muthukaruppasamy S., Dharmaprakash R., Sendilkumar S., Parimalasundar E. Enhancing off-grid wind energy systems with controlled inverter integration for improved power quality. *Electrical Engineering & Electromechanics*, 2024, no. 5, pp. 41-47. doi: https://doi.org/10.20998/2074-272X.2024.5.06.

3. Shivam K., Tzou J.-C., Wu S.-C. A multi-objective predictive energy management strategy for residential grid-connected PV-battery hybrid systems based on machine learning technique. *Energy Conversion and Management*, 2021, vol. 237, art. no. 114103. doi: https://doi.org/10.1016/j.enconman.2021.114103.

4. Lamzouri F.E.Z., Boufounas E.-M., Amrani A.El. Efficient energy management and robust power control of a stand-alone wind-photovoltaic hybrid system with battery storage. *Journal of Energy Storage*, 2021, vol. 42, art. no. 103044. doi: https://doi.org/10.1016/j.est.2021.103044.

5. Benlahbib B., Bouarroudj N., Mekhilef S., Abdeldjalil D., Abdelkrim T., Bouchafaa F., Lakhdari A. Experimental investigation of power management and control of a PV/wind/fuel cell/battery hybrid energy system microgrid. *International Journal of Hydrogen Energy*, 2020, vol. 45, no. 53, pp. 29110-29122. doi: https://doi.org/10.1016/j.ijhydene.2020.07.251.

6. Laxman B., Annamraju A., Srikanth N.V. A grey wolf optimized fuzzy logic based MPPT for shaded solar photovoltaic systems in microgrids. *International Journal of Hydrogen Energy*, 2021, vol. 46, no. 18, pp. 10653-10665. doi: https://doi.org/10.1016/j.ijhydene.2020.12.158.

7. Suresh G., Prasad D., Gopila M. An efficient approach based power flow management in smart grid system with hybrid renewable energy sources. *Renewable Energy Focus*, 2021, vol. 39, pp. 110-122. doi: https://doi.org/10.1016/j.ref.2021.07.009.

8. Bounechba H., Boussaid A., Bouzid A. Experimental validation of fuzzy logic controller based on voltage perturbation algorithm in battery storage photovoltaic system. *Electrical Engineering & Electromechanics*, 2024, no. 5, pp. 20-27. doi: https://doi.org/10.20998/2074-272X.2024.5.03.

9. Zerzouri N., Ben Si Ali N., Benalia N. A maximum power point tracking of a photovoltaic system connected to a three-phase grid using a variable step size perturb and observe algorithm. *Electrical Engineering & Electromechanics*, 2023, no. 5, pp. 37-46. doi: https://doi.org/10.20998/2074-272X.2023.5.06.

10. Jately V., Azzopardi B., Joshi J., Venkateswaran V.B., Sharma A., Arora S. Experimental Analysis of hill-climbing MPPT algorithms under low irradiance levels. *Renewable and Sustainable Energy Reviews*, 2021, vol. 150, art. no. 111467. doi: https://doi.org/10.1016/j.rser.2021.111467.

11. Louarem S., Kebbab F.Z., Salhi H., Nouri H. A comparative study of maximum power point tracking techniques for a photovoltaic grid-connected system. *Electrical Engineering & Electromechanics*, 2022, no. 4, pp. 27-33. doi: https://doi.org/10.20998/2074-272X.2022.4.04.

12. Kaddache M., Drid S., Khemis A., Rahem D., Chrifi-Alaoui L. Maximum power point tracking improvement using type-2 fuzzy controller for wind system based on the double fed induction generator. *Electrical Engineering & Electromechanics*, 2024, no. 2, pp. 61-66. doi: https://doi.org/10.20998/2074-272X.2024.2.09.

13. Mahgoun M.S., Badoud A.E. New design and comparative study via two techniques for wind energy conversion system. *Electrical Engineering & Electromechanics*, 2021, no. 3, pp. 18-24. doi: https://doi.org/10.20998/2074-272X.2021.3.03.

14. Farah N., Talib M.H.N., Mohd Shah N.S., Abdullah Q., Ibrahim Z., Lazi J.B.M., Jidin A. A Novel Self-Tuning Fuzzy Logic Controller Based Induction Motor Drive System: An Experimental Approach. *IEEE Access*, 2019, no. 7, pp. 68172-68184. doi: https://doi.org/10.1109/ACCESS.2019.2916087.

15. Marugán A.P., Márquez F.P.G., Perez J.M.P., Ruiz-Hernández D. A survey of artificial neural network in wind energy systems. *Applied Energy*, 2018, vol. 228, pp. 1822-1836. doi: https://doi.org/10.1016/j.apenergy.2018.07.084.

16. Mansouri M., Bey M., Hassaine S., Larbi M., Allaoui T., Denai M. Genetic algorithm optimized robust nonlinear observer for a wind turbine system based on permanent magnet synchronous generator. *ISA Transactions*, 2022, vol. 129, pp. 230-242. doi: https://doi.org/10.1016/j.isatra.2022.02.004.

17. Guentri H., Allaoui T., Mekki M., Denai M. Power management and control of a photovoltaic system with hybrid

battery-supercapacitor energy storage based on heuristics methods. *Journal of Energy Storage*, 2021, vol. 39, art. no. 102578. doi: https://doi.org/10.1016/j.est.2021.102578.

18. Sabhi K., Talea M., Bahri H., Dani S. Integrating dual active bridge DC-DC converters: a novel energy management approach for hybrid renewable energy systems. *Electrical Engineering & Electromechanics*, 2025, no. 2, pp. 39-47. doi: https://doi.org/10.20998/2074-272X.2025.2.06.

19. Ayat Y., Badoud A.E., Mekhilef S., Gassab S. Energy management based on a fuzzy controller of a photovoltaic/fuel cell/Li-ion battery/supercapacitor for unpredictable, fluctuating, high-dynamic three-phase AC load. *Electrical Engineering & Electromechanics*, 2023, no. 3, pp. 66-75. doi: https://doi.org/10.20998/2074-272X.2023.3.10.

20. Sharma R.K., Mudaliyar S., Mishra S. A DC Droop-Based Optimal Dispatch Control and Power Management of Hybrid Photovoltaic-Battery and Diesel Generator Standalone AC/DC System. *IEEE Systems Journal*, 2021, vol. 15, no. 2, pp. 3012-3023. doi: https://doi.org/10.1109/JSYST.2020.3032887.

21. Kamel A.A., Rezk H., Abdelkareem M.A. Enhancing the operation of fuel cell-photovoltaic-battery-supercapacitor renewable system through a hybrid energy management strategy. *International Journal of Hydrogen Energy*, 2021, vol. 46, no. 8, pp. 6061-6075. doi: https://doi.org/10.1016/j.ijhydene.2020.06.052.

22. Ali Moussa M., Derrouazin A., Latroch M., Aillerie M. A hybrid renewable energy production system using a smart controller based on fuzzy logic. *Electrical Engineering & Electromechanics*, 2022, no. 3, pp. 46-50. doi: https://doi.org/10.20998/2074-272X.2022.3.07.

23. Toghani Holari Y., Taher S.A., Mehrasa M. Power management using robust control strategy in hybrid microgrid for both grid-connected and islanding modes. *Journal of Energy Storage*, 2021, vol. 39, art. no. 102600. doi: https://doi.org/10.1016/j.est.2021.102600.

24. Charrouf O., Betka A., Abdeddaim S., Ghamri A. Artificial Neural Network power manager for hybrid PV-wind desalination system. *Mathematics and Computers in Simulation*, 2020, vol. 167, pp. 443-460. doi: https://doi.org/10.1016/j.matcom.2019.09.005.

25. Taghdisi M., Balochian S. Maximum Power Point Tracking of Variable-Speed Wind Turbines Using Self-Tuning Fuzzy PID. *Technology and Economics of Smart Grids and Sustainable Energy*, 2020, vol. 5, no. 1, art. no. 13. doi: https://doi.org/10.1007/s40866-020-00087-3.

26. Roumila Z., Rekioua D., Rekioua T. Energy management based fuzzy logic controller of hybrid system wind/photovoltaic/diesel with storage battery. *International Journal of Hydrogen Energy*, 2017, vol. 42, no. 30, pp. 19525-19535. doi: https://doi.org/10.1016/j.ijhydene.2017.06.006.

27. Singh P., Lather J.S. Power management and control of a grid-independent DC microgrid with hybrid energy storage system. *Sustainable Energy Technologies and Assessments*, 2021, vol. 43, art. no. 100924. doi: https://doi.org/10.1016/j.seta.2020.100924.

Received 10.11.2024
Accepted 08.01.2025
Published 02.05.2025

H. Chaib[1]*, PhD Student,*
S. Hassaine[1]*, PhD, Professor,*
Y. Mihoub[1]*, PhD, Associate Professor,*
S. Moreau[2]*, PhD, Associate Professor,*
[1] Laboratory of Energy Engineering and Computer Engineering, University of Tiaret, Algeria,
e-mail: housseyn.chaib@univ-tiaret.dz (Corresponding Author); said.hassaine@univ-tiaret.dz; youcef.mihoub@univ-tiaret.dz
[2] Laboratory of Informatics and Automatic Systems (LIAS), Poitiers University, France,
e-mail: sandrine.moreau@univ-poitiers.fr

How to cite this article:
Chaib H., Hassaine S., Mihoub Y., Moreau S. Intelligent power control strategy based on self-tuning fuzzy MPPT for grid-connected hybrid system. *Electrical Engineering & Electromechanics*, 2025, no. 3, pp. 23-30. doi: https://doi.org/10.20998/2074-272X.2025.3.04

UDC 621.3 https://doi.org/10.20998/2074-272X.2025.3.05

L. Djafer, R. Taleb, F. Mehedi, A. Aissa Bokhtache, T. Bessaad, F. Chabni, H. Saidi

Electric drive vehicle based on sliding mode control technique using a 21-level asymmetrical inverter under different operating conditions

Introduction. *Electric vehicles (EVs) have drawn increased attention as a possible remedy for the energy crisis and environmental issues. These days, EVs can be propelled by an extensive range of power electronics to produce the energy required for the motor and operate efficiently at high voltage levels. Multilevel inverters (MLIs) were designed to address the challenges and limitations of traditional converters .**The novelty** of the research that is being presented a 21-asymmetric MLI with reduced switching using pulse width modulation technique for powering electric propulsion system of EVs, with the proposed topology delivering notable enhancements in both performance and cost-efficiency compared to conventional asymmetric designs. **Purpose.** Improving EV performance by utilizing sliding mode control (SMC) technique for controlling a permanent magnet synchronous motor (PMSM) powered by a 21-level reduced switching inverter topology. **Methods.** This study focuses on assessing the feasibility of a 21-asymmetric MLI with reduced switching. This inverter utilize different input voltage levels for various components and modules, enabling the combination and subtraction of these voltages to create multiple voltage levels for use in the traction system of electric vehicles, designed to power a PMSM. The motor's operation is controlled using SMC technique with three distinct surfaces, with consideration for the vehicle's dynamic behavior. **Results.** Proved that, using a 21-asymmetric MLI to optimize the quality of the output voltage for improving the performance of the EV. The proposed topology offers a cost-effective and simple system that is easy to maintain. **Practical value.** To assess the effectiveness and resilience of the suggested control system, we conducted simulations using MATLAB/Simulink. Notably, the target speed adheres to the urban driving schedule in Europe, specifically the ECE-15 cycle.* References 21, tables 2, figures 10.

Key words: **asymmetric multilevel inverter, electric vehicle, permanent magnet synchronous motor, sliding mode control.**

Вступ. *Електромобілі (EVs) привернули підвищену увагу як можливий засіб від енергетичної кризи та екологічних проблем. У наші дні EVs можуть рухатися широким спектром силової електроніки для вироблення енергії, необхідної для двигуна, і працювати ефективно при високих рівнях напруги. Багаторівневі інвертори (MLI) були розроблені для вирішення проблем та обмежень традиційних перетворювачів.* ***Новизна*** *дослідження, яке представлено, 21-асиметричний MLI зі зменшеним перемиканням, що використовує метод широтно-імпульсної модуляції для живлення електричної рухової системи EVs, з запропонованою топологією, що забезпечує помітне покращення як продуктивності, так і економічної ефективності порівняно з традиційними асиметричними конструкціями.* ***Мета***. *Поліпшення продуктивності EVs за рахунок використання методу керування ковзним режимом (SMC) для керування синхронним двигуном з постійними магнітами (PMSM), що працює від топології 21-рівневого інвертора зі зменшеним перемиканням.* ***Методи***. *Це дослідження зосереджено на оцінці здійсненності 21-асиметричного MLI зі зменшеним перемиканням. Цей інвертор використовує різні рівні вхідної напруги для різних компонентів та модулів, що дозволяє комбінувати та віднімати цю напругу для створення кількох рівнів напруги для використання в тяговій системі електромобілів, призначеної для живлення PMSM. Робота двигуна контролюється за допомогою техніки SMC із трьома різними поверхнями з урахуванням динамічної поведінки автомобіля.* ***Результати***. *Доведено, що використання 21-асиметричного MLI для оптимізації якості вихідної напруги покращує продуктивність EV. Запропонована топологія пропонує економічну та просту систему, яку легко обслуговувати.* ***Практична цінність***. *Для оцінки ефективності та стійкості запропонованої системи управління ми здійснили моделювання з використанням MATLAB/Simulink. Зокрема цільова швидкість відповідає міському графіку водіння в Європі, зокрема циклу ECE-15.* Бібл. 21, табл. 2, рис. 10.

Ключові слова: **асиметричний багаторівневий інвертор, електромобіль, синхронний двигун з постійними магнітами, керування ковзним режимом.**

Introduction. The growing challenge of global warming and air emissions from transportation in urban areas has led to the development of various alternative mobility solutions, such as electric vehicles (EV), car sharing, and e-bikes [1]. EV presents multiple benefits: electric energy is more affordable and environmentally friendly compared to oil, electric motors are more efficient than internal combustion engines, EV operate more quietly, and they can be charged at home [2]. Consequently, this remains essential for the research community to prioritize clean, renewable, and environmentally friendly energy sources and to encourage policy and economic leaders to take decisive action to tackle this issue and facilitate the shift to renewable energy. In this situation, the growing presence of EV in a fiercely competitive market drives car manufacturers to create more fuel-efficient automobiles at lower expenses. Key performance criteria for EV encompass reliability, resilience, energy control, battery charging rate, and especially the electric drive system [3].

The fuel cell serves as the primary source of energy in the EV power supply, nevertheless, in low-load situations, the fuel cell may prove inadequate, making it necessary to use a battery as a backup source to prevent a limited range of driving distance and extend the lifespan of the fuel cell [4]. Consequently, energy management is optimized to enable energy distribution among the propulsion system components, along with the appropriate selection of the motor.

A permanent magnet synchronous motor (PMSM) is widely used in EV energy propulsion systems because of its numerous advantages, such as its efficient compact structure, high air-gap flux density, high energy density, favorable torque-to-inertia ratio, and excellent performance effectiveness [5]. PMSM necessitates an effective management strategy, meaning it demands a rapid and precise response, swift recovery from disturbances, and robustness against variations in parameters. As a result, numerous contemporary control techniques, including sliding mode control (SMC), have been advocated to enhance the performance of the PMSM [6].

SMC technique is a popular technique because it effectively rejects internal parameter changes and outside disruptions. SMC has discovered vast application in

electrical power systems and electrical devices for machines [7, 8]. As a result, it has been effectively utilized for controlling the position and speed of PMSMs.

EV typically utilizes large electric motors that necessitate a significant quantity of batteries and sophisticated electronic power converters to supply the necessary high-level electrical power they require. The structure of multilevel inverters (MLIs) enables the synthesis of high-quality, high-voltage waveforms, making them ideal for high-power drive systems. In [9], the authors proposed the effectiveness of drive control using a MLI. The suggested method combines the use of sand cat swarm optimization and spiking neural networks. According to the findings, the suggested approach can outperform current methods based on torque ripple, energy efficiency, and speed tracking [10].

MLIs are capable of operating at both the fundamental switching frequency and a high rate of pulse-width modulation (PWM) switching [11]. It is well known that these inverters can produce low harmonic waveforms for high-voltage signals. However, adding more switching devices results in a system that becomes more complex and expensive, resulting in maintenance challenges [12]. Asymmetric MLIs are viewed as an effective solution for overcoming the limitations of traditional MLIs.

The goal of the paper is introduces a 21-asymmetric MLI with reduced switching for powering electric propulsion system of EV, with the proposed topology delivering notable enhancements in both performance and cost-efficiency compared to conventional asymmetric designs. The new aspect is that the article [13] addressed the 21-level inverter topology in an open loop and it used artificial neural networks for selective harmonic elimination PWM (SHE-ANN) modulation. This article is a continuation of the first, where we used the 21-level inverter within the electric EV's traction system (closed loop) using sinusoidal PWM (SPWM) modulation.

Subject of investigations. This paper presents a 21-hybrid asymmetric MLI reduced switching inverter within the EV's traction system for powering a PMSM with a nominal power of approximately 50 kW and a maximum torque of 255 N·m. Our traction system requires control laws that remain unaffected by disturbances, parameter changes, and nonlinearities. This study will employ a variable structure control approach, commonly referred to as SMC.

The proposed topology used to optimize the quality of the output voltage for improving the performance of the EV while minimizing the number of switching devices. It offers a cost-effective and simple system that is easy to maintain.

Electric propulsion system. Dynamics analysis. The propulsion system must produce enough traction effort at the wheel to counteract the combined forces of aerodynamic drag, rolling resistance, road inclination, and the force necessary to accelerate the vehicle. This section outlines the primary forces that enable a vehicle's operation. Figure 1 illustrates the main forces acting on the EV.

The force needed to drive the EV at the wheels is defined by the following equation [14, 15]:

$$\boldsymbol{F}_T = \boldsymbol{F}_{ro} + \boldsymbol{F}_{ad} + \boldsymbol{F}_{cr} + \boldsymbol{F}_{sf}\,, \tag{1}$$

where $\boldsymbol{F}_T$ is the traction force; $\boldsymbol{F}_{ro}$ is the force of rolling resistance; $\boldsymbol{F}_{ad}$ is the force of aerodynamic resistance; $\boldsymbol{F}_{cr}$ is the climbing resistance force; $\boldsymbol{F}_{sf}$ is the force of Stokes or viscous drag.

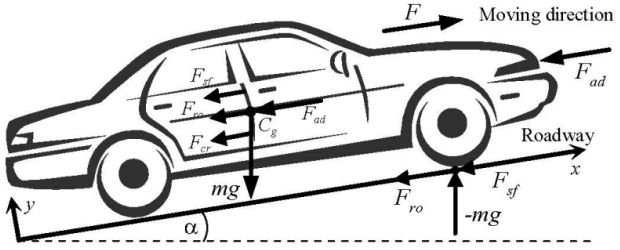

Fig. 1. Fundamental forces acting on an EV

The force of rolling resistance is:

$$\boldsymbol{F}_{ro} = C_d mg\cos\alpha\,. \tag{2}$$

The force that resists rolling $\boldsymbol{F}_{ro}$ is influenced by the vehicle's mass m acceleration due to gravity g, and the wheel's coefficient of rolling resistance C_d. In practice, with contemporary tires engineered for reduced tire resistance, a rolling resistance coefficient C_d is around 0.01 (and approximately 0.015 for conventional tires). The variation in this coefficient depends on the tire's width and the kind of road surface [16, 17].

The force of aerodynamic resistance

$$\boldsymbol{F}_{ad} = \frac{1}{2}PC_f A_f V_r^2 = \frac{1}{2}PC_f A_f \left(V + V_w\right)^2 \tag{3}$$

is proportional to the air density P, the square of the vehicle's speed $\boldsymbol{V}$, the wind speed $\boldsymbol{V}_w$, the vehicle's frontal surface area A_f, the relative speed of the vehicle V_r and its drag coefficient C_f, which varies between 0.25–0.5 depending on the shape of the vehicle body.

Climbing resistance force is:

$$\boldsymbol{F}_{cr} = \pm mg\sin\alpha\,, \tag{4}$$

where m is the vehicle mass, g is the gravitational acceleration constant; α is the grade angle.

The gravitational force acting on a vehicle driving on an inclined road depends on the road's slope. As shown in Fig. 1, this exerted force is positive while the automobile is climbing and negative while descending.

The force of Stokes or viscous drag is:

$$\boldsymbol{F}_{sf} = K_a V_r\,, \tag{5}$$

where K_a is the Stokes coefficient.

In [18] authors occasionally use the EV's acceleration force $\boldsymbol{F}_a$ in place of the viscous friction force $\boldsymbol{F}_{sf}$ as:

$$\boldsymbol{F}_a = m\lambda\frac{\mathrm{d}V_r}{\mathrm{d}t} = m + \sum J\left(\frac{i^2}{r}\right)\frac{\mathrm{d}V_r}{\mathrm{d}t}, \tag{6}$$

where λ is the mass factor, which varies with the engaged gear, ranges from 1.06 to 1.34; J is the moment of inertia at the circumference of the driving wheel; i is the gearbox ratio; r is the wheel radius.

The electric motor produces the traction force required for an EV to counteract the road resistance. Thus, the motion equation is expressed as:

$$K_m m\frac{\mathrm{d}V}{\mathrm{d}t} = \boldsymbol{F}_{tr} - \boldsymbol{F}_T\,, \tag{7}$$

where $\boldsymbol{F}_{tr}$ is the traction force of tires; K_m is the rotational inertia coefficient. The net force $\boldsymbol{F}_{tr} - \boldsymbol{F}_T$ accelerates the vehicle or decelerates it if $\boldsymbol{F}_T$ exceeds $\boldsymbol{F}_{tr}$.

The work A is given by the following expression:

$$A = \sum_{j=1}^{4} F_i \mathrm{d}x\,. \tag{8}$$

When the work is differentiated with respect to time, the resulting expression for mechanical power is:

$$P_{mech} = \frac{dA}{dt} = F\frac{dx}{dt} \Leftrightarrow P_{mech} = F \cdot V \,. \quad (9)$$

Description of the system. Figure 2 presents a diagram of the components of an EV powered by a system of electric traction. The main objective of the suggested design is to achieve speed control through SMC technique. The electric propulsion system comprises a DC voltage source, a 21-level reduced switching MLI, and a induction motor with a nominal power of approximately 50 kW and a maximum torque of 255 N·m.

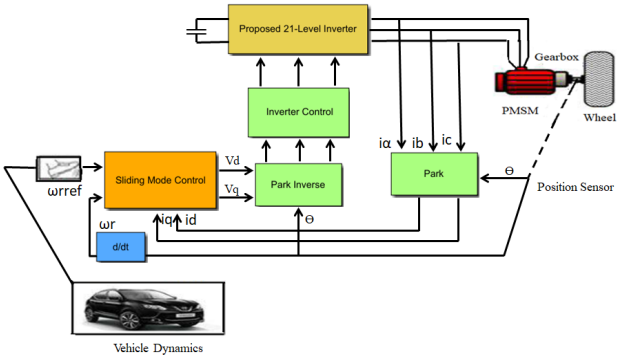

Fig. 2. The components of the traction system

The proposed 21-level inverter topology. Figure 3 shows the circuit model of the proposed 21-level inverter, designed with fewer switching devices. This inverter comprises 2 series-connected cells. The top cell consists of a basic H-bridge, constructed using switches $S_1 - S_4$, as well as 2 bidirectional switches, S_5 and S_6, along with 3-DC sources of equal voltage. The bidirectional switches S_5, S_6 manage the connection of the DC sources to produce the required staircase output voltage waveform. The lower cell contains an additional H-bridge, made up of switches $S_{p1} - S_{p4}$, which is connected to an isolated DC source [13].

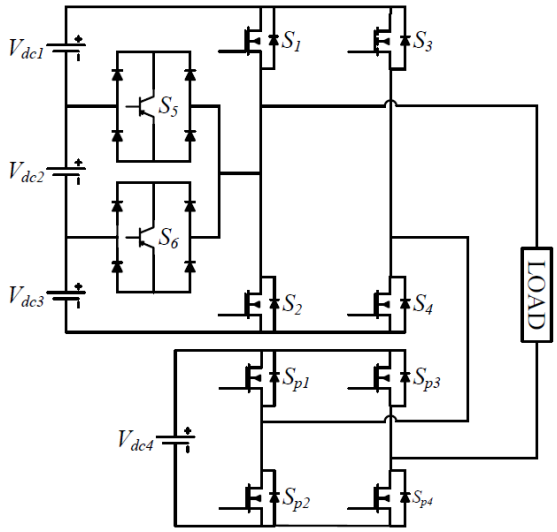

Fig. 3. The suggested 21-level inverter configuration [13]

Table 1 shows the allowed switching configurations for every possible combination. It is important to note that these combinations are only applicable under next conditions:

$$V_{dc1} = V_{dc2} = V_{dc3}\,; \quad (10)$$

$$V_{dc4} = 7 \cdot V_{dc1}\,. \quad (11)$$

Table 1

Output voltage levels (p.u.) with their respective conducting switches for the suggested 21-level inverter [13]

Voltage, p.u.	Switches in ON state	Voltage, p.u.	Switches in ON state
10	S_1, S_4, S_{p1}, S_{p4}	–10	S_3, S_2, S_{p2}, S_{p3}
9	S_4, S_5, S_{p1}, S_{p4}	–9	S_3, S_6, S_{p2}, S_{p3}
8	S_4, S_6, S_{p1}, S_{p4}	–8	S_5, S_3, S_{p2}, S_{p3}
7	S_2, S_4, S_{p1}, S_{p4}	–7	S_2, S_4, S_{p2}, S_{p3}
6	S_3, S_5, S_{p1}, S_{p4}	–6	S_6, S_4, S_{p2}, S_{p3}
5	S_3, S_6, S_{p1}, S_{p4}	–5	S_5, S_4, S_{p2}, S_{p3}
4	S_2, S_3, S_{p1}, S_{p4}	–4	S_1, S_4, S_{p2}, S_{p3}
3	S_1, S_4, S_{p2}, S_{p4}	–3	S_2, S_3, S_{p2}, S_{p4}
2	S_4, S_5, S_{p2}, S_{p4}	–2	S_3, S_6, S_{p2}, S_{p4}
1	S_4, S_6, S_{p2}, S_{p4}	–1	S_3, S_5, S_{p2}, S_{p4}
0	S_2, S_4, S_{p2}, S_{p4}	0	S_2, S_4, S_{p2}, S_{p4}

SMC strategy of the PMSM. The mathematical model of the PMSM in the stationary *d-q* coordinates system is [19, 20]:

$$\begin{cases} i_d = -\dfrac{R}{L_d} i_d + \dfrac{L_q}{L_d} p\omega_r i_q + \dfrac{1}{L_d} V_d; \\ i_q = -\dfrac{R}{L_d} i_q + \dfrac{L_d}{L_q} p\omega_r i_d - \dfrac{\varphi_f}{L_q} p\omega_r + \dfrac{1}{L_d} V_q; \\ \omega = \dfrac{3p}{2J}\left(\varphi_f i_q + \left(L_d - L_q\right) i_d i_q\right) - \dfrac{1}{J} C_r - \dfrac{f}{J}\omega_r, \end{cases} \quad (12)$$

where R is the stator resistance; L_d, L_q are the stator inductances; φ_f is the flux linkage of the permanent magnet; i_d, i_q are the stator currents; V_d, V_q are the stator voltages; ω_r is the mechanical speed; J is the inertia moment; f is the viscous friction coefficient, p is the poles pairs number; C_r is the load torque.

Our traction system requires control laws that remain unaffected by disturbances, parameter changes, and nonlinearities. This study will employ a variable structure control approach, commonly referred to as SMC.

The system represented by the state space equation given bellow is taken into consideration [21]:

$$[\dot{\boldsymbol{X}}] = \boldsymbol{A}[\boldsymbol{X}] + \boldsymbol{B}[\boldsymbol{U}], \quad (13)$$

where the state vector is represented by $[\boldsymbol{X}] \in R^n$, the control input vector by $[\boldsymbol{U}] \in R^n$, and the system parameter matrices by $[\boldsymbol{A}]$ and $[\boldsymbol{B}]$.

Selecting the quantity of switching surface $s(x)$ is the initial stage of the control design. This number typically equals the control vector's $[\boldsymbol{B}]$ dimension. To guarantee the variable x convergence to its reference x_{ref}, the authors [17] suggests the following general purpose for the switching surface:

$$S(x) = \left(\frac{d}{dt} + \lambda\right)^{n-1} e(x)\,, \quad (14)$$

where n is the relative degree; λ is the positive coefficient; and the vector of tracking errors is $e(x) = x_{ref} - x$.

The second step is to identify the control law that satisfies the requirements necessary for a sliding mode like to exist and be reachable [17]:

$$S(x) \cdot \dot{S}(x) < 0\,. \quad (15)$$

There are two parts to the control law:

$$\boldsymbol{U} = \boldsymbol{U}_{eq} + \boldsymbol{U}_n\,; \quad (16)$$

$$\boldsymbol{U_n} = K_x \text{sign}\left(S(x)\right), \quad (17)$$

where $\boldsymbol{U_n}$ is the correction factor; $\boldsymbol{U_{eq}}$ is the equivalent control vector; $\boldsymbol{U}$ is the control vector. $\boldsymbol{U_n}$ should be computed to satisfy the stability requirements for the selected control [17]; K_x is the constant.

In this study, the following sliding surfaces are selected as follows:

$$\begin{cases} S(i_d) = i_{d\,ref} - i_d; \\ S(i_q) = i_{q\,ref} - i_q; \\ S(\omega_r) = \omega_{r\,ref} - \omega_r. \end{cases} \quad (18)$$

The first order derivate of (18), gives:

$$\begin{cases} \dot{S}(i_d) = \dot{i}_{d\,ref} - \dot{i}_d; \\ \dot{S}(i_q) = \dot{i}_{q\,ref} - \dot{i}_q; \\ \dot{S}(\omega_r) = \dot{\omega}_{r\,ref} - \dot{\omega}_r. \end{cases} \quad (19)$$

The control vectors $\boldsymbol{V}_{deq}$, $\boldsymbol{V}_{qeq}$ and $\boldsymbol{i}_{deq}$ are obtained by imposing $\dot{S}(x) = 0$, consequently, the following relation provides the corresponding control components:

$$\begin{cases} \boldsymbol{V}_{deq} = L_d \dot{i}_{d\,ref} + R i_d - \omega_r L_q i_q; \\ \boldsymbol{V}_{qeq} = L_d \dot{i}_{q\,ref} + R i_q - \omega_r L_d i_d + \omega_r \varphi_f; \\ \boldsymbol{i}_{qeq} = \dfrac{J\dot{\omega}_{r\,ref} + pC_r + f\omega_r}{p((L_d - L_q) i_d + \sqrt{\dfrac{3}{2}}\varphi_f)}. \end{cases} \quad (20)$$

When substituting (17) and (20) into (16), the following control vector is applied in order to get good performances, dynamics, and commutations around the surfaces:

$$\begin{cases} \boldsymbol{V}_d = \boldsymbol{V}_{deq} + K_1 \text{sign}(S(i_d)); \\ \boldsymbol{V}_q = \boldsymbol{V}_{qeq} + K_2 \text{sign}(S(i_q)); \\ \boldsymbol{i}_q = \boldsymbol{i}_{qeq} + K_3 \text{sign}(S(\omega_r)), \end{cases} \quad (21)$$

where $K_1 - K_3$ are all positive constants.

Discussion of simulation results. Simulations were performed to characterize the vehicle traction system's behavior, using the model presented in Fig. 2. The simulations illustrate vehicle speed control with SMC technique driven by a novel 21-level inverter topology. The test cycle is the urban ECE-15 cycle (Fig. 4).

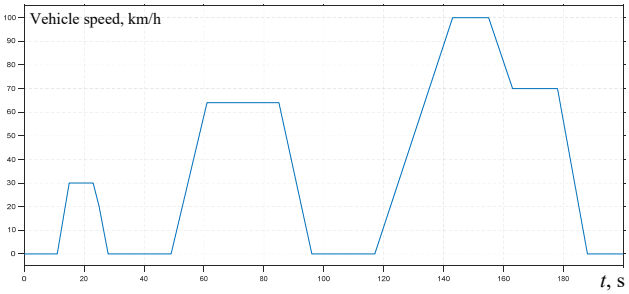

Fig. 4. European urban driving cycle ECE-15

To verify the suggested topology's effectiveness a comparative study has been done to demonstrate the merits of the proposed topology over of 2-level inverter topology. Total harmonic distortion (THD) was chosen as a quality index to evaluate the quality of the generated output voltage:

$$THD = \frac{\sqrt{\sum_{n=3}^{50} H_n^2 H_1}}{X} \cdot 100\% .$$

Figure 5,*a* shows the voltage wave forms generated by 2-level inverter topology. The spectra of the output voltage waveforms are shown in Fig. 5,*b*. THD is 73.39 %.

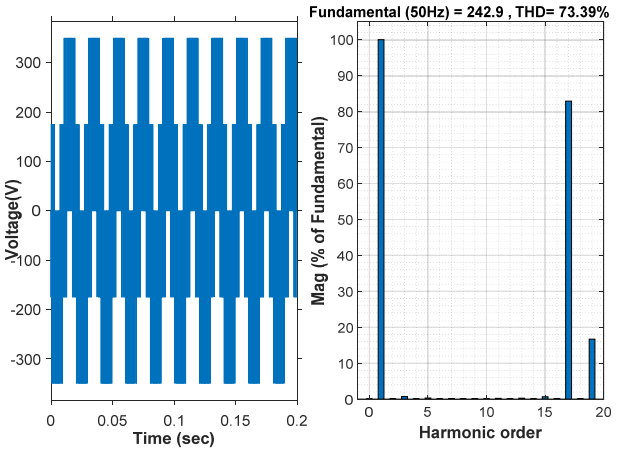

a *b*

Fig. 5. Voltage waveform produced by 2-level inverter along with its corresponding FFT analysis

Figure 6,*a* shows the voltage wave forms generated by a 21-level reduced switching inverter topology. The spectra of the output voltage waveforms are shown in Fig. 6,*b*. THD is 6.19 %.

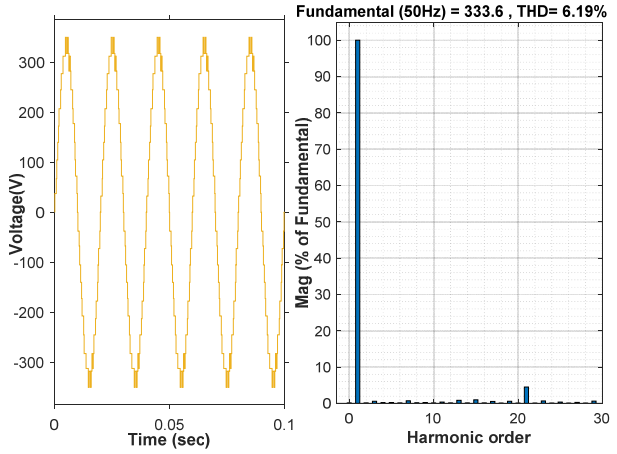

a *b*

Fig. 6. Voltage signal produced by the suggested 21-level inverter along with its corresponding FFT analysis

Reference tracking test. It is worth mentioning that the simulation was conducted using Europe's ECE-15 urban driving cycle. Within this cycle, 3 speed requests were applied in a trapezoidal form (30 rad/s, 65 rad/s, 100 rad/s). Additionally, a 10 % slope was applied between 16 and 23 s. This simulation's objective is to verify whether our method of control can be implemented in real-time and to track the behavior of the vehicle in the different modes under study.

Figures 7, 8 show the vehicle speed response in SMC technique. We observe that the rotation speed of the motor can rapidly track the reference rotation speed, a good tracking dynamics are observed. This command switches very quickly within its limits which impacts the overall command of the vehicle.

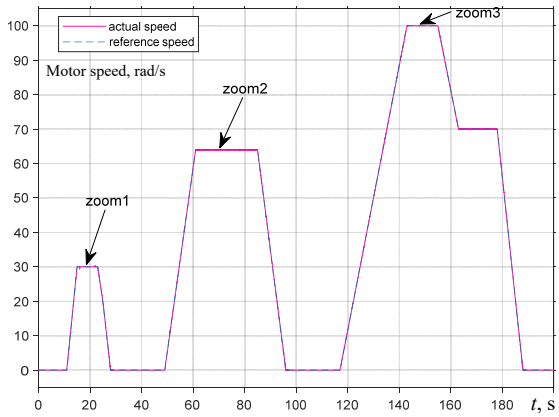

Fig. 7. The vehicle's motor rotation speed

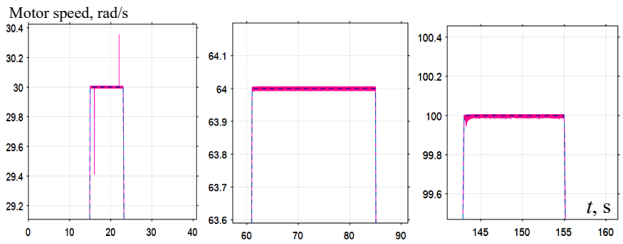

Fig. 8. Zoom of the reference and actual vehicle speed

Figure 9 shows the variation of electromagnetic torque as load torque changes. Figure 10 presents the results for the direct and quadrature currents. As outlined in the control strategy description, this method clearly maintains the direct current constant at zero, allowing only the quadrature component to respond to torque disturbances. This demonstrates the controller's excellent tracking capability ($i_{dref} = 0$). Furthermore, the i_q current and the electromagnetic torque exhibit identical profiles, confirming that decoupling has been successfully achieved.

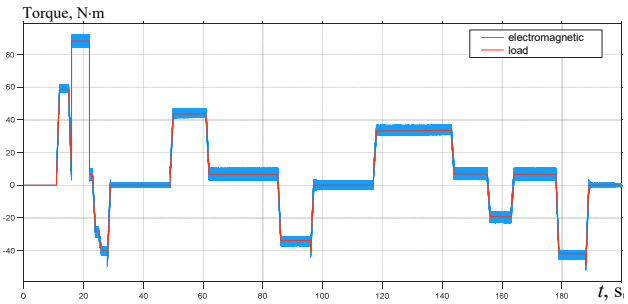

Fig. 9. Electromagnetic and load torques

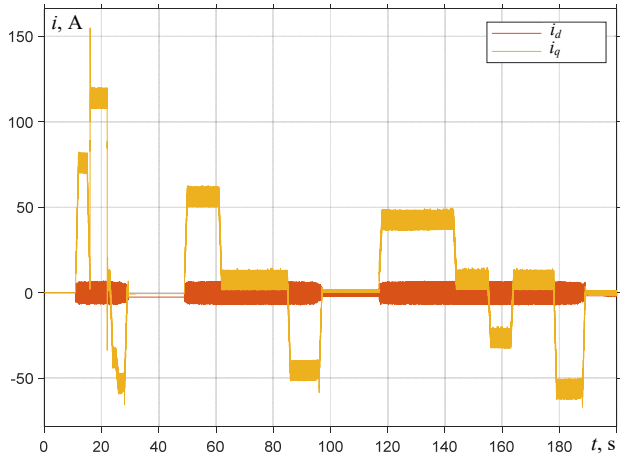

Fig. 10. Direct and quadratic currents

Conclusions. This paper aims to enhance EV performance by utilizing SMC technique for controlling a PMSM powered by a 21-level reduced switching inverter topology. The suggested SMC technique is reliable in situations where there are variations in the desired output due to fluctuations in the propulsion system's load.

Using MATLAB/Simulink proved that, using a 21-asymmetric MLI helps reduce harmonics contributing to optimize the quality of the output voltage, the THD was found to be 6.19 %, for improving the performance of the EV. The proposed topology delivering notable enhancements in both performance and cost-efficiency compared to conventional asymmetric designs. Future studies will propose a new control method that reduce chattering phenomenon of SMC method, to improve the performance of the controller system.

Conflict of interest. The authors declare that they have no conflicts of interest.

REFERENCES

1. Deng R., Xiang Y., Huo D., Liu Y., Huang Y., Huang C., Liu J. Exploring flexibility of electric vehicle aggregators as energy reserve. *Electric Power Systems Research*, 2020, vol. 184, art. no. 106305. doi: https://doi.org/10.1016/j.epsr.2020.106305.

2. Wang Y., John T., Xiong B. A two-level coordinated voltage control scheme of electric vehicle chargers in low-voltage distribution networks. *Electric Power Systems Research*, 2019, vol. 168, pp. 218-227. doi: https://doi.org/10.1016/j.epsr.2018.12.005.

3. Salehifar M., Moreno-Eguilaz M., Putrus G., Barras P. Simplified fault tolerant finite control set model predictive control of a five-phase inverter supplying BLDC motor in electric vehicle drive. *Electric Power Systems Research*, 2016, vol. 132, pp. 56-66. doi: https://doi.org/10.1016/j.epsr.2015.10.030.

4. Phan D., Bab-Hadiashar A., Fayyazi M., Hoseinnezhad R., Jazar R.N., Khayyam H. Interval Type 2 Fuzzy Logic Control for Energy Management of Hybrid Electric Autonomous Vehicles. *IEEE Transactions on Intelligent Vehicles*, 2021, vol. 6, no. 2, pp. 210-220. doi: https://doi.org/10.1109/TIV.2020.3011954.

5. Guezi A., Bendaikha A., Dendouga A. Direct torque control based on second order sliding mode controller for three-level inverter-fed permanent magnet synchronous motor: comparative study. *Electrical Engineering & Electromechanics*, 2022, no. 5, pp. 10-13. doi: https://doi.org/10.20998/2074-272X.2022.5.02.

6. Cai S., Kirtley J.L., Lee C.H.T. Critical Review of Direct-Drive Electrical Machine Systems for Electric and Hybrid Electric Vehicles. *IEEE Transactions on Energy Conversion*, 2022, vol. 37, no. 4, pp. 2657-2668. doi: https://doi.org/10.1109/TEC.2022.3197351.

7. Huang Z., Tang M., Golovanov D., Yang T., Herring S., Zanchetta P., Gerada C. Profiling the Eddy Current Losses Variations of High-Speed Permanent Magnet Machines in Plug-In Hybrid Electric Vehicles. *IEEE Transactions on Transportation Electrification*, 2022, vol. 8, no. 3, pp. 3451-3463. doi: https://doi.org/10.1109/TTE.2022.3152845.

8. Xu W., Junejo A.K., Liu Y., Hussien M.G., Zhu J. An Efficient Antidisturbance Sliding-Mode Speed Control Method for PMSM Drive Systems. *IEEE Transactions on Power Electronics*, 2021, vol. 36, no. 6, pp. 6879-6891. doi: https://doi.org/10.1109/TPEL.2020.3039474.

9. Chindamani M., Ravichandran C.S., Alamelumangai M. Drive Control using Multilevel Inverter for Electric Vehicle Application: A Hybrid SCSO-SNN Technique. *IETE Journal of Research*, 2024, vol. 70, no. 11, pp. 8232-8241. doi: https://doi.org/10.1080/03772063.2024.2378475.

10. Khemis A., Boutabba T., Drid S. Model reference adaptive system speed estimator based on type-1 and type-2 fuzzy logic sensorless control of electrical vehicle with electrical differential.

Electrical Engineering & Electromechanics, 2023, no. 4, pp. 19-25. doi: https://doi.org/10.20998/2074-272X.2023.4.03.
11. Djafer L., Taleb R., Toubal Maamar A.E., Mehedi F., Mostefaoui S.A., Rekmouche H. Analysis and Experimental Implementation of SHEPWM based on Newton-Raphson Algorithm on Three-Phase Inverter using Dspace 1104. *2023 2nd International Conference on Electronics, Energy and Measurement (IC2EM)*, 2023, pp. 1-6. doi: https://doi.org/10.1109/IC2EM59347.2023.10419389.
12. Djafer L., Taleb R., Mehedi F. Dspace implementation of real-time selective harmonics elimination technique using modified carrier on three phase inverter. *Electrical Engineering & Electromechanics*, 2024, no. 5, pp. 28-33. doi: https://doi.org/10.20998/2074-272X.2024.5.04.
13. Chabni F., Taleb R., Helaimi M. ANN-based SHEPWM using a harmony search on a new multilevel inverter topology. *Turkish Journal of Electrical Engineering & Computer Sciences*, 2017, vol. 25, no. 6, pp. 4867-4879. doi: https://doi.org/10.3906/elk-1703-122.
14. Li K., Ding J., Sun X., Tian X. Overview of Sliding Mode Control Technology for Permanent Magnet Synchronous Motor System. *IEEE Access*, 2024, vol. 12, pp. 71685-71704. doi: https://doi.org/10.1109/ACCESS.2024.3402983.
15. Araria R., Berkani A., Negadi K., Marignetti F., Boudiaf M. Performance Analysis of DC-DC Converter and DTC Based Fuzzy Logic Control for Power Management in Electric Vehicle Application. *Journal Européen Des Systèmes Automatisés*, 2020, vol. 53, no. 1, pp. 1-9. doi: https://doi.org/10.18280/jesa.530101.
16. Agrawal A., Singh R., Kumar N., Singh V.P., Alotaibi M.A., Malik H., Marquez F.P.G., Hossaini M.A. Mathematical Modeling of Driving Forces of an Electric Vehicle for Sustainable Operation. *IEEE Access*, 2023, vol. 11, pp. 95278-95294. doi: https://doi.org/10.1109/ACCESS.2023.3309728.
17. Al Halabi M., Al Tarabsheh A. Modelling of Electric Vehicles Using Matlab/Simulink. *SAE Technical Papers*, 2020, vol. 2020-January. doi: https://doi.org/10.4271/2020-01-5086.
18. Abul Masrur M. Hybrid and Electric Vehicle (HEV/EV) Technologies for Off-Road Applications. *Proceedings of the IEEE*, 2021, vol. 109, no. 6, pp. 1077-1093. doi: https://doi.org/10.1109/JPROC.2020.3045721.
19. Gao H., Zhang Z., Liu Y., Huang W., Xue H. Development and Analysis of Dual Three-Phase PMSM With Phase-Shifted Hybrid Winding for Aircraft Electric Propulsion Application. *IEEE Transactions on Transportation Electrification*, 2024, vol. 10, no. 3, pp. 6497-6508. doi: https://doi.org/10.1109/TTE.2023.3334026.
20. Hu S., Liang Z., Zhang W., He X. Research on the Integration of Hybrid Energy Storage System and Dual Three-Phase PMSM Drive in EV. *IEEE Transactions on Industrial Electronics*, 2018, vol. 65, no. 8, pp. 6602-6611. doi: https://doi.org/10.1109/TIE.2017.2752141.
21. Zhang C., He J., Jia L., Xu C., Xiao Y. Virtual line-shafting control for permanent magnet synchronous motor systems using sliding-mode observer. *IET Control Theory & Applications*, 2015, vol. 9, no. 3, pp. 456-464. doi: https://doi.org/10.1049/iet-cta.2014.0477.

Received 15.11.2024
Accepted 31.01.2025
Published 02.05.2025

L. Djafer[1], *PhD Student,*
R. Taleb[2], *Professor,*
F. Mehedi[3], *Associate Professor,*
A. Aissa Bokhtache[1], *Associate Professor,*
T. Bessaad[1], *Associate Professor,*
F. Chabni[4], *Associate Professor,*
H. Saidi[2], *Associate Professor,*
[1] Electrical Engineering Department,
Faculty of Technology, Hassiba Benbouali University of Chlef, Laboratoire Génie Electrique et Energies Renouvelables (LGEER), Chlef, Algeria,
e-mail: lem.djafer@gmail.com (Corresponding Author); a.aissabokhtache@gmail.com; ta.bessaad@gmail.com
[2] Laboratoire Génie Electrique et Energies Renouvelables (LGEER), Electrical Engineering Department,
Hassiba Benbouali University of Chlef, Algeria and Embedded Systems Research Unit of Chlef, Research Centre for Scientific and Technical Information (CERIST), Ben Aknoun, Algeria,
e-mail: r.taleb@univ-chlef.dz, hem.saidi@gmail.com
[3] Laboratoire Génie Electrique et Energies Renouvelables (LGEER), Faculty of Technology,
Hassiba Benbouali University of Chlef, Algeria,
e-mail: f.mehedi@univ-chlef.dz
[4] Electronics Department, Abdellah Morseli University Center of Tipaza, Laboratoire Génie Electrique et Energies Renouvelables (LGEER) of Chlef, Tipaza, Algeria,
e-mail: fayssalc@gmail.com

How to cite this article:
Djafer L., Taleb R., Mehedi F., Aissa Bokhtache A., Bessaad T., Chabni F., Saidi H. Electric drive vehicle based on sliding mode control technique using a 21-level asymmetrical inverter under different operating conditions. *Electrical Engineering & Electromechanics*, 2025, no. 3, pp. 31-36. doi: https://doi.org/10.20998/2074-272X.2025.3.05

UDC 621.3 https://doi.org/10.20998/2074-272X.2025.3.06

H. Khaterchi, M.H. Moulahi, A. Jeridi, R. Ben Messaoud, A. Zaafouri

Improvement teaching-learning-based optimization algorithm for solar cell parameter extraction in photovoltaic systems

Introduction. *This study investigates parameter extraction methods for solar cell analytical models, which are crucial for accurate photovoltaic (PV) system design and performance.* ***Problem.*** *Traditional single-diode models, while widely used, often lack precision, leading to inefficiencies in parameter extraction essential for reliable PV systems.* ***Goal.*** *The work aims to improve the Teaching-Learning-Based Optimization (TLBO) algorithm to enhance the accuracy of parameter extraction in PV models.* ***Methodology.*** *We adopt an enhanced single-diode model, integrating modifications into the TLBO algorithm, including dynamic teaching factor adjustment, refined partner selection, and targeted local searches with the fmincon function. Comparative analysis with experimental data from four PV systems validates the model's accuracy.* ***Results.*** *The enhanced TLBO algorithm achieves superior convergence and reliability in parameter extraction, as evidenced by 500 independent runs.* ***Originality.*** *Key contributions include methodological improvements such as dynamic adjustment of the teaching factor and a new approach to partner selection, which significantly optimizes the algorithm's performance.* ***Practical value.*** *This research provides a robust framework for solar cell parameter extraction, offering practical benefits for PV system designers and researchers in improving model accuracy and efficiency.* References 35, table 1, figures 15.

Key words: **photovoltaic system, teaching-learning-based optimization, Newton-Raphson method, parameter optimization.**

Вступ. *У цьому дослідженні вивчаються методи отримання параметрів для аналітичних моделей сонячних елементів, які мають вирішальне значення для точного проєктування фотоелектричних (PV) систем і їх продуктивності.* ***Проблема***. *Традиційні моделі з одним діодом, хоч і широко використовуються, часто не достатньо точні, що призводить до неефективності вилучення параметрів, необхідного для надійних PV систем.* ***Мета***. *Робота спрямована на покращення алгоритму оптимізації на основі навчання (TLBO) для підвищення точності вилучення параметрів у PV моделях.* ***Методологія***. *Ми приймаємо вдосконалену модель з одним діодом, інтегруючи модифікації до алгоритму TLBO, включаючи динамічне коригування коефіцієнта навчання, уточнений вибір партнера та цільовий локальний пошук з функцією fmincon. Порівняльний аналіз з експериментальними даними із чотирьох PV систем підтверджує точність моделі.* ***Результати***. *Удосконалений алгоритм TLBO досягає значної збіжності та надійності при вилученні параметрів, про що свідчать 500 незалежних запусків.* ***Оригінальність***. *Основні вклади включають методологічні удосконалення, такі як динамічне коригування коефіцієнта навчання та новий підхід до вибору партнера, що значно оптимізує продуктивність алгоритму.* ***Практична цінність***. *Це дослідження забезпечує надійну основу для отримання параметрів сонячних елементів, пропонуючи практичні переваги для розробників та дослідників PV систем у плані підвищення точності та ефективності моделей.* Бібл. 35, табл. 1, рис. 15.

Ключові слова: **фотоелектрична система, оптимізація на основі викладання-навчання, метод Ньютона-Рафсона, оптимізація параметрів.**

1. Introduction. Optimizing solar cell parameters across varying operating conditions is crucial for generating the voltage current curve of photovoltaic (PV) systems and accurately estimating their power output. The accuracy of these parameters is essential for the effective analysis of PV systems, and the choice of parameter extraction method is fundamental to addressing this challenge. Over the years, a range of techniques have been utilized for extracting parameters from solar cells, which can be broadly classified into three types. The first one is analytical methods, which are appreciated for their simplicity and computational speed but may suffer from precision issues because of specific presumptions. Notably, reference [1] gives a detailed analysis of the extraction of solar PV system parameters through the application of optimization techniques based on one- and two-diode models. The second one includes deterministic methods, which necessitate differentiability and convexity and can be sensitive to initial conditions. Examples of such methods include intrinsic proprieties of solar cells [2], the Newton approach [3], the Newton-Raphson method [4], and the nonlinear algorithm method [5]. The third, metaheuristic methods have emerged as viable options for parameter extraction in PV models, aiming to overcome the limitations of previous approaches. These techniques don't require strict conditions and are simple to use.

Current research on metaheuristic algorithms have demonstrated their value in improving accuracy in a number of engineering domains, including microarray data-based cancer classification [6], picture segmentation [7], and identification of faces [8]. Current researches on PV model parameters have been estimated using a variety of metaheuristic techniques. Obviously, these include techniques such as the improved algorithm, namely Genetic Algorithm based on Non-Uniform Mutation (GAMNU) [9], Particle Swarm Optimization (PSO) and Newton–Raphson method [10], nonlinear least squares fitting algorithm [11], and the supply-demand-based optimization algorithm [12]. Other approaches, like chaotic optimization approach [13], adaptive differential evolution [14], symbiotic organic search [15], and Improved Shuffled Complex Evolution algorithm (ISCE) [16] have also been employed. Moreover, an Enhanced Hybrid JAYA and Rao-1 algorithm, called (EHRJAYA) [17], as well as the integration novel hybrid Algorithm based on Rat Swarm optimization with Pattern Search (hARS-PS) [18], have shown significant effectiveness. Similarly, the Improved Gaining-Sharing Knowledge (IGSK) algorithm [19] has also demonstrated success. Other techniques, including chaos game optimization algorithm for estimating the unknown parameters of the three-diode PV model [20], Self-adaptive Ensemble-based Differential Evolution (SEDE) algorithm [21], bio-inspired algorithm called sooty tern optimization algorithm [22], and hybridized interior search algorithm [23] have been successfully implemented. Further methods include an enhanced Spherical Evolution algorithm (SE) based on a novel Dynamic Sine-Cosine mechanism (DSCSE) [24], combined analytical and numerical approaches [25], and newer algorithms like the gorilla troops optimization [26]. The robust approach based on Stochastic Fractal Search (SFS) optimization algorithm is introduced to estimate accurate and reliable values of solar PV parameters for its precise modeling [27] and Supply-Demand Optimization (SDO) algorithm [28] are also part of this diverse toolkit.

Recent studies have explored advanced optimization techniques to improve solar PV systems, including opposition-based on PSO algorithm for Maximum Power Point Tracking (MPPT) [30]. Moreover, a plant-propagation-inspired method for partial shading conditions [31], and a beta-based MPPT controller for efficient power tracking [32]. Other studies have focused on improving power quality with modular inverter structures [33]. Furthermore, authors [34] proposed work enhances system performance by using hysteresis modulation with a Z-source inverter and improves power quality through the inclusion of a shunt active harmonic filter, and designing optimal energy grids with dynamic programming and PSO [35]. These studies offer valuable insights into optimizing solar PV systems and can complement the enhancement of Teaching-Learning-Based Optimization (TLBO) algorithms for solar cell parameter extraction.

In this paper our motivation and contributions, it is as follows, we introduce an enhanced version of the TLBO metaheuristic method. This enhancement includes various modifications aimed at improving the TLBO's performance. The key advancements in this work center around several innovative modifications to the standard TLBO algorithm, significantly enhancing its performance. One of the primary improvements is the dynamic adjustment of the Teaching Factor (TF), which evolves with each generation, allowing the algorithm to better adapt and converge efficiently over time. Additionally, we introduce a new partner selection strategy, designed to improve solution diversity and ensure a more thorough exploration of the search space. An optional mutation step is also incorporated to reduce the likelihood of premature convergence by introducing variability at critical stages of the search. Finally, we embed a local search mechanism using the *fmincon* function, which refines solutions and drives the algorithm toward more precise global optima. These enhancements collectively represent a substantial contribution to the efficiency, accuracy, and robustness of the TLBO algorithm in solving complex optimization problems. Furthermore, we propose an improvement to the SDM by expressing the conventional diode model as two composite functions. To extract the unknown parameters from the modified model, particularly we employ the TLBO method. To validate our novel approach, we compare the results obtained using our proposed model with other recent results and well-established works in the literature that employ the classical model and new metaheuristic algorithms.

2. Methods analysis. This section analyzes the mathematical framework of the electrical model for both the SDM and the PV model of a PV system, depicted in Fig. 1, 2, respectively. We also propose a new variant, the Modified Single-Diode Model (MSDM).

The mathematical SDM gives an analytical current output I_{an}, which is expressed as:

$$I_{an} = I_{ph} - I_D - I_{Rsh}, \tag{1}$$

where I_{an} is the SDM output analytical current; I_{ph} is the photogenerated current; I_D is the diode current; I_{Rsh} is the shunt resistor current.

Equations (2), (3) define the diode current I_D and the shunt resistor current I_{Rsh}:

$$I_D = I_{sd}\left[\exp\left(\frac{V_{Lex} + R_s I_{ex}}{nV_t}\right) - 1\right]; \tag{2}$$

$$I_{Rsh} = \frac{V_{Lex} + R_s I_{ex}}{R_{sh}}; \tag{3}$$

$$V_t = kT/q, \tag{4}$$

where V_{Lex} is the output voltage; I_{sd} is the saturation current; I_{ex} is the experimental current data; R_s is the series resistance; R_{sh} is the shunt resistance; n is the diode ideality factor; V_t is the thermal voltage of the diode; k is the Boltzmann constant; q is the electron charge; T is the cell temperature.

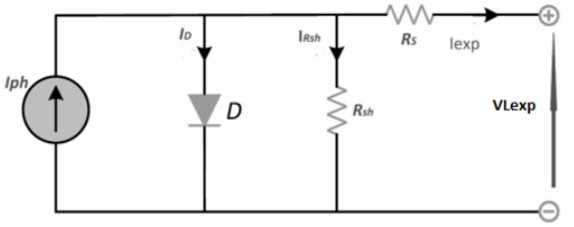

Fig. 1. Equivalent circuit of SDM model

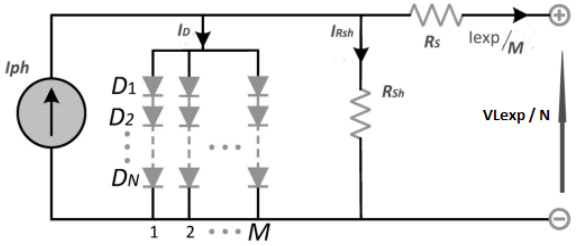

Fig. 2. Equivalent circuit of PV model

According to (1), (2) the 5 unknown parameters to be determined in the SDM are: I_{ph}, I_{sd}, n, R_s and R_{sh}. The goal of our contribution is to ensure that the analytical current I_{an} closely matches the experimental current I_{ex}.

Obviously, the experimental current data of a solar mathematical PV module is given as:

$$I_{ex} = I_{ph}N_p - I_{sd}N_p\left[\exp\left(\frac{q(V_{Lex} + \frac{N_s R_s I_{ex}}{N_p})}{nN_s kT}\right) - 1\right] - \frac{V_{Lex} + \frac{N_s R_s I_{ex}}{N_p}}{R_{sh}\frac{N_s}{N_p}}, \tag{5}$$

where N_p, N_s are the number of cells in parallel and series, and as the solar cells are largely connected in series, for this reason we assume that N_p = 1. The resultant output current of the PV module will be presented as:

$$I_{ex} = I_{ph} - I_{sd}\left[\exp\left(\frac{q(V_{Lex} + N_s R_s I_{ex})}{nN_s kT}\right) - 1\right] - \frac{V_{Lex} + N_s R_s I_{ex}}{R_{sh}N_s}. \tag{6}$$

2.1. Modified Single-Diode Model (MSDM). The previously derived equations including (1), (2) form the basis for the MSDM. By applying these equations, the following expression is obtained:

$$I_{out} = I_{ph} - I_{sd}\left[\exp\left(\frac{V_{Lex} + R_s I_{ex}}{nV_t}\right) - 1\right] - \frac{V_{Lex} + R_s I_{ex}}{R_{sh}}. \tag{7}$$

The output current is represented by the term I_{out}, which was first introduced in (7) and is further described in (8). Typically, the analytical current I_{an} is calculated from the experimental values of V_{Lex} and I_{ex}. The proposed modification involves calculating I_{an} using I_{out}, which is determined by (7). This modification enhances the convergence of the TLBO estimation algorithm and minimizes the Root Means Square Error (RMSE):

$$I_{an} = I_{ph} - I_{sd}\left[\exp\left(\frac{V_{Lex} + R_s I_{out}}{nV_t}\right) - 1\right] - \\ - \frac{V_{Lex} + R_s I_{out}}{R_{sh}}. \quad (8)$$

Finally, (8) defines the MSDM. According to (7), (8) the parameters that must be determined for the MSDM include I_{ph}, I_{sd}, n, R_s and R_{sh}. Note that, an objective function is using based on experimental values, by comparing the analytical current values with the experimental values that minimizes the RMSE. The goal is to minimize the objective function F with respect to the parameter set. In theory, F should be zero when the parameters are precisely determined [3]:

$$F = \min_{X\in[lb,ub]} \sqrt{\frac{1}{N}\sum_{i=1}^{N} (f(V_{Lex}(i), I_{ex}(i), X))^2}. \quad (9)$$

The $f()$ expressions is:

$$f(V_{Lex}, I_{ex}, X) = I_{ex} - I_{an}; \quad (10)$$

$$f(V_{Lex}, I_{ex}, X) = I_{ex} - (I_{ph} - I_{sd}\left[\exp\left(\frac{V_{Lex} + R_s I_{out}}{nV_t}\right) - 1\right] - \\ - \frac{V_{Lex} + R_s I_{out}}{R_{sh}}), \quad (11)$$

where $\boldsymbol{X} = [I_{ph}, I_{sd}, R_s, R_{sh}, n]$ is the vector of unknown parameters; N is the number of data points; $[lb, ub]$ are the lower and upper bounds on parameter vector $\boldsymbol{X}$.

2.2. Teaching-learning-based optimization (TLBO). The TLBO algorithm, developed authors in [29], draws inspiration from the educational process, modeling the interactions and influence between teachers and students within a classroom to optimize solutions. The operation of TLBO is based on two phases, the «Teaching Phase» and the «Learning Phase». The operation of the two phases is explained below.

Initialization phase. The TLBO algorithm begins with the initialization of a population of solutions (learners). Each learner represents a potential solution to the optimization problem, the population size is denoted by N_{pop}, and the problem dimension is denoted by D, learners are initialized randomly within the predefined lower (lb) and upper (ub) bounds of the problem [28].

Teaching phase. During the teaching phase, the algorithm attempts to improve the quality of solutions based on the knowledge of the best solution (Teacher). The best solution in the population is considered the Teacher, the mean (*Mean*) of the population in each dimension is calculated, each learner's solution is updated as:

$$NewSol_i = pop_i + \text{rand}(1, D)[Teacher - TF_{static} Mean], \quad (12)$$

where TF_{static} is the static teaching factor, typically set to 1 or 2; rand(1, D) is a vector of random numbers in [0, 1]:

$$TF_{static} = \text{rand}([1,2], 1, 1). \quad (13)$$

Solutions are bounded within the $[lb, ub]$ limits.

Learning phase. It allows learners to learn from each other. Each learner i is updated by interacting with another randomly chosen learner j. If learner j has a better performance, learner i attempts to learn:

$$NewSol_i = pop_i + \\ \text{rand}(1, D)(pop_i - pop_j)\text{sign}[\text{obj}(j) - \text{obj}(i)], \quad (14)$$

where obj(i), obj(j) are the objective values of the solutions of learners i and j, respectively; solutions are bounded within the the $[lb, ub]$ limits.

Iterative process phase. The teaching and learning phases are repeated for a predefined number of generations or until a convergence criterion is met, the best solution at the end of the iterations is considered the optimal solution. The standard TLBO algorithm is an effective method for solving optimization problems by mimicking the teaching and learning process in a classroom setting. Its simplicity and lack of hyper-parameters make it a robust choice for various applications.

2.3. Modified TLBO using dynamic teaching factor. In this work we will examine the modifications made to the standard TLBO algorithm that can improve the estimation of PV model parameters.

Dynamic teaching factor. One of the main features of our improvement is the dynamic adjustment of the TF based on the current generation number. This adaptation enables TLBO to more effectively adjust to the changing landscape of optimization over successive generations, hence optimizing the search for optimal solutions. The following equation characterizes this factor:

$$TF_{dynamic} = TF_{current} + \\ + \left(1 - \frac{\text{current generation}}{\text{maximun number of generation}}\right), \quad (15)$$

where $TF_{current}$ is the teaching factor for the current generation; $TF_{dynamic}$ is the actual student position of the dynamic teaching factor.

Different partner selection procedure. An alternative partner selection approach was introduced by the algorithm's improved version. This change aims to diversify potential partners, which may help prevent the algorithm from stagnating in local optimal:

$$NewSol_i = pop_i + \\ + \text{rand}(1, D) \cdot [Teacher - TF_{dynamic} \cdot Mean]. \quad (16)$$

2.4. Improved TLBO using dynamic factor with mutation rate. In the first case, this method is based on mutation facultative step. However, this mutation makes it possible to introduce diversity into the individual population, which may be essential for exploring new areas of the research domain. The facultative mutation gives the algorithm additional flexibility to adapt to different kinds of problems.

Note that each student makes mutation with probability P_m. Using a function rand, we apply the mutation rate as follows:

When $P_m >$ rand

$$SolMut_i = NewSol_i + Mut_{rate}[ub - lb]rand; \quad (17)$$

When $P_m <$ rand

$$SolMut_i = NewSol_i, \quad (18)$$

where $SolMut_i$ is the solution mutation; Mut_{rate} is the mutation rate, which is the factor determining the mutation magnitude.

In a second case, we aim to optimize the TLBO algorithm obliviously, we combined the previews modification using local search based on MATLAB function denoted *fmincon*. The updated version includes a local search step that uses the *fmincon* function. This step enables the candidate solutions to be refined using more sophisticated local search techniques. This could have a major impact on raising the caliber of solutions produced by the evolutionary algorithm.

The following representation of the local search step equation is as follows:

$$Optimized_{solution} = \\ = \text{fmincon}\left(F, Current_{solution}, \text{Constraints}\right), \quad (19)$$

where F is the objective function given by (9); $Current_{solution}$ is the solution mutation given by (17); Constraints [*lb*, *ub*] for each parameter. However, the solution that has been optimized with the help of the *fmincon* function is denoted by the term «Optimized Solution» in this equation. The function *fmincon* takes into account the function to minimize, the initial solution, and all requirements that must be met. It conducts local research to find an improved solution within the constraints of the available data. This step allows the quality of the solutions generated by the evolutionary algorithm to be improved by affining them through local optimization (Fig. 3).

```
: function: Improved TLBO
: initialTF = 5 % Initial value of TF
: for each generation gen = 1 to T do
:   Calculate TF = initialTF / (1 + gen)
:   Find [best_obj, best_idx] = min(obj) (minimum objective value and its index)
:   best_student = pop(best_idx, :) (select best solution)
:    for each population member i = 1: NPop do
:             Calculate teach_factor = rand * (best_student - mean(pop))
:             Generate NewSol = pop(i, :) + rand(1, D) .* teach_factor
:             Bound the solution: NewSol = max(min(ub, NewSol), lb)
:             Evaluate NewSolObj = FITNESSFCN(NewSol)
:             if (NewSolObj < obj(i)) then
:                       Update population: pop(i, :) = NewSol
:                       Update objective value: obj(i) = NewSolObj
:             end if
:   end for
:   for each population member i = 1:NPop do
:             Select partner_idx = randi([1, NPop])
:             While partner_idx == I do
:                       Re-select partner_idx = randi([1, NPop])
:             end while
:             if (obj(i) < obj(partner_idx)) then
:                       Generate NewSol = pop(i, :) + rand(1, D) .* (pop(i, :) - pop(partner_idx, :))
:             else:
:                        Generate NewSol = pop(i, :) + rand(1, D) .* (pop(partner_idx, :) - pop(i, :))
:             end if
:             Bound the solution: NewSol = max(min(ub, NewSol), lb)
:             Evaluate NewSolObj = FITNESSFCN(NewSol)
:             if (NewSolObj < obj(i)) then
:                       Update population: pop(i, :) = NewSol
:                       Update objective value: obj(i) = NewSolObj
:             end if
:   end for
:   for each population member i = 1: NPop do
:             if (rand() < 0.05) then % Adjust mutation probability as needed
:                       Generate mutation_factor = rand(1, D) .* (ub - lb) (random mutation)
:                       Generate NewSol = pop(i, :) + mutation_factor
:                       Bound the solution: NewSol = max(min(ub, NewSol), lb)
:                       Evaluate NewSolObj = FITNESSFCN(NewSol)
:                       if (NewSolObj < obj(i)) then
:                                 Update population: pop(i, :) = NewSol
:                                 Update objective value: obj(i) = NewSolObj
:                       end if
:             end if
:   end for
:   Store best objective value for each generation: [BestFVALIter(gen), ~] = min(obj)
: end for
: At the end of all generations:
: Find the best solution: [~, ind] = min(obj)
: X = pop(ind, :) (best individual)
: FVAL = obj(ind) (best objective value)
: Set optimization options: options = optimset('Display', 'off')
: Refine solution using fmincon : [X, FVAL] = fmincon (FITNESSFCN, X, lb, ub, options)
: Store final best objective value: [BestFVALIter(end), ~] = min(FITNESSFCN(X))
: end function
```

Fig. 3. Improved TLBO algorithm

3. Simulation results and discussion. In this study, we delve into the analysis of parameters derived from the TLBO algorithm. The study compares the traditional SDM for PV systems with an enhanced model using the TLBO algorithm. The data set for this analysis comprises a variety of PV devices, including the RTC solar cell from France, the Photowatt-PWP201, STM 6-40/36, and STP6-120/36 PV panels. The performance evaluation is carried out using the RMSE as a benchmark to compare the results from the traditional model and the enhanced model that employs the TLBO algorithm.

Additionally, an assessment of the suggested model and the TLBO algorithm in comparison to a number of accepted techniques, which presented in [17], [19], [23], [24] and SDO [28] are some of these.

To obtain more comprehensive information on solar cell parameter extraction and to illustrate the validity of the new method we carried out several simulation results. Obviously, we execute 30 separate runs to determine the robustness of our suggested model. The TLBO algorithm uses 30 runs, and each run has 500 iterations. The lower limit values (*lb*) of the 5 characteristic parameters I_{ph}(A), I_{sd}(μA), n, R_s(Ω) and R_{sh}(Ω) are the same (0, 0, 1, 0, 0) for the 4 PV devices. The upper limit values (*ub*) of the 5 parameters are respectively (1, 1, 2, 0.5, 100) for the RTC France cell, (2, 5, 2, 1, 2000) for the PWP201, (5, 3, 2, 1, 2000) for STM 6-40/36 and (10, 3, 2, 1, 2000) for STP6-120/36.

3.1. Comparison between the classic SDM and the MSDM. In this study, the simulation results considered for 4 PV devices are analyzed and the modified model is compared with the traditional SDM. However, to find the unknown parameters of the PV systems, the TLBO method is employed. Obviously, for this comparative analysis we perform 30 independent runs presented in Fig. 4–7. The optimal run is selected based on 2 evaluation criteria. The first criterion is the real-time absolute error, denoted as $|I_{ex} - I_{an}|$, where the experimentally measured current is I_{ex}, and the analytically computed current is I_{an}. RMSE's decimal logarithm serves as the basis for the second criterion. The absolute errors for the suggested and classical models $|I_{ex} - I_{an}|$ between the calculated and experimental current values are shown in Fig. 4–7. Obviously, Fig. 4 shows the absolute error for the STM6-40/36 panel, the performance of both models is comparable, though the proposed model exhibits a slight advantage. The absolute inaccuracy for the STP6-120/36 module is shown in Fig. 5, where the proposed model's error ranges from 0 to 0.05, while the inaccuracy of the conventional model varies from 0 to 0.15, highlighting the enhanced functionality of the suggested model. Figure 6 shows the absolute error for the RTC France solar cell, where the proposed model exhibits better convergence towards zero, indicating improved accuracy over the classical model. Additionally, Fig. 7 illustrates the absolute error for the Photowatt-PWP201 module, where the proposed model also achieves more stable and precise results. A thorough comparison of absolute errors between different PV systems is shown in Fig. 4–7, which also emphasizes how much better the suggested model is at precision and convergence than the conventional model.

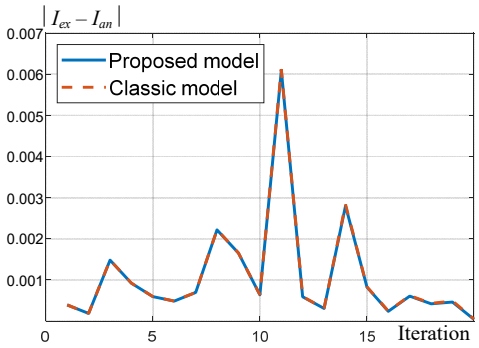

Fig. 4. The absolute error of classical and proposed model for the solar panel STM 6-40/36

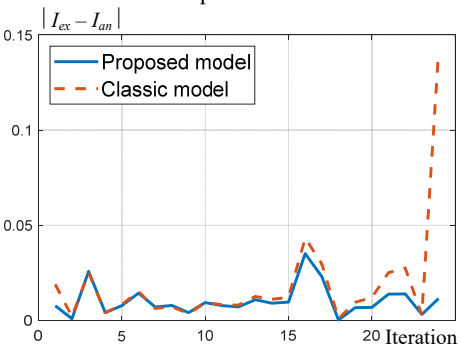

Fig. 5. The absolute error of classical and proposed model for the solar panel STP6-120/36

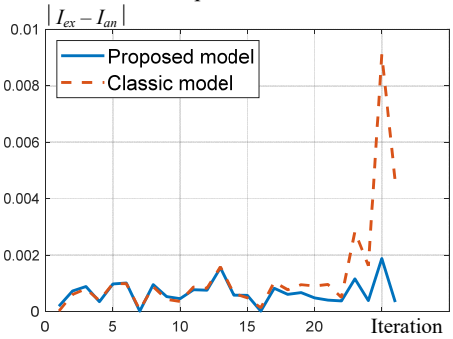

Fig. 6. The absolute error of classical and proposed model for the solar cell RTC France

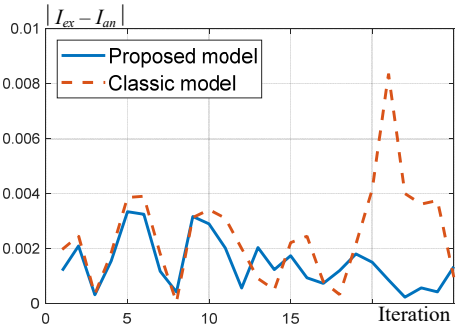

Fig. 7. The absolute error of classical and proposed model for the solar panel Photowatt-PWP201

Figures 8–11 show the evolution of the decimal log of the RMSE for the 4 PV devices. In comparison to the classical model, the suggested model exhibits better convergence over the course of the simulation, as presented in Fig. 8–11. In the initial iterations, the classical model demonstrates better convergence, as indicated by the RMSE evolution for the STM6-40/36 panel shown in Fig. 8. Still, the suggested model performs better at convergence starting with iteration 300. A detailed examination of the convergence behavior for

both models during the simulation results are shown in Fig. 8–11, which show that the suggested model outperforms the traditional model in terms of convergence and accuracy, especially in the later phases.

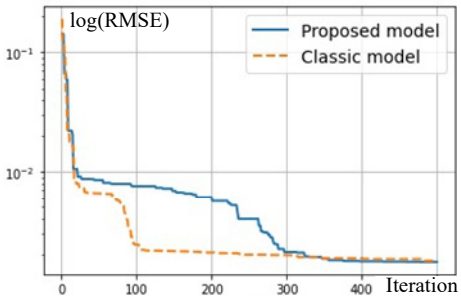

Fig. 8. The decimal log of the best RMSE for the solar panel STM6-40/36

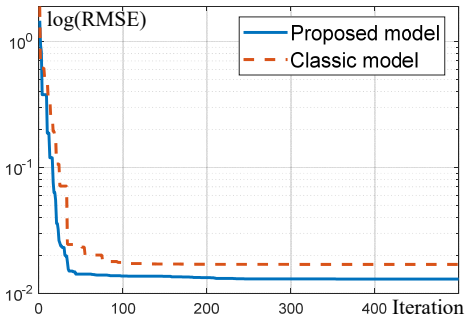

Fig. 9. The decimal log of the best RMSE for the solar panel STP6-120/36

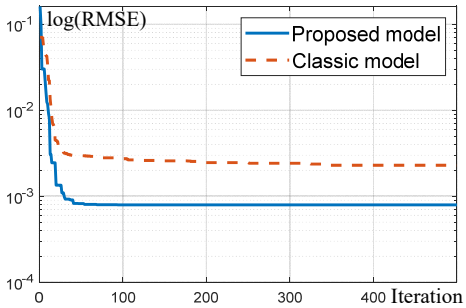

Fig. 10. The decimal log of the best RMSE for the solar cell RTC France

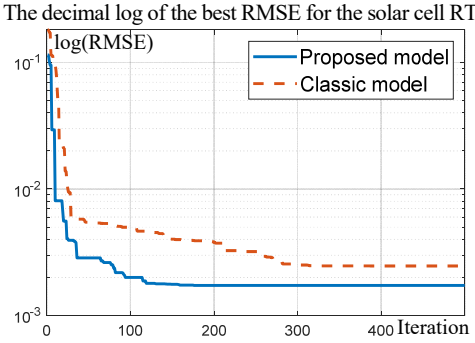

Fig. 11. The decimal log of the best RMSE for the solar panel Photowatt-PWP201

3.2. Statistical analysis and comparison of parameter estimation algorithms. To evaluate the robustness of the proposed model, we conduct several iterations corresponding to the tables of values from the available measurements. This section compares the robustness of the classical model against the modified model. The robustness curves for the suggested model, which is based on the TLBO method, and the classical model, over 30 different runs, are shown in Fig. 12–15. In terms of forecasting the behavior of the 4 PV devices, the analysis of Fig. 12–15 makes it abundantly evident that the suggested model routinely outperforms the traditional models. The evaluation relies on RMSE, a metric that reflects model accuracy, with lower RMSE values signifying better performance. For each of the four PV devices, the suggested model continuously outperforms the conventional models in terms of RMSE values throughout the course of 30 independent runs. This implies that the predicted values of the proposed model are consistently closer to the actual values of the PV devices than those of the classical models.

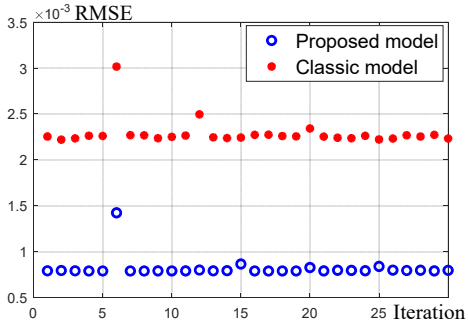

Fig. 12. The different RMSEs for the 30 iterations for the solar cell RTC France

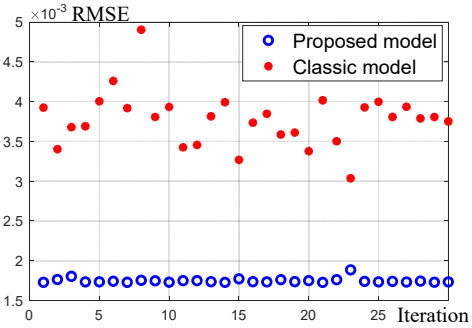

Fig. 13. The different RMSEs for the 30 iterations for the solar panel Photowatt-PWP201

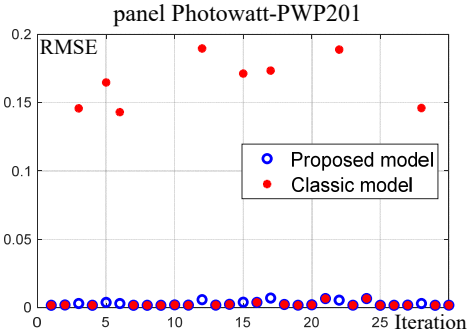

Fig. 14. The different RMSEs for the 30 iterations for the solar panel STM 6-40/36

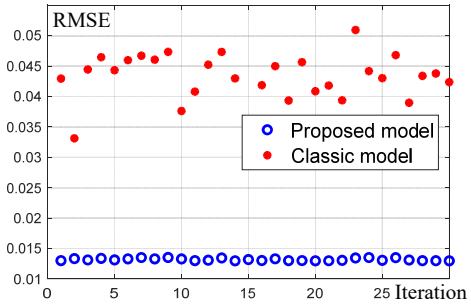

Fig. 15. The different RMSEs for the 30 iterations for the solar panel STP6-120/36

Table 1 presents a performance comparison between the proposed method and other recent works in the literature. This table shows the estimated parameters and

RMSE values for the proposed model and other classic models. The proposed model's RMSE is better than that of classic models across all studied PV systems. This indicates that the proposed model demonstrates higher precision or predictive performance compared to the classic model used in the other works for the analyzed PV systems.

Table 1

Comparing the proposed model with traditional algorithms

Solar cell RTC France						
Algorithm	I_{ph}, A	I_{sd}, A	n	R_s, Ω	R_{sh}, Ω	RMSE
Improved - TLBO	0,76079	$3{,}11945\cdot10^{-7}$	1,47737	0,03621	52,35576	$\mathbf{7{,}89611\cdot10^{-4}}$
GAMNU [9]	0,76077	$3{,}25595\cdot10^{-7}$	1,4821	0,03634	53,89686	$9{,}8618\cdot10^{-4}$
ISCE [16]	0,76078	$3{,}23021\cdot10^{-7}$	1,48118	0,03638	53,71853	$9{,}86022\cdot10^{-4}$
EHRJAYA [17]	0,76078	$3{,}23021\cdot10^{-7}$	1,48118	0.03638	53,71853	$9{,}86022\cdot10^{-4}$
hARS-PS [18]	0,7608	$3{,}23\cdot10^{-7}$	1,481	0,0364	53,714	$9{,}84\cdot10^{-4}$
IGSK [19]	0,76078	$3{,}23\cdot10^{-7}$	1,48118	0,03638	53,71853	$9{,}86022\cdot10^{-4}$
SEDE [21]	0,76078	$3{,}23021\cdot10^{-7}$	1,48118	0,03638	53,71852	$9{,}86022\cdot10^{-4}$
DSCSE [24]	0,76078	$3{,}23021\cdot10^{-7}$	1,48118	0,03638	53,7185	$9{,}86022\cdot10^{-4}$
SFS[27]	0,7609	$3{,}167\cdot10^{-7}$	1,47918	0,03648	53,2805	$7{,}931\cdot10^{-4}$
Solar panel Photowatt-PWP201						
Algorithm	I_{ph}, A	I_{sd}, A	n	R_s, Ω	R_{sh}, Ω	RMSE
Improved - TLBO	1,03235	$1{,}79802\cdot10^{-6}$	1,34714	0,03571	19,65356	$\mathbf{1{,}72569\cdot10^{-3}}$
GAMNU [9]	1,03077	$3{,}01623\cdot10^{-6}$	48,09755	1,21912	906,27545	$2{,}38242\cdot10^{-3}$
ISCE [16]	1,03051	$3{,}48226\cdot10^{-6}$	48,64284	1,20127	981,98228	$2{,}42508\cdot10^{-3}$
EHRJAYA [17]	1,03051	$3{,}48226\cdot10^{-6}$	48,64283	1,20127	981,98222	$2{,}42507\cdot10^{-3}$
hARS-PS [18]	1,0305	$3{,}4822\cdot10^{-6}$	48,6428	1,20120	981,9823	$2{,}42\cdot10^{-3}$
IGSK [19]	1,03051	$3{,}4823\cdot10^{-6}$	48,64283	1,20127	981,9823	$2{,}42507\cdot10^{-3}$
SEDE [21]	1,03051	$3{,}48226\cdot10^{-6}$	48,64284	1,20127	981,98223	$2{,}42507\cdot10^{-3}$
DSCSE [24]	1,03051	$3{,}48226\cdot10^{-6}$	48,6428	1,20127	981,982	$2{,}42507\cdot10^{-3}$
SDO[28]	1,03051	$3{,}48\cdot10^{-6}$	1,35119	0,03337	27,27729	$2{,}425\cdot10^{-3}$
Solar panel STM6-40/36						
Algorithm	I_{ph}, A	I_{sd}, A	n	R_s, Ω	R_{sh}, Ω	RMSE
Improved - TLBO	3,47128	$1{,}19181\cdot10^{-6}$	1,19871	0,0157	27,38766	$\mathbf{1{,}58288\cdot10^{-3}}$
ISCE [16]	1,6639	$1{,}73866\cdot10^{-6}$	1,5203	0.00427	15,92829	$1{,}72981\cdot10^{-3}$
EHRJAYA [17]	1,6639	$1{,}73866\cdot10^{-6}$	1,5203	0.00427	15,92829	$1{,}72981\cdot10^{-3}$
hARS-PS [18]	1,0305	$3{,}4822\cdot10^{-6}$	48,6428	1,2012	981,9823	$2{,}42\cdot10^{-3}$
IGSK [19]	1,6639	$1{,}7387\cdot10^{-6}$	1,5203	0,00427	15,92829	$1{,}72981\cdot10^{-3}$
SDO[28]	1,66391	$1{,}74\cdot10^{-6}$	1,5203	0,00427	15,92829	$1{,}73\cdot10^{-3}$
Solar panel STP6-120/36						
Algorithm	I_{ph}, A	I_{sd}, A	n	R_s, Ω	R_{sh}, Ω	RMSE
Improved - TLBO	7,47482	$1{,}46407\cdot10^{-6}$	1,23924	0,005	14,70737	$\mathbf{1{,}29713\cdot10^{-2}}$
GAMNU [9]	7,469	$2{,}739\cdot10^{-6}$	45,84837	0,16269	1468,618	$1{,}6735\cdot10^{-2}$
ISCE [16]	7,47253	$2{,}335\cdot10^{-6}$	1,2601	0,00459	22,21991	$1{,}66006\cdot10^{-2}$
EHRJAYA [17]	7,47253	$2{,}335\cdot10^{-6}$	1,2601	0,00446	222,19907	$1{,}66\cdot10^{-2}$
IGSK [19]	7,47253	$2{,}335\cdot10^{-6}$	1,2601	0,00459	22,21989	$1{,}66\cdot10^{-2}$
SFS[27]	7,4757	$3{,}01\cdot10^{-6}$	1,2816	0,16	827,5815	$1{,}59\cdot10^{-2}$
SDO[28]	7,47253	$2{,}33\cdot10^{-6}$	1,2601	0,0046	22,21991	$1{,}6601\cdot10^{-2}$

4. Conclusions. This research underscores the significance of precise solar cell modeling to ensure that PV systems are designed effectively. It highlights that in order to improve modeling precision, precise parameter estimate is essential for simple models. In this work, we suggest improving the single-diode model analytically to improve its performance. This improvement incorporates the optimization of unknown parameters and performance evaluation of the model through the application of the TLBO algorithm. When compared to other well-known studies in the field, our findings show that the suggested model outperforms the traditional approach in terms of accuracy and dependability. The application of the TLBO algorithm enables the proposed model to yield more precise and robust results, demonstrating higher rates of convergence. Looking ahead, our future research will explore the use of other metaheuristic algorithms for parameter extraction from single, double and triple diode models. This investigation could offer additional insights and further refine the modeling process. The MPPT issue, which is crucial for maximizing solar power output, will also be covered in our research. To further develop the field of solar cell modeling and PV system design, our future research plan includes investigating alternate metaheuristic algorithms and tackling the MPPT problem.

Conflict of interest. The authors declare that they have no conflicts of interest.

REFERENCES

1. Maniraj B., Peer Fathima A. Parameter extraction of solar photovoltaic modules using various optimization techniques: a review. *Journal of Physics: Conference Series*, 2020, vol. 1716, no. 1, art. no. 012001. doi: https://doi.org/10.1088/1742-6596/1716/1/012001.

2. Tong N.T., Pora W. A parameter extraction technique exploiting intrinsic properties of solar cells. *Applied Energy*, 2016, vol. 176, pp. 104-115. doi: https://doi.org/10.1016/j.apenergy.2016.05.064.

3. Abbassi R., Abbassi A., Jemli M., Chebbi S. Identification of unknown parameters of solar cell models: A comprehensive overview of available approaches. *Renewable and Sustainable Energy Reviews*, 2018, vol. 90, pp. 453-474. doi: https://doi.org/10.1016/j.rser.2018.03.011.

4. Abdulrazzaq A.K., Bognár G., Plesz B. Accurate method for PV solar cells and modules parameters extraction using I–V curves. *Journal of King Saud University - Engineering Sciences*, 2022, vol. 34, no. 1, pp. 46-56. doi: https://doi.org/10.1016/j.jksues.2020.07.008.

5. Beigi A.M., Maroosi A. Parameter identification for solar cells and module using a Hybrid Firefly and Pattern Search Algorithms. *Solar Energy*, 2018, vol. 171, pp. 435-446. doi: https://doi.org/10.1016/j.solener.2018.06.092.

6. Houssein E.H., Abdelminaam D.S., Hassan H.N., Al-Sayed M.M., Nabil E. A Hybrid Barnacles Mating Optimizer Algorithm With Support Vector Machines for Gene Selection of Microarray Cancer Classification. *IEEE Access*, 2021, vol. 9, pp. 64895-64905. doi: https://doi.org/10.1109/ACCESS.2021.3075942.
7. Houssein E.H., Helmy B.E.-D., Elngar A.A., Abdelminaam D.S., Shaban H. An Improved Tunicate Swarm Algorithm for Global Optimization and Image Segmentation. *IEEE Access*, 2021, vol. 9, pp. 56066-56092. doi: https://doi.org/10.1109/ACCESS.2021.3072336.
8. Salama AbdELminaam D., Almansori A.M., Taha M., Badr E. A deep facial recognition system using computational intelligent algorithms. *PLOS ONE*, 2020, vol. 15, no. 12, art. no. e0242269. doi: https://doi.org/10.1371/journal.pone.0242269.
9. Saadaoui D., Elyaqouti M., Assalaou K., Ben Hmamou D., Lidaighbi S. Parameters optimization of solar PV cell/module using genetic algorithm based on non-uniform mutation. *Energy Conversion and Management: X*, 2021, vol. 12, art. no. 100129. doi: https://doi.org/10.1016/j.ecmx.2021.100129.
10. Abdulrazzaq A.K., Bognár G., Plesz B. Evaluation of different methods for solar cells/modules parameters extraction. *Solar Energy*, 2020, vol. 196, pp. 183-195. doi: https://doi.org/10.1016/j.solener.2019.12.010.
11. Elkholy A., Abou El-Ela A.A. Optimal parameters estimation and modelling of photovoltaic modules using analytical method. *Heliyon*, 2019, vol. 5, no. 7, art. no. e02137. doi: https://doi.org/10.1016/j.heliyon.2019.e02137.
12. Shaheen A.M., El-Seheimy R.A., Xiong G., Elattar E., Ginidi A.R. Parameter identification of solar photovoltaic cell and module models via supply demand optimizer. *Ain Shams Engineering Journal*, 2022, vol. 13, no. 4, art. no. 101705. doi: https://doi.org/10.1016/j.asej.2022.101705.
13. Ćalasan M., Jovanović D., Rubežić V., Mujović S., Đukanović S. Estimation of Single-Diode and Two-Diode Solar Cell Parameters by Using a Chaotic Optimization Approach. *Energies*, 2019, vol. 12, no. 21, art. no. 4209. doi: https://doi.org/10.3390/en12214209.
14. Biswas P.P., Suganthan P.N., Wu G., Amaratunga G.A.J. Parameter estimation of solar cells using datasheet information with the application of an adaptive differential evolution algorithm. *Renewable Energy*, 2019, vol. 132, pp. 425-438. doi: https://doi.org/10.1016/j.renene.2018.07.152.
15. Xiong G., Zhang J., Yuan X., Shi D., He Y. Application of Symbiotic Organisms Search Algorithm for Parameter Extraction of Solar Cell Models. *Applied Sciences*, 2018, vol. 8, no. 11, art. no. 2155. doi: https://doi.org/10.3390/app8112155.
16. Gao X., Cui Y., Hu J., Xu G., Wang Z., Qu J., Wang H. Parameter extraction of solar cell models using improved shuffled complex evolution algorithm. *Energy Conversion and Management*, 2018, vol. 157, pp. 460-479. doi: https://doi.org/10.1016/j.enconman.2017.12.033.
17. Zhang Y., Wang Y., Li S., Yao F., Tao L., Yan Y., Zhao J., Gao Z. An enhanced adaptive comprehensive learning hybrid algorithm of Rao-1 and JAYA algorithm for parameter extraction of photovoltaic models. *Mathematical Biosciences and Engineering*, 2022, vol. 19, no. 6, pp. 5610-5637. doi: https://doi.org/10.3934/mbe.2022263.
18. Eslami M., Akbari E., Seyed Sadr S.T., Ibrahim B.F. A novel hybrid algorithm based on rat swarm optimization and pattern search for parameter extraction of solar photovoltaic models. *Energy Science & Engineering*, 2022, vol. 10, no. 8, pp. 2689-2713. doi: https://doi.org/10.1002/ese3.1160.
19. Sallam K.M., Hossain M.A., Chakrabortty R.K., Ryan M.J. An improved gaining-sharing knowledge algorithm for parameter extraction of photovoltaic models. *Energy Conversion and Management*, 2021, vol. 237, art. no. 114030. doi: https://doi.org/10.1016/j.enconman.2021.114030.
20. Ramadan A., Kamel S., Hussein M.M., Hassan M.H. A New Application of Chaos Game Optimization Algorithm for Parameters Extraction of Three Diode Photovoltaic Model. *IEEE Access*, 2021, vol. 9, pp. 51582-51594. doi: https://doi.org/10.1109/ACCESS.2021.3069939.
21. Liang J., Qiao K., Yu K., Ge S., Qu B., Xu R., Li K. Parameters estimation of solar photovoltaic models via a self-adaptive ensemble-based differential evolution. *Solar Energy*, 2020, vol. 207, pp. 336-346. doi: https://doi.org/10.1016/j.solener.2020.06.100.
22. Dhiman G., Kaur A. STOA: A bio-inspired based optimization algorithm for industrial engineering problems. *Engineering Applications of Artificial Intelligence*, 2019, vol. 82, pp. 148-174. doi: https://doi.org/10.1016/j.engappai.2019.03.021.
23. Kler D., Goswami Y., Rana K.P.S., Kumar V. A novel approach to parameter estimation of photovoltaic systems using hybridized optimizer. *Energy Conversion and Management*, 2019, vol. 187, pp. 486-511. doi: https://doi.org/10.1016/j.enconman.2019.01.102.
24. Zhou W., Wang P., Heidari A.A., Zhao X., Turabieh H., Mafarja M., Chen H. Metaphor-free dynamic spherical evolution for parameter estimation of photovoltaic modules. *Energy Reports*, 2021, vol. 7, pp. 5175-5202. doi: https://doi.org/10.1016/j.egyr.2021.07.041.
25. Chennoufi K., Ferfra M. Parameters extraction of photovoltaic modules using a combined analytical - numerical method. *2020 5th International Conference on Cloud Computing and Artificial Intelligence: Technologies and Applications (CloudTech)*, 2020, pp. 1-7. doi: https://doi.org/10.1109/CloudTech49835.2020.9365901.
26. Ginidi A., Ghoneim S.M., Elsayed A., El-Sehiemy R., Shaheen A., El-Fergany A. Gorilla Troops Optimizer for Electrically Based Single and Double-Diode Models of Solar Photovoltaic Systems. *Sustainability*, 2021, vol. 13, no. 16, art. no. 9459. doi: https://doi.org/10.3390/su13169459.
27. Rezk H., Babu T.S., Al-Dhaifallah M., Ziedan H.A. A robust parameter estimation approach based on stochastic fractal search optimization algorithm applied to solar PV parameters. *Energy Reports*, 2021, vol. 7, pp. 620-640. doi: https://doi.org/10.1016/j.egyr.2021.01.024.
28. Ginidi A.R., Shaheen A.M., El-Sehiemy R.A., Elattar E. Supply demand optimization algorithm for parameter extraction of various solar cell models. *Energy Reports*, 2021, vol. 7, pp. 5772-5794. doi: https://doi.org/10.1016/j.egyr.2021.08.188.
29. Rao R.V., Savsani V.J., Vakharia D.P. Teaching–learning-based optimization: A novel method for constrained mechanical design optimization problems. *Computer-Aided Design*, 2011, vol. 43, no. 3, pp. 303-315. doi: https://doi.org/10.1016/j.cad.2010.12.015.
30. Saeed H., Mehmood T., Khan F.A., Shah M.S., Ullah M.F., Ali H. An improved search ability of particle swarm optimization algorithm for tracking maximum power point under shading conditions. *Electrical Engineering & Electromechanics*, 2022, no. 2, pp. 23-28. doi: https://doi.org/10.20998/2074-272X.2022.2.04.
31. Khan S.A., Mahmood T., Awan K.S. A nature based novel maximum power point tracking algorithm for partial shading conditions. *Electrical Engineering & Electromechanics*, 2021, no. 6, pp. 54-63. doi: https://doi.org/10.20998/2074-272X.2021.6.08.
32. Louarem S., Kebbab F.Z., Salhi H., Nouri H. A comparative study of maximum power point tracking techniques for a photovoltaic grid-connected system. *Electrical Engineering & Electromechanics*, 2022, no. 4, pp. 27-33. doi: https://doi.org/10.20998/2074-272X.2022.4.04.
33. Parimalasundar E., Kumar N.M.G., Geetha P., Suresh K. Performance investigation of modular multilevel inverter topologies for photovoltaic applications with minimal switches. *Electrical Engineering & Electromechanics*, 2022, no. 6, pp. 28-34. doi: https://doi.org/10.20998/2074-272X.2022.6.05.
34. Sai Thrinath B.V., Prabhu S., Meghya Nayak B. Power quality improvement by using photovoltaic based shunt active harmonic filter with Z-source inverter converter. *Electrical Engineering & Electromechanics*, 2022, no. 6, pp. 35-41. doi: https://doi.org/10.20998/2074-272X.2022.6.06.
35. Dehghani M., Montazeri Z., Ehsanifar A., Seifi A.R., Ebadi M.J., Grechko O.M. Planning of energy carriers based on final energy consumption using dynamic programming and particle swarm optimization. *Electrical Engineering & Electromechanics*, 2018, no. 5, pp. 62-71. doi: https://doi.org/10.20998/2074-272X.2018.5.10.

Received 06.10.2024
Accepted 20.01.2025
Published 02.05.2025

H. Khaterchi [1]*, PhD,*
M.H. Moulahi [1]*, Associate Professor,*
A. Jeridi [1]*, PhD,*
R. Ben Messaoud [2]*, Doctor of Electrical Engineering,*
A. Zaafouri [1]*, Professor of Electrical Engineering,*
[1] Ecole Nationale Superieure d'ingenieurs de Tunis, Tunisia,
e-mail: hechmi.khaterchi@uvt.tn (Corresponding Author).
[2] Centre de Recherches et des Technologies de l'Energie, Tunisia.

How to cite this article:
Khaterchi H., Moulahi M.H., Jeridi A., Ben Messaoud R., Zaafouri A. Improvement teaching-learning-based optimization algorithm for solar cell parameter extraction in photovoltaic systems. *Electrical Engineering & Electromechanics*, 2025, no. 3, pp. 37-44. doi: https://doi.org/10.20998/2074-272X.2025.3.06

UDC 621.3.013 https://doi.org/10.20998/2074-272X.2025.3.07

X.C. Nguyen, D.T. Le

Adaptive finite-time synergetic control for flexible-joint robot manipulator with disturbance inputs

Introduction. *In this paper, the adaptive finite time controller is designed for flexible-joint manipulator (FJM) to stabilize oscillations and track the desired trajectory based on synergetic control theory (SCT) under disturbance inputs. The problem of the proposed work consists in the development of a mathematical model of the flexible joint while ignoring the nonlinear components of the actuator and synthesizing the control law that ensures the system stability within a settling time. The* ***aim*** *of this study is to use finite-time synergetic controller to ensure the reduction of system tracking error, avoid vibration and achieve steady state in a certain time period. An adaptive synergetic law is developed to solve the problem of uncertainty in the mathematical model of the actuator of FJM and input disturbances.* ***Methodology.*** *First, based on SCT the finite-time controller is constructed via the functional equation of the first manifold. The control law is designed to ensure the movement of the closed-loop system from an arbitrary initial state into the vicinity of the desired attractive invariant manifold, that is, the target attracting manifold. Secondly, to adjust the control law online, an adaptive law is developed to estimate the disturbance acting on the input. Then, the Lyapunov function is used to prove that the system can be stabilized in a sufficiently small neighborhood of the origin within finite time under input disturbances.* ***Novelty****. The implemented controller is effective in ensuring stability over a given time, minimizing the jitter problem while maintaining tracking accuracy and system robustness in the presence of input noise.* ***Results.*** *Numerical simulation and experimental results are presented to illustrate the effectiveness of the proposed method. The research directions of the model were determined for the subsequent implementation of the results in experimental samples.* References 25, table 1, figures 7.

Key words: **flexible-joint manipulator, synergetic control theory, finite-time control, Lyapunov function, adaptive control.**

Вступ*. У роботі розроблено адаптивний кінцевий регулятор часу для гнучкого шарнірного маніпулятора (FJM) для стабілізації коливань та відстеження бажаної траєкторії на основі синергетичної теорії управління (SCT) при вхідних збуреннях. Завдання пропонованої роботи полягає у розробці математичної моделі гнучкого шарніра з ігноруванням нелінійних складових приводу та синтез закону управління, що забезпечує стійкість системи протягом часу встановлення.* ***Метою*** *даного дослідження є використання кінцевочасного синергетичного регулятора для забезпечення зниження помилки відстеження системи, виключення вібрації та досягнення стійкого стану за певний проміжок часу. Розроблено адаптивний синергетичний закон для вирішення проблеми невизначеності в математичній моделі приводу FJM та вхідних збурень.* ***Методологія****. По-перше, на основі SCT будується кінцевий регулятор часу за допомогою функціонального рівняння першого різноманіття. Закон управління розроблений для забезпечення переміщення замкнутої системи з довільного початкового стану в область бажаного притягуючого інваріантного різноманіття, тобто цільового різноманіття. По-друге, для налаштування закону управління в режимі онлайн розробляється адаптивний закон для оцінки обурення, що діє на вході. Потім за допомогою функції Ляпунова доводиться, що система може бути стабілізована у досить малої околиці початку координат за кінцевий час при вхідних збуреннях.* ***Новизна****. Реалізований регулятор ефективний для забезпечення стійкості протягом заданого часу, мінімізуючи проблему коливань, зберігаючи точність відстеження та надійність системи за наявності вхідного шуму.* ***Результати****. Наведено чисельне моделювання та експериментальні результати для ілюстрації ефективності запропонованого методу. Визначено напрями досліджень моделі для подальшої реалізації результатів у експериментальних зразках.* Бібл. 25, табл. 1, рис. 7.

Ключові слова: **гнучко-шарнірний маніпулятор, синергетична теорія управління, кінцевий час управління, функція Ляпунова, адаптивне управління.**

1. Introduction. Nowadays, robotic technology has developed strongly, flexible-joint manipulator (FJM) have been widely used in mechatronic systems. Compared to traditional robot joint drive systems, FJM has smaller structures and lighter weights. FJMs are typical representatives of nonlinear coupling systems, which have complex dynamic relationships between rigid links and flexible joints. In these systems, the joints are often driven by elastic mechanisms such as speed reducers or cables [1], and joints with torsional stiffness are known as flexible joints. The existence of joint flexibility causes oscillations in the output of the system. Reducing output oscillation and improving control quality of flexible joints has become a topical issue of interest to many researchers [2].

To achieve high quality control of servo systems, most control methods require establishing an accurate dynamic model. The modeling and control of single disturbances in flexible joint robot controllers have been extensively studied in many researches [3–11]. In [3] the influence of friction force on the control moment of the FJM system is considered. In [4] the dynamic modeling and analytical modeling for robot manipulators with rigid links and flexible joints are presented. Dynamic equations of flexible-joints are firstly developed using the Lagrangian formulation in minimal joint and motor coordinates. In [6] presents a way to derive a low-order model for multi-space serial arms. Due to the low number of degrees of freedom, this model can be used in real-time systems for control and estimation. To build a more accurate dynamic model, work [7] considers the flexibility of the load. Many researches indicate that small power motors are always prioritized as joint actuators to make the mechanical structure compact enough in the design of robot controllers. Consequently, this leads to the fact that joint actuators cannot provide arbitrarily large torque as required by the unconstrained control laws proposed in most previous controllers. In [8, 9] the presence of actuator dynamics is not considered in controller calculations, assuming motor torque is proportional to the voltage supplied to the actuator, simplifying the mathematical model in the synthesis of control laws. In many real-world situations, flexible joint controllers do not account for motor dynamics and input disturbances. If these impacts on torque are ignored in the control method design, the performance of the FJM controller system will decrease, which can lead to a reduction in the system's control quality. Therefore,

practical problems require considering motor dynamic uncertainties and input disturbances when designing controllers for FJM.

In recent years, many researches have presented control laws have been designed to improve the control quality performance of FJM systems, such as PID controller [10], fuzzy logic controller (FLC) [11–13], sliding mode control [8, 14, 15], backstepping control [9, 16, 17], robust control [18], intelligent control [19], synergetic controller [20, 21] and adaptive control [22]. For example, in [10] the authors designed a PID controller, similar to a rigid robot for the flexible joint robot system, and its effectiveness was demonstrated through simulation. In [12], the authors proposed an adaptive FLC using the backstepping approach and dynamic surface method. In [8], an adaptive SMC was proposed, which improves tracking quality under disturbances and is implemented on a real system. In [15], a finite-time sliding mode controller is designed in combination with a disturbance observer to enhance control quality. A novel hybrid control strategy for single-link flexible articulated robot manipulators, addressing the inherent uncertainties and nonlinear dynamics. By integrating nonlinear reduced-order active disturbance rejection control with backstepping control is presented in the paper [16]. In [18], a robust model predictive controller scheme for flexible joint robots modeled as nonlinear Lipschitz systems with unknown bounded perturbations is designed. In [19], a neural network control method was presented for the flexible joint controller system under disturbance conditions. In research [20], synergetic control theory (SCT) was applied with the proposed sliding manifolds. This research show the control system has high robustness, but they do not consider stabilization time and input disturbances. The research on flexible joint controllers that account for input disturbances and stabilization time are still limited. In [22], a generalized adaptive saturated controller based on backstepping control, singular perturbation separation, and neural networks was designed to achieve tracking control with limited torque inputs.

Purpose and objectives of the article. With the requirement of ensuring the stability of the FJM system in a given time and overcoming the effects of input disturbances and actuator uncertainties. This work proposes a adaptive finite-time synergetic controller to overcome the effects of external disturbances and ensure the stability time, the adaptive control law compensates the disturbance observed at the system input. The main contribution of this study is to develop a controller by constructing manifolds that satisfy the functional equations that ensure a predetermined convergence time, while simultaneously resisting disturbances and reducing static errors, with the best performance and chattering reducing. In addition, the adaptive control law has been used in the ensemble controller to identify input disturbances and actuator uncertainties. The main objective of this work is to evaluate the effectiveness of the proposed control law for the FJM system. Second, deploy and validate the control law on a real system. The Lyapunov method is used to prove the stability, with the contributions of the work highlighted by:

1) The manifold design using regression and functional equations ensures the finite-time stable system to improve the control accuracy, finite-time convergence and fast transient response.

2) The stability analysis is proven according to the Lyapunov criterion, in which the adaptive law is generated.

3) The control law is realized on an embedded system to verify the effectiveness of the proposed control law.

2. Methods.

2.1. Concept of finite-time control.

There is a nonlinear system that can be described as:

$$\boldsymbol{x}(t) = f(\boldsymbol{x}(t), \boldsymbol{u}),\ \boldsymbol{x}(0) = \boldsymbol{x}_0, \tag{1}$$

where $\boldsymbol{x} \in R^n$ is the state variable vector and $f(0, 0) = 0$, $\boldsymbol{u} \in R^p$ is the control signal; $f(\boldsymbol{x}, 0) = 0$ is the continuously nonlinear function in an open neighborhood near the origin. If the convergence time is limited by a function $T(\boldsymbol{x}_0)$, the system without input impact is considered finite-time stable. In other words, the system can achieve convergence with certain predetermined time constants denoted by $T_{\max}$, where $T_{\max}$ is a constant satisfying $T(\boldsymbol{x}_0) < T_{\max}$.

Lemma 1 [25]. Consider the system (1), when $\boldsymbol{u} = 0$ and suppose there exist a Lyapunov function $V(\boldsymbol{x})$, $c>0$, $k>0$ and $0 < \alpha < 1$ such that

$$\dot{V}(\boldsymbol{x}) + cV^{\alpha}(\boldsymbol{x}) + kV(\boldsymbol{x}) \le 0 \tag{2}$$

holds. Then, the equilibrium is finite-time stable and the convergence time is given by

$$T_x(\boldsymbol{x}_0) \le \frac{\ln\left(1 + (k/c)V^{1-\alpha}(\boldsymbol{x}_0)\right)}{k(1-\alpha)}. \tag{3}$$

Similarly, the origin $U = D = R^n$ and $V(\boldsymbol{x})$ is globally finite-time stable if and only if and is radially unbounded.

2.2. Synergetic control law design process. The main steps of the STC controller synthesis process can be summarized as follows [19, 23, 24]. Assume the controlled system is described by the nonlinear differential equation system in the form (3). First, by defining a manifold as a function $\psi_1(\boldsymbol{x})$, the control law is designed to force the system to move to the manifold $\psi_1(\boldsymbol{x}) = 0$. The designer can select the manifold type with characteristics according to the desired control quality criteria. In specific cases, the manifold may be a simple linear combination of the state variables.

When the system has not reached technological maturity, continue the same process, defining m manifolds (with $p \le n–1$) sequentially in a decreasing order. The synthesized controller will ensure the system converges to the next manifold ψ_2 and then to ψ_m. On the final manifold, the system will ensure movement along ψ_m towards the origin. These manifolds will have dynamic characteristics satisfying the equation of the form:

$$T_i\dot{\psi}_i + F_i(\psi_i) = 0, T_i > 0, \tag{4}$$

where T_i is the parameter that affects the rate of convergence to the manifold specified by the macro variable. Simultaneously, the functions $F_i(\psi_i)$ must satisfy the following conditions: $F_i(0) = 0$ and $F_i(\psi_i)(\psi_i)$ for all $\psi_i = 0$, meaning equation (4) is globally asymptotically stable. Additionally, the functions $F_i(\psi_i)$ are chosen in such a way that they satisfy the requirements of the control problem.

The process of designing the control law for system (1) with $p = 1$ is performed as follows: First, take the derivative of the manifold $\psi_i(\boldsymbol{x}) = 0$ and substitute it into (4) combined with system (1) to obtain:

$$T_1 \frac{\partial \psi_1}{\partial t} f_1(\boldsymbol{x}, u) + F_1(\psi_1) = 0\,. \qquad (5)$$

Solving (5) we find the control law u. With such a control law, the system enters the first manifold, leading to system (1) being partitioned into a subsystem of a lower order than the original system. Continue the steps above with the partitioned subsystems until the final manifold is reached to obtain the complete control law of the system.

In this design process, each manifold introduces a new constraint in the state space and reduces the order of the control system, operating towards global stability. The quality of the system can be determined through the form of the functional equation and the form of the manifold. As presented above, the settling time can be predetermined through the choices of functional equation forms. The process summarized here can be easily implemented as a computer program for automatic control law synthesis or can be manually executed for simple systems, such as the synthesis of control for a two-degree-of-freedom FJM.

2.3. Platform introduction and operating principle. In this paper, the flexible joint system built in the laboratory is taken as the research object (Fig. 1), and the nominal parameters of the system are approximately determined, with the model of the DC motor not fully identified. The motor is considered as a proportional link between the output torque and the input voltage. The prototype of the FJM system and the experimental setup are shown in Fig. 1. The system includes a FMJ system, an OMRON E6B2-CWZ6C 1000 (*P/R*) rotary encoder sensor, a 385-P16 Hall magnet encoder sensor, a BTS 7960 motor control power amplifier circuit, a 775 planetary gear reducer motor, and power supply circuits of 3.3 V and 12 V.

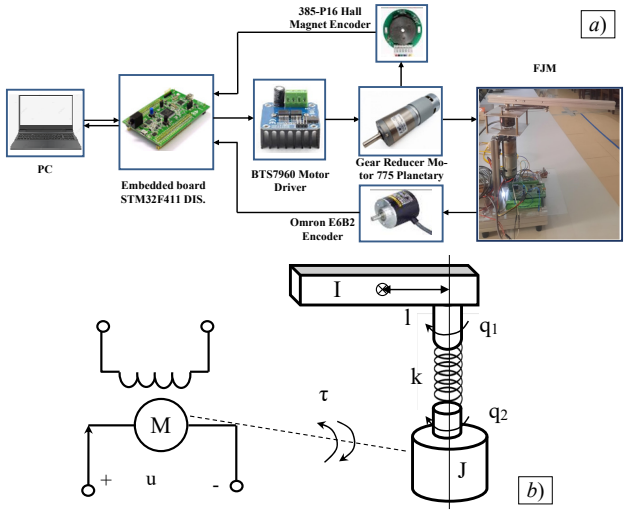

Fig. 1. FJM: *a* – block diagram; *b* – schematic diagram

The STM32F411 embedded board is used as the main board of the real-time control model system. This embedded board has a system frequency of up to 100 MHz and a high-performance 32-bit CPU. The embedded board is the core of the experimental platform and is used to implement real-time algorithms. A large number of peripheral interfaces make the STM32F411 not only capable of good data processing but also facilitate the design of digital systems. The control program is written in C language on the STM32CubeIDE software. Experimental data readings are displayed on MATLAB software through UART communication with a baud rate of 9600 bit/s. The rotational angle data of the link and motor shaft are collected through 2 encoders and read through the interrupt pins of the embedded board. The control algorithm is implemented in embedded software. The control signal is modulated in pulse-width modulation from the general-purpose input/output pins of the embedded board to the voltage amplifier and then to the motor and actuate the link of the FJM.

2.4. Mathematical model of the FJM. This section refers to works [8, 14]. The basis of the controller determines the angular position of the flexible link controlled by a direct current motor with an encoder, while the flexible link will respond based on the action of the motor shaft. The deviation of the soft link response is determined by the stiffness of the joint. Due to unknown motor parameters, it is assumed that the output torque is proportional to the voltage applied to the motor, and its joint can only deform when rotating in the vertical plane in the direction of the joint's rotation. Assuming that the frictional force between the links is very small and can be neglected and the states can be measured, the dynamic equation of the FJM takes the form [9, 21]:

$$\begin{cases} I\ddot{q}_1 + mgl\sin(q_1) + k(q_1 - q_2) = 0; \\ J\ddot{q}_1 - k(q_1 - q_2) = \tau + d, \end{cases} \qquad (6)$$

where q_1, q_2 are the rotation angles of the 2 links of the FJM in Fig. 1. The coefficient k is the stiffness of the flexible joint controller model. The larger the elastic stiffness k, the larger the elastic stiffness and the smaller the flexibility of the flexible joint, and q_1 is closer to q_m. The smaller the k, the smaller the elastic stiffness of the flexible joint, the greater the flexibility, and the easier it is to bend the soft arm. I and J are the moments of inertia of the flexible link and the motor rotor; m is the mass of the flexible link; l is the distance from the center of the flexible link to the flexible – joints; g is the gravitational acceleration; τ is the control torque generated by the motor. In this research, the motor model is not used in the synthesis of the control law, assuming τ is proportional to the voltage supplied to the motor, meaning $\tau = N{\cdot}u$, in there u is the voltage supplied to the motor and N is the coefficient; d is the control torque disturbance and the uncertainty of the motor model.

We define $x_1 = q_1; x_2 = \dot{q}_1; x_3 = q_2; \dot{x}_4 = \dot{q}_2$. The system of equations of FJM (6) is rewritten as:

$$\begin{cases} \dot{x}_1 = x_2; \\ \dot{x}_2 = -\dfrac{k}{I}x_1 - \dfrac{mgl}{I}\sin x_1 + \dfrac{k}{I}x_3; \\ \dot{x}_3 = x_4; \\ \dot{x}_4 = \dfrac{k}{J}(x_1 - x_3) + \dfrac{N}{J}u + \dfrac{d}{J}. \end{cases} \qquad (7)$$

Assumption 1. The unmeasurable factor d is bounded: $|d| = D_{\max}$, where $D_{\max}$ is positive constant.

Assumption 2. If $x_1 = 0$; $x_2 = 0$ and $\dot{x}_2 \to 0$ then $x_3 \to 0$.

The model above shows that the system is complex and non-linear. Importantly, the state vector elements are connected to each other through a chained integration procedure and the last state variable can be obtained by integrating the control input u. The objective of the FJM control problem is that the angle q_1 of link rotates correctly according to the desired signal, the setting time is within the given time t_f and while maintaining control quality under input disturbance d.

2.5. Synthesis of finite-time control law based on SCT without input disturbance. In this section, the FJM control problem is to ensure that link q_1 moves according to the desired trajectory x_{sp} by adjusting the voltage u supplied to the motor to create a torque acting on link q_2. Under the effect of the motor torque acting on link q_2 to bring the system to the desired point in a finite time and keep the system stable at that position. First, the control law is designed when there is no disturbance, which means $d = 0$. From the perspective of SCT, this means that it is necessary to synthesize the control signal $u(\boldsymbol{x})$. The action of the control law will move the links through the joints from the initial position following a given signal or stabilize at the desired position when there is a disturbance to ensure control quality.

From the requirement of FJM control problem to follow the desired value, based on SCT for engineering systems, we propose the first technological invariant corresponding to the control objective:

$$x_1 = x_{sp}. \tag{8}$$

In the first step, based on the purpose of controlling and reducing the order of the system model according to SCT, the first manifold selected has the form:

$$\psi_1 = x_4 - \varphi_1(x_1, x_2, x_3). \tag{9}$$

In the manifold (9) contains the function $\varphi_1(x_1, x_2, x_3)$, which determines the desired properties of the link velocity x_4 at the intersection with the invariant manifold $\psi_1 = 0$. The function $\varphi_1(x_1, x_2, x_3)$ is calculated in the next steps, to ensure that it satisfies the technological invariant (8). According to SCT, to ensure that the manifold $\psi_1 = 0$ and satisfies the finite-time condition, the macro variable ψ_1 is chosen as the solution of the functional equation of the following form:

$$\dot{\psi}_1 + c_1 \operatorname{sgn}(\psi_1)\left|\psi_1\right|^{2\beta-1} + k_1\psi_1 = 0\,, \tag{10}$$

In there $c_1>0$, $k_1>0$ and $0.5 < \beta < 1$. Substituting (9) into (10) we have:

$$\frac{\mathrm{d}}{\mathrm{d}t}(x_4 - \varphi_1) + c_1 \operatorname{sgn}(\psi_1)\left|\psi_1\right|^{2\beta-1} + k_1\psi_1 = 0\,. \tag{11}$$

Substituting $\dot{x}_4$ in the system of equations (7) when $d = 0$ into (11), we obtain the control signal u as follows:

$$u = \begin{pmatrix} -k(x_1 - x_3) + J\sum_{i=1}^{3}\dfrac{\partial\varphi_1}{\partial x_i}\dfrac{\mathrm{d}x_i}{\mathrm{d}t} \\ -J\left(c\operatorname{sgn}(\psi_1)\left|\psi_1\right|^{2\beta-1} + k_1\psi_1\right) \end{pmatrix} / N\,. \tag{12}$$

With the synthesis of the control law u as described, after some time, the manifold ψ_1 will change and asymptotically stabilize to 0 (i.e., x_4 becomes φ_1). At this point, the dynamics of the initial system will become the dynamics of the following system:

$$\begin{cases} \dot{x}_1 = x_2; \\ \dot{x}_2 = -\dfrac{k}{I}x_1 - \dfrac{mgl}{I}\sin(x_1) + \dfrac{k}{I}x_3; \\ \dot{x}_3 = \varphi_1. \end{cases} \tag{13}$$

In the following steps, the synthesis process is carried out sequentially to determine the internal control signals φ_1, $\varphi_2(x_1, x_2)$ and the technological invariant (8). The manifolds are chosen sequentially to ensure system stability and convergence to the following manifolds: $\psi_2 = x_3 - \varphi_2$, $\psi_3 = x_2 - K(x_1 - x_{sp})$. These manifolds satisfy the following functional equations:

$$T_2\dot{\psi}_2 + \psi_2 = 0\,; \tag{14}$$

$$T_3\dot{\psi}_3 + \psi_3 = 0\,, \tag{15}$$

where T_2, T_3 are the positive constants.

With the synthesis steps as described above, the system will move to the final manifold ψ_3. When the system reaches the final manifold, it means that:

$$\psi_3 = 0 \Rightarrow x_2 - K(x_1 - x_{sp}) = 0\,. \tag{16}$$

The condition for (15) to be stable about x_{sp} is $K<0$.

From equations (15) and (16), we find the internal control signals φ_1 and φ_2:

$$\varphi_1 = \sum_{i=1}^{2}\frac{\partial\varphi_2}{\partial x_i}\frac{dx_i}{dt} - \frac{x_3 - \varphi_2}{T_2}\,; \tag{17}$$

$$\varphi_2 = \frac{mgl}{I}\sin(x_1) + x_1 + \frac{IK}{k}(x_2 - \dot{x}_{sp}) - \\ - \frac{I}{kT_3}\left(x_2 - K(x_1 - x_{sp})\right). \tag{18}$$

From (12), (17) and (18), we find the control law u for the FJM. To analyze the stability of system (7) with control law (12) and prove the stability time of the control system, we choose the Lyapunov function of the form:

$$V = \frac{1}{2}\psi_1^2\,. \tag{19}$$

Derivative of function (19) gets:

$$\dot{V} = \psi_1\dot{\psi}_1 = -\psi_1\left(c_1\operatorname{sgn}(\psi_1)\left|\psi_1\right|^{2\beta-1} + k_1\psi_1\right) = \\ = -c_1\left(\psi_1^{\,2}\right)^{\beta} - k_1\psi_1^{\,2} = -\frac{c_1}{2^{\beta}}V^{\beta} - \frac{k_1}{2}V \tag{20}$$

According to the Lyapunov method, $\psi_1 \to 0$ as $t \to \infty$. Combined with SCT $\psi_2 \to 0$, $\psi_3 \to 0$ and $x_1 \to x_{sp}$. Therefore, the system is asymptotically stable. From (20) and according to Lemma 1, the settling time to the first manifold from the initial position is calculated using (3).

2.6 Adaptive synergetic control design. In practice, control systems can be subject to model uncertainties and input disturbances. As presented in the mathematical model of the FJM above, the component of the actuating motor is not fully modeled. For this reason, the finite-time controller must be designed to counteract these input disturbances. A common approach is to design an adaptive control law, incorporating estimated values of uncertainties into the control law. In this section, an adaptive control law is designed to estimate the input disturbance d. The proposed adaptive controller is as follows:

$$u = \begin{pmatrix} -k(x_1 - x_3) - \hat{d} + J\sum_{i=1}^{3} \dfrac{\partial \varphi_1}{\partial x_i} \dfrac{\mathrm{d}x_i}{\mathrm{d}t} \\ -J\left(c\,\mathrm{sgn}(\psi_1)|\psi_1|^{2\beta-1} + k_1\psi_1 \right) \end{pmatrix} / N, \quad (21)$$

where $\hat{d}$ is the estimated value of d.

Consider the Lyapunov function as in (19). The derivative of function (19) with the controller (21) applied to the system (7) when the system enters the first manifold is given by:

$$\dot{V} = \left(-c_1\,\mathrm{sgn}(\psi_1)|\psi_1|^{2\beta-1} - k_1\psi_1 \right)\psi_1, \quad (22)$$

where $\tilde{d} = d - \hat{d}$ is the error between the input disturbance and the observed disturbance. The Lyapunov function for designing adaptive controller has the following form:

$$V_{ad} = V + \frac{1}{2}\gamma\tilde{d}^2, \quad (23)$$

where γ is the positive constant.

The derivative of function (23), we have:

$$\dot{V}_{ad} = -\left(\tilde{d} + c_1\,\mathrm{sgn}(\psi_1)|\psi_1|^{2\beta-1} + k_1\psi_1 \right)\psi_1 + \gamma\tilde{d}\dot{\tilde{d}} = \\ = -\frac{c_1}{2^\beta}V^\beta - \frac{k_1}{2}V + \tilde{d}\left(\gamma\dot{\tilde{d}} - \psi_1 \right). \quad (24)$$

The adaptive controller is determined based on $\dot{V}_{ad}$ being negative:

$$\dot{\hat{d}} = \gamma\psi_1. \quad (25)$$

The function (25) becomes:

$$\dot{V}_{ad} = -\frac{c_1}{2^\beta}V^\beta - \frac{k_1}{2}V \le 0. \quad (26)$$

According to the Lyapunov method and SCT, the controller (21) with the adaptive law (25) ensures that the system (7) is asymptotically stable. The block diagram of the control system with the finite-time adaptive controller for the FJM is shown in Fig. 2.

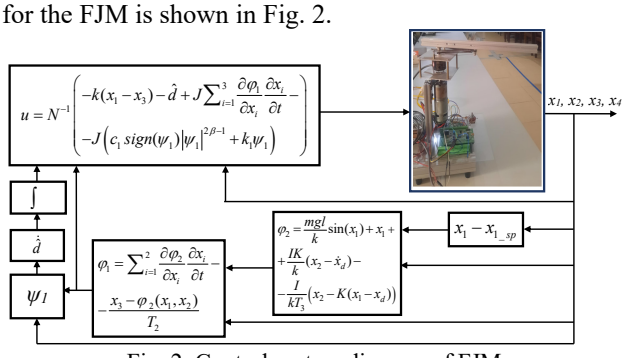

Fig. 2. Control system diagram of FJM

3. Results and discussion. In this section, to verify the effectiveness of the SCT law for flexible joints in the presence of input disturbances, different cases are conducted on numerical simulations and on the experimental model.

3.1 Simulation results. In the simulation, the FJM system is controlled according to the adaptive synergetic controller (21) implemented in MATLAB software. The model parameter values used in the simulation include: m = 0.25 kg; k = 20 N·m/rad; J = 1 kg·m^2; I = 0.2 kg·m^2; g = 9.81 m/s^2; l = 0.35 m; N = 30 N·m/V. The parameters of the proposed control law (23) are as follows: K = –90; T_2 = 0.12; T_3 = 0.12; c_1 = 100; β = 0.9; k_1 = 100; γ = 0.01. The input disturbance d = 50 N·m. The simulation process of implementing the proposed finite-time adaptive synergetic control law is carried out with 2 cases: the first case, where the initial state of the system is at the origin $x_1 = 0$; $x_2 = 0$; $x_3 = 0$; $x_4 = 0$ moving to position $x_{1\text{–}sp} = \pi/2$; $x_{2\text{–}sp} = 0$; $x_{3\text{–}sp} = \pi/2$; $x_{4\text{–}sp} = 0$ in the first 5 s, and in the next 5 s, it moves to position $x_{1\text{–}sp} = -\pi/2$; $x_{2\text{–}sp} = 0$; $x_{3\text{–}sp} = -\pi/2$; $x_{4\text{–}sp} = 0$. The second case, where the initial position of the system is $x_1 = 0$; $x_2 = 0$; $x_3 = 0$; $x_4 = 0$ and then the link q_1 tracks the desired trajectory signal in the form $x_{1\text{–}sp} = \cos\omega t$ with the angular frequency ω = 1 rad/s. The maximum voltage applied to the motor is 12 V.

In the first case, the results indicate that the angle response of link $q_1(x_{1\text{–}pro})$ and $q_2(x_{3\text{–}pro})$ compared to the set value $(x_{1\text{–}sp})$ are shown in Fig. 3. From the graph, we see that the response of link q_1 stabilizes to the desired value with times of 0.495 s and 0.509 s, respectively (Table 1). The response of link q_2 shows oscillations during the transient process. This indicates that the actuator control signal adjusts quickly to ensure the system is stable within the given time according to Lemma 1. The difference in angle response between the two links and the set value is due to input disturbances and the flexible connection between the two links. The angular velocity response of link $q_2(x_{4\text{–}pro})$ is faster than link $q_1(x_{2\text{–}pro})$ to reduce the oscillation of link q_1. The control signal is clearly changing during the transient process to ensure the tracking performance of link q_1. The control signal does not return to zero because of the existence of the input disturbance d.

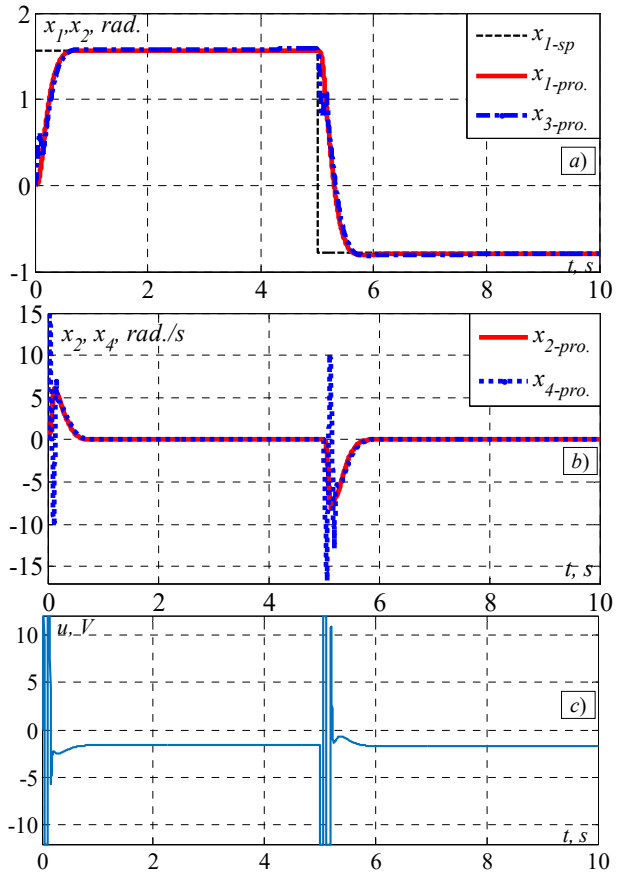

Fig. 3. Stability results in the first case with input disturbance: *a* – angle response; *b* – angular velocity response; *c* – control input

Table 1

Control system performance indicators

x_1	Time 0–5, s			Time 5–10, s		
	T_s, s	$P.O.$, %	e_{ss}, rad	T_s, s	$P.O.$, %	e_{ss}, rad
	0,495	0	0	0.509	0.8	0

*T_s is the settling time; $P.O.$ is the percent overshoot; e_{ss} is the steady-state error.

In the second case, the results indicate that the angle response of link q_1 tracking the setpoint signal and the angle of q_2 are shown in Fig. 4. From the graph, we can see that the response of link q_1 tracks the desired trajectory after 0.52 s. The response of link q_2 shows oscillations during the transient process, but eventually tracks the setpoint angle. During the transient process, the angular response oscillations indicate a change in the rotation direction of link q_2 to cancel out the oscillations in link q_1. The control signal with oscillations during the transient process and then following the periodic value of the setpoint signal once tracking is achieved.

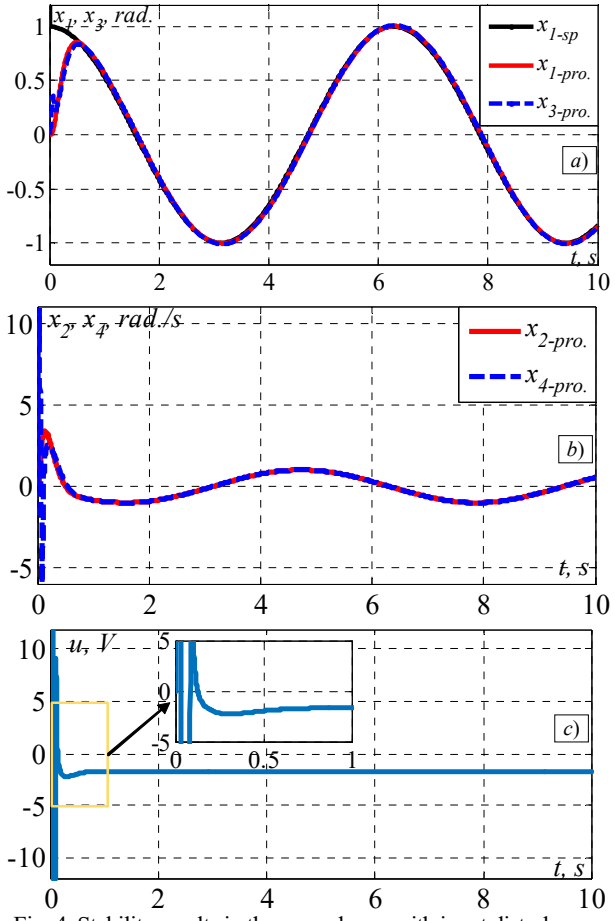

Fig. 4. Stability results in the second case with input disturbance: *a* – angle response; *b* – angular velocity response; *c* – control input

3.2 Experimental verification. To confirm the effectiveness of the proposed controller, experiments were conducted on the experimental model described in section 2 (Fig. 5). The control algorithms were implemented on STM32 cube IDE using C language with a sampling time of 2.5 ms. The experimental results of the proposed controller demonstrate the effectiveness of the proposed method without explicitly modeling the motor and input disturbances. In this case, model errors including of the motor and the controller, are inherent in the model. In the simulation section, these errors are considered as disturbance *d*. The dynamic parameters of the controller and the cases conducted are the same as in the simulation section.

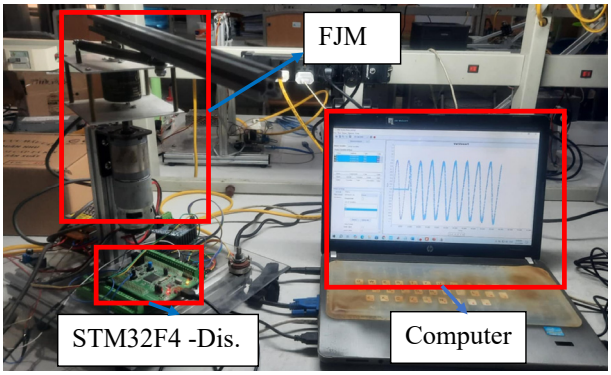

Fig. 5. Experimental platform FJM

The results presented in Fig. 6 show that the angle response of the FJM with the angle feedback of link q_1 stabilizes to the desired value. The angle response stabilizes to zero when the system is stable at the set value. The control signal supplied to the motor. Clearly, when stabilized at the balanced position, the voltage does not completely return to 0. This is due to various sources of disturbance such as friction, backlash in the gearbox, and joints, leading to the above errors. This also leads to the systems response not completely matching the simulation part.

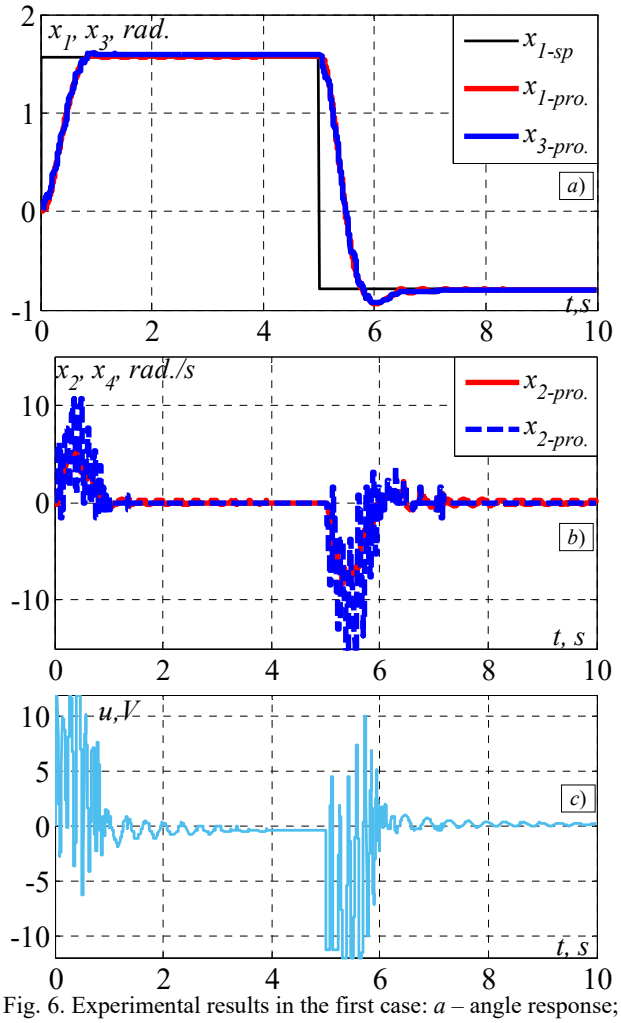

Fig. 6. Experimental results in the first case: *a* – angle response; *b* – angular velocity response; *c* – control input

The tracking performance on the experimental model is shown in Fig. 7. From the results, the angle of link q_1 tracks quite well. Besides, for the set-point signal in the form of an evaluation quantity, the response on the actual system is greatly affected by the motor with a gearbox. However, its results also show the possibility of realizing the controller appearing on real objects.

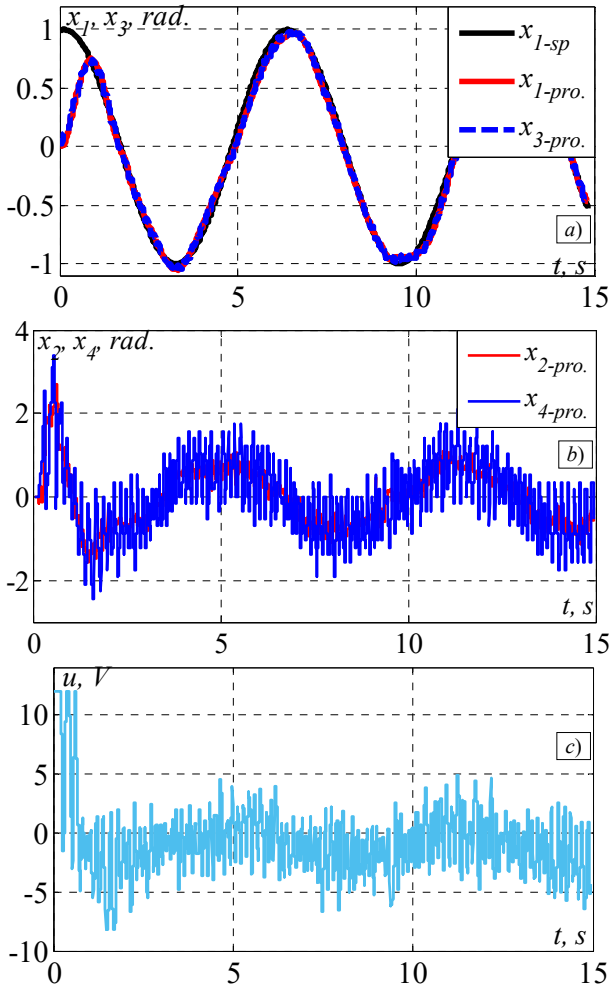

Fig. 7. Experimental results in the second case: *a* – angle response; *b* – angular velocity response; *c* – control input

4. Conclusions. The article presents the synthesis method of the finite-time adaptive synergetic control law for flexible joint systems. The synthesized control law ensures small system tracking errors and avoids oscillations. The finite-time characteristic is established based on the choice of the function equation. The developed adaptive law has well solved the problem of uncertainty in the mathematical model of the actuator and input disturbances. The stability of the system with the proposed control law is proven by the Lyapunov function. The simulation results of the proposed controller demonstrate its effectiveness. With two different tracking signal forms, the results show stability and tracking performance within a specified time. The results show that the system response has no oscillation and no overshoot. The proposed control law has been applied on the experimental model. Experimental results demonstrate the above tracking capability of the developed control method in the presence of input disturbances and without taking into account the mathematical model of the motor. Although the results on the actual system have limitations due to equipment quality and model uncertainty FJM, they also affirm the practical applicability of the control law. Finally, future researches will consider the effects of strong nonlinear disturbances from the actuator. It will also incorporate some modern theories such as fuzzy logic, neural networks, and nature-inspired optimization algorithms to fine-tune controller parameters and design the adaptive law.

Conflict of interest. The authors declare that they have no conflicts of interest.

REFERENCES

1. Spong M.W., Hutchinson S., Vidyasagar M. Robot Modeling and Control. *Industrial Robot*, 2006, vol. 33, no. 5, 403 p.. doi: https://doi.org/10.1108/ir.2006.33.5.403.1.

2. Wang Y., Guan Y., Li H. Observer-Based Finite-Time Sliding-Mode Control of Robotic Manipulator with Flexible Joint Using Partial States. *International Journal of Intelligent Systems*, 2023, vol. 2023, art. no. 8859892. doi: https://doi.org/10.1155/2023/8859892.

3. Yan Z., Lai X., Meng Q., Zhang P., Wu M. Tracking control of single-link flexible-joint manipulator with unmodeled dynamics and dead zone. *International Journal of Robust and Nonlinear Control*, 2021, vol. 31, no. 4, pp. 1270-1287. doi: https://doi.org/10.1002/rnc.5335.

4. Do T.-T., Vu V.-H., Liu Z. Linearization of dynamic equations for vibration and modal analysis of flexible joint manipulators. *Mechanism and Machine Theory*, 2022, vol. 167, art. no. 104516. doi: https://doi.org/10.1016/j.mechmachtheory.2021.104516.

5. Cheng X., Liu H. Bounded decoupling control for flexible-joint robot manipulators with state estimation. *IET Control Theory & Applications*, 2020, vol. 14, no. 16, pp. 2348-2358. doi: https://doi.org/10.1049/iet-cta.2019.1007.

6. Kivila A., Book W., Singhose W. Modeling spatial multi-link flexible manipulator arms based on system modes. *International Journal of Intelligent Robotics and Applications*, 2021, vol. 5, no. 3, pp. 300-312. doi: https://doi.org/10.1007/s41315-021-00201-3.

7. Kumar P., Pratiher B. Nonlinear dynamic analysis of a multi-link manipulator with flexible links-joints mounted on a mobile platform. *Advances in Space Research*, 2023, vol. 71, no. 5, pp. 2095-2127. doi: https://doi.org/10.1016/j.asr.2022.10.031.

8. Chiem N.X., Pham T.X., Thai P.D., Phan T.C. An Adaptive Sliding-mode Controller for Flexible-joint Manipulator. *2023 12th International Conference on Control, Automation and Information Sciences (ICCAIS)*, 2023, pp. 513-518. doi: https://doi.org/10.1109/ICCAIS59597.2023.10382364.

9. Wang L., Shi Q., Liu J., Zhang D. Backstepping control of flexible joint manipulator based on hyperbolic tangent function with control input and rate constraints. *Asian Journal of Control*, 2020, vol. 22, no. 3, pp. 1268-1279. doi: https://doi.org/10.1002/asjc.2006.

10. Gupta N., Pratiher B. Dynamic modeling and effective vibration reduction of dual-link flexible manipulators with two-stage cascade PID and active torque actuation. *Mechanism and Machine Theory*, 2025, vol. 205, art. no. 105867. doi: https://doi.org/10.1016/j.mechmachtheory.2024.105867.

11. Hu Y., Dian S., Guo R., Li S., Zhao T. Observer-based dynamic surface control for flexible-joint manipulator system with input saturation and unknown disturbance using type-2 fuzzy neural network. *Neurocomputing*, 2021, vol. 436, pp. 162-173. doi: https://doi.org/10.1016/j.neucom.2020.12.121.

12. Chang W., Li Y., Tong S. Adaptive Fuzzy Backstepping Tracking Control for Flexible Robotic Manipulator. *IEEE/CAA Journal of Automatica Sinica*, 2021, vol. 8, no. 12, pp. 1923-1930. doi: https://doi.org/10.1109/JAS.2017.7510886.

13. Tang W., Chen G., Lu R. A modified fuzzy PI controller for a flexible-joint robot arm with uncertainties. *Fuzzy Sets and Systems*, 2001, vol. 118, no. 1, pp. 109-119. doi: https://doi.org/10.1016/S0165-0114(98)00360-1.

14. Boussoffara M., Cheikh Ahmed I.B., Hajaiej Z. Sliding mode controller design: Stability analysis and tracking control for flexible joint manipulator. *Revue Roumaine Des Sciences Techniques Serie Electrotechnique et Energetique*, 2021, vol. 66, no. 3, pp. 161-167.

15. Nam D.P., Loc P.T., Huong N. Van, Tan D.T. A Finite-Time Sliding Mode Controller Design for Flexible Joint Manipulator Systems Based on Disturbance Observer. *International Journal of Mechanical Engineering and Robotics Research*, 2019, vol. 8, no. 4, pp. 619-625. doi: https://doi.org/10.18178/ijmerr.8.4.619-625.

16. Ali M., Mirinejad H. Robust tracking control of flexible manipulators using hybrid backstepping/nonlinear reduced-order active disturbance rejection control. *ISA Transactions*, 2024, vol. 149, pp. 229-236. doi: https://doi.org/10.1016/j.isatra.2024.04.026.

17. Zhang Y., Zhang M., Fan C., Li F. A Finite-Time Trajectory-Tracking Method for State-Constrained Flexible Manipulators Based on Improved Back-Stepping Control. *Actuators*, 2022, vol. 11, no. 5, art. no. 139. doi: https://doi.org/10.3390/act11050139.

18. Khan O., Mustafa G., Ashraf N., Hussain M., Khan A.Q., Shoaib M.A. Robust model predictive control of sampled-data Lipschitz nonlinear systems: Application to flexible joint robots. *European Journal of Control*, 2025, vol. 81, art. no. 101147. doi: https://doi.org/10.1016/j.ejcon.2024.101147.

19. Ding S., Peng J., Zhang H., Wang Y. Neural network-based adaptive hybrid impedance control for electrically driven flexible-joint robotic manipulators with input saturation. *Neurocomputing*, 2021, vol. 458, pp. 99-111. doi: https://doi.org/10.1016/j.neucom.2021.05.095.

20. Thang L.T., Son T.V., Khoa T.D., Chiem N.X. Synthesis of sliding mode control for flexible-joint manipulators based on serial invariant manifolds. *Bulletin of Electrical Engineering and Informatics*, 2023, vol. 12, no. 1, pp. 98-108. doi: https://doi.org/10.11591/eei.v12i1.4363.

21. Benbouhenni H., Lemdani S. Combining synergetic control and super twisting algorithm to reduce the active power undulations of doubly fed induction generator for dual-rotor wind turbine system. *Electrical Engineering & Electromechanics*, 2021, no. 3, pp. 8-17. doi: https://doi.org/10.20998/2074-272X.2021.3.02.

22. Cheng X., Zhang Y., Liu H., Wollherr D., Buss M. Adaptive neural backstepping control for flexible-joint robot manipulator with bounded torque inputs. *Neurocomputing*, 2021, vol. 458, pp. 70-86. doi: https://doi.org/10.1016/j.neucom.2021.06.013.

23. Khatir A., Bouchama Z., Benaggoune S., Zerroug N. Indirect adaptive fuzzy finite time synergetic control for power systems. *Electrical Engineering & Electromechanics*, 2023, no. 1, pp. 57-62. doi: https://doi.org/10.20998/2074-272X.2023.1.08.

24. Mahgoun M.S., Badoud A.E. New design and comparative study via two techniques for wind energy conversion system. *Electrical Engineering & Electromechanics*, 2021, no. 3, pp. 18-24. doi: https://doi.org/10.20998/2074-272X.2021.3.03.

25. Truong H.V.A., Phan V.Du, Tran D.T., Ahn K.K. A novel observer-based neural-network finite-time output control for high-order uncertain nonlinear systems. *Applied Mathematics and Computation*, 2024, vol. 475, art. no. 128699. doi: https://doi.org/10.1016/j.amc.2024.128699.

Received 25.10.2024
Accepted 26.01.2025
Published 02.05.2025

X.C. Nguyen [1], *Doctor of Automatic Control,*
D.T. Le[2], *PhD of Automatic Control,*
[1] Department of Automation and Computing Techniques,
Le Quy Don Technical University, Hanoi, Vietnam,
e-mail: chiemnx@mta.edu.vn (Corresponding Author)
[2] Control, Automation in Production and Improvement of Technology Institute (CAPITI), Hanoi, Vietnam,
e-mail: ledanhtuan@gmail.com

How to cite this article:
Nguyen X.C., Le D.T. Adaptive finite-time synergetic control for flexible-joint robot manipulator with disturbance inputs. *Electrical Engineering & Electromechanics*, 2025, no. 3, pp. 45-52. doi: https://doi.org/10.20998/2074-272X.2025.3.07

UDC 621.314 https://doi.org/10.20998/2074-272X.2025.3.08

A. Ayada, D. Guiza, D. Ounnas, N. Tidjani

Design and control of a DC-DC buck converter using discrete Takagi-Sugeno fuzzy models

Introduction. *A DC-DC buck converter plays a crucial role in industrial applications by efficiently stepping down voltage levels to power various electronic components and systems. However, controlling a buck converter is challenging due to its inherently nonlinear behavior. This paper presents a novel fuzzy tracking control approach for the buck converter, based on the combination of time-discrete Takagi-Sugeno (T-S) fuzzy models and the concept of virtual desired variables (VDVs).* ***Originality****. This paper introduces an innovative fuzzy tracking control that integrates time-discrete T-S models and VDVs concept to develop an efficient digital controller.* ***Goal.*** *The proposed fuzzy control strategy aims to regulate the output voltage regardless of sudden change in setpoint, load variation and change in input voltage.* ***Methodology****. The proposed control strategy aims to regulate the output voltage of a DC-DC buck converter. The design starts with a discrete T-S fuzzy controller based on the nonlinear model of the buck converter. A nonlinear tracking controller is developed using a virtual reference model that incorporates the VDVs concept. System stability is analyzed via Lyapunov's method and expressed through linear matrix inequalities.* ***Results****. Simulation tests under varying conditions validate the accuracy and effectiveness of the controller in achieving superior voltage tracking performance. Comparative analysis with a conventional PID controller highlights faster dynamic response and better tracking, showcasing the advantages of the proposed approach.* ***Practical value****. The practical value of this research lies in the development of a robust voltage control strategy for DC-DC buck converters and the establishment of reliable and efficient electrical systems using discrete-time fuzzy T-S control. This work also opens up the prospect for future implementation in experimental prototypes.* References 30, table 2, figures 7.

Key words: **discrete-time Takagi–Sugeno fuzzy models, DC-DC buck converter, linear matrix inequalities.**

Вступ*. Понижуючий DC-DC перетворювач відіграє важливу роль у промисловості, ефективно знижуючи рівні напруги живлення різних електронних компонентів і систем. Однак управління понижуючим перетворювачем є складним завданням через його початковий нелінійний характер. У статті представлено новий підхід до управління нечітким відстеженням для понижуючого перетворювача, заснований на поєднанні дискретних за часом нечітких моделей Такагі-Сугено (T-S) та концепції бажаних віртуальних змінних (VDV).* ***Оригінальність****. У статті наведено інноваційний підхід до управління нечітким відстеженням, який поєднує дискретні за часом моделі T-S та концепцію VDV для розробки ефективного цифрового контролера.* ***Мета****. Запропонована стратегія нечіткого управління спрямована на регулювання вихідної напруги незалежно від раптової зміни уставки, зміни навантаження та зміни вхідної напруги.* ***Методологія****. Запропонована стратегія управління спрямована на регулювання вихідної напруги понижуючого DC-DC перетворювача. Проєктування починається з дискретного нечіткого контролера T-S на основі нелінійної моделі знижувального перетворювача. Нелінійний контролер відстеження розроблено з використанням віртуальної еталонної моделі, що включає концепцію VDV. Стійкість системи аналізується за допомогою методу Ляпунова та виражається через лінійні матричні нерівності.* ***Результати****. Тести моделювання в різних умовах підтверджують точність та ефективність контролера у досягненні високої продуктивності відстеження напруги. Порівняльний аналіз із традиційним PID-регулятором підкреслює швидшу динамічну реакцію та краще відстеження, демонструючи переваги запропонованого підходу.* ***Практична цінність*** *цього дослідження полягає у розробці надійної стратегії управління напругою для понижуючих DC-DC перетворювачів та створення надійних та ефективних електричних систем з використанням дискретного часу нечіткого управління T-S. Ця робота також відкриває перспективи майбутньої реалізації у експериментальних прототипах.* Бібл. 30, табл. 2, рис. 7.

Ключові слова: **дискретні нечіткі моделі Takagi–Sugeno, понижуючий DC-DC перетворювач, лінійні матричні нерівності.**

Introduction. A DC-DC buck converter is an electrical device designed to reduce a DC voltage level to a lower one. It plays a crucial role in contemporary electronics, facilitating effective power control and voltage regulation in many applications. Because of its user-friendly nature, exceptional effectiveness, and adaptability, as well as its ability to work independently and interact harmoniously with energy storage and renewable energy systems, it is used in a diverse array of fields, such as providing power for industrial and residential settings [1–5].

The DC-DC buck converter exhibits considerable nonlinearity and varies structurally throughout each switching period. These characteristics can pose challenges when designing the controller, rendering conventional linear control approaches such as P, PI and PID inadequate for ensuring satisfactory performance across a broad operational spectrum [6, 7]. To tackle this problem, several advanced nonlinear control design strategies have been suggested.

The authors in [8] suggest an active damping method to provide a virtual resistance, thereby modulating the buck converter's output voltage. Active damping offers system stability and results without further power loss, but it comes at the cost of lower output voltage. In [9], a nonlinear feedback linearization technique is introduced to control the buck converter's output voltage of a system that provides power to a constant load. This strong controller does not require a disturbance sensor. However, this approach has disadvantages, such as low precision and slow processing speed. The sliding mode controller's design simplicity and adaptability have established it as the most widely utilized controller [10] and [11]. Nevertheless, the benefits of these improvements are counteracted by an undesired occurrence referred to as «chattering», which involves oscillations with a specific frequency and amplitude. This phenomenon is widely recognized as the primary hindrance to achieving real-time implementation [12, 13].

The use of fuzzy logic control solved the shortcomings of the previous methods [14–17]. Nevertheless, this method sometimes lacks precision because it heavily depends on assumptions. Creating fuzzy rules and membership functions presents a tough task [18]. The authors in [19, 20] describe developing and implementing a robust fuzzy logic control for a DC-DC buck converter. This controller is designed to utilize measurements of the inductor current and output voltage but requires an additional sensor, which inevitably increases the cost and reduces the system's reliability. Several methods were proposed to address this problem based on Takagi-Sugeno (T-S) fuzzy models [21, 22].

T-S fuzzy model employs a collection of fuzzy rules to represent a nonlinear system by utilizing a series of local linear models seamlessly linked together by fuzzy membership functions. T-S fuzzy model has gained significant popularity due to its utilization of an affine dynamic model in its consequence section instead of a fuzzy set. It possesses the subsequent benefits:

1) Numerous established robust tools, such as the Lyapunov's method, can be employed for stability analysis and controller synthesis;

2) T-S fuzzy model is less affected by the problem of high dimensionality compared to other fuzzy models;

3) The structure of the model and the properties of local models can be readily linked to the physical characteristics of the system [23–25].

The accuracy of the mathematical model is crucial for designing a robust controller for the DC-DC buck converter. Thus, accurate modelling of switching DC-DC converters is needed to predict stability and design a suitable controller with enhanced stability and performance. There is currently a revived interest in discrete-time analysis and modeling to aid the implementation of practical digital control for high-frequency DC-DC converters on microcontroller boards. This is driven by the desire to eliminate delay effects in averaged models.

Goal. This paper deals with the design of a new controller for a buck converter system using T-S fuzzy models. The proposed fuzzy control strategy aims to regulate the output voltage, despite changes in reference voltage, load variations, and changes in input voltage. Many simulation tests were conducted under various load and input voltage situations to validate the precision and efficiency of the suggested controller in operating the DC-DC buck converter to drive the desired reference voltage.

Developed fuzzy control scheme. The objective of this work is to construct a T-S fuzzy controller capable of efficiently controlling buck converter states $x = [i_L\ v_o]^T$ to track a specific trajectory $x = [i_{Ld}\ v_{od}]^T$. At first, we construct a digital fuzzy controller utilizing the discrete-time T-S fuzzy model of a buck converter system. Afterward, we create a virtual reference model and a nonlinear controller that drives the considered system to track the desired voltage. The proposed control scheme is illustrated in Fig 1.

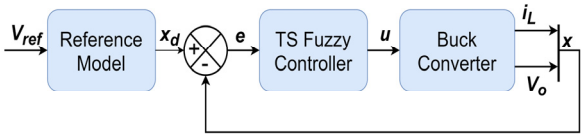

Fig. 1. Proposed fuzzy tracking control scheme

Nonlinear state space system model. Figure 2 depicts the buck converter's schematic, illustrating the components such as the input voltage V_{in}, electronic switch (MOSFET), diode D, capacitor C, load resistor R and inductor L.

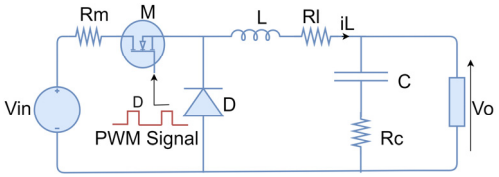

Fig. 2. Schematic representation of a DC-DC buck converter

To represent the buck converter, we use the nonlinear state space system form shown below [21]:

$$\begin{cases} \dot{x}(t) = f(x(t))x(t) + g(x(t))u(t) + \delta; \\ y(t) = \varphi(x(t)), \end{cases} \tag{1}$$

where

$$x(t) = \begin{bmatrix} i_L(t) \\ v_o(t) \end{bmatrix}, \delta = \begin{bmatrix} -\frac{V_D}{L} \\ 0 \end{bmatrix}, \quad g(x(t)) = \begin{bmatrix} \frac{1}{L}v_{in} + v_D - R_M i_L(t) \\ 0 \end{bmatrix};$$

$$f(x(t)) = \begin{bmatrix} -\frac{1}{L}\left(R_L + \frac{RR_c}{R+R_c}\right)i_L(t) - \frac{R}{L(R+R_c)}v_o(t) \\ \left(\frac{R}{C(R+R_c)}\right)i_L(t) - \left(\frac{1}{C(R+R_c)}\right)v_o(t) \end{bmatrix};$$

$$\varphi(x(t)) = \left(\frac{RR_c}{R+R_c}\right)i_L(t) + \left(\frac{R}{R+R_c}\right)v_o(t),$$

where R_L is the inductor's winding resistance; V_D is the diode's threshold voltage; R_C is the filter capacitor's equivalent series resistance; R_M is the transistor's resistance (MOSFET). Current flowing through the inductance, voltage at the output, and duty ratio are represented by the variables i_L, v_o and u, correspondingly.

Discreet-time T-S fuzzy model. The creation of the suggested T-S fuzzy controller necessitated the conversion of the nonlinear model into a fuzzy model, utilizing the current of inductance i_L as the decision variable. The nonlinear state space of the buck converter is expressed in a nonlinear manner:

$$\begin{cases} \dot{x} = A_c x(t) + B_c(i_L)u(t) + E_c; \\ y(t) = v_o = C_c x(t), \end{cases} \tag{2}$$

where

$$A_c = \begin{bmatrix} -\frac{1}{L}\left(R_L + \frac{RR_c}{R+R_c}\right) & -\frac{R}{L(R+R_c)} \\ \frac{R}{C(R+R_c)} & -\frac{1}{C(R+R_c)} \end{bmatrix}; E_c = \begin{bmatrix} -\frac{V_D}{L} \\ 0 \end{bmatrix};$$

$$C_c = \begin{bmatrix} \frac{RR_c}{R+R_c} & \frac{R}{R+R_c} \end{bmatrix}; B_c(i_L) = \begin{bmatrix} \frac{1}{L}(V_{in} + V_D - R_M i_L(t)) \\ 0 \end{bmatrix}.$$

The suggested control strategy necessitates a discrete-time model, which can be obtained from the nonlinear model of the system. This is done assuming that the switching period is significantly less than the time constants of the buck converter circuit. The forward Euler approximation is used to derive the following discrete-time model:

$$\begin{cases} x(k+1) = (I + T_s A_c)x(k) + T_s B_c u(k) + T_s E_c; \\ y(k) = T_s C_c x(k). \end{cases} \tag{3}$$

The T-S discrete-time state-space model of the buck converter can be derived based on this assumption:

$$\begin{cases} x(k+1) = A_d x(k) + B_d u(k) + E_d; \\ y(k) = C_d x(k), \end{cases} \tag{4}$$

where

$$x(k) = \begin{bmatrix} i_L(k) \\ v_o(k) \end{bmatrix}; E_d = \begin{bmatrix} -\frac{T_s V_D}{L} \\ 0 \end{bmatrix};$$

$$A_d=\begin{bmatrix}1-\frac{1}{L}\left(R_L+\frac{RR_c}{R+R_c}\right)T_s & -\frac{RT_s}{L(R+R_c)}\\ \frac{RT_s}{C(R+R_c)} & 1-\frac{T_d}{C(R+R_c)}\end{bmatrix};$$

$$B_d(i_L(k))=\begin{bmatrix}\frac{T_s}{L}(V_{in}+V_D-R_M i_L(k))\\ 0\end{bmatrix};\ C_d=\begin{bmatrix}\frac{T_sRR_c}{R+R_c} & \frac{T_sR}{R+R_c}\end{bmatrix}.$$

Suppose the premise variable $z(k) = i_L(k)$ has borders as: $\underline{i_L} \le i_L \le \overline{i_L}$. In addition, by using the sector nonlinearity transformation [26], the nonlinear system given by (1) can be accurately indicated by a discrete T-S fuzzy model with the inclusion of the subsequent two *If-Then* rules:

$$\begin{aligned}&Rule\ 1: IF\ i_L\ is\ F_{11}\ THEN\\ &\begin{cases}x(k+1)=A_1x(k)+B_1u(k)+E_1;\\ y=C_1x(k).\end{cases}\\ &Rule\ 2: IF\ i_L\ is\ F_{12}\ THEN\\ &\begin{cases}x(k+1)=A_2x(k)+B_2u(k)+E_2;\\ y=C_2x(k).\end{cases}\end{aligned}\tag{5}$$

The membership functions F_{11} and F_{12} are obtained by:

$$F_{11}=\frac{i_L(k)-\underline{i_L}}{\overline{i_L}-\underline{i_L}};\quad F_{12}(i_L)=1-F_{11}.\tag{6}$$

The ultimate result of the fuzzy model is deduced in the following manner:

$$\begin{cases}x(k+1)=\sum_{i=1}^{r}h_i(z(k))(A_ix(k)+B_iu(k)+E);\\ y(k)=\sum_{i=1}^{r}h_i(z(k))C_ix(k),\end{cases}\tag{7}$$

where

$$A_1=A_2=\begin{bmatrix}1-\frac{1}{L}\left(R_L+\frac{RR_c}{R+R_c}\right)T_s & -\frac{RT_s}{L(R+R_c)}\\ \frac{RT_s}{C(R+R_c)} & 1-\frac{T_d}{C(R+R_c)}\end{bmatrix};$$

$$B_1=\begin{bmatrix}\frac{T_s}{L}(V_{in}+V_D-R_M\overline{i_L})\\ 0\end{bmatrix};\ B_2=\begin{bmatrix}\frac{T_s}{L}(V_{in}+V_D-R_M\underline{i_L})\\ 0\end{bmatrix};$$

$$C_1=C_2=\begin{bmatrix}\frac{T_sRR_c}{R+R_c} & \frac{T_sR}{R+R_c}\end{bmatrix};\ E_1=E_2=\begin{bmatrix}\frac{-T_sV_D}{L}\\ 0\end{bmatrix};$$

$$h_i(z)=\omega_i(z)/\sum_{i=1}^{r}\omega_i(z);\ \omega_i(z)=\prod_{j=1}^{n}F_{ij}(z_j);$$

$$\text{for all } k>0,\ h_i(z)\ge 0 \text{ and } \sum_{i=1}^{r}h_i(z)=1.$$

Control design and stability analysis. The following requirements must be met to design T-S fuzzy control:

$$x(k)-x_d(k)\to 0 \text{ as } k\to\infty,\tag{8}$$

where $x_d(k)$ is the desired trajectory variable.

Let us establish the tracking error as:

$$\tilde{x}(k)=x(k)-x_d(k).$$

Subsequently, its equivalent discrete-time derivative can be expressed as:

$$\tilde{x}(k+1)=x(k+1)-x_d(k+1).\tag{9}$$

By replacing (7) with (9) and including the term:

$$\sum_{i=1}^{r}h_i(z)A_i\left(x_d(k)-x_d(k)\right).\tag{10}$$

The first equation of (7) becomes:

$$\tilde{x}(k+1)=\sum_{i=1}^{r}h_i(z)(A_i\tilde{x}(k)+B_iu(k)+A_ix_d(k)+E_i)-x_d(k+1).\tag{11}$$

Let's select a new control variable for (11) that meets the requirements listed below:

$$\sum_{i=1}^{r}h_iB_i\lambda(k)=\sum_{i=1}^{r}h_i(z)(A_ix_d(k)+B_iu(k)+E_i)-x_d(K+1).\tag{12}$$

By employing (12), the discrete derivative of the tracking error, as expressed in (11), can be reformulated in a following manner:

$$\tilde{x}(k+1)=\sum_{i=1}^{r}h_i(i_L(k))(A_i\tilde{x}(k)+B_i\lambda(k)).\tag{13}$$

The fuzzy tracking control problem is addressed by the novel controllers, which are designed to:

- Controller rule 1: If i_L is F_{11} Then $\lambda(k)=K_1\tilde{x}(k)$;
- Controller rule 2: If i_L is F_{12} Then $\lambda(k)=K_2\tilde{x}(k)$.

The final output of the fuzzy controller is as follows:

$$\lambda(k)=\sum_{i=1}^{r}h_i(z(k))K_i\tilde{x}(k).\tag{14}$$

The closed-loop system is represented as follows by substituting (14) into (13):

$$\tilde{x}(k+1)=\sum_{i=1}^{r}\sum_{j=1}^{r}h_i(z)h_j(z)(A_i-B_iK_j)\tilde{x}(k).\tag{15}$$

By permitting $G_{ij} = (A_i - B_iK_j)$, equation (15) can be restated in the following manner:

$$\tilde{x}(k+1)=\sum_{i=1}^{r}\sum_{j=1}^{r}h_i(z)h_j(z)G_{ij}\tilde{x}(k).\tag{16}$$

Stability analysis. The process of acquiring the fuzzy controller involves identifying the gains that meet the conditions stated in the subsequent theorem [27]:

Theorem 1. The system represented by (16) achieves global asymptotic stability if there exist matrices $X=X^T>0, S_{ii}=S_{ii}^T, S_{ij}=S_{ij}^T, Y_i$, verifying the following linear matrix inequalities: $\forall i,j\in\{1,.....r\}$:

$$\begin{bmatrix}-X+S_{ii} & XA_i^T+Y_i^TB_i^T\\ A_iX+B_iY_i & -X\end{bmatrix}<0;\tag{17}$$

$$\begin{bmatrix}-2X+S_{ij}+S_{ij}^T & XA_i^T+Y_j^TB_i^T+XA_j^T+Y_i^TB_j^T\\ * & -2X\end{bmatrix}<0, i<j;\tag{18}$$

$$\begin{bmatrix}S_{11} & S_{12} & \cdots & S_{1r}\\ S_{12} & S_{22} & \cdots & S_{2r}\\ \vdots & \ddots & \vdots & .\\ S_{1r} & S_{2r} & \cdots & S_{rr}\end{bmatrix}>0.\tag{19}$$

The gains of the control law are: $K_i = Y_iX^{-1}$.

Virtual desired variables and control law. The virtual desired variables and tracking control law for the buck converter system may be determined by (12), which can be expressed in the following manner:

$$\sum_{i=1}^{r} h_i B_i (u(k) - \lambda(k)) = -\sum_{i=1}^{r} h_i A_i x_d(k) - \sum_{i=1}^{r} h_i E_i + x_d(k+1). \quad (20)$$

Let's define aggregated matrices as follows:

$$B = \sum_{i=1}^{r} h_i(z) B_i, A = \sum_{i=1}^{r} h_i(z) A_i, E = \sum_{i=1}^{r} h_i(z) E_i. \quad (21)$$

Subsequently, equation (20) can be restated in a concise manner as:

$$B(u(k) - \lambda(k)) = -A x_d(k) - E + x_d(k+1). \quad (22)$$

By applying (22) to the buck converter model, we obtain the following matrix form:

$$\begin{bmatrix} \frac{T_s}{L}(V_{in} + V_D - R_M i_L(k)) \\ 0 \end{bmatrix} [u(k) - \lambda](k) =$$

$$= -\begin{bmatrix} 1 - \frac{1}{L}\left(R_L + \frac{RR_c}{R+R_c}\right)T_s & -\frac{RT_s}{L(R+R_c)} \\ \frac{RT_s}{C(R+R_c)} & 1 - \frac{T_s}{C(R+R_c)} \end{bmatrix} \begin{bmatrix} i_{Ld}(k) \\ v_{od}(k) \end{bmatrix} - \quad (23)$$

$$- \begin{bmatrix} -\frac{T_s V_D}{L} \\ 0 \end{bmatrix} + \begin{bmatrix} i_{Ld}(k+1) \\ v_{od}(k+1) \end{bmatrix}.$$

From (23) it can be extracted the reference inductor current as:

$$i_{Ld}(k) = \frac{\left(1 - \frac{T_s}{C(R+R_C)}\right) v_{od}(k) + v_{od}(k+1)}{\frac{RT_s}{C(R+R_C)}}. \quad (24)$$

Also from (23) it can be extracted the tracking control law as:

$$u(k) = \frac{\left(\frac{T_s}{L}\left(R_L + \frac{RR_C}{R+R_C}\right) - 1\right) i_{Ld}(k) + \frac{RT_s}{L(R+R_C)} v_{od}(k)}{\frac{T_s}{L}(V_m + V_D - R_M i_L(k))} + \quad (25)$$

$$+ \frac{\frac{T_s V_D}{L} + i_{Ld}(k+1)}{\frac{T_s}{L}(V_m + V_D - R_M i_L(k))} + \lambda(k).$$

Simulation results. Several simulation tests were carried out at different load and input voltage conditions to prove the accuracy of the suggested controller for a DC-DC buck converter. The used parameters are shown in Table 1.

Table 1

Buck converter parameters

Parameter	Values
MOSFET resistance R_m, Ω	0.1
Threshold voltage of the diode V_D, V	0.8
Output capacitor C, μF	270
Output capacitor resistance R_C, Ω	0.18
Inductor L, μH	180
Winding resistance of inductor R_L, Ω	0.1
Resistance load R, Ω	25
Input voltage V_{in}, V	12
Switching frequency f, kHz	31

The first test used a constant reference voltage of 6 V. The output voltage, inductor current, duty ratio and PWM signal responses are depicted in Fig. 3,*a–d*, respectively.

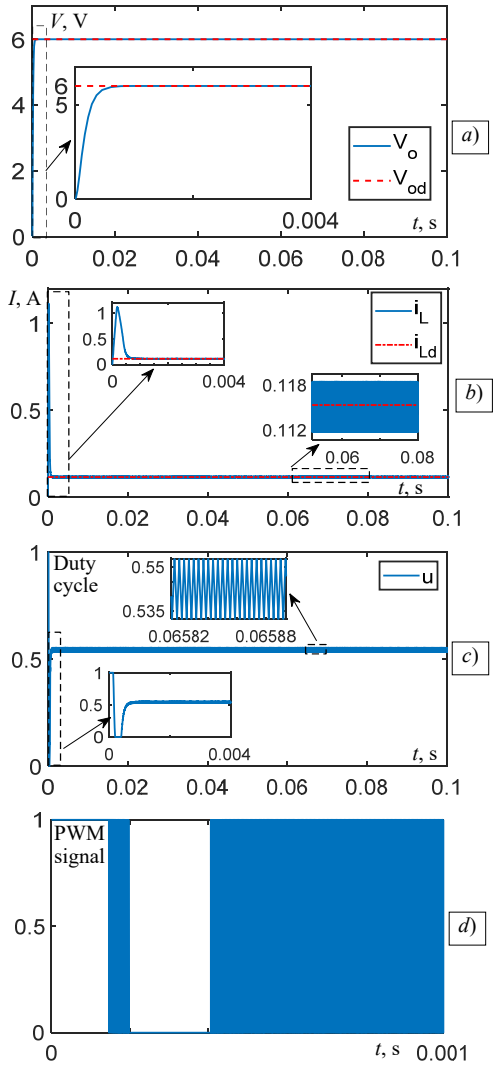

Fig. 3. Simulation results for a fix reference voltage: *a* – output voltage; *b* – inductor current voltage; *c* – duty ratio; d – PWM signal

These results show that the output voltage precisely follows the wished trajectory. Additionally, it has been demonstrated that the time necessary for the system to respond to the reference model is brief, specifically 0.4 ms.

In the second test, a variable reference voltage was used. The output voltage, inductor current, and duty ratio responses are depicted in Fig. 4,*a–c*, respectively. From these results, we notice that despite the random change in the chosen voltage, the output voltage always follows the desired voltage with a minimal response time and limitation of overshoot.

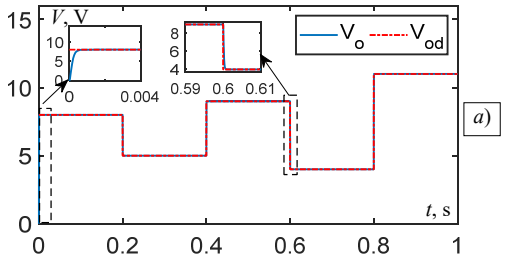

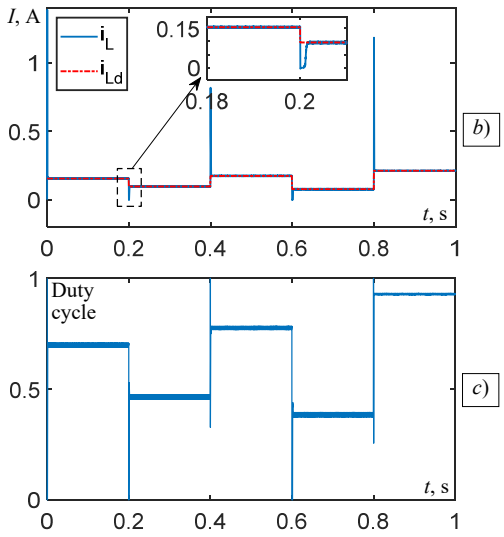

Fig. 4. Simulation results for variable reference voltages: *a* – output voltage; *b* – inductor current voltage; *c* – duty ratio

In the third test, another scenario is used to prove the effectiveness of the proposed controller. A variable voltage is applied to the input of the buck converter, and observing of the response of the output voltage. Figure 5 shows the output voltage response under input voltage variations. Initially, the input voltage was set to 12 V, and the desired output voltage was set to a constant 8 V at t = 15 ms. These results show that the output voltage matches the chosen level quickly and remains constant even when the input voltage changes.

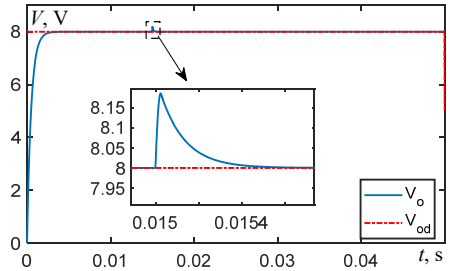

Fig. 5. Responses of the output voltage for input voltage variable

In the fourth test, we randomly changed the load resistance value and noted the output voltage response and how well it followed the desired voltage (Fig. 6).

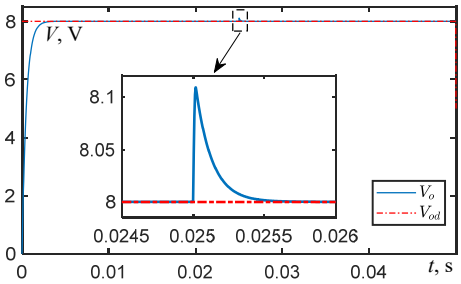

Fig. 6. Responses for resistor load variable

In the next scenario, the reference voltage is kept at 8 V. At time t = 0 s, the converter functions with a load resistance of 25 Ω. Then, at time t = 2.5 ms, the load resistance is modified to 30 Ω. The overshoot in a transient condition is observed to be brief. Subsequently, the output voltage remains constant at 8 V. The results produced by the T-S fuzzy controller, in the last test, are compared to those obtained by the PID controller [28–30] (Fig. 7).

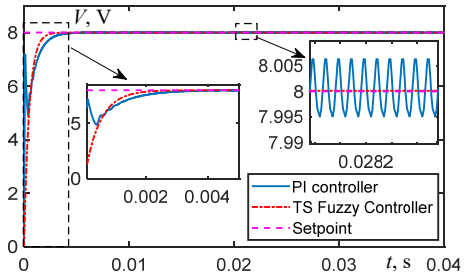

Fig. 7. Performances comparison between PID and T-S controllers

Table 2 presents the comparison results. The performances of the both controllers are evaluate based on the specified parameters of overshoot (efficiency), settling time (accuracy and stability), and rise time (speed).

Table 2

Results of the comparison and evaluation between T-S fuzzy and PID controllers

Method	PID controller	Proposed method
Overshoot, %	0	0
Settling time, ms	4	25
Rise time, ms	28	2

The comparison results indicate that the developed controller provides superior performance and a faster response compared to the conventional PID controller, which has numerous drawbacks, such as a slow response to accurately track the required voltage and significant oscillations around the desired voltage, particularly during variations in the resistor load and input voltage.

Conclusions. This paper presents the control of the output voltage of a DC-DC buck converter. A discrete-time T-S fuzzy model is used to represent the considered system's dynamic and then employed to develop a fuzzy controller. The concept of virtual desired variables is used to extract the desired reference model and nonlinear control law. Sufficient conditions for stability are derived from Lyapunov's method, and then they are converted into linear matrix inequalities to find the controller gains. The simulation results show that the proposed control can drive the output voltage to track its reference exactly with a shorter response time and without any overshooting. A comparison of the suggested controller with the conventional PID shows its superiority in terms of time response and tracking. Exploring practical application and robustness challenges will take center stage in an upcoming research endeavor.

Conflict of interest. The authors declare that they have no conflicts of interest.

REFERENCES

1. Lahiouel Y., Latreche S., Khemliche M., Boulemzaoud L. Photovoltaic fault diagnosis algorithm using fuzzy logic controller based on calculating distortion ratio of values. *Electrical Engineering & Electromechanics*, 2023, no. 4, pp. 40-46. doi: https://doi.org/10.20998/2074-272X.2023.4.06.

2. Bonela A.K., Sarkar M.K., Kumar K. Robust non-fragile control of DC–DC buck converter. *Electrical Engineering*, 2024, vol. 106, no. 1, pp. 983-991. doi: https://doi.org/10.1007/s00202-023-02017-9.

3. Khavari F., Ghamari S.M., Abdollahzadeh M., Mollaee H. Design of a novel robust type-2 fuzzy-based adaptive backstepping controller optimized with antlion algorithm for buck converter. *IET Control Theory & Applications*, 2023, vol. 17, no. 9, pp. 1132-1143. doi: https://doi.org/10.1049/cth2.12445.

4. Benazza B., Bendaoud A., Slimani H., Benaissa M., Flitti M., Zeghoudi A. Experimental study of electromagnetic disturbances in common and differential modes in a circuit based on two DC/DC boost static converter in parallel. *Electrical Engineering & Electromechanics*,

2023, no. 4, pp. 35-39. doi: https://doi.org/10.20998/2074-272X.2023.4.05.
5. Alam Z., Roy T.K., Ghosh S.K., Mahmud M.A. A hybrid non-linear voltage controller design for DC–DC buck converters. *The Journal of Engineering*, 2023, vol. 2023, no. 10, art. no. e12318. doi: https://doi.org/10.1049/tje2.12318.
6. Ounnas D., Guiza D., Soufi Y., Dhaouadi R., Bouden A. Design and Implementation of a Digital PID Controller for DC–DC Buck Converter. *2019 1st International Conference on Sustainable Renewable Energy Systems and Applications (ICSRESA)*, 2019, no. 1-4. doi: https://doi.org/10.1109/ICSRESA49121.2019.9182430.
7. Nanyan N.F., Ahmad M.A., Hekimoğlu B. Optimal PID controller for the DC-DC buck converter using the improved sine cosine algorithm. *Results in Control and Optimization*, 2024, vol. 14, art. no. 100352. doi: https://doi.org/10.1016/j.rico.2023.100352.
8. Wu M., Lu D. D.-C. An active damping method for stabilization of cascaded connected two stage converter systems with constant power loads in DC microgrids. *2014 IEEE International Symposium on Circuits and Systems (ISCAS)*, 2014, pp. 2664-2667. doi: https://doi.org/10.1109/ISCAS.2014.6865721.
9. Li X., Chen X. A Multi-Index Feedback Linearization Control for a Buck-Boost Converter. *Energies*, 2021, vol. 14, no. 5, art. no. 1496. doi: https://doi.org/10.3390/en14051496.
10. Kaplan O., Bodur F. Second-order sliding mode controller design of buck converter with constant power load. *International Journal of Control*, 2023, vol. 96, no. 5, pp. 1210-1226. doi: https://doi.org/10.1080/00207179.2022.2037718.
11. Cheng Y., Wen G., Du H. Design of Robust Discretized Sliding Mode Controller: Analysis and Application to Buck Converters. *IEEE Transactions on Industrial Electronics*, 2020, vol. 67, no. 12, pp. 10672-10681. doi: https://doi.org/10.1109/TIE.2019.2962473.
12. Guiza D., Ounnas D., Soufi Y., Bouden A. DC-DC Buck Converter Control Improvement. *2021 18th International Multi-Conference on Systems, Signals & Devices (SSD)*, 2021, pp. 1419-1424. doi: https://doi.org/10.1109/SSD52085.2021.9429371.
13. Elhajji Z., Dehri K., Bouchama Z., Nouri A.S., Essounbouli N. Robustness analysis of a discrete integral sliding mode controller for dc-dc buck converter using input-output measurement. *Studies in Systems, Decision and Control*, 2023, vol. 474, pp. 273-284. doi: https://doi.org/10.1007/978-981-99-3463-8_11.
14. Hamdi R., Hadri Hamida A., Bennis O. On modeling and real-time simulation of a robust adaptive controller applied to a multicellular power converter. *Electrical Engineering & Electromechanics*, 2022, no. 6, pp. 48-52. doi: https://doi.org/10.20998/2074-272X.2022.6.08.
15. Bhat N.D., Kanse D.B., Patil S.D., Pawar S.D. DC/DC Buck Converter Using Fuzzy Logic Controller. *2020 5th International Conference on Communication and Electronics Systems (ICCES)*, 2020, pp. 182-187. doi: https://doi.org/10.1109/ICCES48766.2020.9138084.
16. Aissaoui M., Bouzeria H., Benidir M., Labed M.A. Harmonics suppression in high-speed railway via single-phase traction converter with an LCL filter using fuzzy logic control strategy. *Electrical Engineering & Electromechanics*, 2024, no. 2, pp. 16-22. doi: https://doi.org/10.20998/2074-272X.2024.2.03.
17. Nebti K., Lebied R. Fuzzy maximum power point tracking compared to sliding mode technique for photovoltaic systems based on DC-DC boost converter. Electrical Engineering & Electromechanics, 2021, no. 1, pp. 67-73. doi: https://doi.org/10.20998/2074-272X.2021.1.10.
18. Ghamari S.M., Narm H.G., Mollaee H. Fractional-order fuzzy PID controller design on buck converter with antlion optimization algorithm. *IET Control Theory & Applications*, 2022, vol. 16, no. 3, pp. 340-352. doi: https://doi.org/10.1049/cth2.12230.
19. Swathy K., Jantre S., Jadhav Y., Labde S.M., Kadam P. Design and Hardware Implementation of Closed Loop Buck Converter Using Fuzzy Logic Controller. *2018 Second International Conference on Electronics, Communication and Aerospace Technology (ICECA)*, 2018, pp. 175-180. doi: https://doi.org/10.1109/ICECA.2018.8474570.
20. Pamuji F.A., Prakosa P.R., Suryoatmojo H., Arumsari N., Effendi M.K., Sudarmanta B., Prasetio K.D. Design and Implementation of Buck Boost Converter for fuzzy Logic Controller Based DC Motor Speed Control. *Przeglad Elektrotechniczny*, 2024, no. 4, pp. 60-66. doi: https://doi.org/10.15199/48.2024.04.12.
21. Guiza D., Soufi Y., Ounnas D., Metatla A. Design and Implementation of Takagi-Sugeno Fuzzy Tracking Control for a DC-DC Buck Converter. *Advances in Electrical and Electronic Engineering*, 2019, vol. 17, no. 3, pp. 234-243 doi: https://doi.org/10.15598/aeee.v17i3.3126.
22. Torres-Pinzón C.A., Paredes-Madrid L., Flores-Bahamonde F., Ramirez-Murillo H. LMI-Fuzzy Control Design for Non-Minimum-Phase DC-DC Converters: An Application for Output Regulation. *Applied Sciences*, 2021, vol. 11, no. 5, art. no. 2286. doi: https://doi.org/10.3390/app11052286.
23. Larbi M., Guechi E.H., Maidi A., Ounnas D., Belharet K. Observer-based 2D tracking control for a vascular microrobot based on the T-S fuzzy model. *International Journal of Automation and Control*, 2023, vol. 17, no. 6, pp. 573-594. doi: https://doi.org/10.1504/IJAAC.2023.134551.
24. Gotz J.D., Bigai M.H., Harteman G., Martins M.S.R., Converti A., Siqueira H.V., Borsato M., Corrêa F.C. Design of a Takagi–Sugeno Fuzzy Exact Modeling of a Buck–Boost Converter. *Designs*, 2023, vol. 7, no. 3, art. no. 63. doi: https://doi.org/10.3390/designs7030063.
25. Moussaoui L., Aouaouda S., Rouaibia R. Fault tolerant control of a permanent magnet synchronous machine using multiple constraints Takagi-Sugeno approach. *Electrical Engineering & Electromechanics*, 2022, no. 6, pp. 22-27. doi: https://doi.org/10.20998/2074-272X.2022.6.04.
26. Ounnas D., Ramdani M., Chenikher S., Bouktir T. An Efficient Maximum Power Point Tracking Controller for Photovoltaic Systems Using Takagi–Sugeno Fuzzy Models. *Arabian Journal for Science and Engineering*, 2017, vol. 42, no. 12, pp. 4971-4982. doi: https://doi.org/10.1007/s13369-017-2532-0.
27. Xiaodong L., Qingling Z. New approaches to H∞ controller designs based on fuzzy observers for T-S fuzzy systems via LMI. *Automatica*, 2003, vol. 39, no. 9, pp. 1571-1582. doi: https://doi.org/10.1016/S0005-1098(03)00172-9.
28. Latreche K., Taleb R., Bentaallah A., Toubal Maamar A.E., Helaimi M., Chabni F. Design and experimental implementation of voltage control scheme using the coefficient diagram method based PID controller for two-level boost converter with photovoltaic system. *Electrical Engineering & Electromechanics*, 2024, no. 1, pp. 3-9. doi: https://doi.org/10.20998/2074-272X.2024.1.01.
29. Gopal Reddy S., Ganapathy S., Manikandan M. Power quality improvement in distribution system based on dynamic voltage restorer using PI tuned fuzzy logic controller. *Electrical Engineering & Electromechanics*, 2022, no. 1, pp. 44-50. doi: https://doi.org/10.20998/2074-272X.2022.1.06.
30. Hassainia S., Ladaci S., Kechida S., Khelil K. Impact of fractional filter in PI control loop applied to induction motor speed drive. *Electrical Engineering & Electromechanics*, 2022, no. 5, pp. 14-20. doi: https://doi.org/10.20998/2074-272X.2022.5.03.

Received 09.11.2024
Accepted 29.01.2025
Published 02.05.2025

A. Ayada[1], *PhD Student,*
D. Guiza[2], *Professor,*
D. Ounnas[2], *Professor,*
N. Tidjani[3], *Professor,*
[1] Laboratory of Mathematics, Informatics and Systems, Tebessi University, Algeria,
e-mail: amira.ayada@univ-tebessa.dz
[2] LABGET Laboratory, Department of Electrical Engineering, Larbi Tebessi University, Algeria,
e-mail: dhaouadi.guiza@univ-tebessa.dz;
djamel.ounnas@univ-tebessa.dz (Corresponding Author)
[3] Department of Electronics, Saad Dahlab University, Algeria,
e-mail: n.tidjani@univ-dbkm.dz

How to cite this article:
Ayada A., Guiza D., Ounnas D., Tidjani N. Design and control of a DC-DC buck converter using discrete Takagi-Sugeno fuzzy models. *Electrical Engineering & Electromechanics*, 2025, no. 3, pp. 53-58. doi: https://doi.org/10.20998/2074-272X.2025.3.08

UDC 621.314 https://doi.org/10.20998/2074-272X.2025.3.09

B. Dwinanto, Setiyono, F. Thalib, H. Siswono

Single-phase power shunt active filter design using photovoltaic as reactive power compensator

Introduction. *The rapid production of electronic equipment circulating and used by the public has resulted in a decline in the power quality in the power system.* ***The goal*** *of the article is to build a parallel active filter for reactive power compensation in a single-phase power system using photovoltaic (PV) as the input DC link voltage for the inverter through simulation modeling using MATLAB/Simulink.* ***Methods.*** *The method used is to design a parallel active filter modeling for a single-phase electrical network that serves loads in the form of AC DC converters with inductive recessive and capacitive recessive loads using MATLAB/Simulink.* ***Results.*** *The simulation results show that the total harmonic distortion (THD) value of the system before being screened is 37.93 % for inductive resistive loads and 18.77 % for capacitive resistive loads, and after going through screening the THD value can drop significantly by 0.35 % for inductive resistive loads and 1.45 % for resistive capacitive loads.* ***Practical value.*** *PV systems can be used as power generators to provide a voltage of 800 V on a single-phase parallel active power filter using a voltage source inverter.* References 30, table 2, figures 11.
Key words: **active shunt filter, compensator, photovoltaic, reactive power, voltage source inverter.**

Вступ. *Швидке виробництво електронного обладнання, яке використовується населенням, призвело до зниження якості електроенергії в енергосистемі.* ***Метою*** *статті є побудова паралельного активного фільтра для компенсації реактивної потужності в однофазній енергосистемі з використанням фотоелектричних (PV) елементів як вхідної напруги постійного струму для інвертора за допомогою імітаційного моделювання з використанням MATLAB/Simulink.* ***Методи***. *Використовуваний метод полягає у розробці моделювання паралельного активного фільтра для однофазної електричної мережі, яка обслуговує навантаження у вигляді перетворювачів змінного струму у постійний з індуктивними рецесивними і ремісивними ємнісними навантаженнями з використанням MATLAB/Simulink.* ***Результати*** *моделювання показують, що значення повного гармонійного спотворення (THD) системи перед екрануванням становить 37,93 % для індуктивних резистивних навантажень і 18,77 % для ємнісних резистивних навантажень, а після проходження екранування значення THD може значно знизитися на 0,35 % для індуктивних резистивних навантажень і 1,45 % для резистивних ємнісних навантажень.* ***Практична цінність***. *PV системи можуть використовуватися як генератори енергії для забезпечення напруги 800 В на однофазному паралельному активному фільтрі потужності з використанням інвертора напруги.* Бібл. 30, табл. 2, рис. 11.
Ключові слова: **активний шунтуючий фільтр, компенсатор, фотовольтаїка, реактивна потужність, інвертор напруги.**

Introduction. The rapid production of electronic equipment circulating and used by the public, such as computer equipment, power converters, and variable frequency drive systems for electric motors or devices based on power electronics, has resulted in a decline in the quality of power in the power system. Because of its nature, this load falls under the category of nonlinear loads. In power systems, the current has high wave distortion, leading to a large total harmonic distortion (THD). Excess heat generated by harmonics can cause power losses and reduce the efficiency of power equipment [1–3].

Various methods for reducing the presence of these harmonics include the use of filters. According to the configuration, there are 3 types of filters: passive, active, and hybrid (a combination of passive and active filters) [4, 5]. The harmonics of this power system occur in odd orders such as 150 Hz, 250 Hz and 350 Hz. Passive filters can be in the form of capacitive receptive (RC) or inductive receptive (RL) elements and are generally used to reduce the highest harmonic distortion at selected frequencies or tune at frequencies that are more dominantly disturbing, and the THD value can be reduced significantly [6, 7].

An active filter is a series of filters that use passive and active electronic elements originating from electronic devices such as operational amplifiers, MOSFETs and transistors in the form of inverters that produce reverse current or anti-harmonics [4]. The output of the inverter is controlled through ignition pulses, one of which uses hysterical current control [8]. Shunt active power filters (SAPFs) offer greater benefits than typical filter solutions because of their ability to map the injection currents more accurately, resulting in economic advantages [9, 10]. Hybrid filters, on the other hand, are a combination of passive and active filters that are commonly utilized in aluminum smelting plants to manage harmonic attenuation [11]. This filter is classified into 2 types, series active filters and parallel active filters, based on their configuration. Series active filters were used to eliminate current harmonics, whereas parallel active filters were used to reduce voltage harmonics.

The efficiency of active filters is determined by various factors such as the control system, filter reactor, DC link capacitor parameters, and electrical system. To achieve improved power quality, three components are necessary: power compensation for current and voltage waveform distortions, reactive power compensation, and compensation for load imbalance [12]. Solar energy is increasingly being used to compensate for the reactive power in electric power systems. In particular, the use of renewable energy, such as solar energy, has been developed for various applications. One such application is the use of SAPF technology. Compared to a thyristor bridge on a voltage source inverter (VSI) with an input reactor inductance equal to or smaller than the input reactor inductance of the SAPF, the SAPF is more efficient in terms of reactive power and harmonic attenuation [13].

Photovoltaic (PV) is practically an endless energy resource, which has made it highly essential recently, especially for electrical power applications in high-luminosity countries [14]. PV technology is a renewable way of converting solar energy into electrical energy. It can be used to address the current harmonics in power systems with parallel active filters [15, 16]. There are 2 varieties of PV systems: grid-connected and stand-alone. Because of its easy energy conversion process and modular scaling, grid-connected PV systems have been used extensively in the commercial sector [17]. When a stand-alone PV system is connected to the grid, it produces fluctuations in the output voltage owing to changes in temperature and irradiation. This makes it necessary to control the voltage and power quality, particularly when unbalanced load conditions occur. This control helps minimize the ripples on the DC

link [18, 19]. The use of PV solar energy is essential to the shift to a low-carbon economy [20].

The goal of the paper is to build a parallel active filter for reactive power compensation in a single-phase power system using PV as the input DC link voltage for the inverter through simulation modeling using the MATLAB/Simulink.

Subject of investigations. This study involved the development of a simulation of the compensation current I_C injected into a single-phase power system with a linear load. Basic concept of parallel SAPF is shown in Fig. 1.

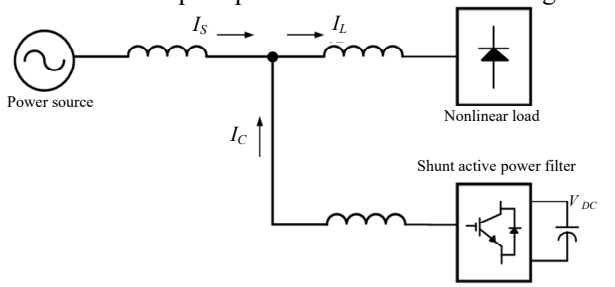

Fig. 1. Basic concept of parallel SAPF

The compensation of the harmonic currents is performed using a closed-loop controlled active power filter. This filter injects a compensation current I_C into the power system mesh whenever the load changes. Based on Fig. 1, the source current I_S can be represented as:

$$i_S = i_L - i_C, \quad (1)$$

where i_S is the source current; i_L is the load current; i_C is the compensation current.

The modeling design of the parallel active filter circuit is shown in Fig. 2.

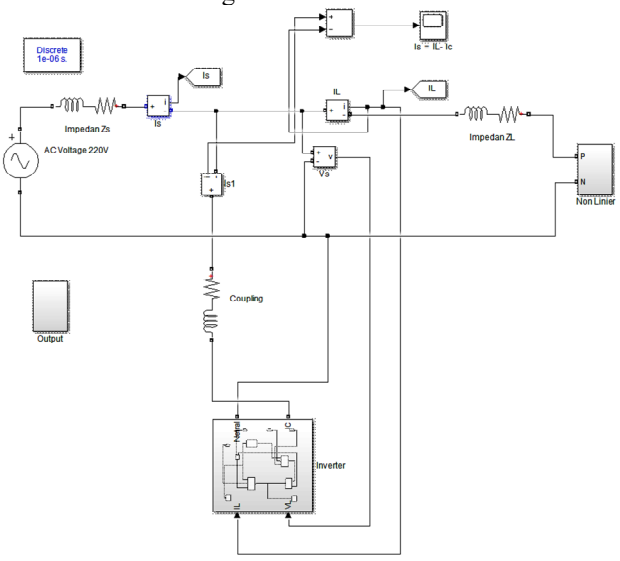

Fig. 2. Single-phase parallel active filter design using PV as a compensator

This circuit involves a single-phase voltage source connected to a nonlinear load, and is equipped with a parallel active filter. The filter comprises a series of low-pass filters and multiple active semiconductor components that collaborate to regulate the shape of the harmonic interference at every frequency order. The compensation current is generated by causing anti-harmonics in the current, which are affected by harmonics. Subsequently, this compensation current is introduced into the circuit. Schematic block of the overall model circuit shown in Fig. 3.

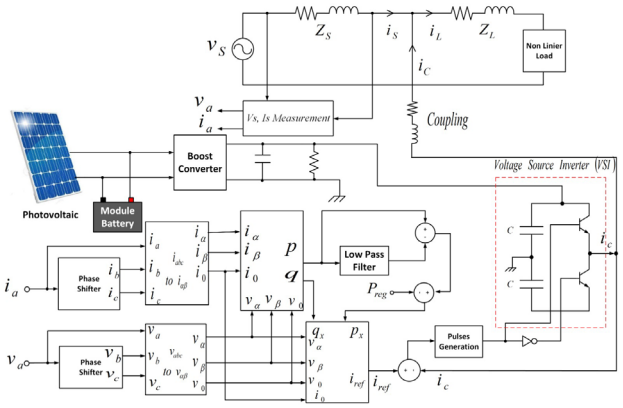

Fig. 3. Schematic block of the overall model circuit

The system has a complete design that includes 3 main parts: a DC power source PV system, a SAPF and a single-phase power system with a nonlinear load. The PV system is a DC power generator that produces 29.3 V voltage and a maximum short circuit current of 7.97 A. To meet the voltage requirements of the VSI, the voltage is increased through a booster circuit to 800 V [21–24]. The filtering process in an electrical system requires a battery module to store energy. The power filter, also known as an active shunt filter, generates a reference current i_{ref}. This process involved multiple stages. In the first stage, a voltage sensor and current sensor measured the magnitudes of the source current and source voltage, respectively. In this study, a single-phase voltage system was used. However, the power quality (PQ) theory is more suitable for 3-phase systems. Therefore, a virtual voltage and current source were created to obtain the parameters v_a, v_b, v_c, i_a, i_b, and i_c. After obtaining these parameters, the next step is to transform them into α–β coordinates. This transformation is known as Clark transformation and is essential for obtaining the i_{ref} quantity.

Results. Static calculations. This section discusses the results presented in the form of pictures, graphs, tables, etc. to make it easier for readers to understand them.

Clark transformation. Mathematical transformation calculations were performed to obtain the single-phase reference current. The reference current generation flow was based on the PQ theory discovered by Akagi in 1983. This theory was presented in [25]. PQ theory is best suited for 3-phase systems. To apply it to single-phase systems or to obtain the other 2-phases, virtual voltages and currents must be created for phases B and C that are 120° apart from phase A. The virtual voltages and currents for phases B and C can be derived from the voltage and current of phase A by shifting them 120° and –120°, respectively:

$$\begin{aligned} v_A &= V_m \sin(\omega t); \\ v_B &= V_m \sin(\omega t + 120°); \\ v_C &= V_m \sin(\omega t - 120°), \end{aligned} \quad (2)$$

where v_A, v_B, v_C are the voltages of phases A, B, C.

Reference signal generation algorithm. Once the virtual voltage and current parameters were obtained from the measurement results of a single-phase power system, the parameter values were converted into single-phase voltage system coordinates. This conversion involves transforming the absolute coordinates of the voltage and current to α–β coordinates using the PQ theory. This transformation is also known as Clark transformation [26, 27]. Reference current generation algorithm is shown in Fig. 4.

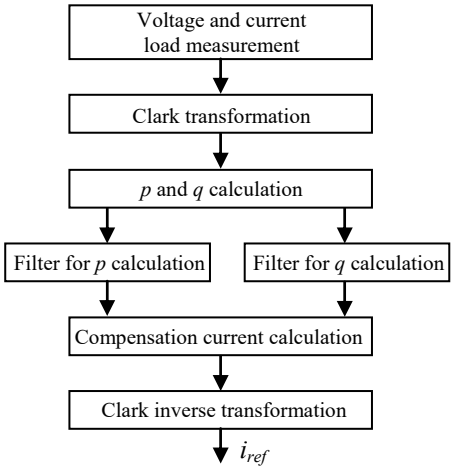

Fig. 4. Reference current generation algorithm

Shown in Fig. 4 is the flow for getting the voltage and current parameters v_α, v_β, i_α, i_β, v_0, i_0:

$$\begin{bmatrix} v_\alpha \\ v_\beta \end{bmatrix} = \sqrt{\frac{2}{3}} \begin{bmatrix} 1 & -1/2 & -1/2 \\ 0 & \sqrt{3}/2 & -\sqrt{3}/2 \end{bmatrix} \begin{bmatrix} v_A \\ v_B \\ v_C \end{bmatrix}; \quad (3)$$

$$\begin{bmatrix} i_\alpha \\ i_\beta \end{bmatrix} = \sqrt{\frac{2}{3}} \begin{bmatrix} 1 & -1/2 & -1/2 \\ 0 & \sqrt{3}/2 & -\sqrt{3}/2 \end{bmatrix} \begin{bmatrix} i_A \\ i_B \\ i_C \end{bmatrix}. \quad (4)$$

The voltages and currents in reference frames α and β are:

$$v_\alpha = \sqrt{\frac{2}{3}} v_A - \frac{1}{\sqrt{6}} v_B - \frac{1}{\sqrt{6}} v_C; \quad (5)$$

$$v_\beta = \frac{1}{\sqrt{6}} v_B - \frac{1}{\sqrt{6}} v_C; \quad (6)$$

$$i_\alpha = \sqrt{\frac{2}{3}} i_A - \frac{1}{\sqrt{6}} i_B - \frac{1}{\sqrt{6}} i_C; \quad (7)$$

$$i_\beta = \frac{1}{\sqrt{6}} i_B - \frac{1}{\sqrt{6}} i_C. \quad (8)$$

The next step is to determine or calculate the values of the active p and the reactive q powers:

$$\begin{bmatrix} p \\ q \end{bmatrix} = \begin{bmatrix} v_\alpha & v_\beta \\ -v_\beta & -v_\alpha \end{bmatrix} \begin{bmatrix} i_\alpha \\ i_\beta \end{bmatrix}. \quad (9)$$

Equation (9) shows that the instantaneous active power p is equal to the sum of $p = v_\alpha i_\alpha + v_\beta i_\beta = \overline{p} + \widetilde{p}$, which can be broken down into 2 components: the $\overline{p}$ component (DC component value) and the $\widetilde{p}$ component (AC component value). The $\overline{p}$ component is the instantaneous average power transferred from the source to the load, whereas the $\widetilde{p}$ component is the average power exchanged between the source and load via ABC coordinates. However, the $\widetilde{p}$ component does not transfer energy from the source to the load; therefore, it must be removed with a filter:

$$\begin{bmatrix} i_{c\alpha} \\ i_{c\beta} \end{bmatrix} = \frac{1}{v_\alpha^2 + v_\beta^2} \begin{bmatrix} v_\alpha & -v_\beta \\ v_\beta & v_\alpha \end{bmatrix} \begin{bmatrix} \widetilde{p} - \Delta\overline{p} \\ q \end{bmatrix}, \quad (10)$$

where $i_{c\alpha}$, $i_{c\beta}$ are the compensation currents in reference frames α and β; $\widetilde{p}$ is the alternating active power component; $\Delta\overline{p}$ is the total direct active power component; q is the reactive power component.

After obtaining the p components, a reverse transformation is carried out to obtain the reference current value [28]:

$$\begin{bmatrix} i_{c\alpha} \\ i_{c\beta} \end{bmatrix} = \frac{1}{v_\alpha^2 + v_\beta^2} \begin{bmatrix} v_\alpha & -v_\beta \\ v_\beta & v_\alpha \end{bmatrix} \begin{bmatrix} p_x \\ q_x \end{bmatrix}, \quad (11)$$

$p_x = \widetilde{p} - \Delta\overline{p}$ and $\Delta\overline{p} = \overline{p}_0$ then $q_x = q = \overline{q} + \widetilde{q}$, where p_x is the unwanted active power component; q_x is the unwanted reactive power component; $\overline{p}_0$ is the active power zero sequence component; $\overline{q}$ is the direct reactive power component; $\widetilde{q}$ is the alternating reactive power component.

The single-phase reference current can be defined as:

$$i_{ref} = \sqrt{\frac{2}{3}} \left[\frac{p_x v_\alpha - q_x v_\beta}{v_\alpha^2 + v_\beta^2} + \frac{i_0}{\sqrt{2}} \right]; \quad (12)$$

where i_0 is the zero sequence current.

Parameter values of the modeling system are presented in Table 1.

Table 1

Parameter values of the modeling system

Parameter	Value	Parameter	Value
Single-phase AC input voltage	220 V	Frequency	50 Hz
Input impedance	R=0.5 Ω; L=35 mH	Load impedance	R_L=20 Ω, L_L=5 mH
Coupling impedance (smoothing)	R_c=1 Ω; L_c=3.5 mH	DC link capacitor	C_1=C_2= 400 V, 50 nF
AC-DC converter	Bridge rectifier diode	Rectifier load	*RL* (R=50 Ω, L= 15 mH; *RC* (R=50 Ω, C = 1,5 nF
K_p	3	K_i	1
PV max power	218.87 W	Open circuit voltage	36.6 V
Max power point voltage	29.3 V	Current short circuit	7.97 A

A boost converter regulator was used to increase the DC input voltage from the battery without the need for a transformer. Figure 5 shows the operation of the boost converter circuit, which can be divided into 2 modes. Mode 1 begins when switch S is turned ON at t = 0. The input current increases, the inductor is formed by a magnetic field with a voltage of $V_L = L\frac{\mathrm{d}i_L}{\mathrm{d}t}$; $C\frac{\mathrm{d}V_C}{\mathrm{d}t} + \frac{V_C}{R} = 0$ and the current increases with a constant slope. This state is $V_{DC} = V_L$. Mode 2 begins when switch S is turned OFF at t = 1. The current flows through L, the diode D and C. The inductor current decreases until switch S is turned on again during the next cycle.

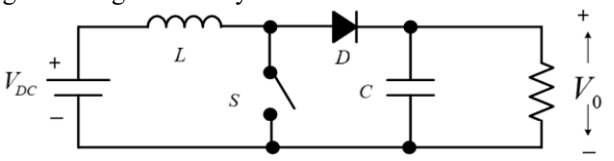

Fig. 5. Boost converter circuit

When switch S is in the OFF mode, $V_{DC} = V_L + V_C$, the voltage across the circuit is the sum of the voltages across the inductor and capacitor. This implies that $L\frac{\mathrm{d}i_L}{\mathrm{d}t} = V_{DC} - V_C$,

where $\frac{di_L}{dt} = \frac{V_{DC} - V_C}{L}$. In this situation, the current decreases, eventually reaching the same level as that when the switch is ON. During the gate switch switching on current, the output current wave pattern increases by $I_{max} - I_{min} = V_{DC} \cdot k / L$, where k is the duty cycle. Similarly, when the switch is turned OFF, the current decreases to $I_{min} - I_{max} = \frac{V_{DC} - V_C}{L}(1-k)$, where

$$V_0 = V_C = \frac{V_{DC}}{1-k}. \quad (13)$$

To increase the input voltage, multiple stages of the boost converter can be arranged, resulting in a conversion ratio that is always higher than that of a single boost converter. This type of converter can be used in various applications, such as Microgrid systems, electric trains, UPS, inverters and wireless energy transfer [24].

PI controller. When an active filter injects a current into the power system, it must always be greater than the current flowing from the source to the load. To achieve this, the voltage of the VSI must be greater than the wire-to-wire voltage of the single-phase source and must be kept constant. PI controller was used to regulate the DC voltage by adjusting the K_p and K_i values [29]. PI controller block is shown in Fig. 6.

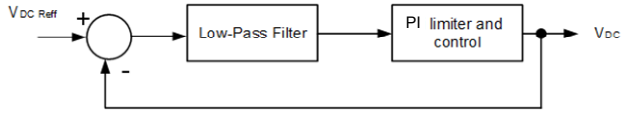

Fig. 6. PI controller block

Voltage source inverter (VSI) is a powerful power conditioner used in active filters. One of the reasons to consider using a VSI over the current source inverter is that it is easier to control the current compared to current source inverter. A VSI uses capacitors for DC energy storage. The single-phase VSI circuit comprises 2 electronic switches that can be in the form of a MOSFET or power transistor placed in parallel with a capacitor bank. MOSFETs are generally preferred for fast switching and low-frequency applications [30]. Table 2 provides information on the relationship between the switch conditions and VSI output voltage. Figure 7 shows the single-phase inverter.

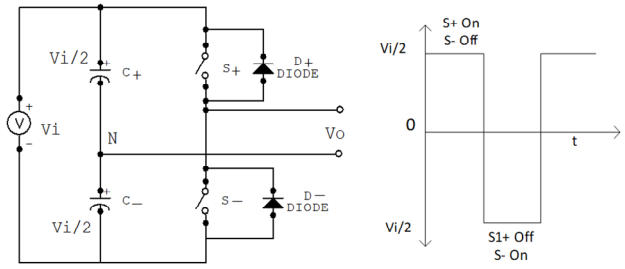

Fig. 7. Single-phase inverter

Table 2

Operation of switches on the inverter

No.	Condition	v_0	Active components
1	S+ ON and S– OFF	$v_i/2$	S+ if $i_0>0$; D+ if $i_0<0$
2	S+ OFF and S– ON	$-v_i/2$	D– if $i_0>0$; S– if $i_0<0$
3	S+ and S– OFF	$-v_i/2$ and $v_i/2$	D– if $i_0>0$; D+ if $i_0<0$

The S+ and S– switches must not operate at the same time, as this can cause a short circuit. The ON and OFF states of the S+ and S– switches are controlled using a modulation technique, specifically pulse width modulation (PWM). The PWM principle in this circuit compares the modulation signal V_C (in this case the expected output alternating voltage) with a carrier signal with a saw waveform (V_Δ). Practically, if $V_C > V_\Delta$ then the S+ switch will be ON and the S– switch will be OFF, and if $V_C < V_\Delta$, then the S+ switch will be OFF and the S– switch will be ON.

RC load observation. Observations and tests were conducted on nonlinear, *RC* and *RL* loads to observe the sinusoidal current waveform patterns before and after filtering. Display of load current, compensation current and source current with non-linear and *RC* loads is shown in Fig. 8, which shows the distorted capacitive load current waveform. The waveform was no longer a pure sinusoidal pattern and appeared uneven. The middle image represents the compensation current waveform injected into the power line. Finally, the last image displays the current waveform that has been compensated for by the injected current, and its shape now returns to a sinusoidal pattern.

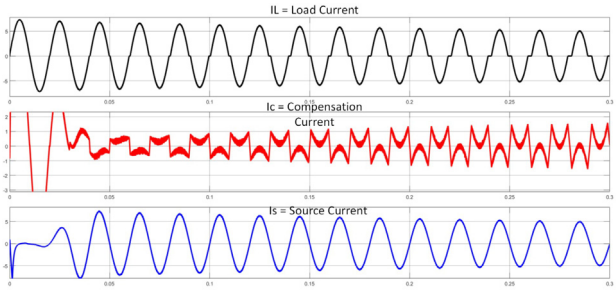

Fig. 8. Display of load current, compensation current and source current with non-linear and *RC* loads

THD measurement for *RC* loads using fast Fourier transform (FFT) is shown in Fig. 9.

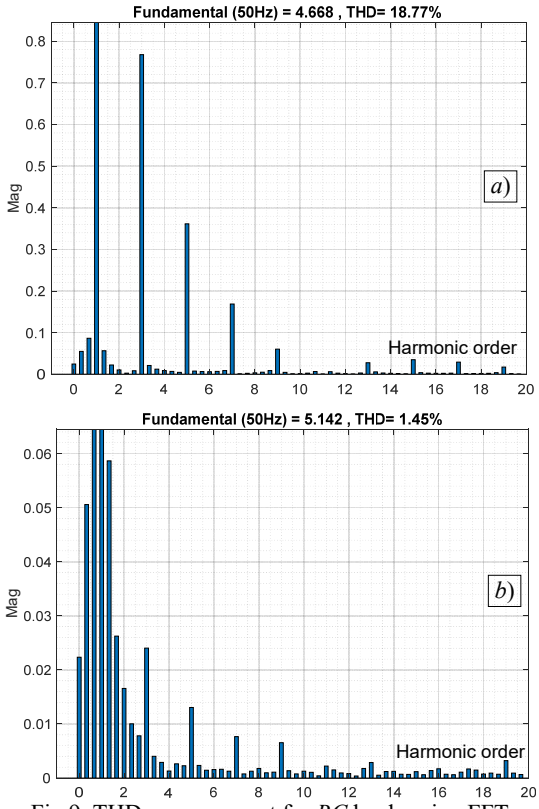

Fig 9. THD measurement for *RC* loads using FFT

Figure 9,*a* shows odd-order harmonic interference at 250, 350, 550, 850 and 950 Hz. Index THD before compensation indicating a value of 18,77 %. The 5th order harmonic was the largest at 250 Hz. Figure 9,*b* shows that the compensation current reduces the THD to 1.45 %.

***RL* load observation.** Display of load current, compensation current and source current with non-linear and *RL* loads is shown in Fig. 10, which shows 3 different current waveforms. The first image depicts a distorted waveform that appears almost square, caused by nonlinear and *RL* loads. The middle image shows the compensation current waveform, whereas the bottom image shows the source-current waveform after the compensation current is applied.

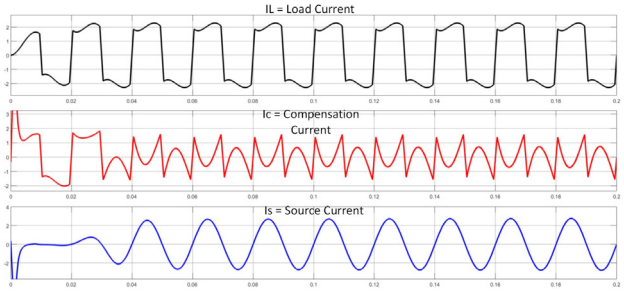

Fig. 10. Display of load current, compensation current and source current with non-linear and *RL* loads

Figure 11 shows the THD measurement at *RL* load using FFT. Figure 11,*a* shows a graph of the THD index before compensation, indicating a value of 36.93 %. Meanwhile, Figure 11,*b* displays a THD index of 0.48 % after filtering.

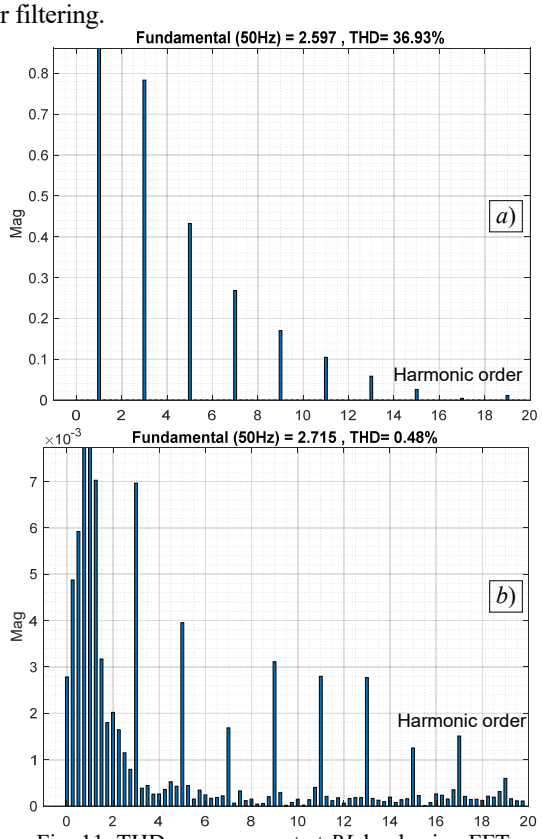

Fig. 11. THD measurement at *RL* load using FFT

Conclusions. The PV systems can be used as a power generator to provide a voltage of 800 V on a single-phase parallel active power filter using a voltage source inverter. This voltage value is achieved by increasing the DC voltage from the boost converter circuit. The PV power can also be used as a reactive power compensator to prevent the presence of harmonics in single-phase power systems. The DC link capacitor functions as a compensation current pattern generator. The instantaneous power theory, which is commonly used in 3-phase power systems, can also be applied to single-phase systems by adding two virtual voltage sources that resemble a 3-phase voltage source. The compensation current has a waveform that is similar to the reference current, and it is obtained through mathematical calculations of the Clark transformation. Test results have shown that this parallel active filter can reduce the THD from 18.77 % to 1.45 % on capacitive loads, and it can reduce the THD value from 37.97 % to 0.48 % on inductive loads.

Acknowledgements. We would like to thank Gunadarma University as the author's institution for its support and assistance during the research. Similarly, thanks to the advice and input from Prof. Ir. Bosono Soerowirjo, PhD, as supervisor for this research.

Conflicts of interest. The authors declare no conflict of interest.

REFERENCES

1. Badoni M., Singh A., Singh B. Adaptive recursive inverse-based control algorithm for shunt active power filter. *IET Power Electronics*, 2016, vol. 9, no. 5, pp. 1053-1064. doi: https://doi.org/10.1049/iet-pel.2015.0170.

2. Sozański K. Three phase active power filter with selective harmonics elimination. *Archives of Electrical Engineering*, 2016, vol. 65, no. 1, pp. 33-44. doi: https://doi.org/10.1515/aee-2016-0003.

3. Alhmoud L. THD Reduction Using Shunt Active Power Filter: A Real Case Study. *Universal Journal of Electrical and Electronic Engineering*, 2019, vol. 6, no. 4, pp. 259-264. doi: https://doi.org/10.13189/ujeee.2019.060407.

4. Alhamrouni I., Hanafi F.N., Salem M., Rahman N.H.A., Jusoh A., Sutikno T. Design of shunt hybrid active power filter for compensating harmonic currents and reactive power. *TELKOMNIKA (Telecommunication Computing Electronics and Control)*, 2020, vol. 18, no. 4, pp. 2148-2157. doi: https://doi.org/10.12928/telkomnika.v18i4.15156.

5. Albasri F.A., Al-Mawsawi S.A., Al-Mahari M. A pot line rectiformer scheme with hybrid-shunt active power filter. *International Journal of Power Electronics and Drive Systems (IJPEDS)*, 2022, vol. 13, no. 1, pp. 1-10. doi: https://doi.org/10.11591/ijpeds.v13.i1.pp1-10.

6. Madhu B.R., Dinesh M.N., Ravitheja B.M. Design of shunt hybrid active power filter (SHAPF) to reduce harmonics in AC side due to Non-linear loads. *International Journal of Power Electronics and Drive Systems (IJPEDS)*, 2018, vol. 9, no. 4, pp. 1926-1936. doi: https://doi.org/10.11591/ijpeds.v9.i4.pp1926-1936.

7. Firoozian M., Hosseinian S.H., Abedi M. A new innovative current controller for selective harmonic compensation using active power filters in a microgrid with renewable energy source. *International Journal of Power Electronics and Drive Systems (IJPEDS)*, 2022, vol. 13, no. 4, pp. 2396-2404. doi: https://doi.org/10.11591/ijpeds.v13.i4.pp2396-2404.

8. Raja Mohamed S., Jeyanthy P.A., Devaraj D. Hysteresis-based Voltage and Current Control Techniques for Grid Connected Solar Photovoltaic Systems: Comparative Study. *International Journal of Electrical and Computer Engineering (IJECE)*, 2018, vol. 8, no. 5, pp. 2671-2681. doi: https://doi.org/10.11591/ijece.v8i5.pp2671-2681.

9. Barnabé F., Rocha M., Clerice G. Enhancement of Power Quality Using Voltage and Hall Effect Current Sensors Applied on Controlled Single-Phase Active Power Filter. *Engineering Proceedings*, 2020, vol. 2, no. 1, art. no. 74. doi: https://doi.org/10.3390/ecsa-7-08212.

10. Gwóźdź M., Ciepliński Ł. An active power filter based on a hybrid converter topology – Part 1. *Bulletin of the Polish Academy of Sciences Technical Sciences*, 2021, vol. 69, no. 1, art. no. e136218. doi: https://doi.org/10.24425/bpasts.2020.136218.

11. Akagi H. Modern active filters and traditional passive filters. *Bulletin of the Polish Academy of Sciences: Technical Sciences*, 2006, vol. 54, no. 3, pp. 255-269.

12. Szromba A. Improving the Efficiency of the Shunt Active Power Filter Acting with the Use of the Hysteresis Current Control Technique. *Energies*, 2023, vol. 16, no. 10, art. no. 4080. doi: https://doi.org/10.3390/en16104080.
13. Azebaze Mboving C.S., Hanzelka Z. Analysis of the Influence of the 6-Pulse Thyristor-Bridge Input Reactor Size on the Shunt Active Power Filter Work Efficiency: A Case Study. *Energies*, 2023, vol. 17, no. 1, art. no. 80. doi: https://doi.org/10.3390/en17010080.
14. Bounechba H., Boussaid A., Bouzid A. Experimental validation of fuzzy logic controller based on voltage perturbation algorithm in battery storage photovoltaic system. *Electrical Engineering & Electromechanics*, 2024, no. 5, pp. 20-27. doi: https://doi.org/10.20998/2074-272X.2024.5.03.
15. Rajakkannu R., Rangaswamy B. An Enhanced Modified Multiport Interleaved Flyback Converter for Photovoltaic-Shunt Active Power Filter (PV-SHAPF) Applications. *International Transactions on Electrical Energy Systems*, 2022, vol. 2022, art. no. 1537319. doi: https://doi.org/10.1155/2022/1537319.
16. Ertekin D., Baltaci K., Çelebi M. Advancing Renewable Energy: An Experimental Study of a Switched-Inductor, Switched-Capacitor Luo Boost Converter for Low-Voltage Applications. *Electronics*, 2023, vol. 12, no. 24, art. no. 5006. doi: https://doi.org/10.3390/electronics12245006.
17. Janardhan G., Surendra Babu N.N.V., Srinivas G.N. Single phase transformerless inverter for grid connected photovoltaic system with reduced leakage current. *Electrical Engineering & Electromechanics*, 2022, no. 5, pp. 36-40. doi: https://doi.org/10.20998/2074-272X.2022.5.06.
18. Mohammed F.A., Bahgat M.E., Elmasry S.S., Sharaf S.M. Design of a maximum power point tracking-based PID controller for DC converter of stand-alone PV system. *Journal of Electrical Systems and Information Technology*, 2022, vol. 9, no. 1, art. no. 9. doi: https://doi.org/10.1186/s43067-022-00050-5.
19. Alharbi M. Control Approach of Grid-Connected PV Inverter under Unbalanced Grid Conditions. *Processes*, 2024, vol. 12, no. 1, art. no. 212. doi: https://doi.org/10.3390/pr12010212.
20. Lanani A., Djamai D., Beddiaf A., Saidi A., Abboudi A. Photovoltaic system faults detection using fractional multiresolution signal decomposition. *Electrical Engineering & Electromechanics*, 2024, no. 4, pp. 48-54. doi: https://doi.org/10.20998/2074-272X.2024.4.06.
21. Shahir F.M., Aberoumandazar M., Babaei E. High Gain DC-DC Boost Converter Applied in Hybrid System of Photovoltaic and Battery. *2021 International Symposium on Devices, Circuits and Systems (ISDCS)*, 2021, pp. 1-4. doi: https://doi.org/10.1109/ISDCS52006.2021.9397922.
22. Palanisamy R., Vijayakumar K., Venkatachalam V., Narayanan R.M., Saravanakumar D., Saravanan K. Simulation of various DC-DC converters for photovoltaic system. *International Journal of Electrical and Computer Engineering (IJECE)*, 2019, vol. 9, no. 2, pp. 917-925. doi: https://doi.org/10.11591/ijece.v9i2.pp917-925.
23. Dos Santos P.M., Serralheiro A.J., Borges B., Torres J.P.N., Charas A. An Experimental Study on Step-Up DC–DC Converters for Organic Photovoltaic Cells. *Journal of Low Power Electronics and Applications*, 2022, vol. 12, no. 2, art. no. 20. doi: https://doi.org/10.3390/jlpea12020020.
24. Salau A.O., Eya C.U., Onyebuchi O.C. Nonzero Staircase Modulation Scheme for Switching DC-DC Boost Converter. *Journal of Control Science and Engineering*, 2020, vol. 2020, art. no. 8347462. doi: https://doi.org/10.1155/2020/8347462.
25. Watanabe E.H., Aredes M., Akagi H. The p-q theory for active filter control: some problems and solutions. *Sba: Controle & Automação Sociedade Brasileira de Automatica*, 2004, vol. 15, no. 1, pp. 78-84. doi: https://doi.org/10.1590/S0103-17592004000100010.
26. Babu M.B., Srinivas L.R., Karunakar T., Amarendra A., Reddy D.S., Ramu M., Swarup Kumar J.N.V.R., Tulasi Ram S.S. Power quality improvement based on VSHDE algorithm incorporating shunt active power filter. *Journal of Electrical Systems*, 2023, vol. 19, no. 1, pp. 1-12.
27. Khan A., Jaffery M.H., Javed Y., Arshad J., Rehman A.U., Khan R., Bajaj M., Kaabar M.K.A. Hardware-in-the-Loop Implementation and Performance Evaluation of Three-Phase Hybrid Shunt Active Power Filter for Power Quality Improvement. *Mathematical Problems in Engineering*, 2021, vol. 2021, art. no. 8032793. doi: https://doi.org/10.1155/2021/8032793.
28. Afonso J., Aredes M., Watanabe E., Martins J. Shunt active filter for power quality improvement. *International Conference UIE 2000 – "Electricity for a Sustainable Urban Development"*, Lisboa, Portugal, 1-4 Nov. 2000, pp. 683-691.
29. Abdolrasol M.G.M., Hannan M.A., Hussain S.M.S., Ustun T.S. Optimal PI controller based PSO optimization for PV inverter using SPWM techniques. *Energy Reports*, 2022, vol. 8, pp. 1003-1011. doi: https://doi.org/10.1016/j.egyr.2021.11.180.
30. Lahlaci M.E., Miloudi M., Miloudi H. Experimental electromagnetic compatibility of conducted electromagnetic interferences from an IGBT and a MOSFET in the power supply. *Electrical Engineering & Electromechanics*, 2024, no. 3, pp. 38-43. doi: https://doi.org/10.20998/2074-272X.2024.3.05.

Received 11.10.2024
Accepted 17.01.2025
Published 02.05.2025

B. Dwinanto[1], *Master of Electrical Engineering,*
Setiyono[1], *Doctor of Information Technology,*
F. Thalib[1], *Doctor of Electrical Engineering,*
H. Siswono[1], *Doctor of Electrical Engineering,*
[1] Department of Electrical Engineering,
Faculty of Industrial Technology,
Gunadarma University, Depok, Indonesia,
e-mail: bambang_dwi@staff.gunadarma.ac.id (Corresponding Author); setiyono@staff.gunadarma.ac.id; farid@staff.gunadarma.ac.id; hartono@staff.gunadarma.ac.id

How to cite this article:
Dwinanto B., Setiyono, Thalib F., Siswono H. Single-phase power shunt active filter design using photovoltaic as reactive power compensator. *Electrical Engineering & Electromechanics*, 2025, no. 3, pp. 59-64. doi: https://doi.org/10.20998/2074-272X.2025.3.09

UDC 621.3.013 https://doi.org/10.20998/2074-272X.2025.3.10

B.I. Kuznetsov, T.B. Nikitina, I.V. Bovdui, K.V. Chunikhin, V.V. Kolomiets, I.V. Nefodova

Simplified method for analytically determining the external magnetostatic field of uncertain extended technical objects based on near-field measurements

Introduction. *An important scientific and technical problem of magnetism of uncertain extended energy-saturated objects - such as naval vessels and submarines is implementation of strict requirements for magnetic silence based on mathematical modeling of magnetic field, adequate to its real measurements.* ***The purpose*** *of the work is to develop a simplified analytical method for determining the external magnetostatic field of extended technical objects with uncertain magnetic field sources based on near-field measurement data using spherical and spheroidal sources in a Cartesian coordinate system.* ***Methodology.*** *Forward problems of magnetostatics solved based on developed method of analytical calculation of magnetostatic field induction of spherical and spheroidal sources in Cartesian coordinate system based on near-field measurements. Geometric inverse problems of magnetostatics for solving prediction and control problems of magnetic silence of technical object calculated based on vector games solution. Both vector games payoff calculated as forward problems solutions Wolfram Mathematica software package used.* ***Results.*** *The results of prediction of magnetic field magnitude in far zone of extended technical objects based on designed multispheroidal magnetic field model in form of spatial elongated spheroidal harmonics in prolate spheroidal coordinate system and in form of multispherical magnetic field model in form of spatial spherical harmonics in spherical coordinate system using measurements near field and taking into account magnetic characteristics uncertainty of extracted technical objects.* ***Originality.*** *For the first time, a method of simplifying the mathematical modeling of the magnetic field of an uncertain long energy- saturated object developed based on development and application of method of analytical calculation of induction of magnetostatic fields of spherical and spheroidal sources in the Cartesian coordinate system. Unlike known methods developed method allows modeling magnetic field directly in Cartesian coordinate system based on near-field measurements without finding magnetic induction projection in prolate spheroidal coordinate system and in spherical coordinate system without their translation from prolate spheroidal coordinate system and in spherical coordinate system in Cartesian coordinate system and vice versa.* ***Practical value.*** *The possibility of a more than 10 times calculation time reduction of magnetic field induction of magnetic field elongated spheroidal sources and the possibility of a more than 4 times calculation time reduction of magnetic field induction of magnetic field spherical sources when magnetic field calculating of uncertain extended energy-saturated object based on development and application of analytical calculation method of magnetostatic field induction of spherical and spheroidal sources in the Cartesian coordinate system based on near-field measurements shown.* References 50, tables 2, figures 4.

Key words: **energy-saturated extended technical objects, magnetic field, multispheroidal model, magnetic silencing, extended spheroidal coordinate system, spatial extended spheroidal harmonics.**

Проблема. *Важливою науково-технічною проблемою магнетизму невизначених протяжних енергонасичених об'єктів таких як військово-морські судна та підводні човни є реалізація жорстких вимог «магнітної тиші» на основі математичного моделювання магнітного поля, адекватного його реальним вимірюванням.* ***Метою*** *роботи є розробка спрощеного аналітичного методу визначення зовнішнього магнітостатичного поля протяжних технічних об'єктів з невизначеними джерелами магнітного поля на основі даних вимірів в ближній зоні з використанням сферичних та сфероїдальних джерел в декартовій системі координат.* ***Методологія.*** *Прямий метод проблеми магнітостатики вирішується на основі розробленого методу аналітичного розрахунку індукції магнітостатичного поля сферичних та сфероїдальних джерел в декартовій системі координат на основі вимірювань ближнього поля. Геометричні обернені задачі магнітостатики для вирішення проблем передбачення і контролю магнітної тиші технічного об'єкта обчислюються на основі розв'язання векторних ігор. Виграші обох векторних ігор обчислюються як рішення прямої проблеми з використанням програмного пакету Wolfram Mathematica.* ***Результати.*** *Результатом прогнозування є величини віддаленого магнітного поля протяжних технічних об'єктів на основі спроектованої мультисфероїдальної моделі магнітного поля в вигляді просторових витягнутих сфероїдальних гармонік в витягнутій сфероїдній системі координат, та в вигляді мультисферичної моделі магнітного поля в вигляді просторових сферичних гармонік у сферичній системі координат з використанням вимірювань ближнього поля з врахуванням невизначеності магнітних характеристик витягнутих технічних об'єктів.* ***Оригінальність.*** *Вперше розроблено метод спрощення математичного моделювання магнітного поля невизначеного протяжного енергонасиченого об'єкта на основі розробки та застосування методу аналітичного розрахунку індукції магнітостатичного поля сферичних та сфероїдальних джерел в декартовій системі координат. На відміну від відомих методів, розроблений метод дозволяє моделювати магнітне поле безпосередньо в декартовій системі координат на основі вимірювань ближнього поля без знаходження проекції магнітної індукції в витягнутій сфероїдальній системі координат та в сферичній системі координат без їх переводу із витягнутій сфероїдальній системі координат, та із сферичної системи координат, в декартову систему координат, чи навпаки.* ***Практична цінність.*** *Показана можливість скорочення, більше ніж у 10 разів, часу розрахунку індукції магнітного поля витягнутих сфероїдальних джерел магнітного поля, та можливість зменшення, більше ніж в 4 рази, часу розрахунку індукції магнітного поля сферичних джерел магнітного поля при обчисленні магнітного поля невизначеного протяжного енергонасиченого об'єкта на основі розробки та застосування методу аналітичного розрахунку індукції магнітостатичного поля сферичних і сфероїдальних джерел в декартовій системі координат на основі вимірювань ближнього поля.* Бібл. 50, табл. 2, рис. 4.

Ключові слова: **енергонасичені протяжні технічні об'єкти, магнітне поле, мультисфероїдальна модель, магнітна тиша, витягнута сфероїдна система координат, просторові протяжні сфероїдні гармоніки.**

Introduction. An important scientific and technical problem of modern magnetism of technical objects is implementation of strict requirements for external magnetic field level. This problem is especially acute for magnetism of spacecraft, naval vessel and submarines [1–4]. The success of solving the problem of magnetism of these technical objects is largely determined by the adequacy of mathematical models of the external magnetic field (MF) to the real values of the magnetic characteristics of these objects [5–7]. To measure the real characteristics of the MF of spacecraft, military ships and submarines, special magnetodynamic measuring stands have been developed, one of which is located at the Anatolii Pidhornyi Institute of Power Machines and Systems of the National Academy of Sciences of Ukraine [8]. Based on the experimentally measured values of the MF components on the bench, a mathematical model of the MF of technical object designed [9–11]. Then, based on the mathematical model of the technical object designed on the basis of measurements of the near MF, the values of the MF parameters in the far zone are calculated. This is the task of MF prediction [6]. Then, based on the calculated

values of the MF parameters in the far zone, the problem of calculating the parameters and coordinates of the location in the space of the technical object of the compensating sources of the MF is solved to meet the requirements for the parameters of the MF of the technical object [6, 7].

The most widely used sources of MF are point sources, the MF of which is described in a spherical coordinate system (SCS). The mathematical model of technical objects is often adopted in the form of a multiple dipole model (MDM). The parameters of the dipoles and the coordinates of their location in the space of the technical object are determined in the course of solving the geometric inverse problem of magnetostatics from the condition of minimizing the error between the measured and predicted by the model values of the parameters of the external MF at the specified points of measurement of space [6].

Despite the fact that the shape of military ships and submarines has a «cigar-shaped» appearance of elongated technical objects, mathematical models of the MF of such objects are also often adopted in MDM form. In the works of [12–16], the expediency of using mathematical models in the form of elongated ellipsoidal sources (EES) of MF, describing the parameters of the MF in prolate spheroidal coordinate systems (PSCS), is shown for such elongated technical objects.

On magnetodynamic stands, measurements of magnetic characteristics of technical objects are usually measured in Cartesian coordinate systems (CCS) related to the center of technical objects. In MDM of the MF of technical objects, the positions of dipole sources of the MF are also specified in CCS related to the center of technical objects. In addition, on magnetodynamic stands, magnetic characteristics of component units of electrical equipment of technical objects are often measured, which are also, as a rule, measured in CCS related to the center of these component units of electrical equipment of technical objects [17–19].

However, mathematical models of concentrated MF sources are calculated in SCS associated with the centers of these sources. Mathematical models of elongated MF sources are calculated in the form of prolate spheroidal MF sources in PSCS associated with the centers of these sources [20, 21].

In classical works on electrodynamics [22–31], solutions of the Laplace equation for the scalar potential of a MF in a SCS and in a PSCS are known. Accordingly, these solutions are written in terms of SCS and PSCS [20, 21]. But for practice, it is often necessary to work in terms of a CCS [32–34]. In addition, it is not the scalar potential that is practically important, but the projections of the magnetic induction.

In modern works, for example, related to the magnetic cleanliness of spacecraft [22–31] and magnetic silence of naval vessel and submarines [17–19], analytical formulas of magnetic induction projections in terms of SCS and PSCS are derived on the basis of solutions to the Laplace equation for the scalar potential of the MF outside the source. Furthermore, in the case of SCS, generalized formulas for the magnetic induction projections for the nth spherical harmonic are derived [35], whereas in the case of PSCS, this is not the case. Instead, only general formulas for the magnetic induction projections are presented, which require taking the derivatives of the scalar potential with respect to the PSCS coordinates [20, 21]. In some instances, for several first spherical harmonics (up to 4), for some reason, the associated Legendre polynomials are written out, thereby obtaining rather cumbersome formulas [21]. An additional inconvenience is the constant necessity to transform both the coordinates from CCS to SCS and the projections of magnetic induction from SCS to CCS (the situation is similar with PSCS). This presents a significant challenge when attempting to calculate the MF from multiple sources, particularly when these sources are both spherical and spheroidal.

The peculiarity of the considered energy-saturated elongated objects is the inaccurate knowledge of magnetic characteristics and their change in different operating modes. Such objects are called uncertain objects [5–7].

The purpose of the work is to develop a simplified analytical method for determining the external magnetostatic field of extended technical objects with uncertain magnetic field sources based on near-field measurement data using spherical and spheroidal sources in a Cartesian coordinate system.

Definition of forward magnetostatics problem for spheroidal sources. Consider analytical formulas for projections of magnetic induction in CCS for spheroidal harmonics of MF in PSCS. Consider multyspheroidal model of original MF of energy-saturated extended technical object in PSCS. Let us assume that initial MF of extended energy-saturated object generated using spheroidal MF sources located at technical object space points with coordinates (x_i, y_i, z_i) in CCS associated with the center of technical object (Fig. 1).

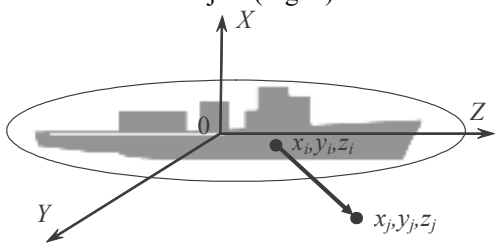

Fig. 1. Energy-saturated extended technical object

The relationship between the right triple of unit vectors $\{x, y, z\}$ of the CCS and the triple $\{\xi, \eta, \varphi\}$ of the PSCS has the form [12–14, 36]:

$$\begin{cases} x = c\sqrt{\left(\xi^2-1\right)\left(1-\eta^2\right)}\cos\varphi; \\ \qquad\qquad\qquad\qquad \xi \in [1,\infty]; \\ y = c\sqrt{\left(\xi^2-1\right)\left(1-\eta^2\right)}\sin\varphi; \Rightarrow \eta \in [-1,1]; \\ \qquad\qquad\qquad\qquad \varphi \in [0,2\pi], \\ z = c\xi\eta; \end{cases} \quad (1)$$

where c is half the focal length of the spheroid whose foci lie on the z-axis at the points $\pm c$. From a geometric point of view, the triple $\{\xi, \eta, \varphi\}$ is a family of prolate spheroids (ξ=const), two-sheeted hyperboloids (η=const) and half-planes (φ=const) passing through the z-axis.

The surfaces of prolate spheroids ξ=const satisfy the equation [12–14, 36]

$$z^2\xi^{-2} + \left(x^2+y^2\right)\left(\xi^2-1\right)^{-1} = c^2, \quad (2)$$

for two-sheeted hyperboloids η=const satisfy the equation [12–14, 36]

$$z^2\eta^{-2} - \left(x^2+y^2\right)\left(1-\eta^2\right)^{-1} = c^2. \quad (3)$$

The solution of the Laplace equation in the PSCS with respect to the scalar potential of the MF for the external region $\xi>\xi_0$ outside the sources has the form [12–14]

$$U=\frac{1}{4\pi}\sum_{n=1}^{\infty}\sum_{m=0}^{n}Q_n^m(\xi)\left(c_n^m\cos m\varphi+s_n^m\sin m\varphi\right)P_n^m(\eta), \quad (4)$$

where P_n^m, Q_n^m are the associated Legendre functions of the first and second kind, respectively, with degree n and order m; c_n^m, s_n^m are constant coefficients characterizing the MF in the PSCS.

The scalar potential $U(\xi, \eta, \varphi)$, presented in the PSCS (4), can also be considered in the CCS $U(x, y, z)$, expressing $\{\xi, \eta, \varphi\}$ through $\{x, y, z\}$ in (1). To do this, it is necessary to solve (2) and (3), respectively, with respect to ξ and η. And to find φ, we divide the second equation by the first in (1). We obtain the following expressions:

$$\begin{cases}\xi=\dfrac{1}{2c}\left[\sqrt{x^2+y^2+(z+c)^2}+\sqrt{x^2+y^2+(z-c)^2}\right];\\ \eta=\dfrac{1}{2c}\left[\sqrt{x^2+y^2+(z+c)^2}-\sqrt{x^2+y^2+(z-c)^2}\right];\\ \varphi=\arctan\dfrac{y}{x}.\end{cases} \quad (5)$$

We can find the projections of magnetic induction using the known relationship $\boldsymbol{B}=-\mu_0\mathrm{grad}U$. Moreover, it should be borne in mind that when taking partial derivatives with respect to x, y, z, the function $U(x, y, z)$ should be perceived as a complex $U[\xi(x, y, z), \eta(x, y, z), \varphi(x, y)]$ and act in accordance with the differentiation of a complex function.

Let us write the partial derivatives with respect to x, y, z of the coordinates ξ, η, φ:

$$\begin{cases}\xi_x'=\dfrac{1}{2c}\left[\dfrac{x}{\sqrt{x^2+y^2+(z+c)^2}}+\dfrac{x}{\sqrt{x^2+y^2+(z-c)^2}}\right];\\ \xi_y'=\dfrac{1}{2c}\left[\dfrac{y}{\sqrt{x^2+y^2+(z+c)^2}}+\dfrac{y}{\sqrt{x^2+y^2+(z-c)^2}}\right];\\ \xi_z'=\dfrac{1}{2c}\left[\dfrac{z+c}{\sqrt{x^2+y^2+(z+c)^2}}+\dfrac{z-c}{\sqrt{x^2+y^2+(z-c)^2}}\right];\end{cases} \quad (6)$$

$$\begin{cases}\eta_x'=\dfrac{1}{2c}\left[\dfrac{x}{\sqrt{x^2+y^2+(z+c)^2}}-\dfrac{x}{\sqrt{x^2+y^2+(z-c)^2}}\right];\\ \eta_y'=\dfrac{1}{2c}\left[\dfrac{y}{\sqrt{x^2+y^2+(z+c)^2}}-\dfrac{y}{\sqrt{x^2+y^2+(z-c)^2}}\right];\\ \eta_z'=\dfrac{1}{2c}\left[\dfrac{z+c}{\sqrt{x^2+y^2+(z+c)^2}}-\dfrac{z-c}{\sqrt{x^2+y^2+(z-c)^2}}\right];\end{cases} \quad (7)$$

$$\begin{cases}\varphi_x'=-\dfrac{y}{x^2+y^2};\\ \varphi_y'=\dfrac{x}{x^2+y^2}.\end{cases} \quad (8)$$

Using recurrence relations for associated Legendre functions [36]:

$$(x^2-1)\frac{\mathrm{d}P_n^m(x)}{\mathrm{d}x}=-(n+1)xP_n^m(x)+(n-m+1)P_{n+1}^m(x), \quad (9)$$

$$(x^2-1)\frac{\mathrm{d}Q_n^m(x)}{\mathrm{d}x}=-(n+1)xQ_n^m(x)+(n-m+1)Q_{n+1}^m(x), \quad (10)$$

let's take the derivative with respect to t from the product of complex functions $P_n^m[x(t)]$ and $Q_n^m[y(t)]$:

$$\begin{aligned}&\frac{\mathrm{d}}{\mathrm{d}t}\left\{P_n^m[x(t)]Q_n^m[y(t)]\right\}=\\ &=\frac{1}{x^2-1}x_t'\left[-(n+1)xP_n^m(x)+(n-m+1)P_{n+1}^m(x)\right]Q_n^m(y)+\\ &+\frac{1}{y^2-1}y_t'\left[-(n+1)yQ_n^m(y)+(n-m+1)Q_{n+1}^m(y)\right]P_n^m(x).\end{aligned} \quad (11)$$

Note that in (11) $x(t)$, $y(t)$ are simply abstract functions that have no relation to the coordinates (1). Now, using (5) – (8), (11) and the relation $\boldsymbol{B}=-\mu_0\mathrm{grad}U$, we write the x-projection of $\boldsymbol{B}$:

$$\begin{aligned}&B_x(x,y,z)=-\mu_0\frac{\partial}{\partial x}\left\{U\left[\xi(x,y,z),\eta(x,y,z),\varphi(x,y)\right]\right\}=\\ &=-\frac{\mu_0}{4\pi}\sum_{n=1}^{\infty}\sum_{m=0}^{n}\left\{\begin{aligned}&m\varphi_x'\left(s_n^m\cos m\varphi-c_n^m\sin m\varphi\right)Q_n^m(\xi)P_n^m(\eta)+\left(c_n^m\cos m\varphi+s_n^m\sin m\varphi\right)\times\\ &\times\left\{\frac{1}{\eta^2-1}\eta_x'\left[-(n+1)\eta P_n^m(\eta)+(n-m+1)P_{n+1}^m(\eta)\right]Q_n^m(\xi)+\right.\\ &\left.+\frac{1}{\xi^2-1}\xi_x'\left[-(n+1)\xi Q_n^m(\xi)+(n-m+1)Q_{n+1}^m(\xi)\right]P_n^m(\eta)\right\}\end{aligned}\right\}.\end{aligned} \quad (12)$$

After simplification and grouping relative to functions $Q_n^m(\xi)$ and $P_n^m(\eta)$ to reduce calculation time, we obtain the final formula for B_x:

$$B_x(x,y,z)=-\frac{\mu_0}{4\pi}\sum_{n=1}^{\infty}\sum_{m=0}^{n}\left\{\begin{array}{l}\left[\left[m\varphi_x'\left(s_n^m\cos m\varphi-c_n^m\sin m\varphi\right)-(n+1)\left(\frac{\eta_x'\eta}{\eta^2-1}+\frac{\xi_x'\xi}{\xi^2-1}\right)\left(c_n^m\cos m\varphi+s_n^m\sin m\varphi\right)\right]\times\right.\\ \times P_n^m(\eta)Q_n^m(\xi)+(n-m+1)\left[\frac{\eta_x'}{\eta^2-1}P_{n+1}^m(\eta)Q_n^m(\xi)+\frac{\xi_x'}{\xi^2-1}P_n^m(\eta)Q_{n+1}^m(\xi)\right]\times\\ \left.\times\left(c_n^m\cos m\varphi+s_n^m\sin m\varphi\right)\right.\end{array}\right\}. \quad (13)$$

Similarly, we obtain formulas for B_y, B_z (note that in the case of B_z the first term in the curly brackets is zero, since $\varphi_z' = 0$):

$$B_y(x,y,z)=-\frac{\mu_0}{4\pi}\sum_{n=1}^{\infty}\sum_{m=0}^{n}\left\{\begin{array}{l}\left[\left[m\varphi_y'\left(s_n^m\cos m\varphi-c_n^m\sin m\varphi\right)-(n+1)\left(\frac{\eta_y'\eta}{\eta^2-1}+\frac{\xi_y'\xi}{\xi^2-1}\right)\left(c_n^m\cos m\varphi+s_n^m\sin m\varphi\right)\right]\times\right.\\ \times P_n^m(\eta)Q_n^m(\xi)+(n-m+1)\left[\frac{\eta_y'}{\eta^2-1}P_{n+1}^m(\eta)Q_n^m(\xi)+\frac{\xi_y'}{\xi^2-1}P_n^m(\eta)Q_{n+1}^m(\xi)\right]\times\\ \left.\times\left(c_n^m\cos m\varphi+s_n^m\sin m\varphi\right)\right.\end{array}\right\}; \quad (14)$$

$$B_z(x,y,z)=-\frac{\mu_0}{4\pi}\sum_{n=1}^{\infty}\sum_{m=0}^{n}\left\{\begin{array}{l}\left[-(n+1)\left(\frac{\eta_z'\eta}{\eta^2-1}+\frac{\xi_z'\xi}{\xi^2-1}\right)\left(c_n^m\cos m\varphi+s_n^m\sin m\varphi\right)\right]P_n^m(\eta)Q_n^m(\xi)+\\ +(n-m+1)\left[\frac{\eta_z'}{\eta^2-1}P_{n+1}^m(\eta)Q_n^m(\xi)+\frac{\xi_z'}{\xi^2-1}P_n^m(\eta)Q_{n+1}^m(\xi)\right]\times\\ \times\left(c_n^m\cos m\varphi+s_n^m\sin m\varphi\right)\end{array}\right\}. \quad (15)$$

Note, that all the formulas (1) – (15) given above are for the case when the technical object is extended along the z axis However, a more familiar coordinate system is also often considered, when the technical object is extended along the x axis. If the technical object is extended along the x-axis, then the CCS must be rotated relative to the PSCS so that the x-axis takes the place of the z-axis, y takes the place of x, and z takes the place of y. In this case, the following replacement must be made in formulas (5) – (8): $x \to y$; $y \to z$; $z \to x$. And in the right-hand parts of formulas (13) – (15): $B_x \to B_y$; $B_y \to B_z$; $B_z \to B_x$.

Definition of forward magnetostatics problem for spherical sources. Let us consider analytical formulas for projections of magnetic induction in CCS using spherical harmonics. The relationship between the right triple of unit vectors $\{x, y, z\}$ in CCS and triple $\{r, \theta, \varphi\}$ in SCS has form [14, 36]:

$$\left\{\begin{array}{l}x=r\sin\theta\cos\varphi;\\ \qquad\qquad r\in[0,\infty];\\ y=r\sin\theta\sin\varphi;\Rightarrow\theta\in[0,\pi];\\ \qquad\qquad \varphi\in[0,2\pi];\\ z=r\cos\theta.\end{array}\right. \quad (16)$$

The solution of the Laplace equation in the SCS with respect to the scalar potential of the MF for the region outside the sphere $r>R_0$, where the sources of this field are contained, has the form [14]

$$U=\frac{1}{4\pi}\sum_{n=1}^{\infty}\frac{1}{r^{n+1}}\sum_{m=0}^{n}\left(g_n^m\cos m\varphi+h_n^m\sin m\varphi\right)\times\ldots \quad (17)$$
$$\ldots\times P_n^m(\cos\theta),$$

where g_n^m, h_n^m, are constant coefficients characterizing the MF in the SCS.

Using (16), we write the relationship between $\{x, y, z\}$ and $\{r, \cos\theta, \varphi\}$ this way:

$$\left\{\begin{array}{l}r=\sqrt{x^2+y^2+z^2};\\ \cos\theta=\dfrac{z}{\sqrt{x^2+y^2+z^2}};\\ \varphi=\arctan\dfrac{y}{x}.\end{array}\right. \quad (18)$$

Let us write the partial derivatives with respect to x, y, z of the coordinate r and the function $\cos\theta$ (φ_x' and φ_y' are already obtained by (8)):

$$\left\{\begin{array}{l}r_x'=\dfrac{x}{\sqrt{x^2+y^2+z^2}};\\ r_y'=\dfrac{y}{\sqrt{x^2+y^2+z^2}};\\ r_z'=\dfrac{z}{\sqrt{x^2+y^2+z^2}};\end{array}\right. \quad (19)$$

$$\begin{cases} (\cos\theta)'_x = -\dfrac{xz}{\sqrt{\left(x^2+y^2+z^2\right)^3}}; \\ (\cos\theta)'_y = -\dfrac{yz}{\sqrt{\left(x^2+y^2+z^2\right)^3}}; \\ (\cos\theta)'_z = \dfrac{x^2+y^2}{\sqrt{\left(x^2+y^2+z^2\right)^3}}. \end{cases} \tag{20}$$

Using the recurrence relation (9), we take the derivative with respect to t of the product of complex functions $\dfrac{1}{r^{n+1}(t)}$ and $P_n^m[x(t)]$:

$$\frac{\mathrm{d}}{\mathrm{d}t}\left\{\frac{1}{r^{n+1}(t)}P_n^m[x(t)]\right\} = -r_t'\frac{n+1}{r^{n+2}}P_n^m(x) + \\ + \frac{1}{x^2-1}x_t'\left[-(n+1)xP_n^m(x)+(n-m+1)P_{n+1}^m(x)\right]\frac{1}{r^{n+1}}. \tag{21}$$

Proceeding in a similar manner as for spheroidal coordinates, using (8), (18) – (21) and the relation $\boldsymbol{B} = -\mu_0 \mathrm{grad} U$, we write the x-projection of $\boldsymbol{B}$:

$$B_x(x,y,z) = -\mu_0\frac{\partial}{\partial x}\{U[r(x,y,z),\cos\theta(x,y,z),\varphi(x,y)]\} = \\ = -\frac{\mu_0}{4\pi}\sum_{n=1}^{\infty}\sum_{m=0}^{n}\left\{\begin{array}{l} m\varphi_x'\dfrac{1}{r^{n+1}}\left(h_n^m\cos m\varphi - g_n^m\sin m\varphi\right)P_n^m(\cos\theta)+\left(g_n^m\cos m\varphi + h_n^m\sin m\varphi\right)\times \\ \times\left\{\begin{array}{l} -r_x'\dfrac{n+1}{r^{n+2}}P_n^m(\cos\theta)+\dfrac{1}{\cos^2\theta-1}(\cos\theta)'_x\times \\ \times\left[-(n+1)\cos\theta\cdot P_n^m(\cos\theta)+(n-m+1)P_{n+1}^m(\cos\theta)\right]\dfrac{1}{r^{n+1}} \end{array}\right. \end{array}\right\}. \tag{22}$$

After simplifying and grouping relative functions $P_n^m\cos\theta$ to reduce calculation time, we obtain the final formula for B_x:

$$B_x(x,y,z) = -\frac{\mu_0}{4\pi}\sum_{n=1}^{\infty}\frac{1}{r^{n+2}}\times \\ \times\sum_{m=0}^{n}\left\{\begin{array}{l} \left[m\varphi_x' r\left(h_n^m\cos m\varphi - g_n^m\sin m\varphi\right)-(n+1)\left(r_x'+\dfrac{(\cos\theta)'_x r\cos\theta}{\cos^2\theta-1}\right)\left(g_n^m\cos m\varphi + h_n^m\sin m\varphi\right)\right]\times \\ \times P_n^m(\cos\theta)+(n-m+1)\dfrac{(\cos\theta)'_x r}{\cos^2\theta-1}\left(g_n^m\cos m\varphi + h_n^m\sin m\varphi\right)P_{n+1}^m(\cos\theta) \end{array}\right\}. \tag{23}$$

Similarly, we obtain formulas for B_y, B_z (note that in the case of B_z the first term in the curly brackets is zero, since ($\varphi_z' = 0$):

$$B_y(x,y,z) = -\frac{\mu_0}{4\pi}\sum_{n=1}^{\infty}\frac{1}{r^{n+2}}\times \\ \times\sum_{m=0}^{n}\left\{\begin{array}{l} \left[m\varphi_y' r\left(h_n^m\cos m\varphi - g_n^m\sin m\varphi\right)-(n+1)\left(r_y'+\dfrac{(\cos\theta)'_y r\cos\theta}{\cos^2\theta-1}\right)\left(g_n^m\cos m\varphi + h_n^m\sin m\varphi\right)\right]\times \\ \times P_n^m(\cos\theta)+(n-m+1)\dfrac{(\cos\theta)'_y r}{\cos^2\theta-1}\left(g_n^m\cos m\varphi + h_n^m\sin m\varphi\right)P_{n+1}^m(\cos\theta) \end{array}\right\}. \tag{24}$$

$$B_z(x,y,z) = -\frac{\mu_0}{4\pi}\sum_{n=1}^{\infty}\frac{1}{r^{n+2}}\sum_{m=0}^{n}\left\{\begin{array}{l} \left[-(n+1)\left(r_z'+\dfrac{(\cos\theta)'_z r\cos\theta}{\cos^2\theta-1}\right)\left(g_n^m\cos m\varphi + h_n^m\sin m\varphi\right)\right]\times P_n^m(\cos\theta)+ \\ +(n-m+1)\dfrac{(\cos\theta)'_z r}{\cos^2\theta-1}\left(g_n^m\cos m\varphi + h_n^m\sin m\varphi\right)P_{n+1}^m(\cos\theta) \end{array}\right\}. \tag{25}$$

It is quite simple to calculate the MF created by several, for example N_1, spheroidal sources with coordinates x_i, y_i, z_i relative to the center of the technical object $\{x_0, y_0, z_0\}=\{0, 0, 0\}$ and several, for example N_2, spherical sources that compensate for the MF in a given area, with coordinates x_j, y_j, z_j relative to the center of the technical object. For this, we use the superposition principle and obtain, for example, for the projection:

$$B_x^{result}(x_p,y_p,z_p) = \\ = \sum_{i=1}^{N_1}B_{xi}(x_p-x_i,y_p-y_i,z_p-z_i)+ \\ + \sum_{j=1}^{N_2}B_{xj}(x_p-x_j,y_p-y_j,z_p-z_j),$$

where B_{xi} is calculated by (13) with its parameters c_i, c_{ni}^m, s_{ni}^m and B_{xj} calculated by (23) with its parameters g_{nj}^m, h_{nj}^m. The same is true for other projections.

Thus, using formulas (13) – (15), (23) – (25), taking into account auxiliary formulas (5) – (8), (18) – (20), based on superposition principle, it is possible to calculate the MF at an arbitrary point in the region outside the spherical and spheroidal sources.

The advantage of these formulas over the known ones [12–14] are:

1) the projections of the magnetic induction in the CCS are explicitly written due to taking direct derivatives with respect to the CCS coordinates;

2) their generalization to the case of the *n*-harmonic;

3) there is no need to transform from one coordinate system to another, which is especially important in the case of calculating the MF from several spherical and spheroidal sources;

4) the relative compactness of the formulas.

Definition of prediction geometric inverse magnetostatics problems. Prediction problem implies design of mathematical model of MF of technical object based on experimentally measured values of MF components, as a rule, in near zone of technical object. The vast majority of mathematical models of MF of various technical objects – spacecraft, naval vessels and submarines – are MDMs.

The main advantage of MDMs is the ease of calculating components of MF generated by each magnetic dipole as a source of MF in rectangular coordinate system connected to center of technical facility. The main disadvantage of MDMs is large number of dipoles required to adequately simulate MF of technical object to actually measured values of MF on magnetodynamic stand. This is especially typical for modeling MF of elongated energy-saturated technical objects.

A significant simplification of modeling MF of elongated energy-saturated technical objects achieved by using elongated spheroidal MF sources in prolate spheroidal coordinate system. Moreover, to obtain required adequacy of mathematical model to actually measured characteristics of MF number of elongated spheroidal MF sources may be required tens or even hundreds of times less compared to number of dipole MF sources [37–42].

The obtained formulas (13) – (15) and (23) – (25) allow us to solve forward problem of magnetostatics. Using these formulas calculated components of MF induction in CCS at any point in space generated by spheroidal and spherical sources of MF. Naturally, in this case, coordinates of spatial location of these MF sources and their harmonics are specified.

The convenience of using these formulas lies in fact that components of projections of resulting MF in CCS are equal to sums of corresponding projections of MF induction of same in CCS, generated by all MF spheroidal and spherical sources.

Consider formulation of geometric inverse problem of design mathematical model of MF based on results of experimental measurements of MF. Introduce vector $\boldsymbol{G}$ of uncertainties in magnetic characteristics of technical object, due to inaccurate knowledge of initial values of magnetic characteristics of blocks of technical object, as well as changes in these magnetic characteristics in different operating modes [43–48].

Typically, MF measurements are carried out in CCS associated with the center of technical object. Let us introduce vector $\boldsymbol{Y}_M(\boldsymbol{G})$ of measured MF components.

Consider design of mathematical model of elongated energy-saturated object in form of set of spheroidal MF sources. Let us introduce vector $\boldsymbol{X}_P$ of desired parameters components of which are coordinates of spatial location and spatial harmonics of MF of these spheroidal MF sources. Then, vector $\boldsymbol{Y}_C(\boldsymbol{X}_P, \boldsymbol{G})$ calculated values of MF calculated based on (13) – (15).

Then solution of predictions geometric inverse problem of magnetostatics reduced to solution of vector game [49]

$$\boldsymbol{E}(\boldsymbol{X}_P, \boldsymbol{G}) = \boldsymbol{Y}_M(\boldsymbol{G}) - \boldsymbol{Y}_C(\boldsymbol{X}_P, \boldsymbol{G}). \qquad (26)$$

To calculate payoff vector game (26) it is necessary to repeatedly solved forward problem of magnetostatics (13) – (15) for elongated spheroidal MF sources.

Definition of control geometric inverse magnetostatics problems. The problem of controlling the magnetic silence of technical object is design of spatial arrangement and spatial harmonic sources of compensating MF. With the help of these compensating MF sources resulting MF of elongated energy-saturated technical object generated in such a way that stringent requirements for magnetic silence of energy-saturated technical object satisfied.

Note that the requirements for magnetic silence of technical object are usually imposed in the far zone. In particular, for military ships and submarines, requirements are imposed on magnitude and rate of change of MF components at control depth when an object moves at given speed.

The designed predictive mathematical model of MF of elongated energy-saturated object calculated based on experimental measurements of MF in near zone. Based on this prediction model of MF in near zone values of characteristics of MF of technical object calculated in far zone, which limited to meet requirements of magnetic silence of technical object.

Introduced uncertainty vector $\boldsymbol{G}_C$ of magnetic characteristics of energy-saturated technical object [43–48]. Then, based on the designed predictive model vector $\boldsymbol{B}(\boldsymbol{G})$ of initial values of magnetic characteristics of technical object, which determines its magnetic silence calculated.

To compensate for the original MF of technical object introduced dipole sources of compensating MF. Introduced vector $\boldsymbol{X}_C$ of required parameters for solving control geometric inverse problem of magnetostatics components of which are coordinates of spatial location and spatial harmonics of compensating dipoles.

Then vector $\boldsymbol{B}_C(\boldsymbol{X}_C, \boldsymbol{G})$ of calculated characteristics of magnetic silence of technical object calculated based on solution of forward problem of magnetostatics (23) – (25) for spherical MF sources.

Then solution of control geometric inverse problem of magnetostatics reduced to solution of vector game

$$\boldsymbol{B}_R(\boldsymbol{X}_C, \boldsymbol{G}_C) = \boldsymbol{B}(\boldsymbol{G}_C) + \boldsymbol{B}_C(\boldsymbol{X}_C). \qquad (27)$$

To calculate payoff vector game (27) it is necessary to repeatedly solved forward problem of magnetostatics (23) – (25) for spherical MF sources.

Inverse magnetostatics problems solution method. Solutions of both vector games (26) and (27) calculated by particle multi-swarm nonlinear optimization algorithms. Number of swarms calculated by number of components in vectors games (26), (27), so that with help of each swarm solution of scalar game calculated.

Each swarm j contained two types of particles i. Position $x_{ij}(t)$ and movement velocity $v_{ij}(t)$ for first type particles calculated from conditions of minimizing payoff game along vectors $\boldsymbol{X}_P$ and $\boldsymbol{X}_C$ of desired parameters and described by following expressions:

$$\begin{aligned} v_{ij}(t+1) &= w_{1j}v_{ij}(t) + c_{1j}r_{1j}(t)\times\ldots \\ \ldots &\times H\left(p_{1ij}(t) - \varepsilon_{1ij}(t)\right)\left[y_{ij}(t) - \ldots\right. \\ \ldots &\left. - x_{ij}(t)\right] + c_{2j}r_{2j}(t)H\left(p_{2ij}(t) - \ldots\right. \\ \ldots &\left. - \varepsilon_{2ij}(t)\right)\left[y_j^*(t) - x_{ij}(t)\right]; \end{aligned} \tag{28}$$

$$x_{ij}(t+1) = x_{ij}(t) + v_{ij}(t+1). \tag{29}$$

Moreover, the best local $y_{ij}(t)$ and global $y_j^*(t)$ position of particle determined from condition of minimizing game vector along vectors $\boldsymbol{X}_P$ and $\boldsymbol{X}_C$ of desired parameters for games (26) and (27) respectively.

Position $g_{ij}(t)$ and movement velocity $u_{ij}(t)$, $z_{ij}(t)$ for second type particles calculated from conditions of minimizing payoff game along vectors $\boldsymbol{G}$ and $\boldsymbol{G}_C$ of magnetic characteristics uncertainty and described by following expressions:

$$\begin{aligned} u_{ij}(t+1) &= w_{2j}u_{ij}(t) + c_{3j}r_{3j}(t)H\times\ldots \\ \ldots &\times\left(p_{3ij}(t) - \varepsilon_{3ij}(t)\right)\left[z_{ij}(t) - \delta_{ij}(t)\right] + \ldots \\ \ldots &+ c_{4j}r_{4j}(t)H\left(p_{4ij}(t) - \varepsilon_{4ij}(t)\right)\times\ldots \\ \ldots &\times\left[z_j^*(t) - \delta_{ij}(t)\right]; \end{aligned} \tag{30}$$

$$g_{ij}(t+1) = \delta_{ij}(t) + u_{ij}(t+1). \tag{31}$$

Moreover, the best local $z_{ij}(t)$ and global $z_j^*(t)$ position of particle calculated from condition of minimizing game vector along vectors $\boldsymbol{G}$ and $\boldsymbol{G}_C$ of magnetic characteristics uncertainty for games (26) and (27) respectively.

To narrow Pareto set of optimal solutions in (28) – (31) binary preference relations of local games used [49].

Simulation results. Let us consider the results of MF modeling of elongated energy-saturated technical object 200 m long and 40 m wide, for which the magnetic silence requirements are set at a control depth of 19 m and 60 m. The initial MF was modeled using 16 dipole sources of the technical object's MF, the measurement of which was performed at 909 points.

For this example, we will consider checking the correctness and efficiency of applying formulas (13) – (15) and (23) – (25). We will check the correctness and efficiency of the formulas on the values of spherical and spheroidal harmonics obtained as a result of optimization. The following harmonic values were obtained:

– for spheroidal c = 45.2171, c_1^0 = –2.97466, c_1^1 = –0.78397, s_1^1 = –1.2093, c_2^0 = –7.61832, c_1^2 = 1.02365, c_2^2 = –0.0247825, s_2^1 = 0.321276, s_2^2 = 0.0174991, c_3^0 = 2.30698, c_3^1 = –0.555808, c_3^2 = 0.0022228, c_3^3 = 0.000110621, s_3^1 = 0.856448, s_3^2 = –0.0155725, s_3^3 = 0.0000373957;

– for spherical g_1^0 = –1811.98, g_1^1 = 1145.52, h_1^1 = 460.332, g_2^0 = –2567.85, g_2^1 = –13073.2, g_2^2 = 3352.89, h_2^1 = –16555.6, h_2^2 = 6747.55, g_3^0 = –54352.8, g_3^1 = 38472.4, g_3^2 = 22857.2, g_3^3 = –9441.96, h_3^1 = 18004.4, h_3^2 = –31867.1, h_3^3 = 8041.49.

These values were obtained on the basis of solving the prediction of the geometric inverse problem of magnetostatics (26) by minimizing the sum of the squares of the differences in the projections of the real MF and the MF models: for spheroidal (13) – (15) and spherical (23) – (25) MF sources up to and including the third harmonics.

The results of calculating the signatures of initial MF (solid lines) with models based on spheroidal (dotted lines) and spherical (dash-dotted lines) harmonics for projections B_x – red, B_y – green, B_z – blue are shown in Fig. 2 – 4, respectively, for 3 cases: Y = –20 m, Y = 0 m and Y = 20 m. Since the technical object is extended, the MF model based on spheroidal harmonics gives better results in approximating the original MF.

The correctness of formulas (23) – (25) for spherical harmonics verified by comparing them with the results obtained by taking numerical partial derivatives with respect to the coordinates x, y, z from (17) taking into account (18) and standard approach [35]. The calculation results of the proposed method and the standard approach [35] are in full agreement with machine accuracy and differ from the results of numerical differentiation by about 10^{-20} T.

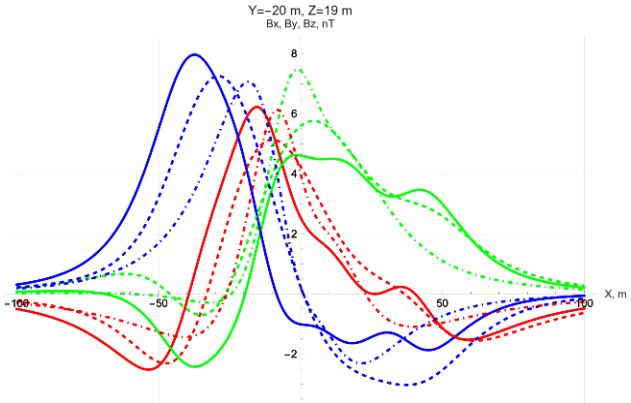

Fig. 2. Magnetic signatures of original, model spherical and model spheroidal MFs for Y = –20 m

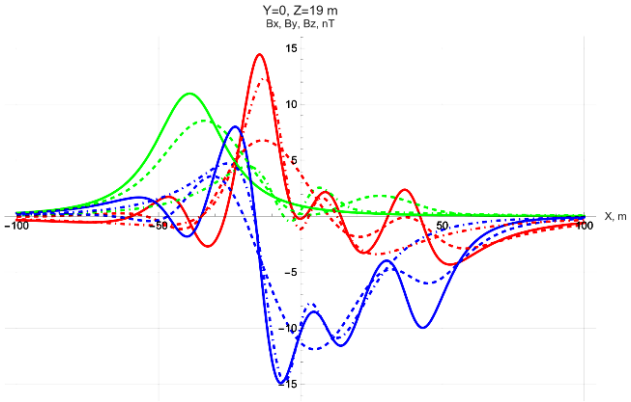

Fig. 3. Magnetic signatures of original, model spherical and model spheroidal magnetic fields for Y = 0 m

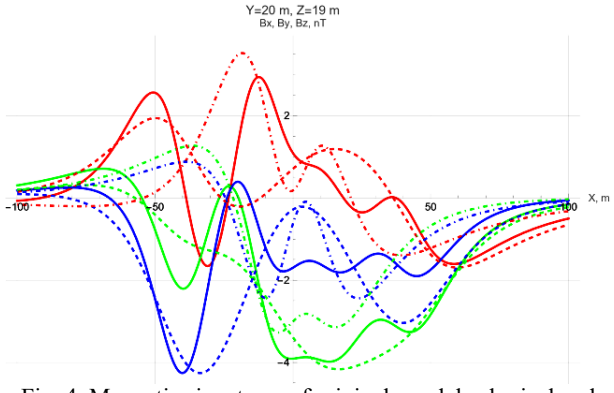

Fig. 4. Magnetic signatures of original, model spherical and model spheroidal MFs for $Y = 20$ m

Table 1 presents a comparison of the calculation time of the standard approach [35] (left column), the proposed method (right column) and the numerical one for spherical harmonics, as well as analytical formulas (13) – (15) taking into account (5) – (8) of the proposed method and the numerical one (numerical taking of derivatives with respect to the coordinates x, y, z from (4) taking into account (5)) for spheroidal harmonics. The cases of the 1st, 2nd and 3rd harmonics are considered. We see the relative parity in the calculation speed of the proposed method and the standard approach [35] and an order of magnitude faster than the calculation speed of the numerical taking of derivatives in the case of spherical harmonics.

Table 1

Comparison of calculation time of analytical and numerical formulas at $z = 19$ m

Coordinates and order of harmonics			Spherical harmonics						Spheroidal harmonics				
			Projections $\boldsymbol{B}$, nT			Time, ms			Projections $\boldsymbol{B}$, nT			Time, ms	
x, m	y, m	n	B_x	B_y	B_z	Analit.		Num.	B_x	B_y	B_z	Analit.	Num.
–100	–20	1	–0,326	0,005	0,134	0,229	0,296	2,622	–0,351	–0,016	0,313	1,492	6,486
–100	–20	2	–0,310	0,039	0,181	0,278	0,479	7,458	–0,186	0,199	0,253	3,449	18,280
–100	–20	3	–0,310	0,038	0,182	0,431	0,773	15,836	–0,242	0,209	0,224	6,055	36,577
–100	0	1	–0,302	0,109	0,134	0,189	0,293	2,543	–0,326	0,130	0,328	1,474	6,601
–100	0	2	–0,261	0,137	0,172	0,374	0,511	7,416	0,009	0,264	0,213	3,396	18,238
–100	0	3	–0,262	0,138	0,172	0,437	0,767	15,993	–0,030	0,297	0,160	5,991	36,670
–100	20	1	–0,211	0,177	0,112	0,195	0,293	2,628	–0,199	0,218	0,278	1,501	6,505
–100	20	2	–0,160	0,186	0,136	0,275	0,481	7,432	0,156	0,180	0,154	3,406	17,987
–100	20	3	–0,160	0,188	0,135	0,424	0,761	15,704	0,150	0,204	0,095	5,933	36,646
–50	–20	1	–1,615	–0,420	1,231	0,187	0,291	2,574	–0,535	–0,430	2,786	1,472	6,474
–50	–20	2	–1,325	–0,006	1,691	0,274	0,591	7,343	–1,520	1,508	2,431	3,400	18,052
–50	–20	3	–1,263	–0,063	1,694	0,423	0,764	15,959	–2,262	0,312	3,211	6,036	36,525
–50	0	1	–1,620	0,749	1,366	0,187	0,290	2,543	0,785	1,574	3,295	1,478	6,607
–50	0	2	–0,761	1,021	1,579	0,281	0,482	7,247	2,711	4,218	–2,443	3,503	17,991
–50	0	3	–0,810	1,005	1,576	0,419	0,758	15,654	–0,417	4,852	–0,338	5,948	36,437
–50	20	1	–0,483	1,198	0,800	0,201	0,291	2,565	1,286	0,864	1,385	1,487	6,476
–50	20	2	0,151	0,935	0,766	0,278	0,482	7,445	2,712	–1,321	–1,984	3,399	18,045
–50	20	3	0,142	0,973	0,723	0,419	0,758	15,651	1,944	–0,406	–2,416	6,089	36,514
0	–20	1	8,631	0,137	7,246	0,188	0,289	1,812	2,736	5,201	3,174	1,948	5,292
0	–20	2	7,634	9,690	3,450	0,275	0,469	3,868	4,941	1,274	3,902	4,691	13,401
0	–20	3	4,026	7,440	0,257	0,415	0,741	7,375	4,268	5,591	0,260	8,411	24,772
0	0	1	26,417	16,701	–13,423	0,194	0,295	1,802	4,472	7,874	–15,782	1,777	5,036
0	0	2	–11,694	–14,365	–33,622	0,291	0,491	3,920	1,621	2,420	4,089	4,205	12,287
0	0	3	–1,140	0,464	–9,774	0,418	0,744	7,281	3,802	0,238	–11,265	7,625	22,729
0	20	1	8,631	–6,433	–9,102	0,190	0,289	1,812	2,736	–7,051	–4,769	1,945	5,323
0	20	2	–2,185	–0,307	1,008	0,277	0,477	3,859	–1,343	–0,271	–1,557	4,677	13,295
0	20	3	0,182	–3,008	–0,631	0,407	0,733	7,427	0,709	–3,390	–0,283	8,393	24,713
50	–20	1	–0,915	1,370	–0,470	0,192	0,291	2,591	–1,382	3,024	–0,495	1,481	6,491
50	–20	2	–1,056	1,058	–0,751	0,340	0,480	7,332	–2,383	4,331	–3,915	3,384	18,292
50	–20	3	–0,957	1,112	–0,732	0,416	0,754	15,656	–1,149	2,594	–2,529	6,085	36,629
50	0	1	–2,220	0,749	–0,993	0,183	0,287	2,528	–5,443	1,574	–4,364	1,493	6,578
50	0	2	–1,626	0,125	–1,198	0,280	0,482	7,239	–4,774	–1,676	–8,815	3,500	18,111
50	0	3	–1,722	0,254	–1,208	0,425	0,765	15,694	–2,190	0,440	–5,484	6,007	36,845
50	20	1	–2,047	–0,593	–0,900	0,200	0,293	2,617	–3,203	–2,591	–1,896	1,483	6,513
50	20	2	–1,068	–0,629	–0,924	0,281	0,483	7,548	–0,953	–3,479	–2,190	3,421	18,310
50	20	3	–1,218	–0,677	–0,907	0,496	0,806	15,889	–1,378	–2,702	–2,557	6,119	36,763
100	–20	1	–0,255	0,186	–0,038	0,193	0,290	2,561	–0,422	0,273	0,039	1,479	6,688
100	–20	2	–0,261	0,153	–0,072	0,290	0,495	7,318	–0,726	0,287	–0,138	3,510	18,209
100	–20	3	–0,260	0,157	–0,072	0,433	0,765	17,801	–0,628	0,283	–0,153	6,013	37,144
100	0	1	–0,350	0,109	–0,055	0,187	0,288	2,552	–0,584	0,130	0,011	1,470	6,455
100	0	2	–0,325	0,066	–0,092	0,274	0,494	7,296	–0,846	–0,013	–0,170	3,377	18,165
100	0	3	–0,328	0,069	–0,092	0,426	0,764	15,637	–0,764	0,032	–0,194	6,155	36,744
100	20	1	–0,369	–0,004	–0,060	0,191	0,293	2,570	–0,574	–0,071	0,004	1,470	6,600
100	20	2	–0,316	–0,034	–0,093	0,286	0,489	7,321	–0,672	–0,273	–0,122	3,507	18,187
100	20	3	–0,321	–0,033	–0,091	0,427	0,764	15,924	–0,650	–0,222	–0,151	6,076	37,415

In the case of spheroidal harmonics, the difference in the calculation speed between the analytical and numerical methods is not as pronounced as for spherical ones, but it still takes place – by 4 or more times. Moreover, in all cases, with an increase in the order of the harmonic, this difference only increases. Let us now proceed to checking the correctness of formulas (13) – (15). The results of comparing the calculation using these formulas with the results calculated by taking numerical partial derivatives with respect to the coordinates x, y, z from (4) taking into account (5) are also consistent and differ by a deviation of about 10^{-20} T. Another way of checking is to consider the MF of a dipole and a spheroid (the case of the 1st harmonic) with an equivalent magnetic moment at large distances from the source.

It is necessary to equate the 1st spheroidal harmonics in this way [13]:

$$c_1^0 = \frac{3}{c^2} g_1^0, \quad c_1^1 = \frac{3}{2c^2} g_1^1, \quad s_1^1 = -\frac{3}{2c^2} h_1^1.$$

And for dipole model [50, formulas (2), (3)]:

$$M_x = g_1^0, \quad M_y = -g_1^1, \quad M_z = -h_1^1.$$

Let us consider the points located on the rays from the source in all 8 coordinate octants. The rays pass through points N_P. The distance from the center on these rays is R_P.

Table 2 presents the results of comparing the projections of the MF of the spheroidal model and the dipole model with an equivalent magnetic moment. As the distance from the field source increases, the relative discrepancies tend to zero.

Table 2

Asymptotic verification of the correctness of formulas (13) – (15) for the case of the 1st harmonic

Direction vector and distance		Projections $\boldsymbol{B}$, nT						Relative divergence, %		
		Spheroidal harmonics			Dipole model					
N_P	R_P	B_x	B_y	B_z	B_x	B_y	B_z	Δ_x	Δ_y	Δ_z
{–1;–1;–1}	1	16,0	–771,6	–1903,5	–30904,7	–43730,6	–56917,1	100,1	98,2	96,7
{–1;–1;–1}	10	2,8	–11,1	–20,4	–30,9	–43,7	–56,9	109,2	74,7	64,2
{–1;–1;–1}	100	–0,02801	–0,04392	–0,05727	–0,03090	–0,04373	–0,05692	9,352	0,423	0,618
{–1;–1;–1}	1000	–0,00003	–0,00004	–0,00006	–0,00003	–0,00004	–0,00006	0,094	0,007	0,009
{–1;–1;1}	1	17,5	754,0	1898,8	–13186,5	–26012,4	56917,1	100,1	102,9	96,7
{–1;–1;1}	10	4,1	2,8	19,1	–13,2	–26,0	56,9	131,3	110,7	66,4
{–1;–1;1}	100	–0,01074	–0,02543	0,05673	–0,01319	–0,02601	0,05692	18,576	2,222	0,329
{–1;–1;1}	1000	–0,00001	–0,00003	0,00006	–0,00001	–0,00003	0,00006	0,191	0,019	0,001
{–1;1;–1}	1	19,7	759,9	1892,9	13186,5	43730,6	–12825,9	99,9	98,3	114,8
{–1;1;–1}	10	6,0	7,8	14,0	13,2	43,7	–12,8	54,2	82,1	209,5
{–1;1;–1}	100	0,01498	0,04257	–0,01128	0,01319	0,04373	–0,01283	13,603	2,644	12,062
{–1;1;–1}	1000	0,00001	0,00004	–0,00001	0,00001	0,00004	–0,00001	0,145	0,025	0,118
{–1;1;1}	1	21,2	–765,7	–1897,6	30904,7	26012,4	12825,9	99,9	102,9	114,8
{–1;1;1}	10	7,3	–6,0	–15,3	30,9	26,0	12,8	76,3	123,1	219,6
{–1;1;1}	100	0,03226	0,02409	0,01074	0,03090	0,02601	0,01283	4,378	7,379	16,265
{–1;1;1}	1000	0,00003	0,00003	0,00001	0,00003	0,00003	0,00001	0,049	0,073	0,162
{1;–1;–1}	1	21,2	–765,7	–1897,6	30904,7	26012,4	12825,9	99,9	102,9	114,8
{1;–1;–1}	10	7,3	–6,0	–15,3	30,9	26,0	12,8	76,3	123,1	219,6
{1;–1;–1}	100	0,03226	0,02409	0,01074	0,03090	0,02601	0,01283	4,378	7,379	16,265
{1;–1;–1}	1000	0,00003	0,00003	0,00001	0,00003	0,00003	0,00001	0,049	0,073	0,162
{1;–1;1}	1	19,7	759,9	1892,9	13186,5	43730,6	–12825,9	99,9	98,3	114,8
{1;–1;1}	10	6,0	7,8	14,0	13,2	43,7	–12,8	54,2	82,1	209,5
{1;–1;1}	100	0,01498	0,04257	–0,01128	0,01319	0,04373	–0,01283	13,603	2,644	12,062
{1;–1;1}	1000	0,00001	0,00004	–0,00001	0,00001	0,00004	–0,00001	0,145	0,025	0,118
{1;1;–1}	1	17,5	754,0	1898,8	–13186,5	–26012,4	56917,1	100,1	102,9	96,7
{1;1;–1}	10	4,1	2,8	19,1	–13,2	–26,0	56,9	131,3	110,7	66,4
{1;1;–1}	100	–0,01074	–0,02543	0,05673	–0,01319	–0,02601	0,05692	18,576	2,222	0,329
{1;1;–1}	1000	–0,00001	–0,00003	0,00006	–0,00001	–0,00003	0,00006	0,191	0,019	0,001
{1;1;1}	1	16,0	–771,6	–1903,5	–30904,7	–43730,6	–56917,1	100,1	98,2	96,7
{1;1;1}	10	2,8	–11,1	–20,4	–30,9	–43,7	–56,9	109,2	74,7	64,2
{1;1;1}	100	–0,02801	–0,04392	–0,05727	–0,03090	–0,04373	–0,05692	9,352	0,423	0,618
{1;1;1}	1000	–0,00003	–0,00004	–0,00006	–0,00003	–0,00004	–0,00006	0,094	0,007	0,009

Conclusions.

1. For the first time a simplified method of mathematical modeling of the external magnetic field of an uncertain extended technical object is proposed, based on the analytical calculation of the magnetic field induction of spherical and spheroidal sources in the Cartesian coordinate system. Unlike known methods, this method allows modeling the magnetic field directly in the Cartesian coordinate system without finding the projection of the magnetic induction in the prolate spheroidal coordinate system and the spherical coordinate system and without their translation from the prolate spheroidal coordinate system and the spherical coordinate system to the Cartesian coordinate system and vice versa.

2. Promising magnetostatics problems are solved using the proposed method based on near-field measurements. Geometric inverse magnetostatics problems for predicting and controlling the magnetic silence of a technical object are calculated based on solving vector games. The payoff in both vector games is calculated as a solution to direct problems using the Wolfram Mathematica software package.

3. The use of the proposed simplified method allows to reduce the calculation time for determining the magnetic field induction of elongated spheroidal magnetic field sources by more than 10 times and makes it possible to reduce the calculation time of magnetic field induction of spherical magnetic field sources by more than 4 times.

4. In the future, it is planned to conduct experimental studies of the efficiency of modeling and reducing the magnetic field of uncertain extended technical objects based on the developed method.

Conflict of interest. The authors declare that they have no conflicts of interest.

REFERENCES

1. Rozov V.Yu., Getman A.V., Petrov S.V., Erisov A.V., Melanchenko A.G., Khoroshilov V.S., Schmidt I.R Spacecraft magnetism. *Technical Electrodynamics. Thematic issue «Problems of modern electrical engineering»*, 2010, part 2, pp. 144-147. (Rus).

2. *ECSS-E-HB-20-07A. Space engineering: Electromagnetic compatibility hand-book. ESA-ESTEC. Requirements & Standards Division*. Noordwijk, Netherlands, 2012. 228 p.

3. Droughts S.A., Fedorov O.P. Space project Ionosat-Micro. Monograph. Kyiv, Akademperiodika Publ., 2013. 218 p. (Rus).

4. Holmes J.J. *Exploitation of A Ship's Magnetic Field Signatures*. Springer Cham, 2006. 67 p. doi: https://doi.org/10.1007/978-3-031-01693-6.

5. Woloszyn M., Jankowski P. Simulation of ship's deperming process using Opera 3D. 2017 18th International Symposium on Electromagnetic Fields in Mechatronics, Electrical and Electronic Engineering (ISEF) Book of Abstracts, 2017, pp. 1-2. doi: https://doi.org/10.1109/ISEF.2017.8090680.

6. Birsan M., Holtham P., Carmen. Using global optimisation techniques to solve the inverse problem for the computation of the static magnetic signature of ships. *Defense Research Establishment Atlantic*, 9 Grove St., PO Box 1012, Dartmouth, Nova Scotia, B2Y 3Z7, Canada.

7. Zuo C., Ma M., Pan Y., Li M., Yan H., Wang J., Geng P., Ouyang J. Multi-objective optimization design method of naval vessels degaussing coils. *Proceedings of SPIE - The International Society for Optical Engineering*, 2022, vol. 12506, art. no. 125060J. doi: https://doi.org/10.1117/12.2662888.

8. Baranov M.I., Rozov V.Y., Sokol Y.I. To the 100th anniversary of the National Academy of Sciences of Ukraine – the cradle of domestic science and technology. *Electrical Engineering & Electromechanics*, 2018, no. 5, pp. 3-11. doi: https://doi.org/10.20998/2074-272X.2018.5.01.

9. Chadebec O., Rouve L.-L., Coulomb J.-L. New methods for a fast and easy computation of stray fields created by wound rods. *IEEE Transactions on Magnetics*, 2002, vol. 38, no. 2, pp. 517-520. doi: https://doi.org/10.1109/20.996136.

10. Rozov V.Yu. Methods for reducing external magnetic fields of energy-saturated objects. *Technical Electrodynamics*, 2001, no. 1, pp. 16-20.

11. Rozov V.Y., Tkachenko O.O., Yerisov A.V., Grinchenko V.S. Analytical calculation of magnetic field of three-phase cable lines with two-point bonded shields. *Technical Electrodynamics*, 2017, no. 2, pp. 13-18. (Rus). doi: https://doi.org/10.15407/techned2017.02.013.

12. Rozov V.Y., Pelevin D.Y., Kundius K.D. Simulation of the magnetic field in residential buildings with built-in substations based on a two-phase multi-dipole model of a three-phase current conductor. *Electrical Engineering & Electromechanics*, 2023, no. 5, pp. 87-93. doi: https://doi.org/10.20998/2074-272X.2023.5.13.

13. Rozov V.Yu., Getman A.V., Kildishev A.V. Spatial harmonic analysis of the external magnetic field of extended objects in a prolate spheroidal coordinate system. *Technical Electrodynamics*, 1999, no. 1, pp. 7-11. (Rus).

14. Rozov V.Yu. Mathematical model of electrical equipment as a source of external magnetic field. *Technical Electrodynamics*, 1995, no. 2, pp. 3-7. (Rus).

15. Volokhov S.A., Dobrodeev P.N., Ivleva L.F. Spatial harmonic analysis of the external magnetic field of a technical object. *Technical Electrodynamics*, 1996, no. 2, pp. 3-8. (Rus).

16. Getman A.V. *Analysis and synthesis of the magnetic field structure of technical objects on the basis of spatial harmonics*. Dissertation thesis for the degree of Doctor of Technical Sciences. Kharkiv, 2018. 43 p. (Ukr).

17. Xiao C., Xiao C., Li G. Modeling the ship degaussing coil's effect based on magnetization method. *Communications in Computer and Information Science*, 2012, vol. 289, pp. 62-69. doi: https://doi.org/10.1007/978-3-642-31968-6_8.

18. Wołoszyn M., Jankowski P. Ship's de-perming process using coils lying on seabed. *Metrology and Measurement Systems*, 2019, vol. 26, no. 3, pp. 569-579. doi: https://doi.org/10.24425/mms.2019.129582.

19. Fan J., Zhao W., Liu S., Zhu Z. Summary of ship comprehensive degaussing. *Journal of Physics: Conference Series*, 2021, vol. 1827, no. 1, art. no. 012014. doi: https://doi.org/10.1088/1742-6596/1827/1/012014.

20. Getman A.V. Spatial harmonic analysis of the magnetic field of the sensor of the neutral plasma component. *Eastern European Journal of Advanced Technologies*, 2010, vol. 6, no. 5(48), pp. 35-38. doi: https://doi.org/10.15587/1729-4061.2010.3326.

21. Getman A. Ensuring the Magnetic Compatibility of Electronic Components of Small Spacecraft. *2022 IEEE 3rd KhPI Week on Advanced Technology (KhPIWeek)*, 2022, no. 1-4. doi: https://doi.org/10.1109/KhPIWeek57572.2022.9916339.

22. Acuña M.H. *The design, construction and test of magnetically clean spacecraft – a practical guide*. NASA/GSFC internal report. 2004.

23. Junge A., Marliani F. Prediction of DC magnetic fields for magnetic cleanliness on spacecraft. *2011 IEEE International Symposium on Electromagnetic Compatibility*, 2011, pp. 834-839. doi: https://doi.org/10.1109/ISEMC.2011.6038424.

24. Lynn G.E., Hurt J.G., Harriger K.A. Magnetic control of satellite attitude. *IEEE Transactions on Communication and Electronics*, 1964, vol. 83, no. 74, pp. 570-575. doi: https://doi.org/10.1109/TCOME.1964.6539511.

25. Junge A., Trougnou L., Carrubba E. Measurement of Induced Equivalent Magnetic Dipole Moments for Spacecraft Units and Components. *Proceedings ESA Workshop Aerospace EMC 2009 ESA WPP-299*, 2009, vol. 4, no. 2, pp. 131-140.

26. Mehlem K., Wiegand A. Magnetostatic cleanliness of spacecraft. *2010 Asia-Pacific International Symposium on Electromagnetic Compatibility*, 2010, pp. 936-944. doi: https://doi.org/10.1109/APEMC.2010.5475692.

27. Messidoro P., Braghin M., Grande M. Magnetic cleanliness verification approach on tethered satellite. *16th Space Simulation Conference: Confirming Spaceworthiness into the Next Millennium*, 1991, pp. 415-434.

28. Mehlem K., Narvaez P. Magnetostatic cleanliness of the radioisotope thermoelectric generators (RTGs) of Cassini. *1999 IEEE International Symposium on Electromagnetic Compatability*, 1999, vol. 2, pp. 899-904. doi: https://doi.org/10.1109/ISEMC.1999.810175.

29. Eichhorn W.L. *Magnetic dipole moment determination by near-field analysis*. Goddard Space Flight Center. Washington, D.C., National Aeronautics and Space Administration, 1972. NASA technical note, D 6685. 87 p.

30. Matsushima M., Tsunakawa H., Iijima Y., Nakazawa S., Matsuoka A., Ikegami S., Ishikawa T., Shibuya H., Shimizu H., Takahashi F. Magnetic Cleanliness Program Under Control of Electromagnetic Compatibility for the SELENE (Kaguya) Spacecraft. *Space Science Reviews*, 2010, vol. 154, no. 1-4, pp. 253-264. doi: https://doi.org/10.1007/s11214-010-9655-x.

31. Boghosian M., Narvaez P., Herman R. Magnetic testing, and modeling, simulation and analysis for space applications. *2013 IEEE International Symposium on Electromagnetic Compatibility*, 2013, pp. 265-270. doi: https://doi.org/10.1109/ISEMC.2013.6670421.

32. Mehlem K. Multiple magnetic dipole modeling and field prediction of satellites. *IEEE Transactions on Magnetics*, 1978, vol. 14, no. 5, pp. 1064-1071. doi: https://doi.org/10.1109/TMAG.1978.1059983.

33. Thomsen P.L., Hansen F. Danish Ørsted Mission In-Orbit Experiences and Status of The Danish Small Satellite Programme. *Annual AIAA/USU Conference on Small Satellites*, 1999, pp. SSC99-I–8.

34. Kapsalis N.C., Kakarakis S.-D.J., Capsalis C.N. Prediction of multiple magnetic dipole model parameters from near field measurements employing stochastic algorithms. *Progress In Electromagnetics Research Letters*, 2012, vol. 34, pp. 111-122. doi: https://doi.org/10.2528/PIERL12030905.

35. Rozov V.Yu., Dobrodeev P.N., Volokhov S.A. Multipole model of a technical object and its magnetic center. *Technical Electrodynamics*, 2008, no. 2, pp. 3-8. (Rus).
36. Abramowitz M., Stegun I.A. (ed.). *Handbook of mathematical functions with formulas, graphs, and mathematical tables*. US Government Printing Office Publ., 1964. 1046 p.
37. Solomentsev O., Zaliskyi M., Averyanova Y., Ostroumov I., Kuzmenko N., Sushchenko O., Kuznetsov B., Nikitina T., Tserne E., Pavlikov V., Zhyla S., Dergachov K., Havrylenko O., Popov A., Volosyuk V., Ruzhentsev N., Shmatko O. Method of Optimal Threshold Calculation in Case of Radio Equipment Maintenance. *Data Science and Security. Lecture Notes in Networks and Systems*, 2022, vol. 462, pp. 69-79. doi: https://doi.org/10.1007/978-981-19-2211-4_6.
38. Ruzhentsev N., Zhyla S., Pavlikov V., Volosyuk V., Tserne E., Popov A., Shmatko O., Ostroumov I., Kuzmenko N., Dergachov K., Sushchenko O., Averyanova Y., Zaliskyi M., Solomentsev O., Havrylenko O., Kuznetsov B., Nikitina T. Radio-Heat Contrasts of UAVs and Their Weather Variability at 12 GHz, 20 GHz, 34 GHz, and 94 GHz Frequencies. *ECTI Transactions on Electrical Engineering, Electronics, and Communications*, 2022, vol. 20, no. 2, pp. 163-173. doi: https://doi.org/10.37936/ecti-eec.2022202.246878.
39. Havrylenko O., Dergachov K., Pavlikov V., Zhyla S., Shmatko O., Ruzhentsev N., Popov A., Volosyuk V., Tserne E., Zaliskyi M., Solomentsev O., Ostroumov I., Sushchenko O., Averyanova Y., Kuzmenko N., Nikitina T., Kuznetsov B. Decision Support System Based on the ELECTRE Method. *Data Science and Security. Lecture Notes in Networks and Systems*, 2022, vol. 462, pp. 295-304. doi: https://doi.org/10.1007/978-981-19-2211-4_26.
40. Shmatko O., Volosyuk V., Zhyla S., Pavlikov V., Ruzhentsev N., Tserne E., Popov A., Ostroumov I., Kuzmenko N., Dergachov K., Sushchenko O., Averyanova Y., Zaliskyi M., Solomentsev O., Havrylenko O., Kuznetsov B., Nikitina T. Synthesis of the optimal algorithm and structure of contactless optical device for estimating the parameters of statistically uneven surfaces. *Radioelectronic and Computer Systems*, 2021, no. 4, pp. 199-213. doi: https://doi.org/10.32620/reks.2021.4.16.
41. Volosyuk V., Zhyla S., Pavlikov V., Ruzhentsev N., Tserne E., Popov A., Shmatko O., Dergachov K., Havrylenko O., Ostroumov I., Kuzmenko N., Sushchenko O., Averyanova Yu., Zaliskyi M., Solomentsev O., Kuznetsov B., Nikitina T. Optimal Method for Polarization Selection of Stationary Objects Against the Background of the Earth's Surface. *International Journal of Electronics and Telecommunications*, 2022, vol. 68, no. 1, pp. 83-89. doi: https://doi.org/10.24425/ijet.2022.139852.
42. Zhyla S., Volosyuk V., Pavlikov V., Ruzhentsev N., Tserne E., Popov A., Shmatko O., Havrylenko O., Kuzmenko N., Dergachov K., Averyanova Y., Sushchenko O., Zaliskyi M., Solomentsev O., Ostroumov I., Kuznetsov B., Nikitina T. Practical imaging algorithms in ultra-wideband radar systems using active aperture synthesis and stochastic probing signals. *Radioelectronic and Computer Systems*, 2023, no. 1, pp. 55-76. doi: https://doi.org/10.32620/reks.2023.1.05.
43. Maksymenko-Sheiko K.V., Sheiko T.I., Lisin D.O., Petrenko N.D. Mathematical and Computer Modeling of the Forms of Multi-Zone Fuel Elements with Plates. *Journal of Mechanical Engineering*, 2022, vol. 25, no. 4, pp. 32-38. doi: https://doi.org/10.15407/pmach2022.04.032.
44. Hontarovskyi P.P., Smetankina N.V., Ugrimov S.V., Garmash N.H., Melezhyk I.I. Computational Studies of the Thermal Stress State of Multilayer Glazing with Electric Heating. *Journal of Mechanical Engineering*, 2022, vol. 25, no. 1, pp. 14-21. doi: https://doi.org/10.15407/pmach2022.02.014.
45. Kostikov A.O., Zevin L.I., Krol H.H., Vorontsova A.L. The Optimal Correcting the Power Value of a Nuclear Power Plant Power Unit Reactor in the Event of Equipment Failures. *Journal of Mechanical Engineering*, 2022, vol. 25, no. 3, pp. 40-45. doi: https://doi.org/10.15407/pmach2022.03.040.
46. Rusanov A.V., Subotin V.H., Khoryev O.M., Bykov Y.A., Korotaiev P.O., Ahibalov Y.S. Effect of 3D Shape of Pump-Turbine Runner Blade on Flow Characteristics in Turbine Mode. *Journal of Mechanical Engineering*, 2022, vol. 25, no. 4, pp. 6-14. doi: https://doi.org/10.15407/pmach2022.04.006.
47. Gontarovskyi P., Smetankina N., Garmash N., Melezhyk I. Numerical analysis of stress-strain state of fuel tanks of launch vehicles in 3D formulation. *Lecture Notes in Networks and Systems*, 2021, vol. 188, pp. 609–619. doi: https://doi.org/10.1007/978-3-030-66717-7_52.
48. Kurennov S., Smetankina N., Pavlikov V., Dvoretskaya D., Radchenko V. Mathematical Model of the Stress State of the Antenna Radome Joint with the Load-Bearing Edging of the Skin Cutout. *Lecture Notes in Networks and Systems*, 2022, vol. 305, pp. 287-295. doi: https://doi.org/10.1007/978-3-030-83368-8_28.
49. Sushchenko O., Averyanova Y., Ostroumov I., Kuzmenko N., Zaliskyi M., Solomentsev O., Kuznetsov B., Nikitina T., Havrylenko O., Popov A., Volosyuk V., Shmatko O., Ruzhentsev N., Zhyla S., Pavlikov V., Dergachov K., Tserne E. Algorithms for Design of Robust Stabilization Systems. *Lecture Notes in Computer Science*, 2022, vol. 13375, pp. 198-213. doi: https://doi.org/10.1007/978-3-031-10522-7_15.
50. Sheinker A., Ginzburg B., Salomonski N., Yaniv A., Persky E. Estimation of Ship's Magnetic Signature Using Multi-Dipole Modeling Method. *IEEE Transactions on Magnetics*, 2021, vol. 57, no. 5, pp. 1-8. doi: https://doi.org/10.1109/TMAG.2021.3062998.

Received 06.10.2024
Accepted 20.01.2025
Published 02.05.2025

B.I. Kuznetsov[1], *Doctor of Technical Science, Professor,*
T.B. Nikitina[2], *Doctor of Technical Science, Professor,*
I.V. Bovdui[1], *PhD, Senior Research Scientist,*
K.V. Chunikhin[1], *PhD, Senior Research Scientist,*
V.V. Kolomiets[2], *PhD, Assistant Professor,*
I.V. Nefodova[2], *PhD, Assistant Professor*
[1] Anatolii Pidhornyi Institute of Power Machines and Systems of the National Academy of Sciences of Ukraine,
2/10, Komunalnykiv Str., Kharkiv, 61046, Ukraine,
e-mail: kuznetsov.boris.i@gmail.com (Corresponding Author)
[2] Bakhmut Education Research and Professional Pedagogical Institute V.N. Karazin Kharkiv National University,
9a, Nosakov Str., Bakhmut, Donetsk Region, 84511, Ukraine.

How to cite this article:
Kuznetsov B.I., Nikitina T.B., Bovdui I.V., Chunikhin K.V., Kolomiets V.V., Nefodova I.V. Simplified method for analytically determining the external magnetostatic field of uncertain extended technical objects based on near-field measurements. *Electrical Engineering & Electromechanics*, 2025, no. 3, pp. 65-75. doi: https://doi.org/10.20998/2074-272X.2025.3.10

UDC 621.3 https://doi.org/10.20998/2074-272X.2025.3.11

B. Yahiaoui, A. Messaoudene, A. Melahi, A. Rahmani, B. Bendahmane, L. Dascalescu

Efficiency of neutralization of electric charges on the surface of dielectric nonwoven fabric of two dual and triode electrode systems

Introduction. *The accumulation of electrostatic charges are exploited in various technological and industrial applications, but they can also pose significant challenges, especially due to the accumulation in inappropriate locations that can reach dangerous levels.* ***Problem***. *The static charges are often considered annoying and constitute one of the main sources of hazards. Thus, their neutralization is more than necessary.* ***The objective*** *of this work is to improve the neutralization rate with equipment that can be easily integrated in the production lines.* ***Novelty***. *The paper reports a comparative study of the neutralization efficiency of two electrode systems, dual and triode, with different high alternating voltages at the industrial frequency of 50 Hz. The use of the industrial frequency of 50 Hz reduces the elements of the neutralization equipment. By connecting the grid to ground, we aim to impose a zero potential on the surface of the initially charged polypropylene fibrous dielectric and to determine the variation of the neutralization rate as a function of the discharge intensity (voltage amplitude).* ***Methodology.*** *The samples were charged during 10 s using a triode-type corona electrode configuration supplied by negative or positive DC high voltage. After 300 s of the charging process. The neutralization was performed during 4 s, using the dual or the triode systems powered by sinusoidal high voltage. Neutralization efficiency is achieved by non-contact sampling of surface potential profiles before and after neutralization.* ***The results*** *show that neutralization efficiency is proportionate to the discharge current intensity. The neutralization using the triode system is more efficient. The results show the possibility of imposing a desired potential on the charged or uncharged dielectric surface by acting on the potential of the metallic grid and the discharge intensity of the triode system.* ***Practical value.*** *The results demonstrate the proportionality of the neutralization efficiency with the discharge intensity for the triode system. Therefore, an adjustment of the voltage amplitude is necessary in order to optimize its efficiency for the dual system.* References 30, figures 7.
Key words: **surface potential, corona discharge, charge neutralization, fibrous electrets, triode system.**

Вступ. *Накопичення електростатичних зарядів використовуються в різних технологічних та промислових застосуваннях, але вони також можуть становити значні проблеми, особливо через накопичення в невідповідних місцях, що може досягати небезпечних рівнів.* ***Проблема*** *полягає в тому, що статичні заряди часто вважаються неприємними і є однією з основних причин небезпек. Тому їх нейтралізація є більш ніж необхідною.* ***Метою*** *роботи є покращення рівня нейтралізації за допомогою обладнання, яке можна легко інтегрувати в виробничі лінії.* ***Новизна.*** *У статті представлено порівняльне дослідження ефективності нейтралізації двох електродних систем:діодної та тріодної, при різних високих змінних напругах на промисловій частоті 50 Гц. Використання промислової частоти 50 Гц зменшує кількість елементів нейтралізаційного обладнання. Підключення сітки до землі дозволяє нав'язати нульовий потенціал на поверхні початково зарядженого поліпропіленового волокнистого діелектрика та визначити зміну рівня нейтралізації залежно від інтенсивності розряду (амплітуди напруги).* ***Методологія.*** *Зразки заряджали протягом 10 с за допомогою електродної конфігурації типу тріода, живленої негативною або позитивною постійною високою напругою. Після 300 с заряджання, нейтралізація проводилась протягом 4 с за допомогою подвійних або тріодних систем, живлених синусоїдальною високою напругою. Ефективність нейтралізації визначалась шляхом безконтактного зняття профілів поверхневого потенціалу до та після нейтралізації.* ***Результати*** *показали, що ефективність нейтралізації пропорційна інтенсивності розрядного струму. Нейтралізація за допомогою тріодної системи є більш ефективною. Результати показують можливість нав'язати бажаний потенціал на зарядженій або незарядженій діелектричній поверхні, впливаючи на потенціал металевої сітки та інтенсивність розряду тріодної системи.* ***Практична цінність.*** *Результати демонструють пропорційність ефективності нейтралізації до інтенсивності розряду для тріодної системи. Тому коригування амплітуди напруги є необхідним для оптимізації її ефективності для подвійної системи.* Бібл. 30, рис. 7.
Ключові слова: **поверхневий потенціал, коронний розряд, нейтралізація зарядів, волокнисті електрети, тріодна система.**

Introduction. The use of static electricity extends to various technological and industrial fields [1, 2], including electrostatic painting, the removal of dust from waste gases [3, 4], the separation of granular materials [5], and the creation of electrets transducers [2]. Fibrous polymers such as polypropylene, polycarbonate, polyurethane and polyethylene are often used in electrostatic filters for their ability to retain electrical charges for a long time [6]. However, the charge accumulated on these materials due to different physical phenomena of charging generally by triboelectric effect are inherent to the manufacturing process and can be harmful either to the operator or to sensitive electronic equipment and components. In the electronics manufacturing industry, the main hazard is the static charge accumulated on the manipulator's suits [7]. Indeed, electrostatic discharges can interrupt the contacts and the connection of increasingly miniaturized electronic components. Electrostatic discharges cause considerable damage in different industries, oil, electronics, textiles, etc. On the other hand, static electricity is subject to several studies aiming to improve some processes [2, 5], to develop new applications and to limit their negative effects [7, 8].

Corona discharge effects are exploited in various industrial applications [9], ranging from surface and material treatment, water treatment and air purification [10, 11] to electrostatic charge neutralization [12] and electrical network diagnostics [13]. Due to various applications, corona discharge is the subject of several researches [14–16]. For open, delicate or sensitive surfaces, the most effective method of controlling static electricity is active neutralization using a corona discharge, because this method does not require direct contact with the surface to be neutralized. Compared with other neutralization methods, corona discharge can be more energy-efficient [17–19].

The corona electrode is energized by different amplitudes of high voltages (HV) at high frequencies [8]. Several studies have been carried out on the active neutralization of the charge present on the surface of films [20–22], granules and non-woven fibrous materials [23]. In previous studies, the authors used the same method to evaluate the effect of wave forms of the HV at different

frequencies on the neutralization efficiency using dual electrode system [24]. Also, they evaluated the effect of charging time, neutralization time, the frequency and the amplitude of AC HV on the neutralization efficiency [23]. Using the triode system, the authors were interested in the effects of successive neutralizations with increasing discharge intensities and also the effects of the neutralization modes (fixed or scanning) on the neutralization efficiency [25]. Despite the high degree of neutralization obtained in previous work, the complete neutralization has not been achieved yet.

The aim of this work is to improve the neutralization efficiency and to evaluate the effect of the voltage level at industrial frequency (50 Hz) as well as the effect of the polarity of the deposited charge on the neutralization efficiency. We also aim to compare the neutralization efficiency of two electrode systems, dual and triode, under the same ambient conditions.

The use of the industrial frequency of 50 Hz allows to directly using the output voltages of the autotransformer (without the function generator and the amplifier). Polypropylene samples are charged by negative or positive corona discharge using a triode electrode system. After the surface potential decay becomes almost zero [26, 27], the samples are subjected to an AC corona discharge generated by the dual electrode system in the first part of the tests and by the triode system with the grid connected directly to ground for the second part of the tests. During neutralization, both electrode systems are powered by high sinusoidal voltages at industrial frequency (50 Hz). This work aims to improve the neutralization efficiency with a simple device that is easy to incorporate into the production chain.

Materials and methods. The experiments were performed at ambient air temperature (18 °C to 23.5 °C) and relative humidity (50 % to 61 %). The samples used are 120×9 mm (Fig. 1,*e*), cut from the same nonwoven sheet of polypropylene. The electric charging of the samples was performed using a triode electrode system (Fig. 1,*a*,*b*) [28, 29], composed of a HV wire-type dual electrode [24], facing a grounded plate electrode (aluminum, 165×115 mm), and a grid electrode. The HV electrode consists in a tungsten wire (diameter 0.2 mm) suspended by a metallic cylinder (diameter 26 mm) at 34 mm distance from the axis.

The wire and the cylinder were energized from the same adjustable HV supply, 100 kV, 3 mA (model SL300 Spellman) as shown in Fig. 1,*a*. The distances between the wire and the grid and between the grid and the surface of the plate electrode were 15 mm.

The metallic grid (Fig. 1,*d*) is connected to the ground through a series of calibrated resistors of an equivalent resistance R. In this way, for a current intensity I, a well-defined potential $V_g = I \cdot R$ is imposed between the grid and the grounded plate on which the samples are placed.

Part of the charge generated by the corona electrode will be discharged to ground through the resistors connected to the grid, the other part, the ions which pass through the grid, will be retained by the surface of the sample. The potential at the surface of the sample is limited by the potential of the grid V_g or by the partial discharges of the deposited charge.

In all the experiments described hereafter, the samples were charged for 10 s. The grid potential V_g = 1.2 kV for negative and positive polarity.

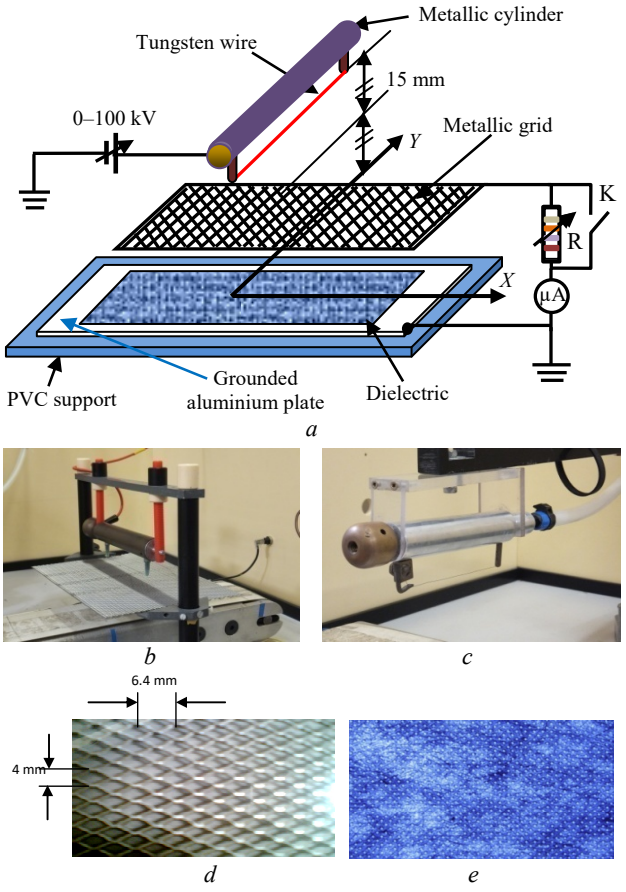

Fig. 1. *a* – configuration of electrode system type «triode» used for charging and neutralization; *b* – triode system «wire – grid – plane»; *c* – dual electrode system used for neutralization; *d* – metallic grid; *e* – fibrous polypropylene sample

The sample carrier consisted of a polyvinyl chloride PVC plate; to which plate electrode was firmly fixed. A conveyor belt supported the sample carrier and transferred it from the charging position to the surface potential measurement and charge neutralization sections of the experimental set-up. The speed of the conveyor can be adjusted from 1 cm/s to 6 cm/s, for the various needs of the experiments.

The efficiency of the neutralization is obtained by comparing the profiles of the potential of the surface charge before and after neutralization [8, 24]. Non-contact measurement of the surface potential is used to take multiple profiles without affecting the sample charge state.

As soon as the HV supply of the corona charger was turned off, the conveyor belt transferred the samples at a constant speed through the measurement section. Thus the repartition of the surface potential along the central axis OX of the sample was measured with an electrostatic voltmeter (model 341B), equipped with an electrostatic probe (model 3450, Trek Inc., Medina, NY), and recorded via an electrometer (model 6514, Keithley Instruments, Cleveland), connected to a computer. The acquisition and processing of experimental data was performed using an ad-hoc virtual instrument, developed in LabView environment.

In the first part of the experiment the neutralization was performed with a dual wire-type electrode similar to the one described above. The neutralizer–sample spacing was 50 mm (Fig. 2).

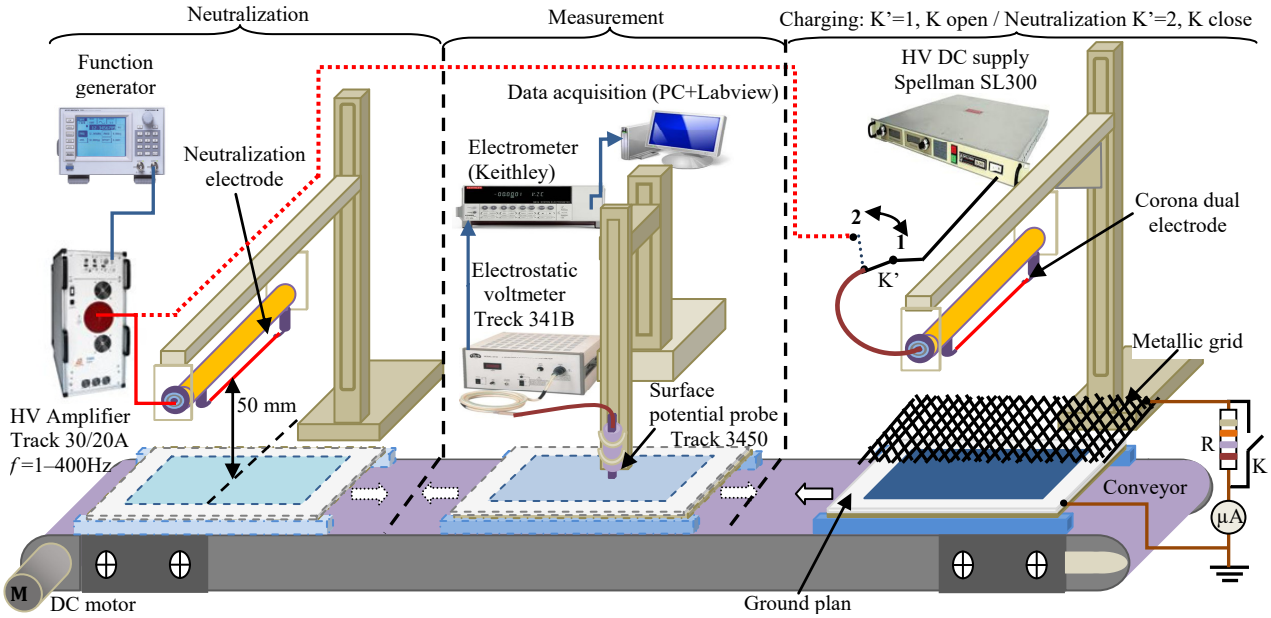

Fig.2. Experimental setup

In the second part of the experiment, the neutralization is carried out by the triode system, used previously to charge the sample, by closing the switch *K* and putting the switch K' on position 2 (Fig. 2). Closing the switch K imposes a zero potential to the grid. The intensity of the discharge is measured by the micro-ammeter connecting the grid to the ground. In both systems, the neutralization electrode was connected to a HV amplifier 30 kV, 20 mA (model 30/20A, Trek Inc., Medina, NY).

The amplitude U_n and the frequency f of the HV were adjusted using a synthesized function generator (model FG300, Yokogawa, Japan). In order to follow the decay of the surface potential and get a relatively stable charge, neutralization is carried out after 300 s of the charging turn off. For both neutralizing electrode configurations, the corona electrode is energized by high alternative voltage at industrial frequency (50 Hz).

The neutralization with the dual electrode system is performed in motion at a speed of 3 cm/s.

In triode configuration, the neutralization is in static mode, the sample is centered under the active electrode of the triode system during the discharge which takes 4 s. The profiles of the surface potential are obtained just before and after the neutralization using the previously described method.

Each experiment was repeated 3 times, and each run is performed on a new sample. If the tests show a disparity, further tests will be performed.

The neutralization rate N % is expressed as a function of V_{01} and V_{02}, the maximum recorded values (absolute values) of the potential along the central axis OX of the sample, respectively before and after neutralization:

$$N\,[\%] = [1 - \text{abs}\,(V_{02}/V_{01})]\cdot 100. \qquad (1)$$

In the first part of the experiments, we used the dual system, the amplitude of the sinusoidal neutralization voltage was varied through 6 levels: U_n = 16, 18, 20, 21, 22, 24 kV at 50 Hz frequency. In the second part of the experiments, the neutralization is carried out by 3 sinusoidal voltage amplitudes: U_n = 6, 12.5, 15 kV, associated with respectively 3 grid current values: I_g = 10, 50, 100 μA.

Results and discussion. The non-uniform distribution of the surface potential is due to the inhomogeneous structure of the non-woven dielectric and the partial discharges that can occur due to the local intensification of the electric field [26, 27].

Samples are charged for 10 s with positive or negative corona discharge. Each test is carried out on a new sample. The neutralization is performed after 300 s after charging, so that any variations in the profile of the surface potential before and after neutralization are only linked to the neutralization and not to the decline [6]. Thus, the effect of the surface potential decay on the efficiency of neutralization can be neglected. The decay of surface potential is due to the combined action of several physical mechanisms (partial discharges, recombination, lateral and transversal conduction) and also influenced by the value of the charge potential [6, 26, 27].

The efficiency of the neutralization of electrostatic charges on the surface of the dielectric is obtained by comparing the surface potential profiles just before and after neutralization. It is calculated as the ratio between the maximum electrical potential measured at the surface of the dielectric before (V_{01}) and after exposing them to the bipolar ions generated by an AC corona discharge (V_{02}) [23, 24].

Dual electrode system neutralization efficiency. In the neutralization with the dual system, the sample passes through the AC zone discharge with a constant speed of 3 cm/s. Several amplitude values of the corona electrode voltage were tested.

Figures 3, 4 show the surface potential profiles before and after neutralization with a double electrode system at high sinusoidal voltages at the frequency of 50 Hz. We notice a non-symmetry of the surface potential profiles shown in these figures and this is due to the inhomogeneous surfaces and structures of the samples used (non-woven fabric). Symmetry will be obtained if the samples are with a homogeneous surface such as films are used.

At the amplitude of 16 kV, the neutralization did not occur; this is due to the fact that this amplitude value is slightly higher than the threshold value of the corona

discharge. The few electrons created in the ionization zone do not have enough energy to ionize other molecules and create other additional electrons. The positive ions do not have time to leave the drift zone before the arrival of the negative alternation (Fig. 3,*a*). On the other hand, for the positive charge, we notice a significant neutralization where the maximum potential is 1.29 kV and decreases to 0.81 kV after neutralization. This means that the negative ions arrive at the surface of the sample before the positive half-wave, due to the fact, that the mobility of the negative ions is greater than that of the positive ions as shown in Fig. 4,*a*.

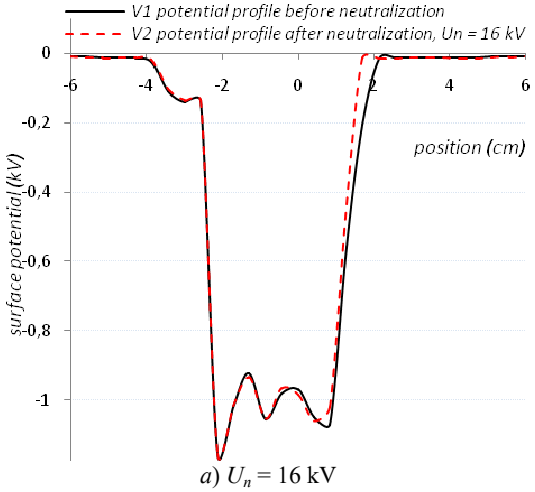

a) U_n = 16 kV

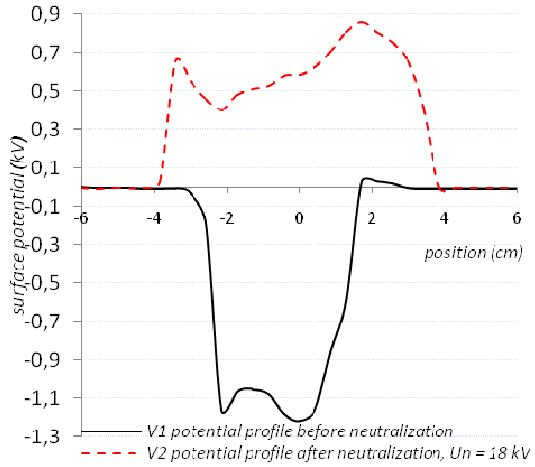

b) U_n = 18 kV

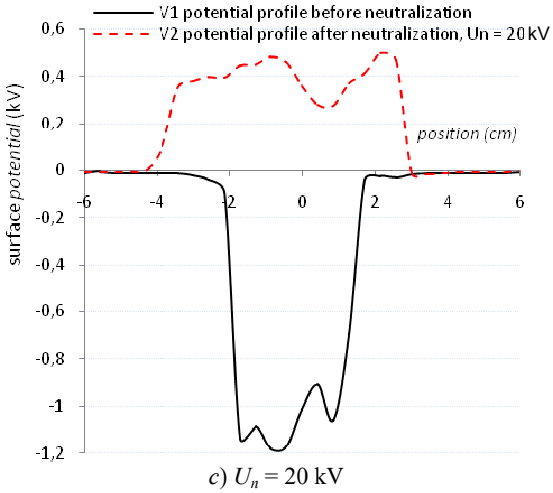

c) U_n = 20 kV

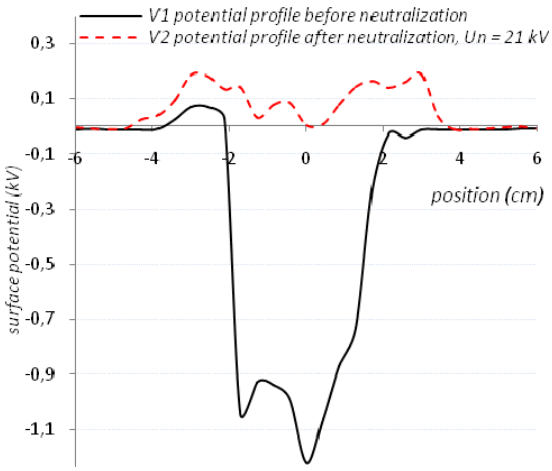

d) U_n = 21 kV

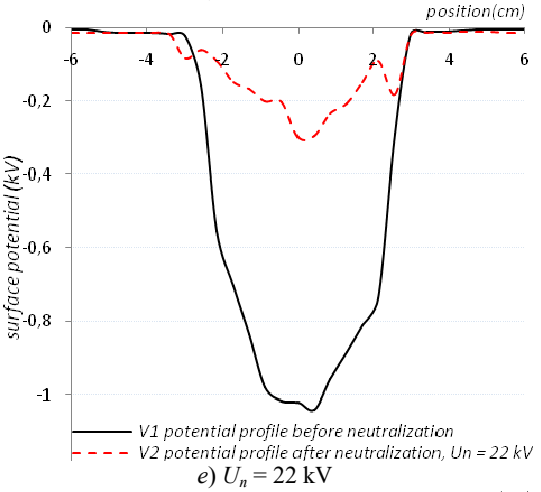

e) U_n = 22 kV

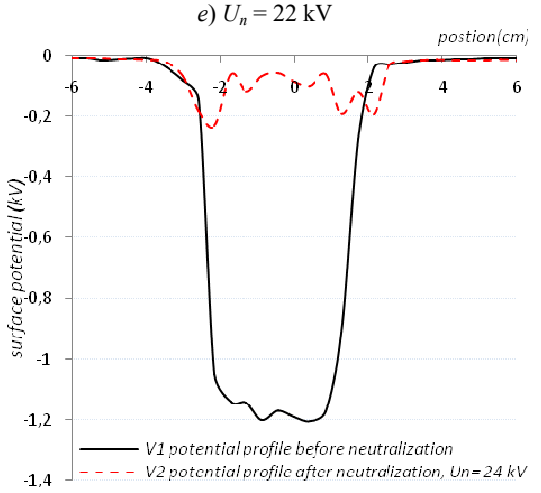

f) U_n = 24 kV

Fig. 3. Typical surface potential profiles before and after neutralization with dual electrode, <u>*negative*</u> initial charge

At the large inter-electrode distances or at weak electric fields, there is an accumulation of space charges. Indeed; for weak electric fields the positive ions do not have time to be evacuated during the positive alternation. Their presence around the conductor increases the existing electric field. Therefore the following discharge mode takes place at a lower applied voltage.

However, in the neutralization with a voltage of 18 kV, the potential after neutralization is positive, with 856 V as the maximum value, while the initial potential was negative with a maximum value of |–1.2| kV. This means that all the initial charges are completely neutralized and new charges

are deposited (Fig. 3,*b*). The surface occupied by the positive charges is wider than the initial negatively charged surface; this difference is due to the mode of charge and neutralization; fixed mode for depositing the charge and scanning mode for neutralization. For the initial positive charge, the neutralization is greater but the polarity of the charge on the sample has not changed. The maximum potential decreases from 1010 V to 231 V after neutralization (Fig. 4,*b*).

Figures 3,*c*,*d* illustrate the profiles of the surface potential before and after neutralization with the amplitudes of sinusoidal high voltages of 20 kV and 21 kV respectively. The initial negative charges are completely neutralized and positive charges are deposited at the surface of samples.

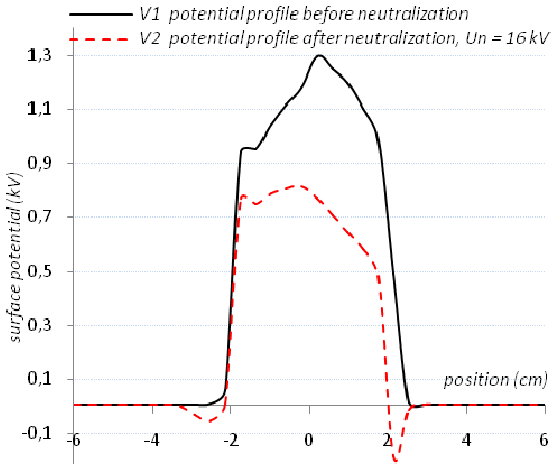

a) U_n = 16 kV

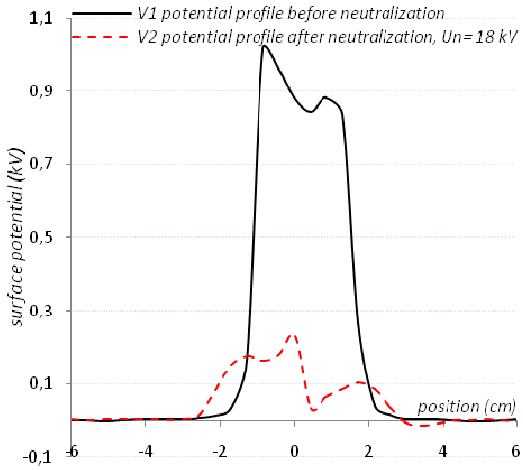

b) U_n = 18 kV

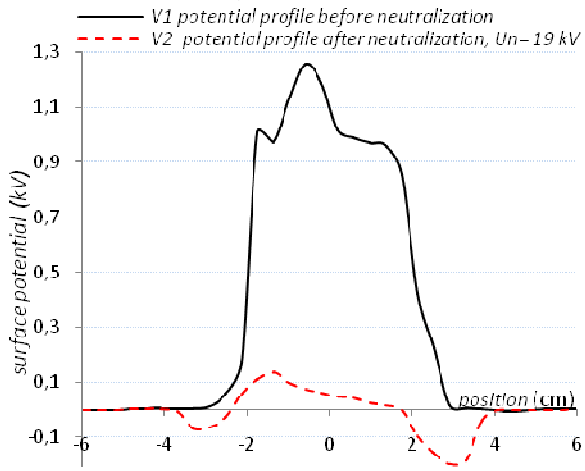

c) U_n = 19 kV

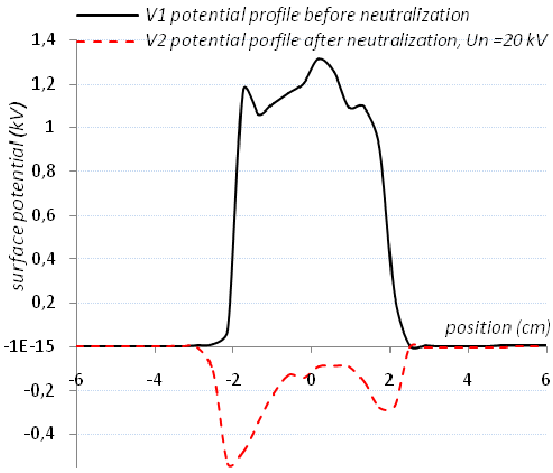

d) U_n = 20 kV

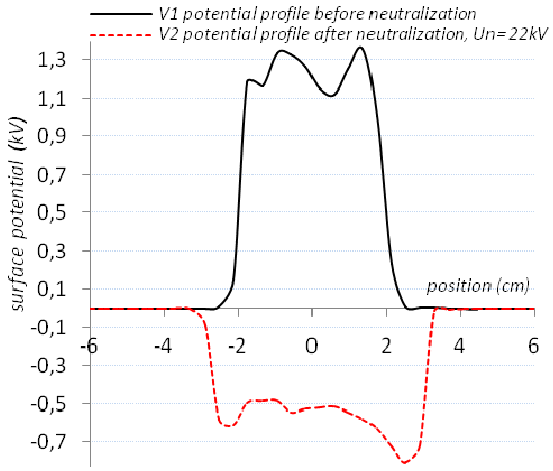

e) U_n = 22 kV

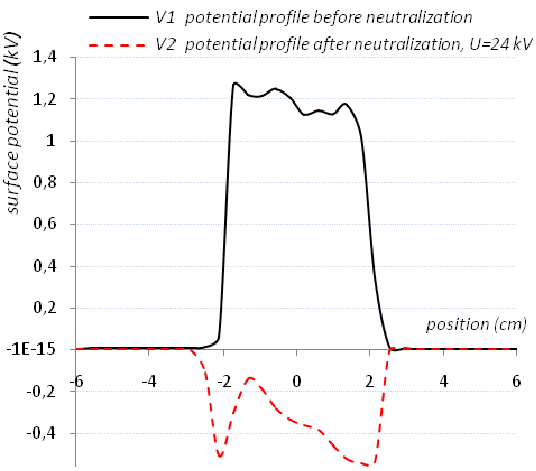

f) U_n = 24 kV

Fig. 4. Typical surface potential profiles before and after neutralization with dual electrode, *positive* initial charge

The charge deposited by the magnitude of 20 kV is greater than that registered by the amplitude of 21 kV. The maximum values of the surface potential after neutralization are 500 V and almost 200 V for the amplitudes 20 kV and 21 kV respectively. At these voltage amplitude values, the electric field is not strong enough to create a significant number of positive ions and allow them to reach the sample surface during the positive half-wave. While for the initial positive charge, this is completely neutralized and there is a deposit of new negative charge as shown in Fig. 4,*c*,*d*. This means that the positive charge on

the surface of the samples contributed to the corona discharge by reinforcing the electric field during the negative half-wave and reducing it during the positive half-wave. Knowing that, the negative corona discharge appears at higher voltages than the positive corona discharge.

However, at the amplitudes of 22 and 24 kV, the surface potential is negative after neutralization with maximum values |–230| V and |–300| V respectively (Fig. 3,*e*,*f*). These results show the existence of a value of voltage between 21 kV and 22 kV which provides complete neutralization without depositing new charges.

For the initial positive charges, after neutralization we have deposition of new negative charges, where the maximum surface potentials are |–809| V and |–538| V for the respective amplitudes of 22 kV and 24 kV (Fig. 4,*e*,*f*). This means that all the initial charge is completely neutralized.

At the alternating voltage amplitudes greater than 22 kV, the positive ions produced during the positive half-wave do not all have time to be evacuated before the arrival of the negative half-wave. This positive space charge reinforces the electric field during the negative alternation and the majority of the ions which arrive at the surface of the sample are negative ions. In this case, there will be a tendency to deposit a negative charge on the surface of the samples.

The variation of the neutralization rate N [%] and the ratio V_{02}/V_{01} [%] are displayed in Fig. 5. V_{01} and V_{02} are respectively the maximum values of the surface potential before and after neutralization. When the samples are negatively charged, at the voltage of 16 kV, the potentials V_{01} and V_{02} are too close; with this amplitude no neutralization is obtained. However, for the voltages of 18, 20, 21 kV, the surface potential after neutralization is positive whereas the potential before neutralization was negative.

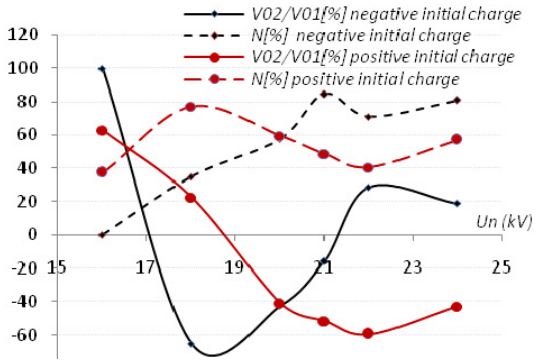

Fig. 5. Surface potential ratio V_{02}/V_{01} [%] and neutralization rate N [%] as a function of high sinusoidal voltage amplitudes U_n (kV) for 2 polarities of deposited charges

The change of sign of the rate V_{02}/V_{01} means that the initial charge is completely neutralized and a new charge of opposite sign is deposited. This also means that complete neutralization and without deposition of any new charge can be achieved in this voltage range.

The maximum neutralization of a rate greater than 85 % is obtained at the voltage of 21 kV. On the other hand, when the samples are positively charged, at a voltage of 16 kV, we obtain a neutralization rate of almost 38 % and the maximum neutralization of almost 78 % at 18 kV. This means that at these voltages, the charge on the sample contributes to the discharge. However, for voltages of 20, 21, 22, 24 kV, the surface potential after neutralization is negative while the potential before neutralization was positive.

The change in sign of the voltage ratio V_{02}/V_{01} means that complete neutralization and without deposition of new charge can be achieved in the range of voltage.

We note for the voltages of 22 kV and 24 kV the charge on the surface of the samples is negative whatever the initial charge of the samples.

Neutralization efficiency of the triode system. Samples are charged for 10 s by negative corona discharge with current intensity I = 50 μA. The neutralization is carried out with triode system in static mode. The corona electrode of the triode system of neutralization is powered by alternating sinusoidal voltages corresponding 6, 12.5 and 15 kV with associated grid currents intensity I_g of 10, 50 and 100 μA respectively. The samples are exposed for 4 s to bipolar ions generated by an alternating corona discharge (AC).

Figure 6 shows the surface potential profiles before and after neutralization with high alternating voltages, for 3 HV sinusoidal amplitude (6, 12.5 and 15 kV). The profile of the surface potential is slightly affected at the extremities of the potential profile, where there was a decrease of a few volts due to exposure to the corona discharge at the amplitude of 6 kV associated to the current grid of 10 μA (Fig. 6,*a*). At this amplitude, there is not any neutralization obtained in the middle of the sample. This means that the discharge intensity is not sufficient and most of the ions lose their charges by hitting the grid connected to ground [30].

The discharge is between the active electrode and the grid. However, the amplitude voltage of 12.5 kV, associated to grid current intensity I_g = 50 μA, a maximum neutralization is achieved in the middle of the sample, just below the corona electrode, with a surface potential close to –25 V.

At the edges of the profile, the surface potential is similar to the profile before naturalization, this means that the energy of the discharge is not sufficient to allow the neutralizing charges to deflect towards the sample extremities (Fig. 6,*b*) [20, 25].

The surface potential profiles obtained before and after neutralization with the voltage amplitude of 15 kV, associated to grid current of 100 μA are presented in Fig. 6,*c*.

At this voltage, almost all the deposited charges are neutralized. The surface potential profile after neutralization is completely flattened with a small peak surface potential with a value that does not exceed –40 V. Indeed, under these conditions the corona discharge is assisted by an intense electric field which accelerates a portion of the positive ions and allows them to reach the negatively charged surface of the sample [28].

So, the neutralization of electrostatic charges on the surface of a fibrous dielectric material is more efficient at higher voltage and higher current intensities of alternative corona discharge.

Figure 7 presents the variation of the neutralization rate N [%] and the ratio V_{02}/V_{01} [%] as function of the neutralization voltage with the triode system, V_{01} and V_{02} being respectively the maximum values of the surface potential before and after neutralization. At the amplitude of 6 kV, the neutralization is not obtained, the surface

potential profiles before and after neutralization are almost the same ($V_2 \approx V_1$). However, for the amplitude of 12.5 kV, the ratio of surface potentials just before and after neutralization V_{02}/V_{01} is equal to 40 %, which leads to a neutralization rate of 60 %.

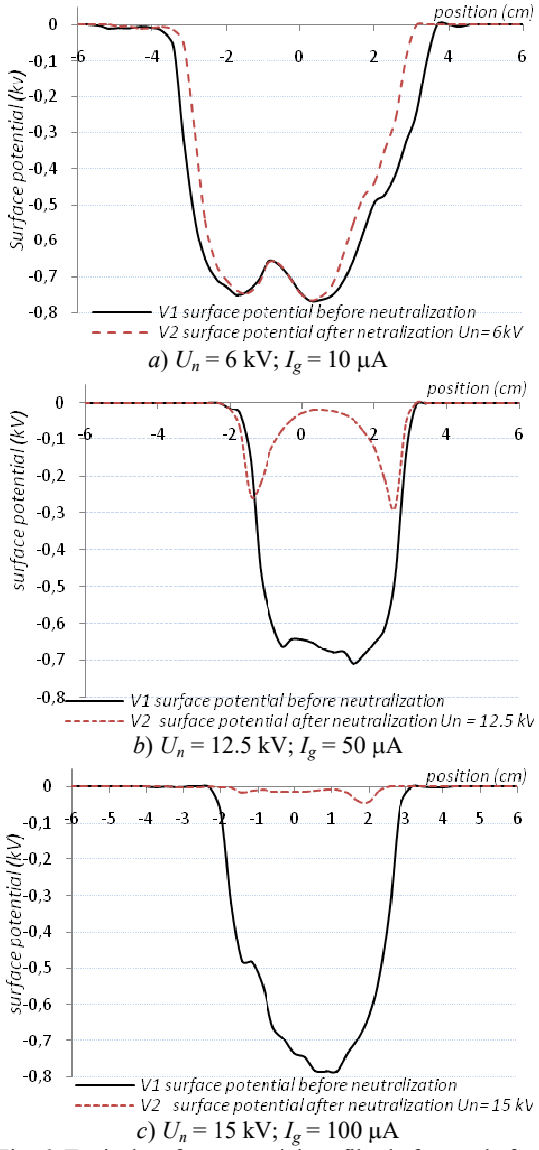

a) U_n = 6 kV; I_g = 10 μA

b) U_n = 12.5 kV; I_g = 50 μA

c) U_n = 15 kV; I_g = 100 μA

Fig. 6. Typical surface potential profiles before and after neutralization with triode electrode system

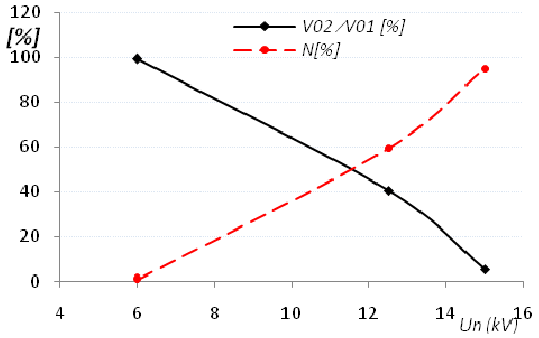

Fig. 7. Neutralization rate N [%] and surface potential ration V_{02}/V_{01} [%] as function of the neutralization voltage U_n, kV

For the neutralization voltage of amplitude 15 kV, an almost complete neutralization of 95 % of the charges deposited on the sample surface is achieved. The results show that the ratio V_{02}/V_{01} is positive for all voltage level; this means that there is no deposition of a new charge of the same polarity or of polarity opposite to the initial charge.

Indeed, with the neutralization by triode system, only ions of polarity opposite to the charges of the dielectric can cross the grid, due to the fact that the electric field is reinforced by the negative surface charge of the sample during the positive alternation.

However, the field is weakened by the negative charges on the sample surface during the negative alternation. The negative ions will therefore be repelled by the negative charges of the sample and evacuated from the grid towards the ground. During the negative alternation, the discharge is between the corona electrode and the grid.

Conclusions. The neutralization by high alternating voltages at industrial frequency is an advantage; this allows the network voltage to be used by amplifying only the voltage without any frequency adjustment.

Dual system. For certain voltages levels, the entire initial charge is neutralized but new charges of opposite sign are deposited. Proper adjustment of the exposure time and amplitude of the high voltage is necessary to ensure neutralization of all charges without depositing new ones. For low neutralization voltage amplitudes, the polarity of the charge to be neutralized has a significant effect on the neutralization rate.

Triode system. The neutralization with the triode system is more efficient, the grid connected to the ground prevents the deposition of new charges of opposite sign on the surface of the fibrous media. There is no deposition of new charge. The neutralization efficiency of electrostatic charge is proportional to the intensity of the discharge current. It is important to find the relationship between the exposure time and the intensity of the discharge with the neutralization efficiency. In industrial applications, the neutralization in scan mode is more convenient. The efficiency of the neutralization using a triode system can be improved by scan mode and optimizing its scanning speed.

Conflict of interest. The authors declare that they have no conflicts of interest.

REFERENCES

1. Young R.H. Kinetics of xerographic discharge by surface charge injection. *Journal of Applied Physics*, 1992, vol. 72, no. 7, pp. 2993-3004. doi: https://doi.org/10.1063/1.351507.

2. Zhou Q., Li L., Bi X., Zhang G., Cao Z., Meng H., Lan Q., Liang C., Chen X., Ma J. Electrostatic elimination of charged particles by DC-type bipolar electrostatic eliminator. *Powder Technology*, 2022, vol. 408, art. no. 117774. doi: https://doi.org/10.1016/j.powtec.2022.117774.

3. Benaouda I., Zelmat M.E.M., Ouiddir R., Dascalescu L., Tilmatine A. Analysis of a novel insulating conveyor-belt tribo-electrostatic separator for highly humid granular products. *Journal of Electrostatics*, 2019, vol. 100, art. no. 103357. doi: https://doi.org/10.1016/j.elstat.2019.103357.

4. Kang M.S., Yu G., Shin J., Hwang J. Collection and decomposition of oil mist via corona discharge and surface dielectric barrier discharge. *Journal of Hazardous Materials*, 2021, vol. 411, art. no. 125038. doi: https://doi.org/10.1016/j.jhazmat.2021.125038.

5. Kachi M., Nemamcha M., Lazhar H., Dascalescu L. Neutralization of charged insulating granular materials using AC corona discharge. *Journal of Electrostatics*, 2011, vol. 69, no. 4, pp. 296-301. doi: https://doi.org/10.1016/j.elstat.2011.04.005.

6. Tabti B., Yahiaoui B., Bendahmane B., Dascalescu L. Surface potential decay dynamic characteristics of negative-corona-charged fibrous dielectric materials. *IEEE Transactions on Dielectrics and Electrical Insulation*, 2014, vol. 21, no. 2, pp. 829-835. doi: https://doi.org/10.1109/TDEI.2013.003854.

7. Antoniu A., Tabti B., Plopeanu M.-C., Dascalescu L. Accelerated Discharge of Corona-Charged Nonwoven Fabrics. *IEEE Transactions on Industry Applications*, 2010, vol. 46, no. 3, pp. 1188-1193. doi: https://doi.org/10.1109/TIA.2010.2045331.
8. Yahiaoui B., Tabti B., Megherbi M., Antoniu A., Plopeanu M.-C., Dascalescu L. AC corona neutralization of positively and negatively charged polypropylene non-woven fabrics. *IEEE Transactions on Dielectrics and Electrical Insulation*, 2013, vol. 20, no. 5, pp. 1516-1522. doi: https://doi.org/10.1109/TDEI.2013.6633678.
9. Moreau E., Benard N. Ionic wind produced by volume corona discharges and surface dielectric barrier discharges: What role do streamers play? *Journal of Electrostatics*, 2024, vol. 132, art. no. 103988. doi: https://doi.org/10.1016/j.elstat.2024.103988.
10. Boiko M.I., Makogon A.V. Features of distribution of electric field strength and current density in the reactor during treatment of liquid media with high-voltage pulse discharges. *Electrical Engineering & Electromechanics*, 2024, no. 5, pp. 58-63. doi: https://doi.org/10.20998/2074-272X.2024.5.08.
11. Molchanov O., Krpec K., Horák J. Nox removal from Small-Scale biomass combustion in DC Corona: Influence of discharge polarity on plasma chemical kinetics. *Chemical Engineering Science*, 2024, vol. 300, art. no. 120597. doi: https://doi.org/10.1016/j.ces.2024.120597.
12. Huang H., Chen W., Mi J., Zhang Y., Bi N., Du S. Study on the application of atomized corona discharge combined with screen electrode in dust collection. *Journal of Electrostatics*, 2024, vol. 130, art. no. 103953. doi: https://doi.org/10.1016/j.elstat.2024.103953.
13. Hassan W., Shafiq M., Hussain G.A., Choudhary M., Palu I. Investigating the progression of insulation degradation in power cable based on partial discharge measurements. *Electric Power Systems Research*, 2023, vol. 221, art. no. 109452. doi: https://doi.org/10.1016/j.epsr.2023.109452.
14. Tuan Dung N., Besse C., Rogier F. An implicit time integration approach for simulation of corona discharges. *Computer Physics Communications*, 2024, vol. 294, art. no. 108906. doi: https://doi.org/10.1016/j.cpc.2023.108906.
15. Tao S., Zhu Y., Chen C., Liu J., Chen M., Shangguan W. Removal of air pollutant by a spike-tubular electrostatic device: Multi-stage direct current corona discharge enhanced electrostatic precipitation and oxidation ability. *Process Safety and Environmental Protection*, 2022, vol. 165, pp. 347-356. doi: https://doi.org/10.1016/j.psep.2022.06.069.
16. Abouelatta M.A., Ward S.A., Sayed A.M., Mahmoud K., Lehtonen M., Darwish M.M.F. Measurement and assessment of corona current density for HVDC bundle conductors by FDM integrated with full multigrid technique. *Electric Power Systems Research*, 2021, vol. 199, art. no. 107370. doi: https://doi.org/10.1016/j.epsr.2021.107370.
17. Khalifehei M., Higuera F.J. Neutralization of an electrospray by a corona discharge. *Journal of Aerosol Science*, 2020, vol. 145, art. no. 105547. doi: https://doi.org/10.1016/j.jaerosci.2020.105547.
18. Mustika W.S., Hapidin D.A., Saputra C., Munir M.M. Dual needle corona discharge to generate stable bipolar ion for neutralizing electrosprayed nanoparticles. *Advanced Powder Technology*, 2021, vol. 32, no. 1, pp. 166-174. doi: https://doi.org/10.1016/j.apt.2020.11.026.
19. Oudaifia N., Kachi M., Moussaoui A., Boudefel A. Cylindrical electrodes for neutralization of insulating flowing particles. *Journal of Electrostatics*, 2021, vol. 110, art. no. 103556. doi: https://doi.org/10.1016/j.elstat.2021.103556.
20. Settaf B., Ziari Z., Sahli S. Effect of the applied high voltage on the neutralization efficiency of negative charges accumulated on polypropylene film surface. *2023 International Conference on Electrical Engineering and Advanced Technology (ICEEAT)*, 2023, pp. 1-4. doi: https://doi.org/10.1109/ICEEAT60471.2023.10426438.
21. Messaoudène A., Mekidèche M.R., Bendahmane B., Tabti B., Dascalescu L. Experimental study of controlled active neutralization of polypropylene films. *Journal of Electrostatics*, 2020, vol. 103, art. no. 103407. doi: https://doi.org/10.1016/j.elstat.2019.103407.
22. Messaoudene A., Mekideche M.R., Bendahmane B., Tabti B., Medles K., Dascalescu L. Optimization of the Active Neutralization of Polypropylene Film Using Response Surface Methodology. *IEEE Transactions on Industry Applications*, 2020, vol. 56, no. 5, pp. 5463-5471. doi: https://doi.org/10.1109/TIA.2020.3001538.
23. Yahiaoui B., Megherbi M., Smaili A., Antoniu A., Tabti B., Dascalescu L. Distribution of Electric Potential at the Surface of Corona-Charged Polypropylene Nonwoven Fabrics After Neutralization. *IEEE Transactions on Industry Applications*, 2013, vol. 49, no. 4, pp. 1758-1766. doi: https://doi.org/10.1109/TIA.2013.2256412.
24. Yahiaoui B., Megherbi M., Tabti B., Dascalescu L. Sinusoidal, Triangular, or Square Alternating Voltages Neutralization of Electrostatic Charges on the Surface of Polypropylene Nonwoven Fabric. *IEEE Transactions on Industry Applications*, 2015, vol. 51, no. 1, pp. 685-691. doi: https://doi.org/10.1109/TIA.2014.2336985.
25. Bendahmane B., Messaoudene A., Dascalescu L. Alternating Current Corona neutralization of charged filters media. *2020 IEEE 3rd International Conference on Dielectrics (ICD)*, 2020, pp. 910-913. doi: https://doi.org/10.1109/ICD46958.2020.9341941.
26. Chen G. A new model for surface potential decay of corona-charged polymers. *Journal of Physics D: Applied Physics*, 2010, vol. 43, no. 5, art. no. 055405. doi: https://doi.org/10.1088/0022-3727/43/5/055405.
27. Malathip K., Techaumnat B., Sasamoto R., Nishijima K. Experimental and Numerical Study on the Charge Decay on Solid Insulator Surface. *2020 8th International Conference on Condition Monitoring and Diagnosis (CMD)*, 2020, pp. 430-433. doi: https://doi.org/10.1109/CMD48350.2020.9287267.
28. Messaoudene A., Mekideche M.R., Bendahmane B., Tabti B., Medles K., Dascalescu L. Experimental modeling and optimization of the active neutralization of a PP film, using design of experiments methodology. *2019 IEEE Industry Applications Society Annual Meeting*, 2019, pp. 1-4. doi: https://doi.org/10.1109/IAS.2019.8912025.
29. Messaoudène A., Dascalescu L., Bendahmane B., Yahiaoui B., Mekidèche M. R. Experimental study of the active and controlled neutralization of polypropylene nonwoven media. *Electrical Engineering International Conference (EEIC'2019)*, 4-5 December 2019, Bejaia, Algeria.
30. Bouteffaha A., Bendaoud A., Reguig A., Dascalescu L. Effects of the grid geometry on the performances of a triode-type corona electrode system. *Journal of Electrostatics*, 2019, vol. 101, art. no. 103367. doi: https://doi.org/10.1016/j.elstat.2019.103367.

Received 04.11.2024
Accepted 31.01.2025
Published 02.05.2025

B. Yahiaoui[1], *PhD, Lecturer,*
A. Messaoudene[1], *PhD, Lecturer,*
A. Melahi[1], *PhD Student, Lecturer,*
A. Rahmani[1], *PhD, Lecturer,*
B. Bendahmane[1], *PhD, Professor,*
L. Dascalescu[2], *PhD, Professor,*
[1] Electrical Engineering Department,
University of Bejaia, Algeria,
e-mail: belkacem.yahiaoui@univ-bejaia.dz (Corresponding Author)
[2] Université de Poitiers, France.

How to cite this article:
Yahiaoui B., Messaoudene A., Melahi A., Rahmani A., Bendahmane B., Dascalescu L. Efficiency of neutralization of electric charges on the surface of dielectric nonwoven fabric of two dual and triode electrode systems. *Electrical Engineering & Electromechanics*, 2025, no. 3, pp. 76-83. doi: https://doi.org/10.20998/2074-272X.2025.3.11

UDC 621.3 https://doi.org/10.20998/2074-272X.2025.3.12

Z. Ahmed, L.S. Nasrat, M. Rihan

The effect of SiO_2 microparticle concentration on the electrical and thermal properties of silicone rubber for electrical insulation applications

Introduction. *Polymeric insulators, first developed in the 1950s, have since seen substantial advancements in both design and manufacturing, making them increasingly appealing to users and manufacturers in the electrical industry. Extensive testing in both laboratory and outdoor environments has consistently demonstrated that polymeric insulators outperform traditional porcelain and glass counterparts. Among the various polymeric materials, silicone rubber (SiR) has emerged as one of the most promising candidates for high-voltage insulators. Its superiority is attributed to a unique combination of properties, including a non-conductive chemical structure, high dielectric strength, and excellent resistance to scaling. To further enhance these properties, SiR is often combined with fillers to form composite materials. These SiR composites are at the forefront of advanced high-voltage insulation systems, offering improved mechanical, thermal, and electrical performance. As a result, they not only meet the rigorous demands of high-voltage applications but also provide a significantly extended service life.* ***Goal.*** *This study aims to enhance the dielectric and thermal properties of SiR by incorporating micron-sized silicon dioxide (SiO_2) filler.* ***Methodology.*** *SiR-based composite samples were prepared by incorporating micron-sized SiO_2 at weight fractions of 10 %, 20 %, 30 %, and 40 % of the total composition. Initially, the samples were heated to specific temperatures (25°C, 60°C, 80°C, and 100°C) before undergoing dielectric strength testing to evaluate their performance under varying thermal conditions. Additionally, the samples were subjected to thermal aging for durations of 10, 20, and 30 minutes at the same temperatures before dielectric strength assessment.* ***The results*** *indicated that increasing the filler concentration enhanced the dielectric strength of the SiR/SiO_2 composites. The highest breakdown voltage was observed at a filler concentration of 30 %.* ***Practical value.*** *Incorporating micron-sized SiO_2 filler into the SiR matrix enhanced the composite's resistance to thermal stress. Compared to SiR-based composites with varying SiO_2 concentrations, pure SiR exhibited the lowest dielectric strength.* References 48, tables 5, figures 8.
Key words: **dielectric strength, silicone rubber, micron-sized silica dioxide, thermal behavior, neural network.**

Вступ. *Полімерні ізолятори з моменту розробки в 1950-х роках значно удосконалилися як у проєктуванні, так і у виробництві, що робить їх все більш привабливими для користувачів та виробників електротехнічної продукції. Великі випробування як у лабораторних, так і промислових умовах демонструють, що полімерні ізолятори переважають традиційні порцелянові і скляні аналоги. Серед різних полімерних матеріалів силіконовий каучук (SiR) став найперспективнішим матеріалом для високовольтних ізоляторів. Його перевага пояснюється унікальним поєднанням властивостей, включаючи непровідну хімічну структуру, високу діелектричну міцність та відмінну стійкість до утворення накипу. Для подальшого покращення цих властивостей, SiR часто поєднують з наповнювачами для формування композитних матеріалів. Ці композити SiR знаходяться на передньому краї сучасних систем високовольтної ізоляції, пропонуючи покращені механічні, теплові та електричні характеристики. В результаті вони не тільки відповідають жорстким вимогам високовольтних застосувань, а й забезпечують значно більший термін служби.* ***Метою*** *дослідження є покращення діелектричних та теплових властивостей SiR шляхом включення наповнювача діоксиду кремнію (SiO_2) мікронного розміру.* ***Методологія***. *Зразки композиту SiR були приготовлені шляхом включення різних вагових відсотків мікронного розміру SiO_2 відповідно 10 %, 20 %, 30 % та 40 % від загальної ваги. Потім діелектрична міцність цих зразків була оцінена за чотирьох температур: 25 °C, 60 °C, 80 °C і 100 °C для оцінки ефективності ефекти в різних умовах. Крім того, зразки старіли протягом 10, 20 і 30 хвилин при тих же температурах перед випробуванням.* ***Результати*** *досліджували вплив термічної поведінки на характеристики напруги пробою композитів SiR, зістарених у різний час і за різних температур. Результати показують, що збільшення концентрації наповнювача збільшує діелектричну міцність SiR композитів. Найкраща пробивна напруга досліджених зразків була отримана при концентрації наповнювача 30 %.* ***Практична цінність***. *Додавання наповнювача SiO_2 мікронного розміру в матрицю SiR підвищує опір полімерних композитів термічним механічним напругам. У порівнянні з SiR, завантаженим SiO_2 у різних концентраціях, чистий SiR має найнижчу діелектричну міцність.* Бібл. 48, табл. 5, рис. 8.
Ключові слова: **діелектрична міцність, силіконова гума, діоксид кремнію мікророзміру, термічна поведінка, нейронна мережа.**

Introduction. Electrical insulators are critical components in power systems, ensuring the safe and efficient transmission and distribution of electricity. As power systems evolve to meet increasing demands and integrate renewable energy sources [1–5], the role of insulators becomes even more vital [6–8]. Polymeric materials come in several forms, including high-density polyethylene, silicone rubber (SiR), ethylene propylene diene monomer, and ethylene rubber [9, 10].

Because SiR has several advantages, including high dielectric strength (DS) and scale resistance, it is widely used in electrical applications. However, it is expensive and has poor mechanical strength and tracking resistance [11–14]. Therefore, pure silicone is grafted with some fillers to enhance its mechanical, thermal, and electrical properties and increase its service life; this combination is named SiR composites [15–18]. A composite is a material composed of two or more distinct constituent materials. These constituents exhibit significant differences in their physical and chemical properties compared to the individual components before combination [19].

Fillers like alumina trihydrate, aluminum oxide, zinc oxide, titanium oxide, calcium carbonate, and barium titanate that are added to SiR have gotten a lot of attention [20–22]. A lot of research has been done on how mixtures of micro- and nanosized fillers affect the mechanical, electrical, and thermal properties of SiR-based composites [23–25]. Developing micro- and nanocomposite materials can enhance the thermal and electrical characteristics [26–31]. The DS of polymers in HV applications is a crucial factor in assessing their dielectric performance [32–35].

Neural networks (NN) are a class of artificial intelligence models that draw inspiration from the design and operation of biological NNs, like those found in the human brain [36]. Because of their effectiveness, speed, and ability to handle complex nonlinear functions, they are frequently used to solve complicated and challenging real-world problems. This technique has been applied in several complicated engineering applications in various fields, including classification, prediction, intricate practical transformation models, and many other domains [37, 38].

The goal of the paper is to improve the SiR's dielectric strength under varying environmental conditions by adding an appropriate weight percentage of

inorganic filler. This work investigates, evaluates, and records the impact of micron-sized silica filler on the electrical and thermal properties of SiR insulators.

The NNs technique has been adopted to define the DS of the unmanufactured samples that have filler ratios in between the filler ratios of the manufactured samples. The goal is to define the DS of the unmanufactured samples, which have filler ratios in between those of the manufactured samples. Samples define the DS of the unmanufactured samples that have filler ratios in between the filler ratios of the manufactured samples.

Materials. In this study, the following chemical components were used:

1. The high-temperature vulcanized solid SiR was supplied by the German Company Sonax. Solid SiR contains high-molecular-weight polymers and relatively long polymer chains.

2. The filler used in this study is silicon dioxide (SiO_2) in micron-sized powder form. Supplied by Nanotech Egypt, it has a particle size of 20 μm ± 5 nm.

Sample preparation. The samples were fabricated in the form of discs with a diameter of 5 cm and a thickness of 2 mm for the DS test. Five different concentrations of SiR/SiO_2 composites were prepared, as specified in Table 1.

Table 1

Formulations of the prepared SiR/SiO_2 composite samples

Composite symbol	Mixtures of specimens
B	100 wt. % SiR
S10	90 wt. % SiR + 10 wt. % micron-sized SiO_2
S20	80 wt. % SiR + 20 wt. % micron-sized SiO_2
S30	70 wt. % SiR + 30 wt. % micron-sized SiO_2
S40	60 wt. % SiR + 40 wt. % micron-sized SiO_2

Micron-sized silica filler was added to the SiR base polymer to create the SiR composite samples. Filler concentrations are expressed as a percentage of the base polymer's total weight. The mixture is placed in a two-cylinder mill in the lab, which has a 470 mm diameter, 300 mm of operating distance, and a 1 mm gap between the cylinders. A day was given to the specimens prior to vulcanization. Figure 1 shows the rolling machine that is used for SiR processing. The samples were cut to the dimensions that were most appropriate for each testing procedure. It can be noted that the samples' color changes when SiO_2 filler is added (Fig. 2).

Dielectric strength test, which is a fundamental examination of an insulating material's electrical properties, is measured in voltage per unit length (kV/mm) [6, 39]. It illustrates how the insulating material withstands the intensity of an electric field without changing or losing its insulating properties. The shape of the used samples in the test should be a disc with a 1 mm thickness and a 5 cm diameter. Figure 3 shows the dielectric breakdown strength testing circuit. HV AC is applied to evaluate the breakdown voltage of the tested samples in various situations. To reduce surges on the transformer's HV side and more accurately determine the specimen's breakdown voltage, it is important to remember that the voltage applied to the specimen should be changed gradually and slowly. Because of the importance of the results, the test of each set was repeated many times, the data was gathered with high precision each time, and then the average value of the tested sample for each set was calculated and recorded.

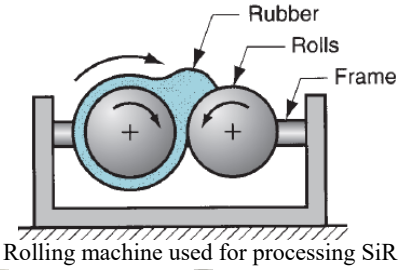

Fig. 1. Rolling machine used for processing SiR samples

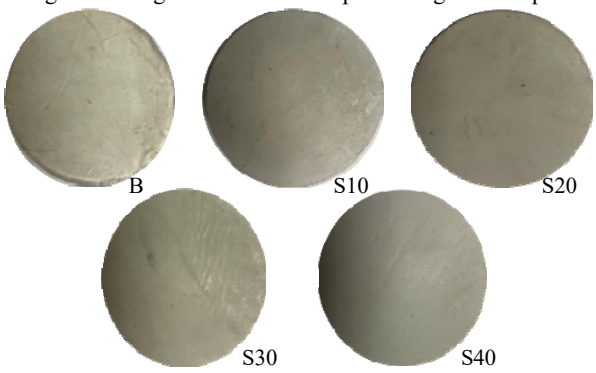

Fig. 2. Images of prepared SiR/SiO_2 composite samples

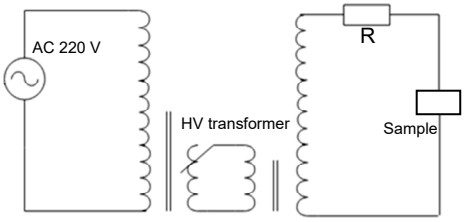

Fig. 3. The dielectric breakdown strength test laboratory circuit

Dielectric strength test procedure. In the testing circuit (Fig. 3), the test cells were energized using a test transformer (220 V / 100 kV) to determine the breakdown strength. The test cells were filled with transformer oil [40]. The DS of composite samples aged under multiple thermal-electrical stresses for different aging durations was evaluated at four temperature levels ranging from 25 °C to 100 °C, categorized as follows.

1) In the first scenario, the studied composite samples were heated until they reached different temperatures (25 °C, 60 °C, 80 °C, and 100 °C) with an initial exposure time of 0 min to these temperatures and then subjected to the DS tests. The first temperature (25 °C) represents normal ambient operating conditions. To simulate short-circuit conditions the temperature was set to 60 °C. The third temperature (80 °C) was selected to represent high-fault conditions under operating voltages exceeding 30 kV. Finally, the fourth temperature (100 °C) was chosen to simulate operation under heavy loading conditions and in environments with elevated temperatures.

2) In the second scenario, the composite samples subjected to thermal stress were analyzed as a function of aging time. They underwent thermal aging for 10, 20, and 30 minutes at the same test temperatures specified in the previous first scenario.

Experimental results and discussion. Dielectric strength results under the first scenario. Figure 4 presents the relationship between DS and the concentration of micro-sized SiO_2 under varying temperatures, evaluated according to the conditions of the first scenario.

At 25 °C, the breakdown voltages of S10, S20, S30, and S40 were 29.93, 34.8, 36.58, and 33.1 kV/mm, respectively. These values were higher than the DS of the pure sample (B), which measured 28.06 kV/mm.

A similar trend was observed at 60 °C, where the DS values of S10, S20, S30, and S40 increased to 27.01, 31.9, 33.02, and 30.47 kV/mm, respectively, surpassing the DS of B (26.21 kV/mm).

At 80 °C, the DS values of S10, S20, S30, and S40 were 24, 28.13, 29.64, and 27.44 kV/mm, respectively, again exceeding the DS of B (22.51 kV/mm).

Finally, at 100 °C, the DS values of S10, S20, S30, and S40 were 18.69, 19.87, 21.3, and 19.42 kV/mm, respectively, demonstrating improved performance compared to the DS of B (16.01 kV/mm).

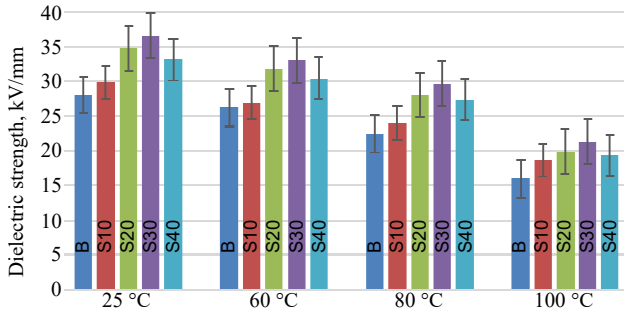

Fig. 4. Dielectric strength of the studied samples evaluated under the conditions of the first scenario

Dielectric strength results under the second scenario. According to the second scenario, additional sets of B, S10, S20, S30, and S40 were subjected to thermal aging at 25 °C, 60 °C, 80 °C, and 100 °C for 10, 20, and 30 minutes before undergoing the DS test.

Effect of 10-minute thermal aging. As shown in Fig. 5, incorporating different concentrations of SiO_2 into the composite samples (S10, S20, S30, and S40) and aging them for 10 minutes at 25 °C resulted in AC DS enhancements of 4 %, 22 %, 28 %, and 16 %, respectively. The corresponding DS values were 27.23, 32.01, 33.65, and 30.59 kV/mm, compared to the pure SiR (B) sample, which exhibited a DS of 26.32 kV/mm.

At 60 °C, the DS values of S10, S20, S30, and S40 increased to 25.27, 29.67, 31.28, and 28.09 kV/mm, respectively, surpassing the DS of B (24.03 kV/mm).

At 80 °C, the DS values of S10, S20, S30, and S40 were 23.84, 24.88, 27.09, and 24.02 kV/mm, respectively, all higher than the DS of B (20.01 kV/mm).

At 100 °C, the DS values of S10, S20, S30, and S40 reached 16.23, 17.00, 19.06, and 15.88 kV/mm, respectively, significantly exceeding the DS of B (12.54 kV/mm).

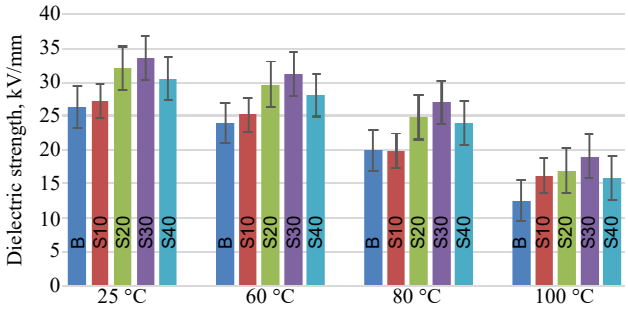

Fig. 5. Effect of 10-minute thermal aging on the dielectric strength of the studied samples

Effect of 20-minute thermal aging. At 25 °C, the DS of the studied samples S10, S20, S30, and S40 improved by approximately 5 %, 22 %, 30 %, and 18 %, respectively, reaching 26.1, 30.5, 32.39, and 29.37 kV/mm, compared to the DS of the pure SiR (B) sample, which was 25 kV/mm, as illustrated in Fig. 6.

At 60 °C, the DS values of S10, S20, S30, and S40 increased to 21.19, 25.47, 27.77, and 24.78 kV/mm, respectively, compared to sample B (20.44 kV/mm).

At 80 °C, the DS values were further enhanced to 18.89, 19.78, 21.66, and 18.27 kV/mm for S10, S20, S30, and S40, respectively, compared to 15 kV/mm for the B sample.

At 100 °C, the DS values of S10, S20, S30, and S40 were enhanced to 14.02, 15.49, 17.62, and 14.36 kV/mm, respectively, compared to sample B (10 kV/mm).

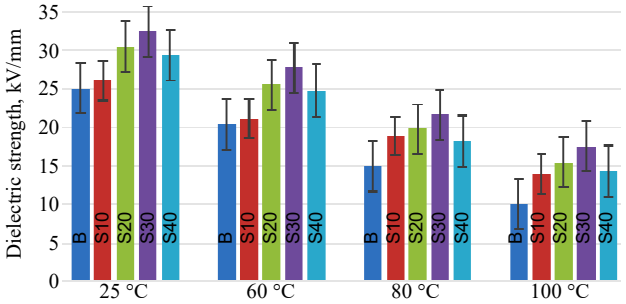

Fig. 6. Effect of 20-minute thermal aging on the dielectric strength of the studied samples

Effect of 30-minute thermal aging. At 25 °C, the DS values of S10, S20, S30, and S40 increased to 22.44, 26.59, 29.00, and 25.09 kV/mm, respectively, compared to the DS of sample B (21.52 kV/mm).

As shown in Fig. 7, comparable improvements were observed at 60°C, where the DS values of S10, S20, S30, and S40 increased to 20.11, 21.13, 23.09, and 20.45 kV/mm, respectively, while the DS of sample B was 16 kV/mm.

At 80°C, the DS values of S10, S20, S30, and S40 increased to 17.77, 18.59, 20.59, and 17.30 kV/mm, respectively, compared to 14 kV/mm for sample B.

At 100°C, the DS values for S10, S20, S30, and S40 improved by 43 %, 60 %, 83 %, and 47 %, respectively, compared to the DS of sample B.

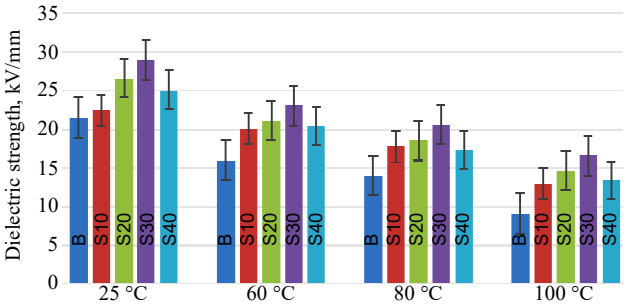

Fig. 7. Effect of 30-minute thermal aging on the dielectric strength of the studied samples

These results confirmed the overall trend observed in AC DS testing: the DS increased with higher SiO_2 filler concentration, peaking at 30 wt %. Beyond this concentration, a decline in DS was observed, likely due to agglomeration or conduction path formation between filler particles. The initial improvement is attributed to the formation of interaction zones within the SiR matrix [41–43].

These zones enhanced the interfacial area, thereby increasing the probability of charge trapping (e.g., electrons) at filler-matrix interfaces, which suppresses carrier mobility and improves breakdown strength [44–46].

Neural network (NN) modeling. An artificial neural network (NN) typically comprises an input layer, one or more hidden layers, and an output layer. Its performance depends on factors such as the number of neurons in each layer [47, 48]. Figure 8 presents the general architecture of the NN used in this study.

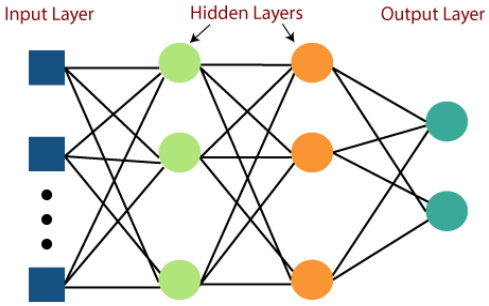

Fig. 8. General structure of a multilayer NN

NN validation in the first scenario application. Table 2 presents the experimental and NN-predicted DS values of SiR-based composite samples according to the first scenario. Four samples were used for model training, while the fifth sample served as a test case. The NN model demonstrated high prediction accuracy, with error percentages ranging from 0.0033 % (S40 at 80 °C) to 0.0977 % (S20 at 25 °C).

Table 2

Experimental and NN results for the dielectric strength of SiR-based composite samples (first scenario)

Sample	*T*, °C	Dielectric strength, kV/mm		
		Experimental results	NN estimations	Error, %
B	25 °C	28.06	28.036	0.0855
S10		29.93	29.9271	0.0097
S20		34.8	34.766	0.0977
S30*		36.58	36.6004	0.0558
S40		33.1	33.1013	0.0039
B	60 °C	26.21	26.2113	0.0050
S10		27.01	27.0064	0.0133
S20		31.9	31.8902	0.0307
S30*		33.02	33.0178	0.0067
S40		30.47	30.459	0.0361
B	80 °C	22.51	22.4921	0.0795
S10		24	24.0152	0.0633
S20		28.13	28.1262	0.0135
S30*		29.64	29.6365	0.0118
S40		27.44	27.4409	0.0033
B	100 °C	16.01	16.0142	0.0262
S10		18.69	18.6777	0.0658
S20		19.87	19.8523	0.0891
S30*		21.3	21.303	0.0141
S40		19.42	19.4027	0.0891

*Note. * Indicates samples used for model testing.*

NN validation (effect of 10-minute thermal aging). Table 3 summarizes the DS results for the studied samples. Again, the NN model was trained on four samples and tested on the fifth. The prediction error ranged from 0.0015 % (S10 at 25 °C) to 0.1448 % (S40 at 100 °C), validating the model's reliability.

Table 3

Experimental and NN results for the dielectric strength of SiR-based composite samples (effect of 10-minute thermal aging)

Sample	*T*, °C	Dielectric strength, kV/mm		
		Experimental results	NN estimations	Error, %
B	25 °C	26.32	26.3148	0.0198
S10		27.23	27.2296	0.0015
S20		32.01	32.0112	0.0037
S30*		33.65	33.6472	0.0083
S40		30.59	30.5911	0.0036
B	60 °C	24.03	24.018	0.0499
S10		25.27	25.2658	0.0166
S20		29.67	29.7121	0.1419
S30*		31.28	31.2765	0.0112
S40		28.09	28.0675	0.0801
B	80 °C	20.01	20.0075	0.0125
S10		19.84	19.8314	0.0433
S20		24.88	24.8847	0.0189
S30*		27.09	27.0826	0.0273
S40		24.02	24.0321	0.0504
B	100 °C	12.54	12.5411	0.0088
S10		16.23	16.2272	0.0173
S20		17	17.012	0.0706
S30*		19.06	19.0562	0.0199
S40		15.88	15.857	0.1448

*Note: * Indicates samples used for model testing.*

NN validation (effect of 20-minute thermal aging). Table 4 presents the NN prediction results for the DS of the studied samples subjected to 20-minute thermal aging at various temperatures.

Table 4

Experimental and NN results for the dielectric strength of SiR-based composite samples (effect of 20-minute thermal aging)

Sample	*T*, °C	Dielectric strength, kV/mm		
		Experimental results	NN estimations	Error, %
B	25 °C	25.01	25.012	0.0080
S10		26.1	26.1014	0.0054
S20		30.5	30.521	0.0689
S30*		32.39	32.387	0.0093
S40		29.37	29.371	0.0034
B	60 °C	20.44	20.438	0.0098
S10		21.19	21.1903	0.0014
S20		25.47	25.4712	0.0047
S30*		27.77	27.772	0.0072
S40		24.78	24.7835	0.0141
B	80 °C	15.01	15.013	0.0200
S10		18.89	18.8874	0.0138
S20		19.78	19.7801	0.0005
S30*		21.66	21.6622	0.0102
S40		18.27	18.266	0.0219
B	100 °C	10	10.0034	0.0340
S10		14.02	14.0201	0.0007
S20		15.49	15.4912	0.0077
S30*		17.62	17.622	0.0114
S40		14.36	14.3613	0.0091

*Note: * Indicates samples used for model testing.*

The trained NN model effectively estimated the DS values, with prediction errors ranging from 0.0005 % (S20 at 80 °C) to 0.0689 % (S20 at 25 °C).

NN validation (effect of 30-minute thermal aging). Finally, Table 5 summarizes the performance of the NN model in predicting the DS of samples subjected to 30-minute thermal aging. The model demonstrated high

predictive accuracy, with errors ranging from 0.0015 % for sample S20 at 25 °C to 1.0988 % for sample B at 100 °C.

Table 5

Experimental and NN results for the dielectric strength of SiR-based composite samples (effect of 30-minute thermal aging)

Sample	*T*, °C	Dielectric strength, kV/mm		
		Experimental results	NN estimations	Error, %
B	25 °C	21.52	21.5204	0.0019
S10		22.44	22.4411	0.0049
S20		26.59	26.5904	0.0015
S30*		29	29.0031	0.0107
S40		25.09	25.085	0.0199
B	60 °C	16	16.0012	0.0075
S10		20.11	20.101	0.0448
S20		21.13	21.1364	0.0303
S30*		23.09	23.0881	0.0082
S40		20.45	20.285	0.8068
B	80 °C	14	14.152	1.0857
S10		17.77	17.7864	0.0923
S20		18.59	18.48	0.5917
S30*		20.59	20.5865	0.0170
S40		17.3	17.3021	0.0121
B	100 °C	9.11	9.2101	1.0988
S10		13	13.001	0.0077
S20		14.61	14.6082	0.0123
S30*		16.64	16.5723	0.4069
S40		13.43	13.425	0.0372

*Note: * Indicates samples used for model testing.*

Conclusions.

1. Experimental studies conducted at four temperature levels (25 °C, 60 °C, 80 °C, and 100 °C) revealed an enhancement in the dielectric strength of the silicone rubber (SiR)-based composites filled with micron-sized silicon dioxide (SiO_2) particles, in comparison to the unfilled (pure) SiR sample.

2. The optimal dielectric strength was observed at a filler concentration of 30 wt %. Beyond this concentration, the dielectric strength declined, possibly due to the formation of conduction channels between filler particles within the SiR matrix.

3. The neural network technique accurately predicted the dielectric strength of SiR insulation filled with micron-sized silicon dioxide. This approach significantly reduced the costs associated with extensive testing and material procurement.

Acknowledgements. The authors express all their gratitude to the staff of the Department of Electrical Engineering, Aswan University, National Research Centre, Department of Polymers and Dyes, and Electrical Voltage Laboratory, where all the samples were made, and experimentations were carried out.

Conflict of interest. The authors declare that they have no conflicts of interest.

REFERENCES

1. Rihan M., Sayed A., Abdel-Rahman A.B., Ebeed M., Alghamdi T.A.H., Salama H.S. An artificial gorilla troops optimizer for stochastic unit commitment problem solution incorporating solar, wind, and load uncertainties. *PLOS ONE*, 2024, vol. 19, no. 7, art. no. e0305329. doi: https://doi.org/10.1371/journal.pone.0305329.

2. Bakeer A., Magdy G., Chub A., Jurado F., Rihan M. Optimal Ultra-Local Model Control Integrated with Load Frequency Control of Renewable Energy Sources Based Microgrids. *Energies*, 2022, vol. 15, no. 23, art. no. 9177. doi: https://doi.org/10.3390/en15239177.

3. Rashad A., Kamel S., Jurado F., Rihan M., Ebeed M. Optimal design of SSSC and crowbar parameters for performance enhancement of Egyptian Zafrana wind farm. *Electrical Engineering*, 2022, vol. 104, no. 3, pp. 1441-1457. doi: https://doi.org/10.1007/s00202-021-01397-0.

4. Rihan M., Nasrallah M., Hasanin, B. Performance analysis of grid-integrated brushless doubly fed reluctance generator-based wind turbine: modelling, control and simulation. *SN Applied Sciences*, 2020, vol. 2, no. 1, art. no. 114. doi: https://doi.org/10.1007/s42452-019-1907-0.

5. Noureldeen O., Rihan M., Hasanin B. Stability improvement of fixed speed induction generator wind farm using STATCOM during different fault locations and durations. *Ain Shams Engineering Journal*, 2011, vol. 2, no. 1, pp. 1-10. doi: https://doi.org/10.1016/j.asej.2011.04.002.

6. Ghazzaly A., Nasrat L., Ebnalwaled K., Rihan M. Recent Advances in Strengthening Electrical, Mechanical and Thermal Properties of Epoxy-Based Insulators for Electrical Applications. *SVU-International Journal of Engineering Sciences and Applications*, 2024, vol. 5, no. 2, pp. 153–161. doi: https://doi.org/10.21608/svusrc.2024.284150.1216.

7. El Sherkawy E., Nasrat L.S., Rihan M. The effect of thermal ageing on electrical and mechanical properties of thermoplastic nanocomposite insulation of power high-voltage cables. *Electrical Engineering & Electromechanics*, 2024, no. 3, pp. 66-71. doi: https://doi.org/10.20998/2074-272X.2024.3.09.

8. Sherkawy E.E., Nasrat L.S., Rihan M. Electrical and Mechanical Performances for Low-Density Polyethylene Nano Composite Insulators. *South Asian Research Journal of Engineering and Technology*, 2024, vol. 6, no. 2, pp. 53-60. doi: https://doi.org/10.36346/sarjet.2024.v06i01.007.

9. Rihan M., Ahmed Z., Nasrat L.S. Advancing High-Voltage Polymeric Insulators: A Comprehensive Review on the Impact of Nanotechnology on Material Properties. *SVU-International Journal of Engineering Sciences and Applications*, 2025, vol. 6, no. 1, pp. 93-105. doi: https://doi.org/10.21608/svusrc.2025.337910.1250.

10. Rihan M., Hassan A., Ebnalwaled K., Nasrat L.S. Electrical Insulators Based on Polymeric Materials: Toward New Cutting-edge Enhancements. *SVU-International Journal of Engineering Sciences and Applications*, 2025, vol. 6, no. 1, pp. 86-92. doi: https://doi.org/10.21608/svusrc.2025.311186.1233.

11. Nzenwa E., Adebayo A. Analysis of insulators for distribution and transmission networks. *American Journal of Engineering Research (AJER)*, 2019, vol. 8, pp. 138-145.

12. Haque S.M., Ardila-Rey J.A., Umar Y., Mas'ud A.A., Muhammad-Sukki F., Jume B.H., Rahman H., Bani N.A. Application and Suitability of Polymeric Materials as Insulators in Electrical Equipment. *Energies*, 2021, vol. 14, no. 10, art. no. 2758. doi: https://doi.org/10.3390/en14102758.

13. Ashokrao Fuke C., Anna Mahanwar P., Ray Chowdhury S. Modified ethylene-propylene-diene elastomer (EPDM)-contained silicone rubber/ethylene-propylene-diene elastomer (EPDM) blends: Effect of composition and electron beam crosslinking on mechanical, heat shrinkability, electrical, and morphological properties. *Journal of Applied Polymer Science*, 2019, vol. 136, no. 29, art. no. 47787. doi: https://doi.org/10.1002/app.47787.

14. Zhu Y. Influence of corona discharge on hydrophobicity of silicone rubber used for outdoor insulation. *Polymer Testing*, 2019, vol. 74, pp. 14-20. doi: https://doi.org/10.1016/j.polymertesting.2018.12.011.

15. Chudnovsky B.H. *Transmission, distribution, and renewable energy generation power equipment: Aging and life extension techniques*. CRC Press, 2017. 677 p. doi: https://doi.org/10.1201/9781315152790.

16. Hollaway L.C. Advanced Fiber Reinforced Polymer Composites. *High-Performance Construction Materials: Science and Applications*, 2008, pp. 207–263. doi: https://doi.org/10.1142/9789812797360_0005.

17. Ghassemi M. Accelerated insulation aging due to fast, repetitive voltages: A review identifying challenges and future research needs. *IEEE Transactions on Dielectrics and Electrical Insulation*, 2019, vol. 26, no. 5, pp. 1558-1568. doi: https://doi.org/10.1109/TDEI.2019.008176.

18. Ramalla I., Gupta R.K., Bansal K. Effect on superhydrophobic surfaces on electrical porcelain insulator, improved technique at polluted areas for longer life and reliability. *International Journal of Engineering & Technology*, 2015, vol. 4, no. 4, art. no. 509. doi: https://doi.org/10.14419/ijet.v4i4.5405.

19. Pandey J.C., Singh M. Dielectric polymer nanocomposites: Past advances and future prospects in electrical insulation perspective. *SPE Polymers*, 2021, vol. 2, no. 4, pp. 236-256. doi: https://doi.org/10.1002/pls2.10059.

20. Meyer L., Jayaram S., Cherney E.A. Thermal conductivity of filled silicone rubber and its relationship to erosion resistance in the inclined plane test. *IEEE Transactions on Dielectrics and Electrical Insulation*,

2004, vol. 11, no. 4, pp. 620-630. doi: https://doi.org/10.1109/TDEI.2004.1324352.
21. Zha J.-W., Dang Z.-M., Li W.-K., Zhu Y.-H., Chen G. Effect of micro-Si_3N_4-nano-Al_2O_3 co-filled particles on thermal conductivity, dielectric and mechanical properties of silicone rubber composites. *IEEE Transactions on Dielectrics and Electrical Insulation*, 2014, vol. 21, no. 4, pp. 1989-1996. doi: https://doi.org/10.1109/TDEI.2014.004330.
22. Zha J.-W., Zhu Y.-H., Li W.-K., Bai J., Dang Z.-M. Low dielectric permittivity and high thermal conductivity silicone rubber composites with micro-nano-sized particles. *Applied Physics Letters*, 2012, vol. 101, no. 6, art. no. 062905. doi: https://doi.org/10.1063/1.4745509.
23. Ramirez I., Cherney E., Jarayam S. Silicone rubber and EPDM micro composites filled with silica and ATH. *2011 Annual Report Conference on Electrical Insulation and Dielectric Phenomena*, 2011, pp. 20-23. doi: https://doi.org/10.1109/CEIDP.2011.6232586.
24. Saman N.M., Ahmad M.H., Buntat Z. Application of Cold Plasma in Nanofillers Surface Modification for Enhancement of Insulation Characteristics of Polymer Nanocomposites: A Review. *IEEE Access*, 2021, vol. 9, pp. 80906-80930. doi: https://doi.org/10.1109/ACCESS.2021.3085204.
25. Ansorge S., Schmuck F., Papailiou K. Impact of different fillers and filler treatments on the erosion suppression mechanism of silicone rubber for use as outdoor insulation material. *IEEE Transactions on Dielectrics and Electrical Insulation*, 2015, vol. 22, no. 2, pp. 979-988. doi: https://doi.org/10.1109/TDEI.2015.7076799.
26. Suchitra M., Vinay B.K., Parameshwara S., Umashankar M., Panchami S.V. Effect of Combining Nano- and Microfillers for the Assessment of Thermal Class of Glass Fiber-Reinforced Epoxy Composites for Outdoor Insulation. *IEEE Transactions on Dielectrics and Electrical Insulation*, 2023, vol. 30, no. 6, pp. 2896-2904. doi: https://doi.org/10.1109/TDEI.2023.3285860.
27. Lokanathan M., Acharya P.V., Ouroua A., Strank S.M., Hebner R.E., Bahadur V. Review of Nanocomposite Dielectric Materials With High Thermal Conductivity. *Proceedings of the IEEE*, 2021, vol. 109, no. 8, pp. 1364-1397. doi: https://doi.org/10.1109/JPROC.2021.3085836.
28. Du G., Wang J., Liu Y., Yuan J., Liu T., Cai C., Luo B., Zhu S., Wei Z., Wang S., Nie S. Fabrication of Advanced Cellulosic Triboelectric Materials via Dielectric Modulation. *Advanced Science*, 2023, vol. 10, no. 15, art. no. 2206243. doi: https://doi.org/10.1002/advs.202206243.
29. Niu H., Ren Y., Guo H., Małycha K., Orzechowski K., Bai S.-L. Recent progress on thermally conductive and electrical insulating rubber composites: Design, processing and applications. *Composites Communications*, 2020, vol. 22, art. no. 100430. doi: https://doi.org/10.1016/j.coco.2020.100430.
30. Bjellheim P., Helgee B. AC breakdown strength of aromatic polymers under partial discharge reducing conditions. *IEEE Transactions on Dielectrics and Electrical Insulation*, 1994, vol. 1, no. 1, pp. 89-96. doi: https://doi.org/10.1109/94.300236.
31. Ieda M. Dielectric Breakdown Process of Polymers. *IEEE Transactions on Electrical Insulation*, 1980, vol. EI-15, no. 3, pp. 206-224. doi: https://doi.org/10.1109/TEI.1980.298314.
32. Helgee B., Bjellheim P. Electric breakdown strength of aromatic polymers: dependence on film thickness and chemical structure. *IEEE Transactions on Electrical Insulation*, 1991, vol. 26, no. 6, pp. 1147-1152. doi: https://doi.org/10.1109/14.108152.
33. Bezprozvannych G.V., Grynyshyna M.V. Effective parameters of dielectric absorption of polymeric insulation with semiconductor coatings of power high voltage cables. *Electrical Engineering & Electromechanics*, 2022, no. 3, pp. 39-45. doi: https://doi.org/10.20998/2074-272X.2022.3.06.
34. Zolotaryov V.M., Chulieieva O.V., Chulieiev V.L., Kuleshova T.A., Suslin M.S. Influence of doping additive on thermophysical and rheological properties of halogen-free polymer composition for cable insulation and sheaths. *Electrical Engineering & Electromechanics*, 2022, no. 2, pp. 35-40. doi: https://doi.org/10.20998/2074-272X.2022.2.06.
35. Gurin A.G., Golik O.V., Zolotaryov V.V., Antonets S.Y., Shchebeniuk L.A., Grechko O.M. A statistical model of monitoring of insulation breakdown voltage stability in the process of enameled wires production. *Electrical Engineering & Electromechanics*, 2019, no. 1, pp. 46-50. doi: https://doi.org/10.20998/2074-272X.2019.1.08.
36. Shanmuganathan S., Samarasinghe S. *Artificial Neural Network Modelling*. Springer International Publishing, 2016. 472 p. doi: https://doi.org/10.1007/978-3-319-28495-8.
37. Kalogirou S.A. Artificial neural networks in renewable energy systems applications: a review. *Renewable and Sustainable Energy Reviews*, 2001, vol. 5, no. 4, pp. 373-401. doi: https://doi.org/10.1016/S1364-0321(01)00006-5.
38. Abdolrasol M.G.M., Hussain S.M.S., Ustun T.S., Sarker M.R., Hannan M.A., Mohamed R., Ali J.A., Mekhilef S., Milad A. Artificial Neural Networks Based Optimization Techniques: A Review. *Electronics*, 2021, vol. 10, no. 21, art. no. 2689. doi: https://doi.org/10.3390/electronics10212689.
39. Lothongkam C. *Dielectric Strength Behaviour and Mechanical Properties of Transparent Insulation Materials Suitable to Optical Monitoring of Partial Discharges*. Dr.-Ing. Dissertation. Leibniz University Hannover, 2014. 154 p.
40. *ASTM D149-09. Standard Test Method for Dielectric Breakdown Voltage and Dielectric Strength of Solid Electrical Insulating Materials at Commercial Power Frequencies*. 2013, 13 p. doi: https://doi.org/10.1520/D0149-09.
41. Essawi S., Nasrat L., Ismail H., Asaad J. Improvement of dielectric strength and properties of cross-linked polyethylene using nano filler. *International Journal of Electrical and Computer Engineering (IJECE)*, 2022, vol. 12, no. 3, pp. 2264-2272. doi: https://doi.org/10.11591/ijece.v12i3.pp2264-2272.
42. Ullah I., Akbar M. Anti-aging characteristics of RTV-SiR aided HV insulator coatings: Impact of DC polarity and fillers. *Materials Chemistry and Physics*, 2022, vol. 278, art. no. 125634. doi: https://doi.org/10.1016/j.matchemphys.2021.125634.
43. Pleşa I., Noţingher P., Schlögl S., Sumereder C., Muhr M. Properties of Polymer Composites Used in High-Voltage Applications. *Polymers*, 2016, vol. 8, no. 5, art. no. 173. doi: https://doi.org/10.3390/polym8050173.
44. Laurent C., Teyssedre G., Le Roy S., Baudoin F. Charge dynamics and its energetic features in polymeric materials. *IEEE Transactions on Dielectrics and Electrical Insulation*, 2013, vol. 20, no. 2, pp. 357-381. doi: https://doi.org/10.1109/TDEI.2013.6508737.
45. Danikas M.G., Tanaka T. Nanocomposites-a review of electrical treeing and breakdown. *IEEE Electrical Insulation Magazine*, 2009, vol. 25, no. 4, pp. 19-25. doi: https://doi.org/10.1109/MEI.2009.5191413.
46. Vinod P., Desai B.M.A., Sarathi R., Kornhuber S. Investigation on the thermal properties, space charge and charge trap characteristics of silicone rubber nano–micro composites. *Electrical Engineering*, 2021, vol. 103, no. 3, pp. 1779-1790. doi: https://doi.org/10.1007/s00202-020-01195-0.
47. Basheer I.A., Hajmeer M. Artificial neural networks: fundamentals, computing, design, and application. *Journal of Microbiological Methods*, 2000, vol. 43, no. 1, pp. 3-31. doi: https://doi.org/10.1016/S0167-7012(00)00201-3.
48. Ciresan D.C., Meier U., Masci J., Gambardella L.M., Schmidhuber J. Flexible, high performance convolutional neural networks for image classification. *Proceedings of the Twenty-Second International Joint Conference on Artificial Intelligence*, 2011, pp. 1237-1242. doi: https://doi.org/10.5591/978-1-57735-516-8/IJCAI11-210.

Received 02.10.2024
Accepted 30.12.2024
Published 02.05.2025

Zahraa Ahmed [1], *PhD, Projects Design Engineering,*
Loai S. Nasrat [2], *Professor,*
Mahmoud Rihan [3], *Associate Professor,*
[1] Department of Projects Design Engineering,
Upper Egypt Electricity Distribution Company, Luxor, Egypt,
e-mail: zahraaabdelkareem92@gmail.com (Corresponding Author)
[2] Electrical Power and Machines Engineering Department,
Faculty of Engineering, Aswan University, Egypt,
e-mail: loainasrat@aswu.edu.eg
[3] Electrical Power and Machines Engineering Department,
Faculty of Engineering, South Valley University, Qena, Egypt,
e-mail: mahmoudrihan@eng.svu.edu.eg

How to cite this article:
Ahmed Z., Nasrat L.S., Rihan M. The effect of SiO_2 microparticle concentration on the electrical and thermal properties of silicone rubber for electrical insulation applications. *Electrical Engineering & Electromechanics*, 2025, no. 3, pp. 84-89. doi: https://doi.org/10.20998/2074-272X.2025.3.12

АНДРІЄНКО ПЕТРО ДМИТРОВИЧ

(до 85-річчя з дня народження)

Доктор технічних наук, професор, заслужений винахідник УРСР, академік Транспортної академії наук України, завідувач кафедри «Електричні та електронні апарати» Національного університету «Запорізька політехніка» Андрієнко Петро Дмитрович народився 26 квітня 1940 р. в п. Ханженково Донецької області.

В 1962 р. Петро Дмитрович закінчив Одеський політехнічний інститут, електротехнічний факультет, а в 1967 році – факультет «Автоматики і телемеханіки». Молодий спеціаліст був розподілений на роботу у Всесоюзний інститут трансформаторобудування (ВІТ) у м. Запоріжжя. Працював інженером в бюро електроприводу, розробляв привод першої в СРСР автоматичної лінії розкрою рулонної електротехнічної сталі. У 1964 р. перейшов на роботу в СКБ напівпровідникової техніки, перетворене в НДІ «Перетворювач», на посаду старшого інженера лабораторії тиристорних агрегатів.

З 1965 по 2008 рр. пройшов шлях від старшого інженера, керівника групи, начальника лабораторії, відділу, до заступника директора Всесоюзного науково-дослідного інституту, згодом – директора Українського інституту силової електроніки ВАТ НДІ «Перетворювач». Під його керівництвом і з безпосередньою участю були створені найбільші в СРСР серії тиристорних агрегатів постійного струму типу АТ, АТР, АТВ потужністю до 1000 кВт, частотно-регульовані електроприводи серії ЕКТ, ЭКТР, ЭКТ-1 потужністю до 500 кВт.

Отримані результати під час розробки виробів нової техніки згодом стали основою його кандидатської дисертації «Захист реверсивних тиристорних агрегатів», яку він успішно захистив у 1971 р. в Одеському політехнічному інституті, а пізніше і докторської дисертації «Тиристорні перетворювачі частоти з автономним інвертором для електроприводу», захист якої відбувся в Інституті електродинаміки НАН України у 1990 р.

За період незалежності України під його керівництвом була створена низка нових типів перетворювачів: для магістрального аміакопроводу «Тольятті – Одеса» потужністю 2000 кВт, 6 кВ; для тягової електропередачі змінного струму першого українського дизель-поїзда типу ДЕЛ-02, електровоза ВЛ-40У, електропоїздів, для першої української вітроустановки з аеродинамічною мультиплікацією типу ТГ-1000, ТГ-750.

Андрієнко П.Д. є автором понад 200 наукових праць, у тому числі 3 монографії, 3 навчальних посібника, понад 100 авторських свідоцтв та патентів.

У 1990 р Андрієнко П.Д. був удостоєний звання «Заслужений винахідник УРСР».

Велику увагу приділяє підготовці кадрів. Під його керівництвом захищено 2 докторські та 10 кандидатських дисертацій. З 1980 р. по 2011 р. Петро Дмитрович працював доцентом, а потім професором у ЗНТУ (за сумісництвом). З 2011 р. по теперішній час є завідувачем кафедри «Електричні і електронні апарати» Національного університету «Запорізька політехніка». Під його керівництвом на кафедрі активно впроваджуються у навчальний процес нові методи і форми навчання: технології 3D друку, навчання англійською мовою, організовано студентське науково-конструкторське бюро, новий комп'ютерний клас для підготовки магістрів та аспірантів. В 2023 р. відбувся перший набір студентів за спеціальністю «Електроніка».

Професор Андрієнко П.Д. неодноразово був членом спеціалізованих вчених рад із захисту кандидатських і докторських дисертацій. Він є членом редколегій наукових журналів «Електротехніка і електроенергетика», «Прикладні аспекти інформаційних технологій» та «Вісник сучасних інформаційних технологій». Займаючись педагогічною діяльністю, він не переривав своєї науково-практичної діяльності, будучи першим заступником генерального директора з науки ТОВ «НДІ Перетворювач», керівником українського технічного комітету ТК 31 «Силова електроніка».

За плідну науково-технічну, педагогічну, громадську роботу Андрієнко П.Д. нагороджений орденами: «Трудового Червоного Прапора» (1981 р), «За заслуги» III ступеня (1998 р), «За заслуги перед Запорізьким краєм» III ступеня (2015 р), та II ступеня (2020 р.), медаллю «Ветеран праці». Нагороджений почесними грамотами Запорізької обласної ради та обладміністрації.

В 2023 р. призначено довічно стипендію Кабінету Міністрів України за видатні заслуги у сфері вищої освіти та науково – педагогічної діяльності.

Широко відомі його особисті людські якості, що поєднують вимогливість і принциповість керівника з толерантністю та високою порядністю, незмінну наукову культуру і такт з вмінням відстоювати свої наукові погляди і життєві цінності.

Ректорат, електротехнічний факультет Національного університету «Запорізька політехніка», колектив кафедри «Електричні і електронні апарати» щиро вітають Петра Дмитровича з ювілеєм, зичать йому міцного здоров'я, подальших творчих успіхів у його багатогранній та плідній науковій і педагогічній діяльності. Нехай доля шле міцне здоров'я та гарний настрій на довгі літа, а віра, надія і любов будуть вірними супутниками на життєвому шляху.

Редакційна колегія журналу «Електротехніка і електромеханіка» приєднується до цих щирих побажань.

КИРИЛЕНКО ОЛЕКСАНДР ВАСИЛЬОВИЧ

(до 75-річчя з дня народження)

Директор Інституту електродинаміки НАН України, доктор технічних наук, професор, академік НАН України О.В. Кириленко народився 20 травня 1950 р. У 1973 р. закінчив Київський політехнічний інститут (нині НТУ України «КПІ ім. І. Сікорського») за фахом інженер-електрик. У період 1973–1975 рр. працював на кафедрі «Електричні мережі та системи» КПІ. Починаючи з 1975 р. і дотепер Олександр Васильович працює в Інституті електродинаміки НАН України, в різні періоди обіймаючи посади: молодшого наукового співробітника, завідувача лабораторії, завідувача відділу, вченого секретаря інституту, заступника директора інституту з наукової роботи, а з 2007 р. – директора Інституту електродинаміки НАН України.

Науковий ступінь кандидата технічних наук отримав у 1981 р., звання старшого наукового співробітника – у 1986 р., докторську дисертацію захистив у 1993 р., звання професора отримав у 1996 р., членом-кореспондентом НАН України був обраний у 1997 р., а академіком НАН України – у 2006 р.

Кириленко Олександр Васильович – відомий вчений як в України, так і за її межами завдяки своїм працям у галузі електроенергетики, що пов'язані з підвищенням надійності та ефективності функціонування електроенергетичних об'єктів та систем, розробкою методів моделювання електричних мереж та електроенергетичних об'єктів. Його різнобічні дослідження процесів функціонування електроенергетичних систем забезпечили розвиток теорії створення систем керування такими процесами, дозволили запропонувати принципи, методи побудови відповідних інтегрованих інформаційно-управляючих систем та їхніх елементів і створити відповідні апаратні та програмні засоби. Ним запропоновано нові підходи до побудови систем контролю та діагностики в електроенергетиці, вирішено питання забезпечення їхньої надійності та відмовостійкості, точності та швидкодії, досліджено особливості формалізації та розв'язання задач параметричної оптимізації аналогових елементів та пристроїв автоматики електроенергетичних систем. Розвинуто теорії аналізу та оптимізації первинних перетворювачів струму, що призначені для роботи зі стабільними величинами похибок в усталених та перехідних режимах роботи, запропоновано методи відновлення сигналу в таких пристроях.

Сьогодні ним розробляється концепція та методологія побудови інтегрованих інформаційно-управляючих систем потужних електроенергетичних об'єктів системного значення як складових системи керування функціонуванням електроенергетичних систем. В даний час Олександр Васильович активно працює над розвитком теорії побудови інтелектуальних інформаційно-керуючих систем в електроенергетиці, орієнтованих на реалізацію основних положень концепції Smart Grid, приділяючи значну увагу науково-технічним питанням забезпечення ефективності інноваційного розвитку та керованості об'єднаної електроенергетичної системи (ОЕС) України за умов впровадження нової моделі ринку електроенергії, зростання частки відновлюваних джерел енергії в структурі її генеруючих потужностей, синхронної роботи ОЕС України з ENTSO-E. Ним заснована наукова школа з моделювання режимів електроенергетичних об'єктів та створення інтелектуальних інформаційно-керуючих систем.

Результати наукових робіт Кириленка О.В. висвітлено в численних публікаціях (понад 300), серед яких – понад 20 монографій, 5 навчальних посібників та підручників.

Олександр Васильович успішно поєднує наукову, організаційну, педагогічну та громадську діяльність. За останні роки під керівництвом О.В. Кириленко підготовлено 3 доктори та 11 кандидатів технічних наук. Він є академіком-секретарем Відділення фізико-технічних проблем енергетики НАН України, очолює експертну раду з електротехніки та енергетики Департаменту атестації наукових кадрів МОН України та технічний комітет зі стандартизації «Керування енергетичними системами та пов'язані з ним процеси інформаційної взаємодії» (ТК 162), ходить до складу спеціалізованої вченої ради з захисту докторських дисертацій, редколегій багатьох фахових періодичних видань.

Наукові досягнення і громадська діяльність О.В. Кириленка відзначена державними преміями та нагородами: 1983 р. – медаллю Академії наук УРСР та премією для молодих вчених; 1988 р. – золотою медаллю ВДНГ СРСР; 1995 р. – премією ім. С.О. Лебедєва НАН України; 1999 р. – державною премією України в галузі науки і техніки за роботу «Розробка наукових основ та засобів підвищення енергетичної ефективності та їх впровадження у системах управління постачанням і використанням електроенергії, природного газу та тепла»; 2008 р. – присвоєно звання «Заслужений діяч науки і техніки України»; 2009 р. – присвоєно звання лауреата «Лідер паливно-енергетичного комплексу-2009» у номінації «Вчений»; 2020 р. – нагороджений орденом князя Ярослава Мудрого V ст.

Ректорат та колектив НТУ «ХПІ» щиро вітає Олександра Васильовича з ювілеєм, бажає міцного здоров'я, щастя, успіхів та натхнення у його подальшій науковій діяльності.

Редакційна колегія журналу «Електротехніка і електромеханіка» приєднується до цих щирих побажань.

Матеріали приймаються за адресою:
Кафедра "Електричні апарати", НТУ "ХПІ", вул. Кирпичева, 2, м. Харків, 61002, Україна
Електронні варіанти матеріалів по e-mail: a.m.grechko@gmail.com

Довідки за телефонами: +38 067 359 46 96 Гречко Олександр Михайлович

Передплатний індекс: 01216